Synthesis and characterisation of new layered oxychalcogenide materials

Withers, Neil D.

Abstract

Synthesis and characterisation of new layered oxychalcogenide materials. Ph.D. Thesis
Neil Withers 2004.

Chapter One describes oxychalcogenide phases found in the literature with layered and three-dimensional structures. An attempt is made to systematise the structures of a range of materials to help understand their structural chemistry. Synthetic details and physical properties are also reported. Potential applications of these materials are discussed, with emphasis placed on compounds similar to those discussed in later chapters.

Chapter Two gives full details of the synthetic methods, characterisation techniques and physical property measurements employed in the work described in the following chapters.

Chapter Three contains the results of experiments on $La_2O_3M_2Se_2$ (M = Mn, Co) materials, including synthesis, room temperature structure and thermal behaviour by powder X-ray and neutron diffraction, magnetic and conductivity properties. The low temperature magnetic structures of both compounds have been determined and reveal antiferromagnetic ordering of spins within M_2O layers.

Chapter Four reports the synthesis and room temperature structure of the $A_2MCu_2O_2X_2$ (A = Sr, Ba; M = Mn, Co, Ni, Zn; X = S, Se) family of compounds. The results of variable temperature powder X-ray diffraction, magnetometry and conductivity experiments on these compounds are also discussed. They show smooth thermal expansion properties except $Ba_2CoCu_2O_2S_2$ and $Sr_2NiCu_2O_2Se_2$, which show deviations between 100 and 200 K, indicative of structural/magnetic phase transitions at low temperature. Varying magnetic properties are found and a number of the compounds are found to be semiconductors.

Chapter Five discusses attempts to prepare the $A_2MO_2Ln_2O_2X_2$ (A = Sr, Ba; M = Co, Mn, Fe; Ln = La, Y, Gd; X = S, Se) family of compounds. The potential stability of such compounds is investigated using bond valence calculations.

Chapter Six outlines the work done in indexing, solving and refining the crystal structure of an α,α thiophene tin tetramer from powder X-ray diffraction data.

Synthesis and characterisation of new layered oxychalcogenide materials

Neil D. Withers M.Sci (Dunelm)
The College of St. Hild and St. Bede
University of Durham

Supervisor: Dr John S. O. Evans

A thesis submitted in partial fulfilment of the requirements for the degree of Doctor of Philosophy.

Department of Chemistry
University of Durham
2004

Acknowledgements

This *Ph.D.* would have been impossible with the help of a great many people, all of whom deserve thanks:

First and foremost, John Evans, for starting me off on this whole thing as a 4th year project student, and then for believing in me enough to take me on as a Ph.D. student. And that was only the beginning – thanks for four (+?) years of constant help and support and never being too busy to answer the stupidest of questions.

Thanks to all the lab people; Simon Allen for being all-knowing when I was a youth of a 4th year and a great music and food educator, Ian King for being all-drinking when I was a youth of a 4th year and fellow football/cricket/procrastinating fan, Amber Thompson for being slightly less lost than I was as a 4th year, Rich (I) Gover for much lab/gsas/topas assistance over 3 years and for a caffeine addiction, Clare Crossland for bringing some insanity to the office, Lue Howard for many film discussions, Matt Hampson for the Ramones and feats of eating, Graham Stinton for being more stressed in his first year than I was in continuation, Loc Nguyen for being a smiling new addition to the office, Amin El-Meligi for the arrows and Ivana Evans for crystallography gossip, some wonderful meals and some valuable proof reading.

The various fourth year project students who we have helped and hindered – Rich (II) Cordiner, Joanna Brindley, Nick Warmingham, Malcolm Tait, Rich (III) Harrington, Becky Ward, Pete Hickey and Sarah Lister – have all helped and hindered me down the years.

Lots of people in the physics department – Dr. Ian Terry and Sean Giblin for much guidance and help with magnetic measurements. Dr. Andy Brinkman, Dr. Arnab Basu, Dr. Rainer Schmidt and Ben Cantwell for conductivity measurements, Dr. Ken Durose for the generous use of his *I-V* measuring facilities and Guillaume Zoppi for showing us how to use them.

Many thanks to Simine Short at the IPNS, Argonne, for the neutron data collected on the SEPD diffractometer.

Within the chemistry department, I'd like to thank all the technical staff, especially Brian Hall (king of gloveboxes) and Malcolm & Peter the glassblowers, if for nothing more than being so much better than me with a blowtorch and quartz! Joe and the guys from stores, the mechanical workshops for making stuff, Barry Barker and Kelvin for fixing stuff, especially the d5 chiller. Thanks to Dr. Andy Hughes for initial glovebox use, first year help (and for the Open Day distractions) and Prof. Judith Howard's crystallography group (especially Dima) for their more comprehensive toolkit.

I'd like to thank everyone past and present at Hild Bede, especially Mikey Bruce and Tim Owen, Dr. Vernon Armitage, Dr. Alan Pearson and Carol Carr and my tutor group, for everything, especially for providing the most fun place and the most fun people to live with for the past 8 years.

Finally, family thanks to Mum, Dad and Paul. M+D for, well, everything really.

Declaration

The work described in this thesis is entirely my own work, except where I have acknowledged help from a named person or given a reference to a published source or a thesis.

The research presented was performed in the Department of Chemistry, University of Durham between October 2000 and December 2004, the results of which have not been submitted for a degree in this or any other university.

This thesis conforms to the word limit set out in the Degree Regulations. It contains ~47,000 words including appendices and footnotes but excluding references, or experimental data included on the CD located on the inside cover of the thesis.

Date: N. Withers Signature: 26/2/2005.

Statement of Copyright

Glossary of abbreviations

CCR = closed circuit refrigerator

CSD = Cambridge structural database

ESD = estimated standard deviation

FC = field cooled

GSAS = general structure analysis suite

IPNS = intense pulsed neutron source

MPMS = magnetic properties measurement system

OFET = organic field effect transistor

PDF = powder diffraction file

PSD = position sensitive detector

SQUID = superconducting quantum interference device

TOF = time of flight

TOPAS = total pattern analysis suite

ZFC = zero field cooled

Table of contents

Table of figures

Chapter 1 Introduction and literature review

Chapter 2 Experimental

Chapter 3 $La_2O_3M_2X_2$ compounds

Chapter 4 $A_2MCu_2O_2X_2$ compounds

Chapter 5 $A_2MO_2Ln_2O_2X_2$ compounds

Chapter 6 Structure solution using powder X-ray diffraction

Table of tables

Chapter 1 Introduction and literature review

Chapter 2 Experimental

Chapter 3 $La_2O_3M_2X_2$ compounds

Chapter 4 $A_2MCu_2O_2X_2$ compounds

Chapter 5 $A_2MO_2Ln_2O_2X_2$ compounds

Chapter 6 Structure solution using powder X-ray diffraction

Willpower weak...and temptation strong.
[Do right woman - do right man, Penn/Moman 1967]

Aim for the stars and you'll hit the ceiling.
[John Squire]

If it we knew what it was we were doing, it would not be called research, would it?
[Einstein]

One o'clock struck, two, three, four - and still the slips flew about all round him; still the untiring pen scraped its way ceaselessly from top to bottom of the page; still the white chaos of paper rose higher and higher all round his chair.
[The Woman in White, Collins]

Furthermore I humbly beseech all who read this ... that they will not forget frequently to ask for God's mercy upon my weaknesses ... of mind.
[Preface to The Ecclesiastical History of the English People, Bede]

But, like those young trees which thwart the efforts of the gardener and turn obstinately toward the side whence come air and sunshine, the younger brother grew and shot forth luxurious branches only on the side of idleness, ignorance and debauchery.
[The Hunchback of Notre-Dame, Victor Hugo]

Someday soon this will all be someone else's dream.
[Never Forget, Take That]

Out of darkness cometh light.
[Motto of the city of Wolverhampton, c.f. slogan in a recent ad campaign for Guinness]

"Begin at the beginning," the King said gravely, "and go on till you come to the end: then stop"
[Alice's Adventures in Wonderland, Lewis Carroll]

Chapter 1 Introduction and literature review

This chapter introduces the subject of oxychalcogenide materials with reference to their syntheses, structures, properties and potential applications. The chapter is divided into two sections; oxychalcogenides with layered structures, and those with extended three dimensional structures. Particular emphasis is placed on compounds similar to those discussed in the later chapters of this thesis, and in light of this, only quaternary and higher oxychalcogenides are considered.

1.1 General introduction

Oxychalcogenides, materials with both oxygen and another group 16 element (S, Se or Te; commonly denoted *X* throughout this chapter and thesis) in the 2- oxidation state, are unusual materials with interesting properties. Unusual, because in the presence of oxygen chalcogens would more normally be found in a higher oxidation state, as typified by SO_4^{2-} and SO_3^{2-}, the sulfate and sulfite ions. Indeed, there are few naturally occurring minerals with both oxygen and a chalcogen in the 2- state: kermesite[1] (SbO_2S_2) and sarabauite[2] ($CaSb_{10}S_6O_{10}$) being well known examples. They are interesting because many of the oxychalcogenide compounds and their doped/intercalated derivatives in the literature have novel and desirable properties. These include ionic conductivity,[3] ferromagnetism[4,5] and anti-ferromagnetism[6] and interesting optical properties (such as phosphorescence for use in television screens[7,8] and high gain lasers). With many layered oxychalcogenides featuring similar metal/oxygen layers to those found in cuprate superconductors and materials with important magnetic properties, there has been an increase in the interest in such materials. One of the important factors in oxychalcogenide chemistry is the ability to control the properties of the materials through not only the cationic sub-lattice, but also the anionic sub-lattice.

There are many different types of oxychalcogenides, with a variety of metals from the whole periodic table involved, indeed metals from the *s*-, *p*-, *d*- and *f*-blocks form oxychalcogenide compounds. However, they can be broadly categorised into those that form materials with layered structures and those that form structures with a three-dimensional connectivity.

Figure 1.1 shows which of the elements that are found in oxychalcogenides are in a solely oxygen coordinated environment, solely chalcogen coordinated or coordinated by both oxygen and a chalcogen. This is a good illustration of the number and variety of existing and possible oxychalcogenide compounds. In addition, it serves to show where there are gaps in the existing materials known, for instance where there is one member of a group missing;

such as there are chromium and tungsten oxychalcogenide phases known, but there are no extended molybdenum (the other member of Group 6) containing oxychalcogenides.

Present in O only coordination

1	2											13	14	15	16	17	18
								H									He
Li	Be											B	C	N	O	F	Ne
Na	Mg	3	4	5	6	7	8	9	10	11	12	Al	Si	P	S	Cl	Ar
K	Ca	**Sc**	**Ti**	V	**Cr**	**Mn**	**Fe**	**Co**	**Ni**	**Cu**	**Zn**	**Ga**	Ge	As	Se	Br	Kr
Rb	**Sr**	**Y**	Zr	Nb	Mo	Tc	Ru	Rh	Pd	Ag	Cd	**In**	Sn	Sb	Te	I	Xe
Cs	Ba	**La**	Hf	**Ta**	**W**	Re	Os	Ir	Pt	Au	Hg	Tl	Pb	Bi	Po	At	Rn
Fr	Ra	Ac	Rf	Db	Sg	Bh	Hs	Mt									

La	**Ce**	**Pr**	**Nd**	**Pm**	**Sm**	**Eu**	**Gd**	Tb	Dy	Ho	Er	Tm	Yb	Lu
Ac	Th	Pa	U	Np	Pu	Am	Cm	Bk	Cf	Es	Fm	Md	No	Lr

Present in *X* only coordination

1	2											13	14	15	16	17	18
								H									He
Li	Be											B	C	N	O	F	Ne
Na	Mg	3	4	5	6	7	8	9	10	11	12	Al	Si	P	S	Cl	Ar
K	Ca	Sc	**Ti**	V	**Cr**	Mn	Fe	Co	**Ni**	**Cu**	Zn	**Ga**	**Ge**	As	Se	Br	Kr
Rb	Sr	Y	Zr	Nb	Mo	Tc	Ru	Rh	Pd	**Ag**	Cd	**In**	**Sn**	**Sb**	Te	I	Xe
Cs	Ba	La	Hf	Ta	W	Re	Os	Ir	Pt	Au	Hg	Tl	Pb	**Bi**	Po	At	Rn
Fr	Ra	Ac	Rf	Db	Sg	Bh	Hs	Mt									

La	**Ce**	Pr	**Nd**	Pm	**Sm**	Eu	Gd	Tb	Dy	Ho	**Er**	Tm	Yb	**Lu**
Ac	Th	Pa	U	Np	Pu	Am	Cm	Bk	Cf	Es	Fm	Md	No	Lr

Present in O and *X* coordination

1	2											13	14	15	16	17	18
								H									He
Li	Be											B	C	N	O	F	Ne
Na	Mg	3	4	5	6	7	8	9	10	11	12	Al	Si	P	S	Cl	Ar
K	**Ca**	**Sc**	**Ti**	**V**	**Cr**	**Mn**	**Fe**	**Co**	Ni	Cu	**Zn**	**Ga**	Ge	As	Se	Br	Kr
Rb	**Sr**	**Y**	**Zr**	**Nb**	Mo	Tc	Ru	Rh	Pd	Ag	Cd	In	Sn	Sb	Te	I	Xe
Cs	**Ba**	**La**	**Hf**	**Ta**	**W**	Re	Os	Ir	Pt	Au	Hg	Tl	Pb	**Bi**	Po	At	Rn
Fr	Ra	Ac	Rf	Db	Sg	Bh	Hs	Mt									

La	**Ce**	**Pr**	**Nd**	**Pm**	**Sm**	**Eu**	**Gd**	Tb	**Dy**	Ho	Er	Tm	Yb	Lu
Ac	**Th**	Pa	**U**	**Np**	Pu	Am	Cm	Bk	Cf	Es	Fm	Md	No	Lr

Figure 1.1 Periodic tables showing metals that form oxychalcogenide compounds highlighted. Top shows metals which are only coordinated by O atoms, middle only by *X* atoms, bottom those which are coordinated by both O and *X* atoms.

1.2 Layered oxychalcogenides

Many of the layered oxychalcogenides form tetragonal (or pseudo tetragonal) phases which can be described in terms of an approximately 4 Å square unit cell. This attribute arises since there is a natural relationship between transition metal—oxygen bonds being approximately 2

Å in length, with eight coordinate lanthanoid—oxygen bonds being approximately $2\sqrt{2}$ Å (2.282 Å) long and transition metal—sulfur bonds also being $2\sqrt{2}$ Å long. There is therefore a natural epitaxy possible between layers such that many of the structures can conceptually be broken down into and described in terms of repetitions of simple building blocks.

In fact, many of the structures can be described in terms of repetitions of the blocks shown in Figure 1.2.

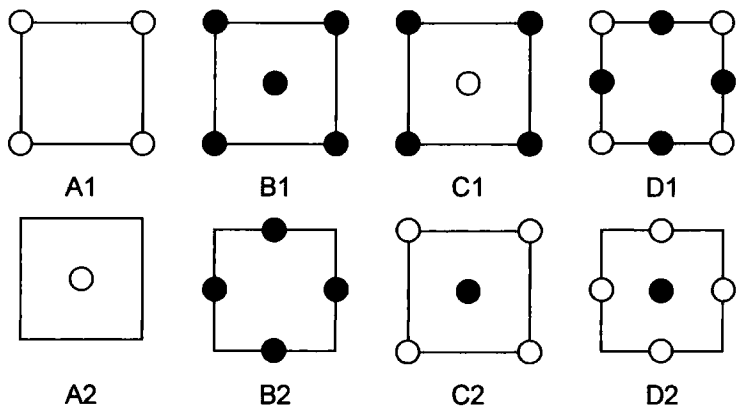

Figure 1.2 Units for describing layered oxychalcogenides. White and black circles represent different atoms.

For example, repeated stacking of layers in the order [D1(Ti, O), C1(Ba, O)]$_\infty$ (where the atoms in parentheses occupy the white and black sites in Figure 1.2) results in the cubic perovskite structure of $BaTiO_3$ with octahedral transition metals and twelve coordinate calcium (Figure 1.3);

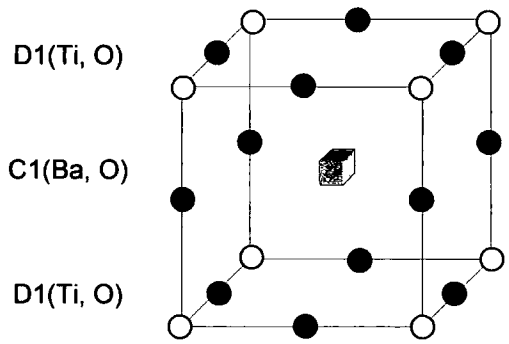

Figure 1.3 Perovskite structure; Ti sites shown as filled circles, O sites open circles, 12 coordinate hole filled cube.

Stacking layers [D1(Ni, F), C2(K, F), C1(K, F), D2(Ni, F)]$_\infty$ gives the K_2NiF_4 structure, analogous to that of La_2CuO_4. A1(S), B2(Cu), A2(S) gives rise to an infinite edge sharing layer of CuS_4 tetrahedra as found in many layered oxychalcogenides, for example LaOCuS (*vide infra*), while A1(La), B2(O), A2(La) gives the La_4O tetrahedra also found in LaOCuS. An

example of the layers found in the compounds discussed in Chapter 3, the $La_2O_3M_2X_2$ family, is shown in Figure 1.4.

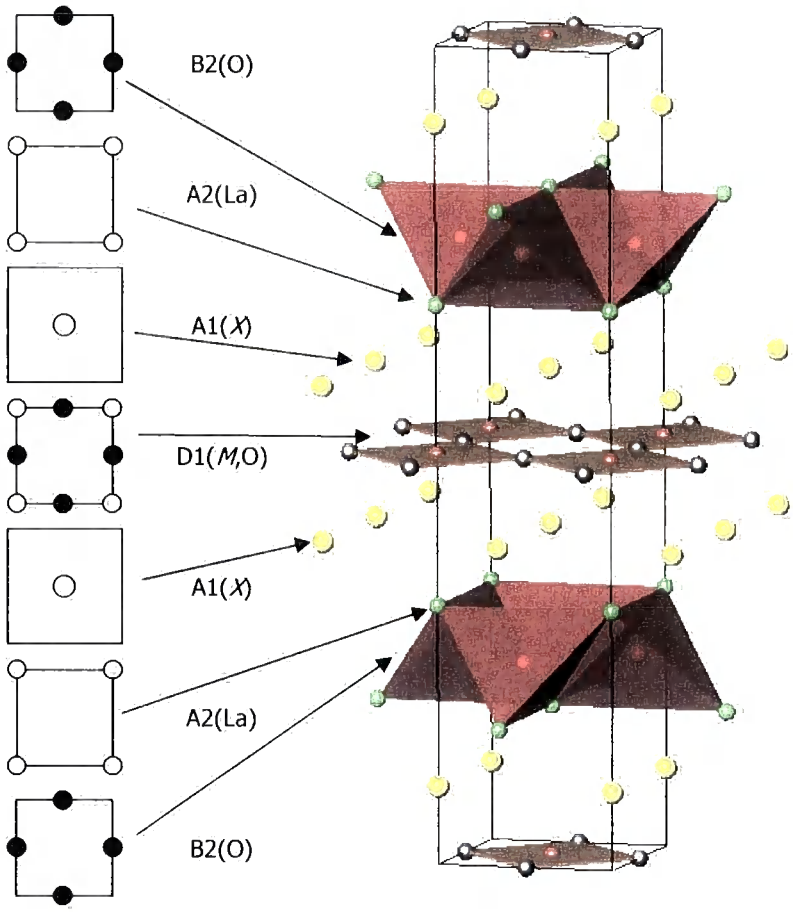

Figure 1.4 Layer stacking in $La_2O_3M_2X_2$ compounds, with 3D polyhedral view on the right. La_4O tetrahedra in red and M_4O polyhedra in orange.

The wealth of potential combinations of these building blocks, the large combination of elements, subtle distortions and non-stoichiometry leads to a large number of potential materials. Within the range of layered oxychalcogenides four distinct groups emerge; those which contain *Ln*/O (*Ln* = lanthanoid element) layers, those which contain Cu/*X* layers, those which contain both these layers and those which contain neither. The materials are discussed in turn in sections 1.2.1 to 1.2.4.

1.2.1 Compounds with both $[Ln_2O_2]^{2+}$ and $[Cu_2X_2]^{2+}$ layers

Amongst the earliest oxychalcogenide phases prepared were the *Ln*OCu*X* phase which features two rigid and stable layers widely found in other compounds (*vide infra*); the $[Ln_2O_2]^{2+}$ and $[Cu_2X_2]^{2-}$ layers. These compounds have been widely studied and used as transparent semiconductors; doping investigations on both metal sites have been performed and solid solutions made using S/Se.

The *Ln*OCu*X* materials are isostructural and crystallise in the *P4/nmm* spacegroup. The structure consists of alternating layers of O—O edge sharing LnO_4 tetrahedra and *X*—*X* edge sharing CuX_4 tetrahedra, as shown in Figure 1.5. The $[Ln_2O_2]$ layer can be described as PbO type, and the $[Cu_2X_2]$ layer described as anti-PbO type. The structural stability of these two layers is key to many of the oxychalcogenides outlined in the following sections.

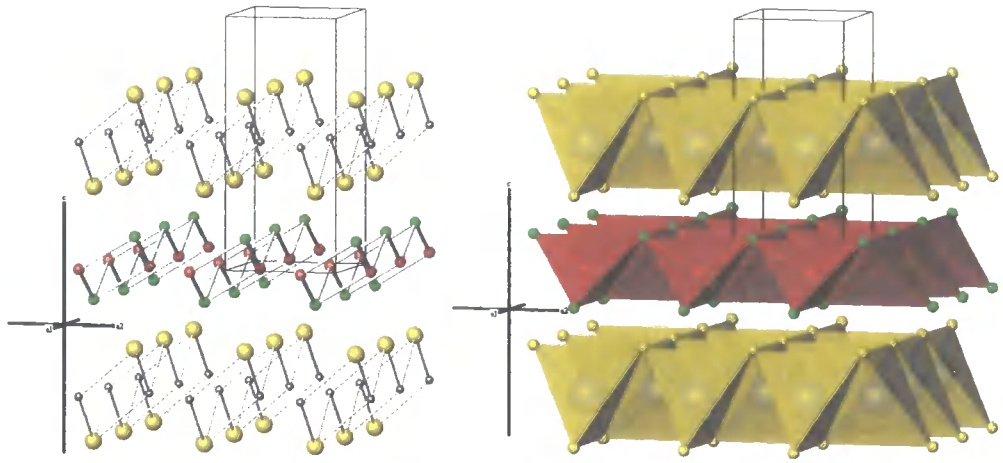

Figure 1.5 The structure of *Ln*OCu*X* compounds in ball and stick (left) and polyhedral views (right). Left, *Ln* in green, O in red, Cu in grey, *X* in yellow. Right, Ln_4O tetrahedra in red, CuX_4 tetrahedra in yellow.

The various *Ln*OCu*X* compounds and their derivatives are summarised in Table 1.1. Due to the similarity with these lanthanoid compounds the bismuth containing compounds which also share this structure are also in Table 1.1 and discussed in this section.

Table 1.1 Compounds with both $[Ln_2O_2]^{2+}$ and $[Cu_2X_2]^{2-}$ layers

Compound	Space group
*Ln*OCuS (*Ln* = La,[9] Ce, Pr, Nd, Sm, Eu, Bi)[10,11]	*P4/nmm*
*Ln*OCuSe (*Ln* = Y, La, Nd, Sm, Gd, Dy, Bi)[12, 13, 14]	*P4/nmm*
$LaCuOS_{1-x}Se_x$, (x = 0.0, 0.25, 0.5, 0.75, and 1.0)[15,16]	*P4/nmm*
$(La_{1-x}Sr_xO)CuS$[17]	*P4/nmm*
$(La_{1-x}Ca_xO)Cu_{1-x}Ni_xS$ $(0 \leq x \leq 0.1)$[18,19]	*P4/nmm*
$BiOCu_{1-x}Se$ $(x = 0 - 0.02)$[20]	*P4/nmm*
$Bi_{1-x}Sr_xOCuSe$ $(x = 0 - 0.1)$[20]	*P4/nmm*

These compounds have attracted much recent study because of their interesting optoelectronic properties; LaOCuS,[9] PrOCuS and NdOCuS[11] are transparent *p*-type semiconductors. The band gap of LaOCuS can be controlled[15,16] by use of the $LaOCuS_{1-x}Se_x$ solid solution, which has been reported as being complete between $0 \leq x \leq 1$. This varied from 3.1 to 2.8 eV for $x = 0$ and 1 respectively.

Doping Sr onto the La site has been reported to result in the $(La_{1-x}Sr_x)OCuS$ $(0 \leq x \leq 0.07)$[17] series of compounds. They were found to change the semiconductive behavior of (LaO)CuS to metallic conducting. This was shown to be due to hole carriers, both above and below a phase transition at 320 K on heating and 200 K on cooling, below which temperatures the conduction is enhanced.

The Ca and Ni doped (for La and Cu respectively) $(La_{1-x}Ca_xO)Cu_{1-x}Ni_xS$ $(0 \leq x \leq 0.1)$[18,19] system was also reported to change from semiconducting behaviour in the parent phase to metallic conducting at $x = 0.03$. Materials with $x \leq 0.02$ are semiconducting, those with $x > 0.03$ are metallic, and $x = 0.03$ itself shows a semiconductor-metal transition at around 150 K. With only the Ca substitution for La (*i.e.* $La_{1-x}Ca_xOCuS$) this transition is not observed and the system is semiconducting for $x \leq 0.05$.

BiOCuSe is isostructural to the *Ln*OCu*X* compounds; with PbO type Bi_2O_2 layers and the familiar Cu_2X_2 layers. This is, like many other Cu/*X* oxychalcogenide phases (*vide infra*), potentially copper deficient, as the $BiOCu_{1-x}Se$ $(x = 0 - 0.02)$[20] phases show. The $x = 0$, (*i.e.* BiOCuSe) phase is semiconducting and the reported decrease in resistivity with increasing x (and thus decreasing Cu content) suggests that the carriers originate from the Cu deficiency. Doping Sr on the Bi site results in the $Bi_{1-x}Sr_xOCuSe$ $(x = 0 - 0.1)$[20] series of compounds and the replacement of Bi^{3+} ions with Sr^{2+} again increases the conductivity of these compounds by increasing the hole density.

Band structure calculations on Cu_2X_2 layers[21] have shown the conduction arises from holes in bands around the Fermi level, equally distributed among Cu and *X* atoms. Thus, correct doping will increase the number of holes and the conduction of the material.

The stability of the Ln_2O_2 and Cu_2X_2 layers, as shown by the range of compounds above, leads to many compounds in which either the oxide or chalcogenide layers have been substituted for other layers, as shown in the following two sections.

1.2.2 Compounds with $[Ln_2O_2]^{2+}$ layers[22,23]

There is a very wide range of oxychalcogenides that contain the $[Ln_2O_2]^{2+}$ layers discussed above and metal chalcogenide layers. The majority of these are *p*-block metals, *B*, and these

make up the bulk of the compounds discussed in this section. The few $[Ln_2O_2]^{2+}$ oxychalcogenides that feature *d*- or *f*-block metal chalcogenide layers are described after these.

The *Ln*/O/*B*/*X* oxychalcogenides are based around the rigid $[Ln_2O_2]^{2+}$ layers made up of O—O edge sharing LnO_4 tetrahedra shown in Figure 1.6 (these layers are shown in red in the figures throughout in this section). In between these rigid oxide layers are various $[B_mX_n]^{2-}$ layers, with the *B* in tetrahedra or octahedra of *X* atoms (these layers are shown in yellow in the figures throughout this section). The arrangements of these *B* centred polyhedra give rise to two, three or four layers of X atoms; compounds are divided by the number of *X* layers in Table 1.2. They are all synthesised by reaction of Ln_2O_2X with the relevant metal chalcogenide in an evacuated sealed quartz ampoule at 950 – 1000 °C for two to seven days.

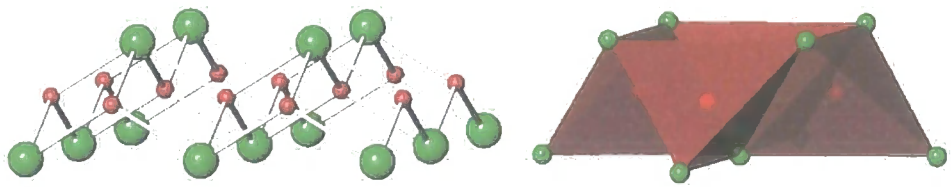

Figure 1.6 The structure of a $[Ln_2O_2]^{2+}$ layer; left, ball and stick view; right, polyhedral. *Ln* atoms in green, O atoms in red. Ln_4O tetrahedra in red.

Table 1.2 *Ln*/O/*B*/*X* (*B* = group 13, 14, 15 metal) compounds.

Layers of *X* atoms	Compound	Ref	Space group	*a*/Å	*b*/Å	*c*/Å	Structure type
2	$(PrO)_4Ga_2S_5$	24	*Pbca*	18.25	22.69	5.77	$(NdO)_4Ga_2S_5$
	$(NdO)_4Ga_2S_5$	24	*Pbca*	18.22	22.52	5.73	$(NdO)_4Ga_2S_5$
	$(SmO)_4Ga_2S_5$	24	*Pbca*	18.06	22.48	5.67	$(NdO)_4Ga_2S_5$
	$(LaO)_4Ge_{1.5}S_5$	22	*Pbca*	18.20	22.23	5.93	$(NdO)_4Ga_2S_5$
	$(CeO)_4Ge_{1.5}S_5$	22	*Pbca*	18.11	23.09	5.84	$(NdO)_4Ga_2S_5$
	$(PrO)_4Ge_{1.5}S_5$	22	*Pbca*	18.07	23.01	5.80	$(NdO)_4Ga_2S_5$
	$(NdO)_4Ge_{1.5}S_5$	22	*Pbca*	18.03	22.80	5.76	$(NdO)_4Ga_2S_5$
	$(LaO)_4Ge_{1.5}Se_5$	22	*Pbca*	18.92	23.82	5.96	$(NdO)_4Ga_2S_5$
3	$(LaO)_4Ga_{1.33}S_4$	25	*P4/mmm*	4.12	-	18.54	$(LaO)_4Ga_{1.33}S_4$
	$(CeO)_4Ga_{1.33}S_4$	25	*P4/mmm*	4.05	-	18.44	$(LaO)_4Ga_{1.33}S_4$
	$(CeO)_4Ga_2S_5$	26	*I4/mmm*	3.99	-	18.33	$(CeO)_4Ga_2S_5$
	$(LaO)_4Sn_2S_6$	27	*Pbnm*	5.876	5.862	19.03	$(LaO)_4Sn_2S_6$
	$(CeO)_4Sn_2S_6$	27	*Pbnm*	5.767	5.776	19.02	$(LaO)_4Sn_2S_6$
	$(PrO)_4Sn_2S_6$	27	*Pbnm*	5.731	5.748	19.01	$(LaO)_4Sn_2S_6$
	$(LaO)_4Sn_2Se_6$	27	*Pbnm*	5.950	5.95	6.30	$(LaO)_4Sn_2S_6$
	$(NdO)_4Sn_2S_6$	27	*Pbnm*	5.710	5.711	19.00	$(LaO)_4Sn_2S_6$
4	$(LaO)GaSe_2$	28	$P2_1ab$	5.95	5.96	12.26	$(LaO)GaSe_2$
	$(LaO)InSe_2$	23	$P2_1ab$	5.89	5.86	13.16	$(LaO)GaSe_2$
	$(CeO)BiS_2$	29	*P4/mmm*	4.01	-	13.50	$(CeO)BiS_2$
	$(LaO)Sb_2Se_6$	23	*P4/mmm*	4.13	-	5.97	$(CeO)BiS_2$

While there are many *Ln*/*O*/*B*/*X* compounds they share 6 different structure types; these are described below.

In $(NdO)_4Ga_2S_5$,[24] the structure which all of the compounds with two layers of X atoms share, the layers of X atoms are made up of corner sharing GaS_4 tetrahedra in which the gallium atoms are in the median positions of sulfur tetrahedra between the $[Nd_2O_2]^{2+}$ layers. In contrast to most structures in this section, both of these layers are not planar but wavy. The oxide layers are less wavy than the sulfur layers. The differing sizes of the layers are believed to cause this unusual distortion. The unusual structure of $(NdO)_4Ga_2S_5$ is shown in Figure 1.7.

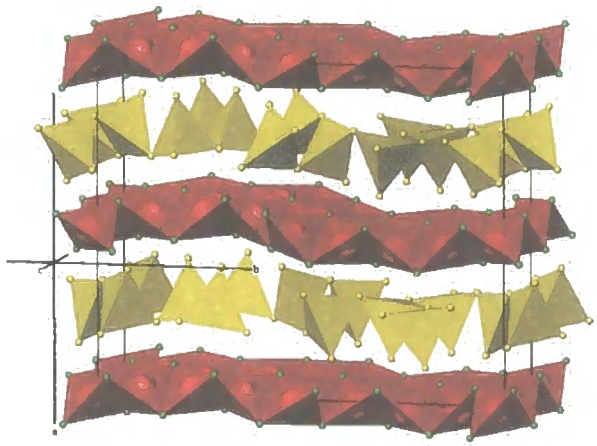

Figure 1.7 The structure of $(NdO)_4Ga_2S_5$ showing "wavy" nature. Nd_4O tetrahedra in red, GaS tetrahedra in yellow.

In the compounds with three layers of *X* atoms there are three structure types; $(LaO)_4Sn_2S_6$,[27] $(CeO)_4Ga_2S_5$[26] and $(LaO)_4Ga_{1.33}S_4$.[25] The positions of the *X* atoms in between the $[Ln_2O_2]^{2+}$ layers are the same for all of the compounds; two crystallographically distinct sites which make up octahedra of *X* atoms, or four edge-sharing tetrahedra. The centres of these tetrahedra give four potential metal atom sites, but they are so close together they cannot be occupied simultaneously. In $(LaO)_4Sn_2S_6$ the tin occupancy is ordered, with only one site of the four occupied. In order to balance the charges the sulfur sites are not fully occupied, giving rise to corner sharing SnS_4 tetrahedra as shown in Figure 1.8. However, in $(CeO)_4Ga_2S_5$ (Figure 1.8) the gallium occupancy is disordered with one of the four N_p = 8 sites being occupied on average, one S site (N_p = 2) is ¼ occupied and the remaining S site (N_p = 4) is fully occupied. In $(LaO)_4Ga_{1.33}S_4$ there is one layer of gallium sulfide with the sulfur sites totally filled and the gallium sites a quarter filled. The other layer only has one of the three sulfur sites filled and one third of a gallium atom on the four metal sites. This results in $(CeO)_4Ga_2S_5$ and $(LaO)_4Ga_{1.33}S_4$ having GaS_6 octahedra, as shown in Figure 1.8.

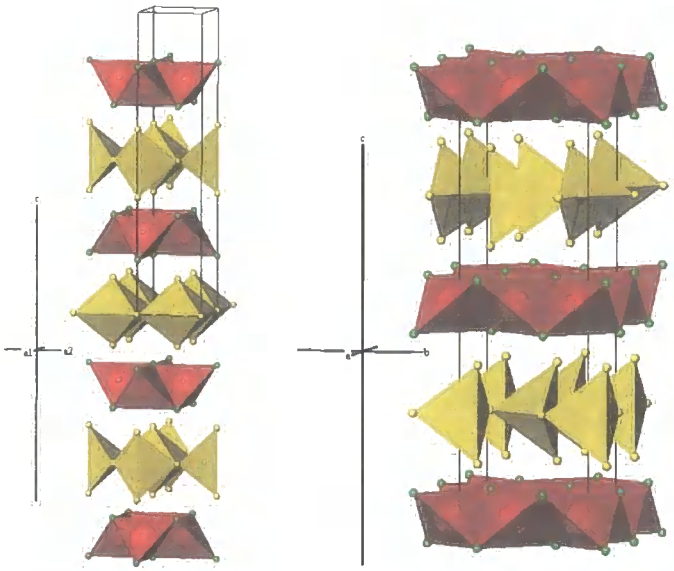

Figure 1.8 Left, structure of $(CeO)_4Ga_2S_5$, Ce_4O tetrahedra in red, GaS octahedra in yellow. Right, structure of $(LaO)_4Sn_2S_6$. La_4O tetrahedra in red, SnS_4 tetrahedra in yellow.

The compounds with four layers of *X* atoms have two different structure types, those of $(CeO)BiS_2$[29] and $(LaO)GaSe_2$. [28] These can both be described as having two layers of BS_n polyhedra in between the $[Ln_2O_2]^{2+}$ layers. In the case of $(CeO)BiS_2$, the structure of which is shown in Figure 1.9, these are distorted edge-sharing octahedra with the Bi—S distance very long in the direction parallel to the *c*-axis (3.34 Å). In $(LaO)GaSe_2$ the layers are both of $GaSe_4$ tetrahedra, again shown in Figure 1.9. These are corner sharing both within each layer and between the two.

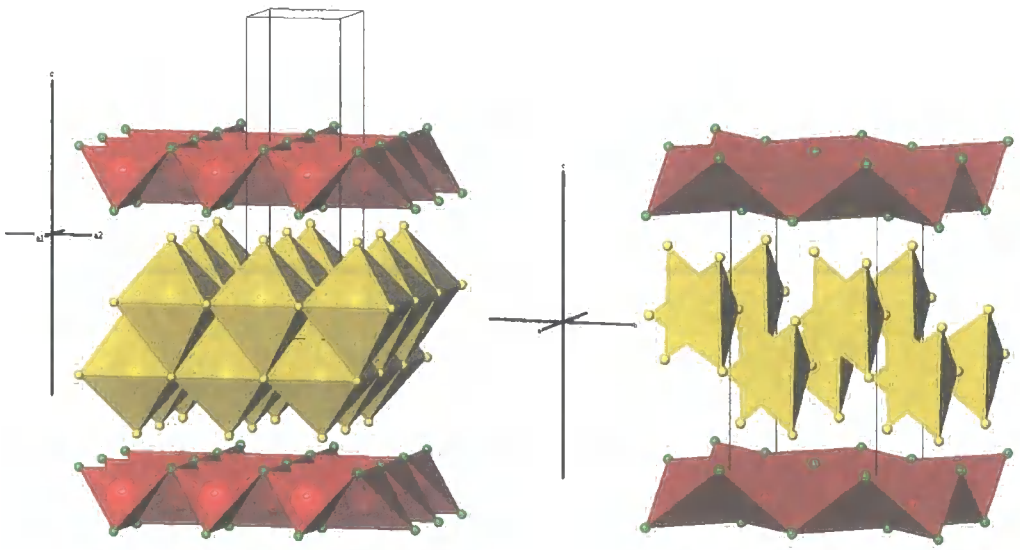

Figure 1.9 Left, structure of $(CeO)BiS_2$. Ce_4O tetrahedra in red, BiS octahedra in yellow. Right, structure of $(LaO)GaSe_2$. La_4O tetrahedra in red, GaSe tetrahedra in yellow.

While there are many oxychalcogenide compounds with lanthanoids and transition metals, most of these form three dimensional structures and are discussed in Section 1.3 below. However, the $La_2O_3Fe_2X_2$ (X = S, Se) compounds have been reported[30] to crystallise in the *I4/mmm* space group with cell parameters of a = 4.0408, c = 17.8985 Å and a = 4.0788, c = 18.648 Å for S and Se respectively.

These isostructural compounds have a novel feature; that of a face-sharing network of transition metal oxychalcogenide octahedra. This is very unusual and when the structure was first reported it was the only four-fold network of face sharing octahedra known. These octahedra are very distorted due to there being two *trans* oxygen atoms and the remaining atoms being chalcogens. For example, the Fe—O bond length is 2.039 Å and the Fe—Se bond length is 2.722 Å. These layers are connected to the next by square anti-prisms of chalcogen and oxygen atoms around the central lanthanum atom. The structure is shown in Figure 1.10.

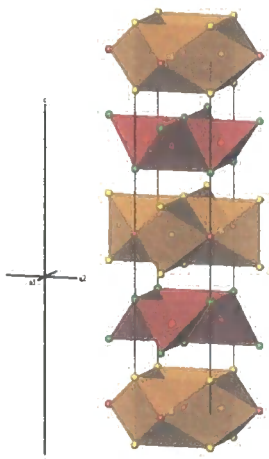

Figure 1.10 The structure of $La_2O_3Fe_2X_2$. La atoms in green, O atoms in red, Fe atoms in dark grey, X atoms in yellow. La_4O tetrehedra in red and FeO_4S_2 octahedra in orange.

There are two U/O/Ln/S oxychalcogenides, $(UO)_2ErS_3$[31] and $(UOS)_4LuS$,[32] known. $(UO)_2ErS_3$ has the same structure as $(LaO)_4Ga_{1.33}S_4$, with U taking the place of La in $[U_2O_2]$ layers separated by a single layer of edge sharing ErS_6 octahedra as shown in Figure 1.11.

$(UOS)_4LuS$ has a more three dimensional structure than $(UO)_2ErS_3$, with LuS_6 octahedra corner sharing with slabs of U/O/S polyhedra. There are two types of uranium environments one eight fold and one nine-fold. The eight coordinate U is in a square anti-prismatic UO_4S_4 environment, with O ligands at one base and S the other. These are S face sharing with the one of the S faces of the double layer of nine coordinate mono-capped square anti-prisms UO_4S_5. The structure or $(UOS)_4LuS$ is shown in Figure 1.11.

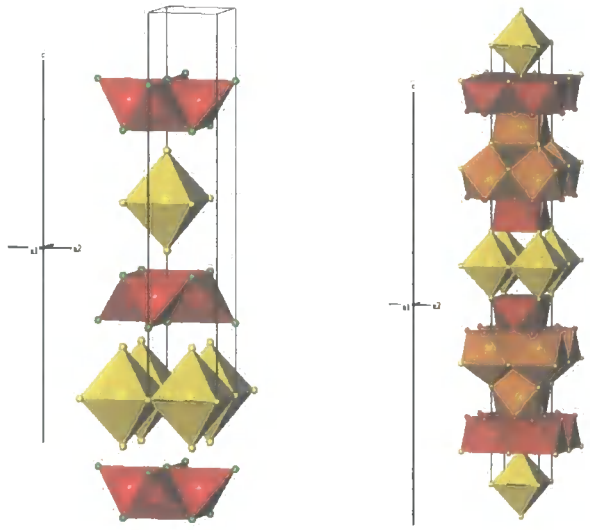

Figure 1.11 Left, the structure of $(UO)_2ErS_3$. U_4O tetrahedra in red, ErS_6 octahedra in yellow. Right, the structure of $(UOS)_4LuS$. Eight coordinate UO_4S_4 square anti-prisms in brick red, nine coordinate UO_4S_5 mono-capped square anti-prisms in orange, Lu/S octahedra in yellow.

1.2.3 Compounds with Cu/*X* layers

As with the $[Ln_2O_2]^{2+}$ compounds the compounds described in this section all feature a common rigid layer, in this case containing chalcogenides and copper in a $[Cu_2X_2]^{n-}$ layer as found in the *Ln*OCu*X* compounds in Section 1.2.1. The $[Cu_2X_2]$ layer is made up of *X*—*X* edge sharing CuX_4 tetrahedra and is shown in Figure 1.12 in yellow, as it is throughout this section. It can formally be $[Cu_2X_2]^{2-}$ or $[Cu_2X_2]^{-}$ depending on the material, this electronic flexibility being a potential advantage in material design. In contrast to the $[Ln_2O_2]$ compounds which contain different metal chalcogenide layers in between rigid oxide layers, the Cu/*X* compounds have rigid sulfide or selenide layers with various metal oxide, M_xO_y, layers (shown in red throughout this section) and *s*-block cations (*A* = Na, Sr, Ba) in between. These M_xO_y layers feature one, two, three or five layers of O atoms; compounds are categorised in this fashion in Table 1.3. The majority of these compounds are synthesised by reaction of a stoichiometric mix of reagents sealed under vacuum in a quartz ampoule and heated to 800 – 900 °C.

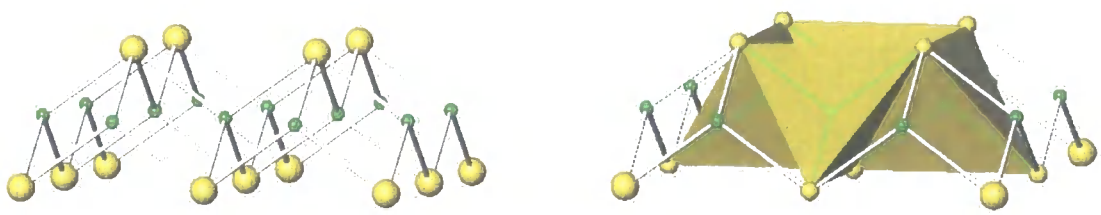

Figure 1.12 Cu_2X_2 layers, Cu atoms in green, *X* atoms in yellow. Ball and stick (left) and polyhedral (right) views.

Table 1.3 Cu/*X* compounds.

No. of O layers	Ref.	Compound	Space group
1	6	$Sr_2MnCu_2O_2S_2$	*I4/mmm*
	33	$Sr_2CoCu_2O_2S_2$	*I4/mmm*
	33	$Ba_2CoCu_2O_2S_2$	*I4/mmm*
	34	$Sr_2Cu_2CoO_2(S_{1-x}Se_x)_2$	*I4/mmm*
	35	$Sr_2NiCu_2O_2S_2$	*I4/mmm*
	35	$Sr_2CuCu_2O_2S_2$	*I4/mmm*
	6	$Sr_2ZnCu_2O_2S_2$	*I4/mmm*
	36	$Sr_{2-x}Na_xCu_2ZnO_2S_2$	*I4/mmm*
	37	$Sr_4Mn_2Cu_5O_4S_5$	*I4/mmm*
	38	$Na_{1.9}Cu_2Se_2.Cu_2O$	*I4/mmm*
2	39,40	$Bi_2LnO_4Cu_2Se_2$ (*Ln* = Y, Gd, Sm, Nd, La)	*I4/mmm*
3	35	$Sr_3Cu_2Sc_2O_5S_2$	*I4/mmm*
	41	$Sr_3Cu_2Fe_2O_5S_2$	*I4/mmm*
4	41	Sr_2CrCuO_3S	*P4/nmm*
	42	Sr_2MnCuO_3S	*P4/nmm*
	41	Sr_2FeCuO_3S	*P4/nmm*
	43	$Sr_2CuFe_{1-x}Ga_xO_3S$ (x = 0, 0.05)	*P4/nmm*
	36	$Sr_{2-x}Na_xCuGaO_3S$	*P4/nmm*
	41	Sr_2InCuO_3S	*P4/nmm*
5	42	$Sr_4Mn_3Cu_2O_{7.5}S_2$	*P4/nmm*
	42	$Sr_4Mn_3Cu_2O_{7.5}Se_2$	*P4/nmm*
	43	$Sr_{4-x}La_xCu_2Mn_3O_{7.5}S_2$ (x = 0, 0.10, 0.20, 0.40)	*P4/nmm*

The structures of the various $[Cu_2X_2]$ containing compounds are discussed first, followed by brief summaries of the electronic and magnetic properties reported in the literature.

The compounds with 1 layer of O atoms ($A_2MCu_2O_2X_2$,[6,33,34,35,36] $Sr_4Mn_2Cu_5O_5S_5$[37] and $Na_{1.9}Cu_2Se_2.Cu_2O$[38]) consist of the $[Cu_2X_2]$ layers separated by square planar layers of M_xO_y. For $A_2MCu_2O_2X_2$ and $Sr_4Mn_2Cu_5O_5S_5$ this is a MO_2 layer with the metal atom in a square planar environment coordinated by oxygen atoms. The structure of the $Sr_2MCu_2O_2S_2$ compounds is shown on the left side of Figure 1.13. The structure of $Sr_4Mn_2Cu_5O_4S_5$ has a double layer of $[Cu_2S_2]$ units, making a $[Cu_3S_3]$ layer. $Na_{1.9}Cu_2Se_2.Cu_2O$, however, has a different square planar M_2O layer (similar to that found in the $La_2O_3Fe_2X_2$ materials in Figure 1.10) in which the oxygen is in square planar coordination by metal atoms.

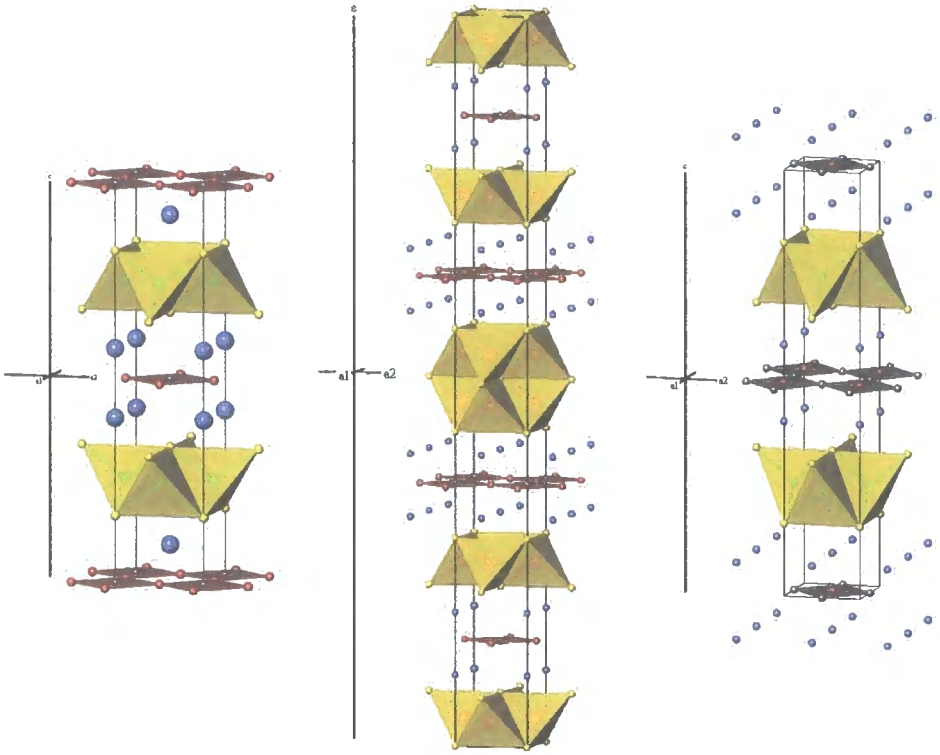

Figure 1.13 The structure of one O atom layer $[Cu_2X_2]$ compounds. Left, $A_2MCu_2O_2X_2$; middle, $Sr_4Mn_3Cu_5O_4S_5$; right, $Na_{1.9}Cu_2Se_2.Cu_2O$. CuX_4 tetrahedra are shown in yellow, MO_2 square planar layers in red, M_2O square planar layers in grey and A atoms in blue.

The only compounds with two layers of O atoms are the $Bi_2LnO_4Cu_2Se_2$ (*Ln* = Y, La, Sm, Nd, Gd)[39,40] series of compounds. In this structure type, shown in Figure 1.14, the *Ln* is in a rock salt type cubic environment coordinating to oxygen, while the Bi is in an Aurivillius type BiO_4Se_4 square anti-prism. These layers lie between the common $[Cu_2Se_2]$ layers.

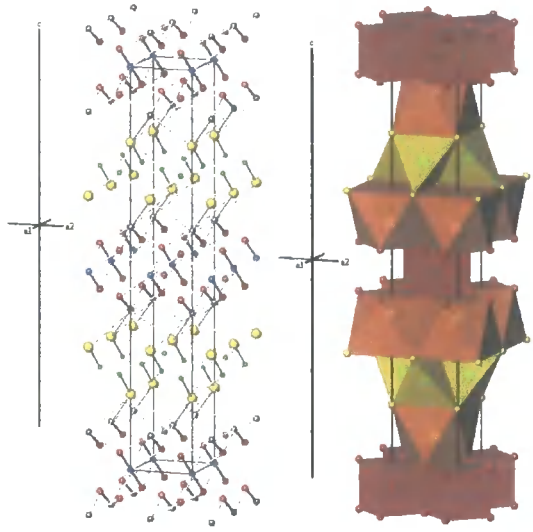

Figure 1.14 The structure of $Bi_2YO_4Cu_2Se_2$; left, ball and stick view; right, polyhedral. Bi atoms are in grey, Y atoms in blue, O atoms in red, Cu atoms in green, Se atoms in yellow. Cu/Se tetrahedra are in yellow, Y/O cubes in red, Bi/O/Se square anti-prisms in orange.

The compounds with three layers of oxygen atoms ($Sr_3M_2Cu_2O_5S_2$, M = Sc, Fe)[35,41] have (MO_2) (SrO) (MO_2) perovskite-like layers, shown in Figure 1.3, with corner sharing square-pyramidal MO_2 metal oxide units. The structure is shown in Figure 1.15.

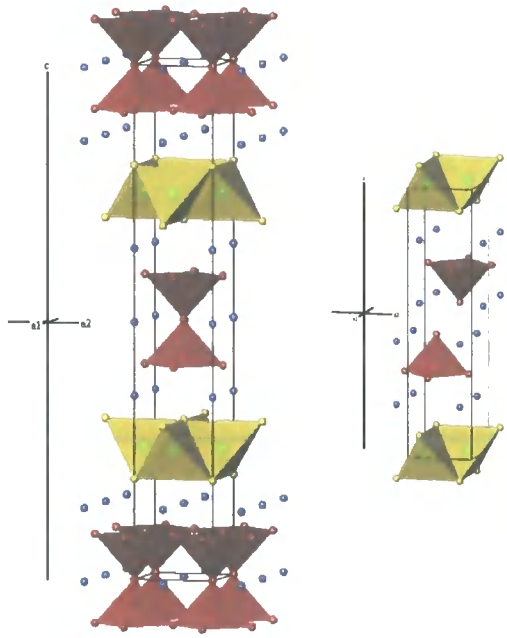

Figure 1.15 Left, the structure of $Sr_3M_2Cu_2O_5S_2$ compounds with 3 layers of O atoms. Right, the structure of Sr_2MCuO_3S compounds with 4 layers of O atoms. CuS_4 tetrahedra in yellow, MO_5 square pyramids in red, Sr atoms in blue.

The structure of the compounds with 4 O atom layers (Sr_2MCuO_3S[36,41,42,43]) is similar to that of those with 3 layers (Figure 1.15). However, in this case the oxide layers can be described as two MO_4 square pyramidal units in a (MO_3) (SrO) (SrO) (MO_3) slab. The relationship between

these layers and those of the 3 layer compounds is similar to that between perovskite and K_2NiF_4, such that one can consider the layers as intergrowths of perovskite and rock salt slabs in between the $[Cu_2S_2]$ slabs, as shown in Figure 1.15.

The only known compounds with 5 O atom layers ($Sr_4Mn_3Cu_2O_{7.5}X_2$)[42,43] contain a triple Mn perovskite slab, with two square-pyramidal and one octahedral Mn. This (MnO_2) (SrO) ($MnO_{1.5}$) (SrO) (MnO_2) block is very similar to the (CuO_2) (BaO) (CuO_δ) (BaO) (CuO_2) slab found in $YBa_2Cu_3O_{7-\delta}$ and is shown in Figure 1.16.

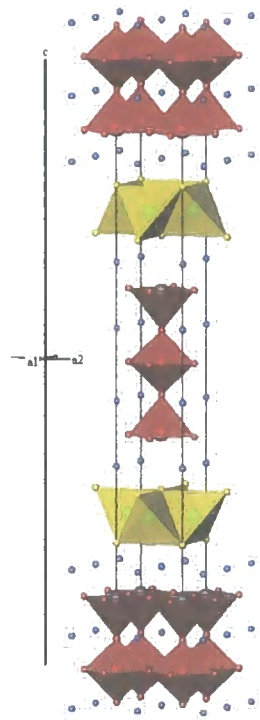

Figure 1.16 The structure of $Sr_4Mn_3Cu_2O_{7.5}X_2$ compounds, with 5 layers of O atoms. CuS_4 tetrahedra in yellow, MO_5 square pyramids in red, Sr atoms in blue.

The electronic and magnetic properties of the $[Cu_2X_2]$ containing compounds are summarised below; the compounds have again been divided by the number of O atom layers in the structure for clarity.

One of the compounds with one layer of O atoms, $Sr_2CoCu_2O_2S_2$ was reported[33] to have a resistivity of about 4 Ω cm at 300 K, while the resistivity of $Ba_2CoCu_2O_2S_2$ was reported[33] to be of the order of 40 000 Ω cm. These compounds have a small Cu deficiency and a compound with 12.5 % Cu deficiency, $Sr_2CoCu_{1.75}O_2S_2$, was prepared and found to have a lower resistivity than the parent "stoichiometric" compound. Magnetic susceptibility data for these compounds showed successive broad maxima, described by the authors as suggesting low dimensional antiferromagnetic transitions of the Co^{2+} cations. The Sr containing phase showed a difference between the field cooled and zero-field cooled data suggestive of spin

glass freezing of ferrimagnetic clusters. The *M* = Mn, Zn analogues of the *A* = Sr phases were found[6] to have low conductivities and the Mn phase showed a peak in magnetic susceptibility data at 29.5 K suggesting antiferromagnetic ordering of the Mn^{2+} cation. An μ_{eff} of 5.3 μ_B and a Weiss temperature θ = -28 K were calculated from a fit to the Curie-Weiss law using the data between 200 and 300 K.

Sodium doping on the Sr site of the M = Zn phase decreases the resistivity by 7 orders of magnitude for the x = 0.10 sample at room temperature to 8.3 Ω cm. $Sr_{2-x}Na_xCu_2ZnO_2S_2$ was reported[36] to show semiconducting behaviour for low values of x and degenerate-semiconducting behaviour for x = 0.06 and 0.10 at low temperatures. Introducing Se into the $Sr_2CoCu_2O_2S_2$ gives $Sr_2CoCu_2O_2(S_{1-x}Se_x)$;[34] increasing the Se content results in, as would be expected, a lattice expansion and a crossover from low dimensional variable range hopping conduction to a power law dependence of resistivity at low temperatures. However, the application of high pressure makes the phase an insulator.

Initial conductivity experiments on $Sr_4Mn_2Cu_5O_4S_5$ were reported[37] which gave a resistivity of 5 and 7 Ω cm at 290 and 100 K respectively, suggesting semiconducting behaviour. $Na_{1.9}Cu_2Se_2.Cu_2O$[38] is a metallic conductor due to the non-stoichiometry in sodium, which creates electron holes. The resistivity increases from 5 x 10^{-6} Ω cm at 5 K to 1.1 x 10^{-4} Ω cm at room temperature.

$BiYO_4Cu_2Se_2$, with two layers of O atoms, was reported[30] to have a room temperature resistivity of ~2 x 10^{-2} Ω cm and this was found to vary linearly with temperature, suggesting metallic conduction. The Nd, Sm and Gd containing compounds have been shown[31] to be paramagnetic from 10 – 300 K.

One of the compounds with four layers of O atoms, Sr_2CuMnO_3S has[42] a very high resistivity, over 1 MΩ cm. The *M* = Cr, Fe, In phases have been reported[41] as being semiconductors with the magnetic susceptibility of the Cr phase showing a broad maximum at around 60 K, reported as being indicative of antiferromagnetic ordering of the Cr^{3+} in the CrO_3 square-pyramidal layer. Above 150 K a fit to a Curie-Weiss law results in an effective moment of 3.81 μ_B and a Weiss temperature of -175(4) K. Sodium has been doped[36] on the Sr site for the *M* = Ga material which reduced the resistivity from 4.5 x 10^3 Ω cm to 41.7 Ω cm at room temperature for $Sr_{2-x}Na_xCuGaO_3S$ at values of x = 10 and ~1 x 10^3 Ω cm for x = 0.06.

Only the *M* = Mn phases of the potential five O atom layer compounds have been reported; $Sr_4Cu_2Mn_3O_{7.5}S_2$[42] and its La doped relative $Sr_{4-x}La_xCu_2Mn_3O_{7.5}S_2$ (x = 0, 0.10, 0.20, 0.40),[43] the lattice parameters of which decrease with increasing x. Compounds at all values of x are semiconducting, with the resistivity dramatically falling with increasing x; that of the x = 0.40 sample is reported to be one hundred times lower than that of the x = 0 sample. The

selenium analogue of this has been reported;[42] $Sr_4Mn_2Cu_2O_{7.5}Se_2$ is isostructural with the sulfur phase and it is more conducting than the sulfur analogue, with a resistivity of 10 Ω cm.

1.2.4 Other layered compounds; $Ln_2Ti_2S_2O_5$ compounds

The $Ln_2Ti_2S_2O_5$ (*Ln* = Y,[44] Pr,[45] Nd,[45] Sm,[45] Tb[46]) family share a defect Ruddlesden–Popper[47] structure type, closely related to that of the high-T_c superconductors such as $La_2CaCu_2O_6$. $Nd_2Ti_2S_2O_5$ is synthesised by reaction of NdS_2O, TiS_2 and S in 1:1:1 ratios at 1000 °C in an evacuated quartz ampoule for one week. The praseodymium analogue is synthesised by reaction of Pr_6O_{11}, TiS_2, Ti and S in a 1:2:2:3 ratio in the same conditions, which are also used to obtain $Sm_2Ti_2S_2O_5$ from Sm_2O_3, TiO_2 and TiS_2. The lanthanoid atoms are in a nine coordinate environment, in a slightly distorted double rock salt layer of LnS. This is intergrown along the *c*-axis with defective double perovskite $TiSO_5$ blocks (see Figure 1.17). This layer has corner sharing $TiSO_5$ octahedra and the 12 coordinate *A* site of this perovskite block is not filled. For $Nd_2Ti_2S_2O_5$ Curie-Weiss behaviour has been reported above 260 K and below 175 K. The Nd^{3+} ions are believed to be anti-ferromagnetically coupled, resulting in a lower room temperature magnetic moment (10.04 μ_B) than would be expected for four independent ions (14.48 μ_B). The *Ln* = Y, Nd[48] compounds have been targeted for Group 1 metal intercalations, including Li,[49] K[50] and Na.[44]

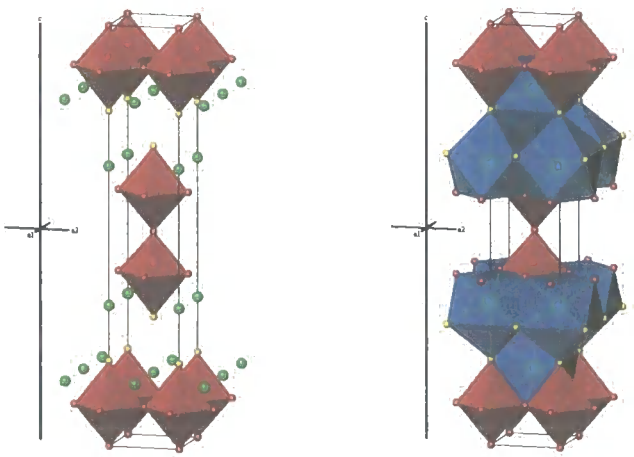

Figure 1.17 The structure of $Ln_2Ti_2S_2O_5$; left, without LnO_4S_5 polyhedra; right, with. $TiSO_5$ polyhedra are shown in red, *Ln* atoms in green, LnO_4S_5 mono capped square anti-prisms in turquoise.

1.3 Oxychalcogenides with three dimensional structures

There are many oxychalcogenides with three dimensional structures that are made up of lanthanoids (*Ln*) and transition metals (*M*) with O and sulfur/selenium (*X*). These structures are made up of three dimensional arrays of corner, edge or face sharing polyhedra, rather than the conceptual layers or slabs described in the previous section.

As the layered compounds could be considered as made up of stable and rigid units, layers of Ln_2O_2 or Cu_2X_2, with the other structural units fitting in between, one way of understanding many three dimensional oxychalcogenides is in terms of chains or layers of MO_nX_m octahedra (or tetrahedra in some cases) with the LnO_nX_m polyehdra in between. In the following sections the seemingly complex set of structures reported to date are described in terms of one or more of five structural units. These are either chains of polyhedra or layers consisting of interlocking chains. The chains can be separated according to the connectivity of the polyhedral units they contain. Figure 1.18 shows the unit described as a "*C* chain"; a chain of corner sharing octahedra. Figure 1.18 also shows an "*E* chain"; a chain of edge sharing octahedra.

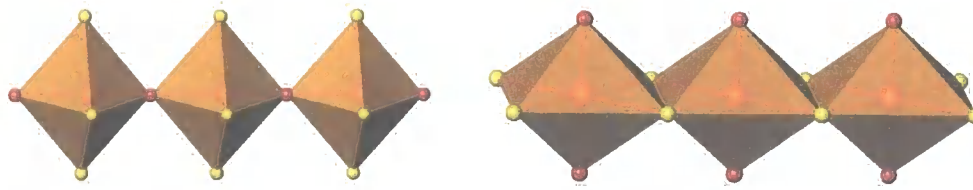

Figure 1.18 Left, a diagram of a "*C* chain"; a chain of corner sharing octahedra. Right, a diagram of an "*E* chain"; a chain of edge sharing octahedra. Different combinations of O and *X* positions are possible.

While many structures can be described in terms of these two simple structural motifs, certain combinations of them are also common, and are shown in Figure 1.19, Figure 1.20 and Figure 1.21. Figure 1.19 shows a "*C-C* chain" or two parallel *C* chains linked by shared corners and a "*C-E* chain", two parallel *C* chains linked by shared edges.

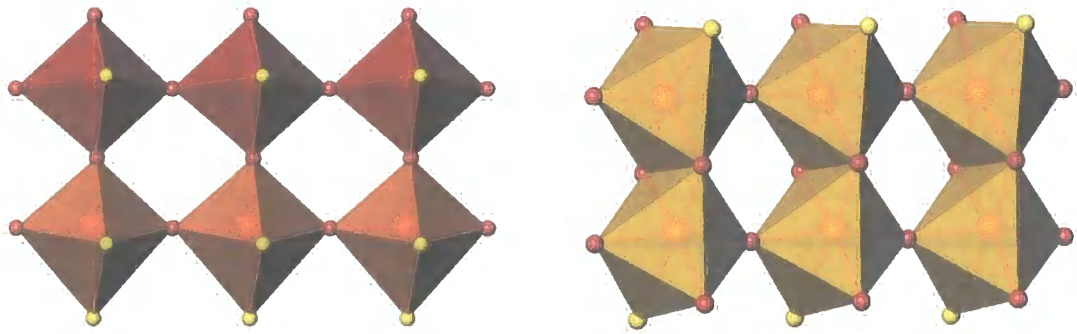

Figure 1.19 Left, a diagram of a "*C-C* chain"; two corner sharing chains interlinked by corner sharing. Right, a diagram of a "*C-E* chain"; two corner sharing chains interlinked by edge sharing.

Figure 1.20 shows an "*E-E* chain" which is two parallel *E* chains linked by shared edges and a layer, "*L*", made up of interconnected *E* chains. Figure 1.21 shows an "*S*" layer which is a slab of linked, parallel *C* and *E* chains.

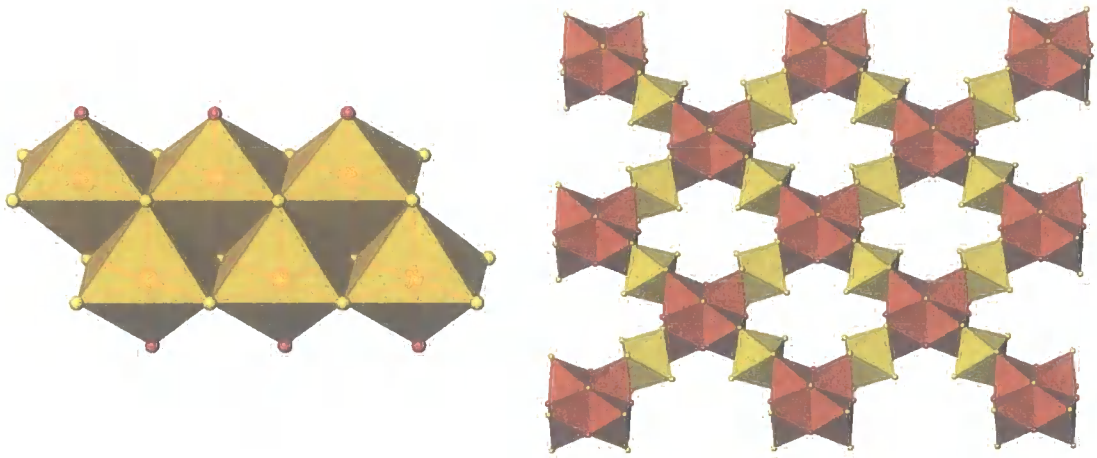

Figure 1.20 Left, a diagram of an "*E-E* chain"; two edge sharing chains interlinked by edge sharing. Right, a diagram of a "*L*" layer of interlinked edge sharing chains.

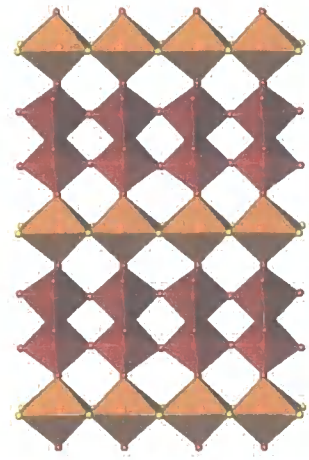

Figure 1.21 A diagram of an "*S*" layer; various *E* and *C* chains making up a two dimensional slab.

Within this framework of chains and layers are the LnO_nX_m polyhedra which are all 7, 8 or 9 coordinate mono- bi- and tri-capped trigonal prisms, varying from all *X* coordination to half *X* half O coordination (these are shown in colours from green for all O to blue for all S in the figures throughout this section). The transition metals are also in predominantly *X* coordination, again from all *X* to half *X* half O, in octahedra (shown in colours from red for all O to yellow for all S in the figures throughout this section).

Many of the compounds have mixed valence transition metal ions, some with a random distribution of different ions in crystallographically non-equivalent sites, others in distinct sites; others again do not have mixed valence ions.

These *Ln*/O/*M*/X compounds have been arranged in this section in terms of the *M* atom contained, with *M* = Ti being by far the most prevalent. Within the Ti section they are further subdivided by the chains and layers they contain, with materials presented in order of increasing dimensionality of the MO_nX_m units.

1.3.1 *Ln*/Ti/O/*X* compounds

Table 1.4 summarises the *Ln*/Ti/O/*X* compounds reported to date together with the types of chains and layers they contain, space group, which compounds feature mixed valence Ti and which compounds have Ti in all O or all *X* environments. In the compounds with mixed valence, the Ti^{3+} and Ti^{4+} are randomly distributed through the different Ti sites; with no charge ordering between specific sites.

Table 1.4 A summary of *Ln*/Ti/O/*X* compounds.

Chain/layer type	Compound	Space group	Mixed valence	All O or all *X*
C	$La_{16}Ti_5S_{17+x}O_{17}$ (*Ln* = La,[51] Nd[52])	*I4/m*		
E	$Gd_4TiSe_4O_4$[53]	*C2/m*		
E	$La_4Ti_2O_4Se_8$[54]	*Cmcm*		
E	$La_6Ti_3O_5Se_9$[54]	*C2/m*	✓	
E	$Ln_{3.67}Ti_2O_3Se_6$[55] (*Ln* = Ce, Nd, Sm)	*C2/m*	✓	
C-C	$La_6Ti_2O_5S_8$[56]	$P2_1/m$		
C-E, C	$La_4Ti_3O_8S_4$[56]	*C2/m*		TiO_6
3 x *C-E*	$Ln_3Ti_3Se_2O_8$ (*Ln* = Nd,[57] Sm[58])	$P2_1/m$		TiO_6
L	$La_{14}Ti_8O_4S_{33}$[59]	*C2/m*	✓	TiS_6
L	$Ln_{20}Ti_{11}O_6S_{44}$ (*Ln* = La,[60] Ce[61])	*Pmmn*		TiS_6
L-L	$La_8Ti_{10}O_4S_{24}$[62]	*P4/mmm*	✓	TiS_6
L-L	$La_{8+x}Ti_{8+y}O_4S_{24}$ ($x + y \leq 2$)[63]	*P4/mmm*	✓	TiS_6

One dimensional MO_nX_m chains are found in many materials, these include the $Ln_{16}Ti_5S_{17+x}O_{17}$ (*Ln* = La,[51] Nd;[52] x = 0, 0.75 respectively) compounds which are isostructural and contain two *C* chains, both O bridged, one of TiO_2S_4 octahedra and one of TiO_4S_2. These are within a $[Ln_2S_2]$ framework that defines channels in which the TiO_2S_4 *C* chains lie. Their structure is shown in Figure 1.22.

The structure of $Gd_4TiSe_4O_4$[53] is shown in Figure 1.22 and consists of *E* chains of TiO_2Se_4 octahedra interconnected by "ribbons" of 8 coordinate GdO_3Se_5 and GdO_4Se_4 bicapped trigonal prisms. $Gd_4TiSe_4O_4$ displays Curie-Weiss paramagnetism between 30 and 300 K and has a large ferromagnetic component between 2.5 and 3 K. Between 1 and 2.5 K it is reported to exhibit anti-ferromagnetic long range order.

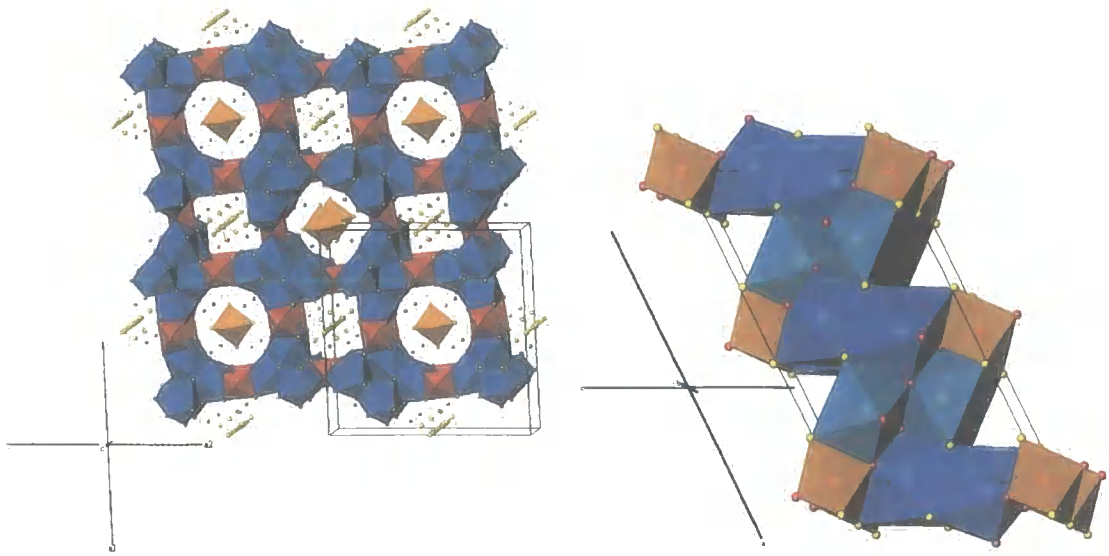

Figure 1.22 Left, the structure of $Ln_{16}Ti_5S_{17+x}O_{17}$ (Ln = La, Nd; x = 0, 0.75 respectively) compounds. TiO_4S_2 octahedra are shown in dark orange, TiO_2S_4 in light orange, LnO_4S_5 polyhedra in blue. Right, the structure of $Gd_4TiSe_4O_4$. GdO_4Se_4 bi-capped trigonal prisms are shown in turquoise, GdO_3Se_5 in blue, TiO_2Se_4 octahedra in orange.

$La_4Ti_2O_4Se_5$[54] has E chains of TiO_2Se_4 octahedra running parallel to the a axis. These are connected by LaO_3Se_5 and LaO_4Se_4 polyhedra as shown in Figure 1.23. $La_6Ti_3O_5Se_9$[54] has two E chains; one of $TiOSe_5$ octahedra and one of TiO_2Se_4 octahedra. These are connected by $LaSe_7$, $LaOSe_7$, LaO_3Se_5, LaO_5Se_4 and LaO_3Se_5 polyhedra and the structure is shown in Figure 1.23.

The series $Ln_{3.67}Ti_2O_3Se_6$ (Ln = Ce, Nd, Sm)[55] has two E chains; one of $TiOSe_5$ and one of TiO_2Se_4, between which are various LnO_nX_m polyehdra. Their structure is shown in Figure 1.23. All three compounds in this series have been reported to be paramagnetic between 5 and 300 K, with the Ln = Ce, Nd compounds following Curie-Weiss behaviour between 100 and 300 K.

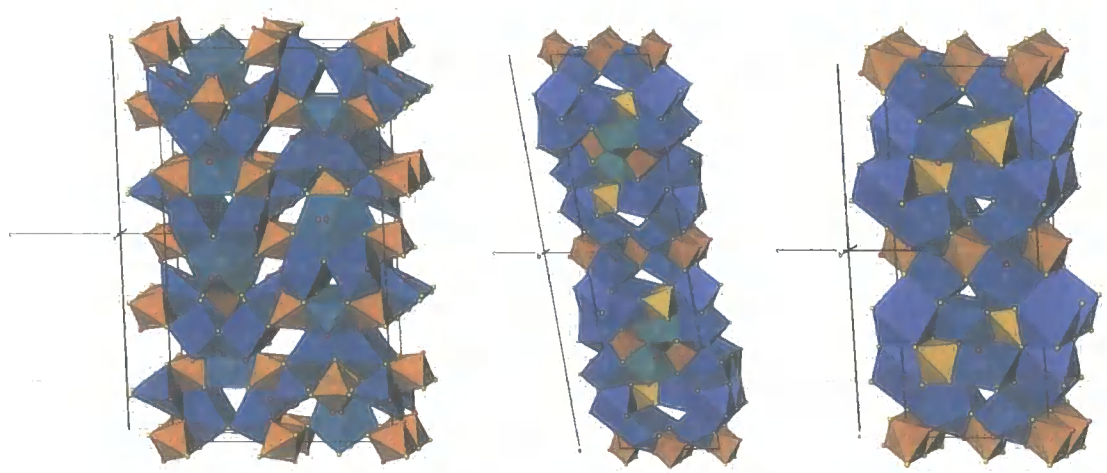

Figure 1.23 Left, the structure of $La_4Ti_2O_4Se_5$. TiO_2Se_4 octahedra in orange, LaO_3Se_5 polyhedra in blue, LaO_4Se_4 in turquoise. Centre, the structure of $La_6Ti_3O_5Se_9$. $TiOSe_5$ octahedra in yellow, TiO_2Se_4 in

orange. $LaSe_7$, $LaOSe_7$ polyhedra in blue, LaO_3Se_5, LaO_5Se_4, LaO_3Se_5 in turquoise. Right, the structure of $Ln_{3.67}Ti_2O_3Se_6$ (*Ln* = Ce, Nd, Sm). $TiOSe_5$ octahedra are shown in yellow, TiO_2Se_4 octahedra in orange, LnO_3Se_5 and LnO_3Se_6 polyhedra in pale blue, $LnSe_7$ in bright blue.

In $La_4Ti_3S_4O_8$[56] there are three different Ti/O/S chains; an *E* chain of TiO_2S_4 octahedra, a *C* chain of TiO_6 octahedra and a *C-C* chain of TiO_5S. The latter two are linked by a bridging oxygen to form a trimeric chain. The structure is shown in Figure 1.24, which also shows the LaO_5S_4 and LaO_4S_5 tri-capped trigonal prisms.

A *C-C* chain is formed in $La_6Ti_2S_8O_5$[56] from corner sharing TiO_3S_3 and TiO_5S octahedra which share a bridging oxygen. The lanthanum atoms are in seven, eight or nine coordination mono-, bi- or tri - capped trigonal prisms, as shown in Figure 1.24. Magnetic susceptibility data are reported to show weak temperature independent paramagnetism for $La_6Ti_2S_8O_5$, while $La_4Ti_3S_4O_8$ follows Curie-Weiss behaviour.

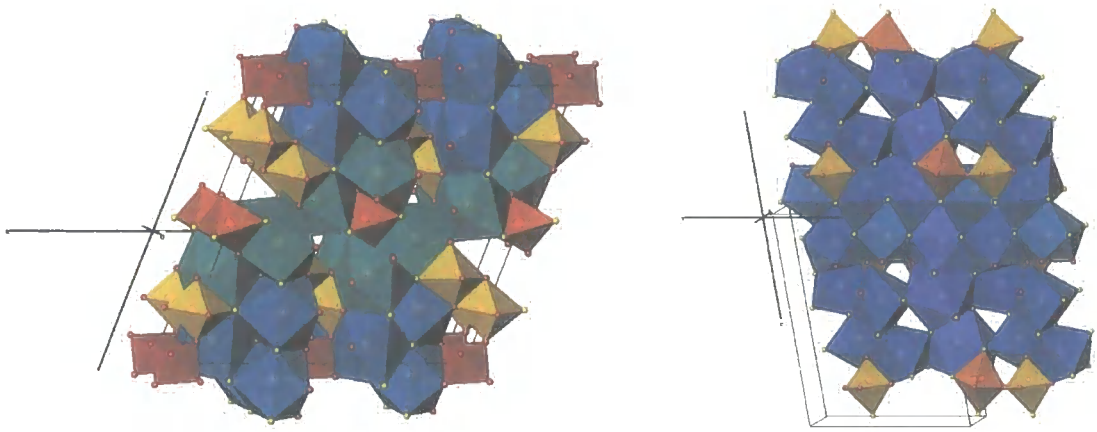

Figure 1.24 Left, the structure of $La_4Ti_3S_4O_8$. TiO_5S octahedra are shown in dark orange, TiO_2S_4 octahedra in lighter orange, TiO_6 octahedra in red, LaO_5S_4 polyhedra in turquoise, LaO_4S_5 in blue. Right, the structure of $La_6Ti_2S_8O_5$. TiS_3O_3 octahedra are shown in orange, $TiSO_5$ octahedra in red, $LaOS_8$ tri-capped trigonal prisms in bright blue, LaO_3S_5, LaO_3S_6, LaO_2S_5, LaO_4S_5 in other blues.

$Ln_3Ti_3O_8Se_2$ (*Ln* = Nd,[57] Sm[58]) is more oxygen rich than other *Ln*/Ti/O/*X* compounds and has three *C* chains (two of TiO_6 and one of TiO_5Se octahedra) that share O—O edges, resulting in trimeric one dimensional chains that extend along the *b* axis. LnO_4Se_4 and LnO_7Se_2 polyhedra also form ribbons that extend in the same direction. The structure is shown in Figure 1.25. $Sm_3Ti_3O_8Se_2$ is reported to show complex paramagnetic behaviour.

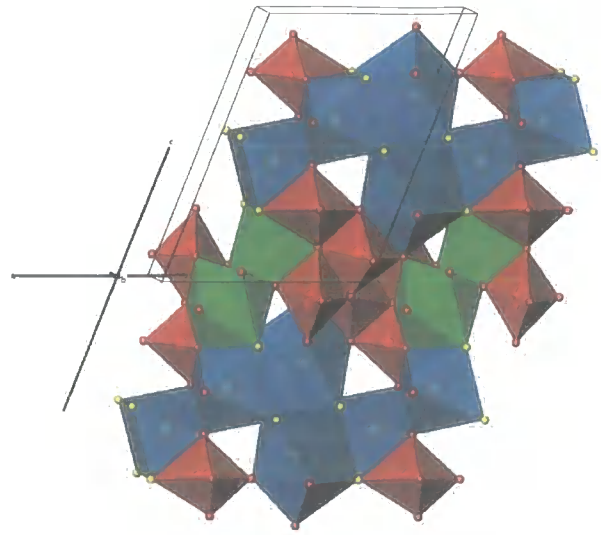

Figure 1.25 The structure of $Ln_3Ti_3O_8Se_2$ (*Ln* = Nd, Sm). TiO_6 octahedra are shown in red, TiO_5Se octahedra in brick red, LnO_4Se_4 in turquoise and LnO_7Se_2 in green.

$La_{14}Ti_8S_{33}O_4$[59] has clusters of four face sharing TiO_2S_4 octahedra that are connected to TiS_6 octahedra to make up an *L* layer (made up of interconnecting *E* chains). Within this framework are other TiS_6 octahedra and the $LaOS_8$ and LaS_9 nine coordinate polyhedra, as shown in Figure 1.26.

The $Ln_{20}Ti_{11}S_{44}O_6$ (*Ln* = La,[60] Ce[61]) compounds are isostructural and also have *L* layers of TiS_6 and TiO_2S_4 octahedra. They also have an additional pair of isolated corner-sharing oxygen bridged $TiOS_5$ octahedra found separated from the main layers. Within this framework are $LnOSe_7$, $LnOSe_8$, $LnSe_9$ polyhedra, which have been omitted from the structure shown in Figure 1.26 for clarity.

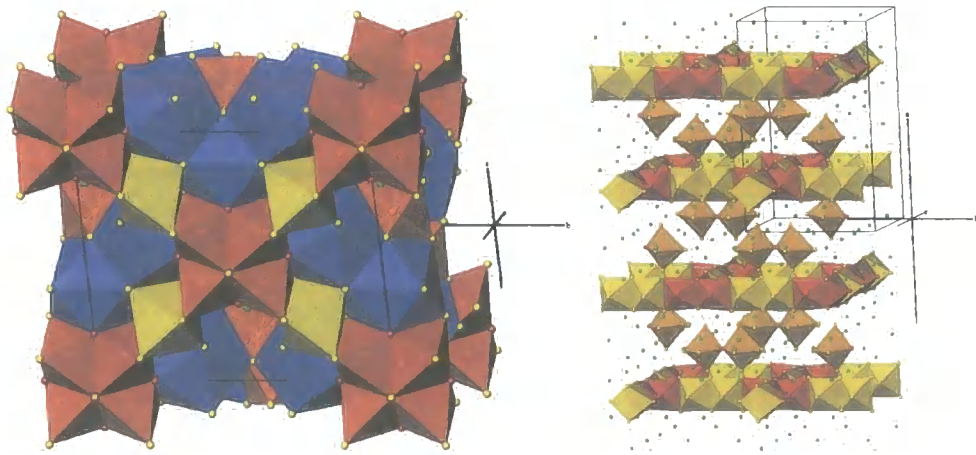

Figure 1.26 Left, the structure of $La_{14}Ti_8O_4S_{33}$. TiO_2S_4 octahedra are shown in orange, TiS_6 in yellow, $LaOS_8$ and LaS_9 polyhedra in blue. Right, the structure of $Ln_{20}Ti_{11}S_{44}O_6$ (*Ln* = La, Ce). TiS_6 octahedra are shown in yellow, $TiOS_5$ in dark yellow, TiO_2S_4 octahedra in orange, $LnOSe_7$, $LnOSe_8$, $LnSe_9$ polyhedra omitted for clarity.

The series of compounds $La_{8+x}Ti_{8+y}O_4S_{24}$ ($x + y \leq 2$)[62,63] can be considered as made up of the same *L* layers of TiO_2S_4 clusters and TiS_6 octahedra as $La_{14}Ti_8S_{33}O_6$, but are interconnected by chains making up a three dimensional network, in which the $LaOS_8$ polyhedra fit. The structure is shown in Figure 1.27 with the $LaOS_8$ polyhedra omitted for clarity.

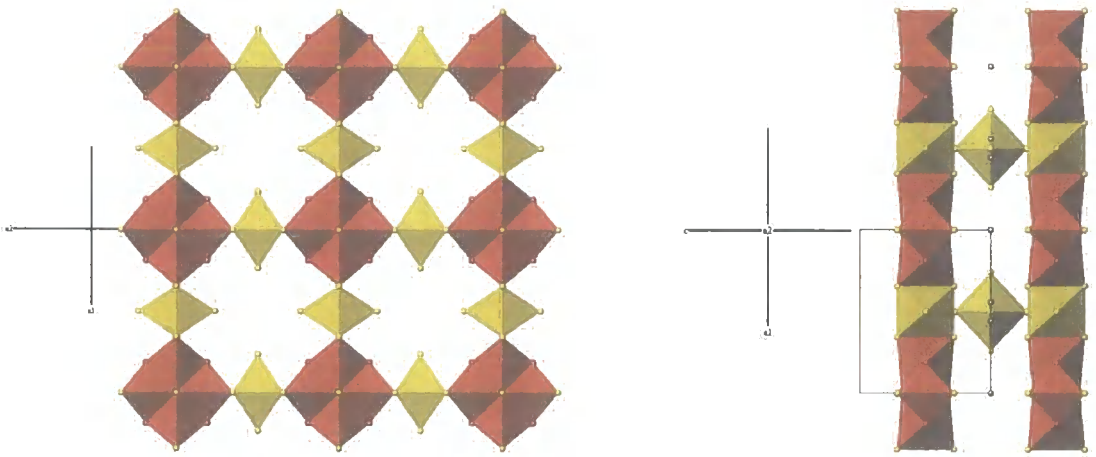

Figure 1.27 The structure of $La_8Ti_{10}O_4S_{24}$. TiS_6 octahedra are shown in yellow, TiS_2O_4 octahedra in orange, $LaOS_8$ omitted. Left shows *L* layers, right shows *L* layers connected by TiS_6 octahedra.

1.3.2 *Ln*/V/O/*X* compounds

There are two different types of lanthanoid vanadium oxychalcogenides; the $Ln_5V_3O_7S_6$ (*Ln* = La – Nd)[55] and the $Ln_7VO_4Se_8$ compounds (*Ln* = Nd, Sm, Gd).[64] They both feature *E* chains of VO_2X_4 octahedra. The compounds and their space groups are summarised in Table 1.5.

Table 1.5 *Ln*/O/V/*X* compounds

Ln	S	Space group	Se	Space group
La	$La_5V_3O_7S_6$	*Pmnm*		
Ce	$Ce_5V_3O_7S_6$	*Pmnm*		
Pr	$Pr_5V_3O_7S_6$	*Pmnm*		
Nd	$Nd_5V_3O_7S_6$	*Pmnm*	$Nd_7VO_4Se_8$	*Pbam*
Sm			$Sm_7VO_4Se_8$	*Pbam*
Gd			$Gd_7VO_4Se_8$	*Pbam*

$Ln_5V_3O_7S_6$ has two separate S—S sharing *E* chains of VO_2S_4 octahedra, in between which are LnO_4S_5 and LnO_5S_4 tri-capped trigonal prisms, as shown in Figure 1.28. The vanadium sites are mixed V^{3+}/V^{4+} valence, again with a random distribution throughout the structure.

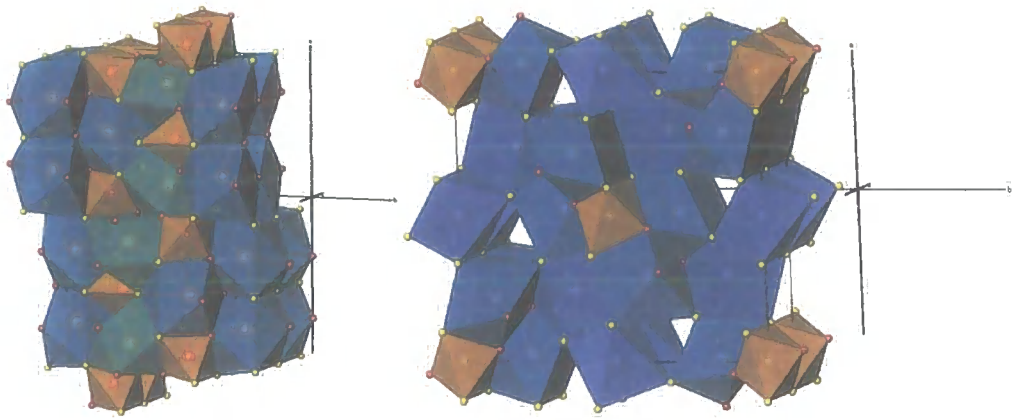

Figure 1.28 Left, the structure of $Ln_5V_3O_7S_6$. VO_2S_4 octahedra are shown in orange, LnO_4S_5 and LnO_5S_4 tri-capped trigonal prisms turquoise. Right, the structure of $Ln_7VO_4Se_8$ (*Ln* = Nd, Sm, Gd). VO_2Se_4 octahedra are shown in orange, *Ln*Se6 and $LnOSe_6$ polyhedra in bright blue, LnO_3Se_5 in paler blue.

In the structures of the $Ln_7VO_4Se_8$ (*Ln* = Nd, Sm, Gd) compounds are *E* chains of VO_2Se_4 octahedra and $LnOSe_6$ and LnO_3Se_5 polyehdra. The structure is shown in Figure 1.28. $Gd_7VO_4Se_8$ has been reported to be paramagnetic between 5 and 300 K, obeying the Curie-Weiss law with a Curie constant of 52.3 emu K^{-1} mol^{-1} and a Weiss temperature of 14.3 K.

1.3.3 *Ln*/Ta/O/*X*

The known Ta oxychalcogenides[65,66] are included together with their space group and unit cell parameters in Table 1.6.

Table 1.6 *Ln*/Ta/O/*X* compounds.

Ln	Se	*a*/Å	*b*/Å	*c*/Å	Space group
La	$La_2Ta_3O_8S_2$	9.929	11.951	7.666	*Pnnm*
Ce	$Ce_2Ta_3O_8Se_2$	9.947	11.848	7.647	*Pnnm*
Pr	$Pr_2Ta_3O_8Se_2$	9.910	11.814	7.624	*Pnnm*
Nd	$Nd_2Ta_3O_8Se_2$	9.898	11.777	7.597	*Pnnm*

These compounds are isostructural, with orthorhombic symmetry, *Pnnm* space group and very similar unit cell sizes. There are two types of tantalum sites; one is in a distorted octahedral site of six oxygen atoms and, the other a distorted octahedral environment with two *trans* oxygen and four selenium atoms. The TaO_6 octahedra form *E* chains and the TaO_2Se_4 octahedra form *C-E* chains. These are connected to form *S* layers which extend along the *ac* plane. In between these are LnO_7Se_2 polyhedra. The structure is illustrated in Figure 1.29.

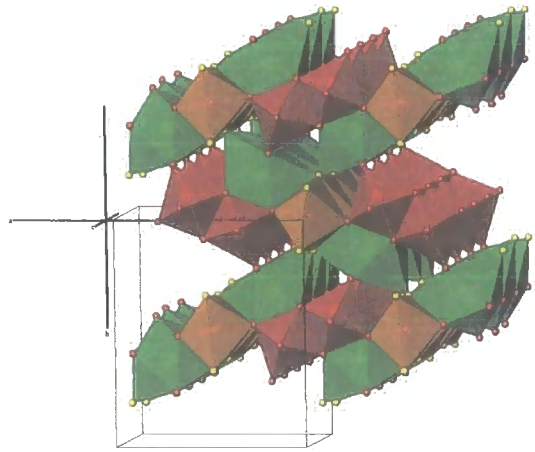

Figure 1.29 The structure of $Ln_2Ta_3O_8Se_2$ (Ln = La – Nd). TaO_6 and TaO_2Se_4 octahedra are shown in red and orange respectively, LnO_7Se_2 in green.

$La_2Ta_3O_8Se_2$ has mixed Ta^{4+}/Ta^{5+} cations in distinct sites as might be expected, the Ta^{5+} ions are in the all O environment and the Ta^{4+} ions in the Ta_2OSe_4 environment.

1.3.4 *Ln*CrOX_2 compounds

The *Ln*CrOX_2 (*Ln* = La, Ce, Pr, Nd, Sm) compounds fall into two different structural groups; those with *Ln* = La have the *Pbnm* space group, and the remaining *Ln* containing compounds have *B*2/*m*, as shown in Table 1.7.

Table 1.7 *Ln*CrOX_2 compounds

Ln	S	Space group	Se	Space group
La	$LaCrOS_2$[5]	*Pbnm*	$LaCrOSe_2$[67]	*Pbnm*
Ce	$CeCrOS_2$[68]	*B*2/*m*	$CeCrOSe_2$[67]	*B*2/*m*
Pr	$PrCrOS_2$[60]	*B*2/*m*		
Nd	$NdCrOS_2$[60]	*B*2/*m*	$NdCrOSe_2$[67]	*B*2/*m*
Sm	$SmCrOS_2$[60]	*B*2/*m*		

The *Ln* atoms in this family of materials are in a nine coordinate environment with three oxygen atoms and six chalcogenide atoms. This means that the differences between members of this sub group are all in the differences in environment of the chromium atom.

In LaCrOX_2 there are *E*-*E* chains of $CrOX_5$ octahedra (two parallel *E* chains connected by shared edges) and LaO_3X_6 polyhedra, while in *Ln*$CrOS_2$ (*Ln* = Ce, Pr, Nd) there are two *E* chains (one of CrS_6 and one of CrO_2S_4 octahedra), which are connected to make *S* layers, in between which are LnO_3S_6 polyhedra. Both structures are shown in Figure 1.30.

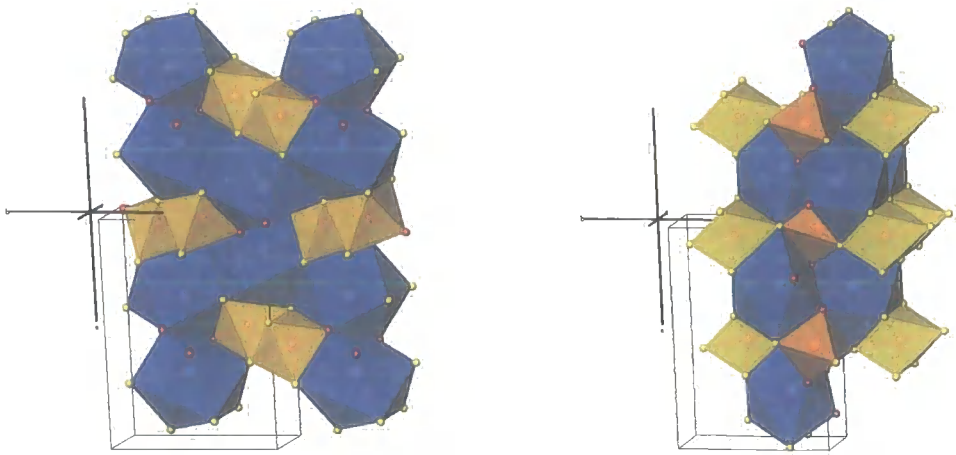

Figure 1.30 Left, the structure of $LaCrOX_2$. $CrOS_5$ octahedra are shown in yellow, LaO_3S_6 polyhedra in blue. Right, the structure of $LnCrOS_2$ (Ln = Ce, Pr, Nd). CrS_6 and CrO_2S_4 octahedra are shown in yellow and orange respectively, CeO_3S_6 in blue.

1.3.5 La/In/O/S

Two 3 dimensional lanthanum indium oxysulfides, $La_5In_3O_3S_9$ and $LaInS_2O$, have recently been reported,[69] but while the latter has been indexed to an orthorhombic a = 20.5421 Å, b = 14.8490 Å, c = 3.9829 Å cell, its structure solution has not yet been reported. In $La_5In_3O_3S_9$ the indium atoms are in all sulfur environments, either in tetrahedra or octahedra. The octahedra form E chains which are connected by edges to form an S layer, while the tetrahedra lie between these layers. The lanthanum is in the typical 7, 8 and 9 coordinate mixed O and S environments.

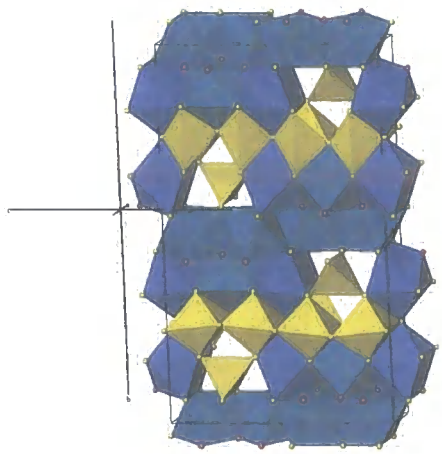

Figure 1.31 The structure of $La_5In_3O_3S_9$. InS_4 tetrahedra and InS_6 octahedra are shown in yellow, LaO_3S_4, LaO_4S_5 in turquoise and $LaOS_7$ in blue.

1.4 Conclusions

The widely differing structures and properties of both layered and three dimensional oxychalcogenides well illustrates the potential of "building block" style approaches to understand structure and target syntheses and materials. The more well studied materials, such as the *Ln*OCu*X* series of compounds, have found potential applications and their properties are able to be further enhanced by subtle doping and intercalation strategies, as are some of the other materials mentioned in this chapter. The ability to interchange not just metals and chalcogenides, but whole structural motifs, such as layers or chains, offers a wide range of potential compounds with a wide range of properties.

1.5 References

(1) Kapeik, V. *Naturwissenschafen,* **1967**, *54*, 114.

(2) Nakai, I.; Nagashima, K.; Koto, K. and Morimoto, N. *Acta Crystallogr. B,* **1978**, *34*, 1337-1339.

(3) Palazzi, M.; Carcaly, C. and Flahaut, J. *J. Solid State Chem.,* **1980**, *35*, 150-155.

(4) Wintenberger, M.; Vovan, T. and Guittard, M. *Solid State Commun.,* **1985**, *53*, 227-230.

(5) Wintenberger, M.; Dugue, J.; Guittard, M.; Nguyen Huy, D. and Vo Van, T. *J. Solid State Chem.,* **1987**, *70*, 295-302.

(6) Zhu, W. J. and Hor, P. H. *J. Solid State Chem.,* **1997**, *130*, 319-321.

(7) Yu, S. H.; Han, Z. H.; Yang, J.; Zhao, H. Q.; Yang, R. Y.; Xie, Y.; Qian, Y. T. and Zhang, Y. H. *Chem. Mater.,* **1999**, *11*, 192-194.

(8) Ueda, K.; Inoue, S.; Hirose, S.; Kawazoe, H. and Hosono, H. *Appl. Phys. Lett.,* **2000**, *77*, 2701-2703.

(9) Palazzi, M. *Compt. Rend. Acad. Sci. Paris,* **1981**, *292*, 789-791.

(10) Ueda, K.; Takafuji, K. and Hosono, H. *J. Solid State Chem.,* **2003**, *170*, 182.

(11) Ueda, K.; Takafuji, K.; Hiramatsu, H.; Ohta, H.; Kamiya, T.; Hirano, M. and Hosono, H. *Chem. Mater.,* **2003**, *15*, 3692-3695.

(12) Kusainova, A. M.; Berdonosov, P. S.; Akselrud, L. G.; Kholodkovskaya, L. N.; Dolgikh, V. A. and Popovkin, B. A. *J. Solid State Chem.,* **1994**, *112*, 189-191.

(13) Berdonosov, P. S.; Kusainova, A. M.; Kholodkovskaya, L. N.; Dolgikh, V. A.; Akselrud, L. G. and Popovkin, B. A. *J. Solid State Chem.,* **1995**, *118*, 74-77.

(14) Zhu, W. J.; Huang, Y. Z.; Dong, C. and Zhao, Z. X. *Mater. Res. Bull.,* **1994**, *29*, 143-147.

(15) Ueda, K. and Hosono, H. *J. Appl. Phys.,* **2002**, *91*, 4768-4770.

(16) Ueda, K. and Hosono, H. *Thin Solid Films,* **2002**, *411*, 115-118.

(17) Ohtani, T. and Tachibana, Y. *Inst. Phys. Conf. Ser.,* **1998**, *152*, 1009-1012.

(18) Takase, K.; Shimizu, T.; Makihara, K.; Sato, H.; Negishi, H.; Takahashi, Y.; Takano, Y.; Sekizawa, K.; Kuroiwa, Y.; Aoyagi, S.; Utsumi, A.; Wada, A.; Ino, A.; Namatame, H. and Taniguchi, M. *Physica B,* **2003**, *329-333*, 898-899.

(19) Takano, Y.; Mori, K.; Koizumi, K.; Ozaki, H. and Sekizawa, K. *J. Alloy Compd.,* **1998**, *275-277*, 447-449.

(20) Ohtani, T.; Tachibana, Y. and Fujii, Y. *J. Alloy Compd.,* **1997**, *262-263*, 175-179.

(21) Vajenine, G. V. and Hoffmann, R. *Inorg. Chem.,* **1995**, *35*, 451-457.

(22) Guittard, M.; Benazeth, S.; Dugue, J.; Jaulmes, S.; Palazzi, M.; Laruelle, P. and Flahaut, J. *J. Solid State Chem.,* **1984**, *51*, 227-238.

(23) Guittard, M. and Flahaut, J. *New Front. Rare Earth Sci. Appl., Proc. Int. Conf. Rare Earth Dev. Appl.,* **1985**, *2*, 1460-1463.

(24) Dugue, J. and Guittard, M. *Acta Crystallogr. B,* **1982**, *38*, 2368-2371.

(25) Jaulmes, S.; Carre, D.; Palazzi, M. and Guittard, M. *Compt. Rend. Acad. Sci. Paris,* **1985**, *301*, 259-262.

(26) Jaulmes, S.; Godlewski, E.; Palazzi, M. and Etienne, J. *Acta Crystallogr. B,* **1982**, *38*, 1707-1710.

(27) Laruelle, P.; Guittard, M. and Benazeth, S. *Acta Crystallogr. C,* **1985**, *41*, 649-651.

(28) Benazeth, S.; Guittard, M. and Laruelle, P. *Acta Crystallogr. C,* **1984**, 345-347.

(29) Ceolin, R. and Rodier, N. *Acta Crystallogr. B,* **1976**, *32*, 1476-1479.

(30) Mayer, J. M.; Schneemeyer, L. F.; Siegrist, T.; Waszczak, J. V. and Vandover, B. *Angew. Chem.-Int. Edit. Engl.,* **1992**, *31*, 1645-1647.

(31) Jaulmes, S.; Julienpouzol, M.; Guittard, M.; Vovan, T.; Laruelle, P. and Flahaut, J. *Acta Crystallogr. C,* **1986**, *42*, 1109-1111.

(32) Jaulmes, S.; Julienpouzol, M.; Dugue, J.; Laruelle, P.; Vovan, T. and Guittard, M. *Acta Crystallogr. C,* **1990**, *46*, 1205-1207.

(33) Zhu, W. J.; Hor, P. H.; Jacobson, A. J.; Crisci, G.; Albright, T. A.; Wang, S. H. and Vogt, T. *J. Am. Chem. Soc.,* **1997**, *119*, 12398-12399.

(34) Lorenz, B.; Zhu, W. J.; Ting, S. T. and Hor, P. H. *Koatsuryoku no Kagaku to Gijutsu,* **1998**, *7*, 583-585.

(35) Otzschi, K.; Ogino, H.; Shimoyama, J.-I. and Kishio, K. *J. Low Temp. Phys.,* **1999**, *117*, 729-733.

(36) Ueda, K.; Hirose, S.; Kawazoe, H. and Hosono, H. *Chem. Mater.,* **2001**, *13*, 1880-1883.

(37) Barrier, N. and Clarke, S. J. *Chem. Commun.,* **2003**, 164-165.

(38) Park, Y.; DeGroot, D. C.; Schindler, J. L.; Kannewurf, C. R. and Kanatzidis, M. G. *Chem. Mater.,* **1993**, *5*, 8-10.

(39) Evans, J. S. O.; Brogden, E. B.; Thompson, A. L. and Cordiner, R. L. *Chem. Commun.,* **2002**, 912-913.

(40) Harrington, R., M.Chem. Thesis, University of Durham, Durham, 2003.

(41) Zhu, W. J. and Hor, P. H. *J. Solid State Chem.,* **1997**, *134*, 128-131.

(42) Zhu, W. J. and Hor, P. H. *J. Solid State Chem.*, **2000**, *153*, 26-29.

(43) Naganuma, J.; Kamihara, Y. and Matoba, M. *Nippon Oyo Jiki Gakkaishi,* **2002**, *26*, 376-379.

(44) Clarke, S. J.; Denis, S. G.; Rutt, O. J.; Hill, T. L.; Hayward, M. A.; Hyett, G. and Gal, Z. A. *Chem. Mater.*, **2003**, *15*, 5065-5072.

(45) Goga, M.; Seshadri, R.; Ksenofontov, V.; Gutlich, P. and Tremel, W. *Chem. Commun.*, **1999**, 979-980.

(46) Lafond, A.; Leynaud, O.; Andre, G.; Bouree, F.; Caldes, M. and Meerschaut, A. *Mater. Sci. Forum,* **2004**, *443-444*, 387-390.

(47) Ruddlesden, S. N. and Popper, P. *Acta Crystallogr.*, **1958**, *11*, 54-55.

(48) Denis, S. G. and Clarke, S. J. *Chem. Commun.*, **2001**, 2356-2357.

(49) Hyett, G.; Rutt, O. J.; Gal, Z. A.; Denis, S. G.; Hayward, M. A. and Clarke, S. J. *J. Am. Chem. Soc.*, **2004**, *126*, 1980-1991.

(50) Rutt, O. J.; Hill, T. L.; Gal, Z. A.; Hayward, M. A. and Clarke, S. J. *Inorg. Chem.*, **2003**, *42*, 7906-7911.

(51) Meignen, V.; Lafond, A.; Cario, L.; Deudon, C. and Meerschaut, A. *Acta Crystallogr. C,* **2003**, *C59*, i63-i64.

(52) Boyer-Candalen, C.; Deudon, C. and Meerschaut, A. *J. Solid State Chem.*, **2000**, *152*, 554-559.

(53) Meerschaut, A.; Lafond, A.; Meignen, V. and Deudon, C. *J. Solid State Chem.*, **2001**, *162*, 182-187.

(54) Tougait, O. and Ibers, J. A. *J. Solid State Chem.*, **2001**, *157*, 289-295.

(55) Tougait, O. and Ibers, J. A. *Chem. Mater.*, **2000**, *12*, 2653-2658.

(56) Cody, J. A. and Ibers, J. A. *J. Solid State Chem.*, **1995**, *114*, 406-412.

(57) Person, H. and Urland, W. *J. Alloy Compd.*, **2001**, *323*, 57-60.

(58) Meignen, V.; Deudon, C.; Lafond, A.; Boyer-Candalen, C. and Meerschaut, A. *Solid State Sci.*, **2001**, *3*, 189-194.

(59) Tranchitella, L. J.; Fettinger, J. C. and Eichhorn, B. W. *Chem. Mater.*, **1996**, *8*, 2265-2271.

(60) Deudon, C.; Meerschaut, A.; Cario, L. and Rouxel, J. *J. Solid State Chem.*, **1995**, *120*, 164-169.

(61) Cody, J. A.; Deudon, C.; Cario, L. and Meerschaut, A. *Mater. Res. Bull.*, **1997**, *32*, 1181-1192.

(62) Cario, L.; Deudon, C.; Meerschaut, A. and Rouxel, J. *J. Solid State Chem.*, **1998**, *136*, 46-50.

(63) Tranchitella, L. J.; Fettinger, J. C.; Heller-Zeisler, S. F. and Eichhorn, B. W. *Chem. Mater.*, **1998**, *10*, 2078-2085.

(64) Tougait, O. and Ibers, J. A. *J. Solid State Chem.*, **2000**, *154*, 564-568.

(65) Brennan, T. D.; Aleandri, L. E. and Ibers, J. A. *J. Solid State Chem.*, **1991**, *91*, 312-322.

(66) Brennan, T. D. and Ibers, J. A. *J. Solid State Chem.*, **1992**, *98*, 82-89.

(67) Vo Van, T. and Nguyen Huy, D. *Compt. Rend. Acad. Sci. Paris,* **1981**, *293*, 933-936.

(68) Dugue, J.; Vovan, T. and Villiers, J. *Acta Crystallogr. B,* **1980**, *36*, 1291.

(69) Kabbour, H.; Cario, L.; Moelo, Y. and Meerschaut, A. *J. Solid State Chem.*, **2004**, *177*, 1053-1059.

Chapter 2 Experimental

This chapter describes the synthesis and characterisation methods used throughout this thesis, including full synthetic details and descriptions of room temperature X-ray powder diffraction, variable temperature X-ray powder diffraction using a Bruker D8 and PheniX He ccr, neutron powder diffraction, SQUID magnetometry and conductivity measurements.

2.1 Synthetic details

This section describes the syntheses of the compounds that are discussed in the following chapters. Oxychalcogenides, containing both oxide and sulfide/selenide ions, need to be prepared in controlled atmospheres to prevent oxidation of the chalcogen. All the compounds discussed in this thesis were synthesised using evacuated and sealed quartz ampoules to control the amount of oxygen present at the high temperatures required for synthesis. In addition to this, many of the reagents were stored in a nitrogen atmosphere glovebox, with low oxygen and moisture content, to ensure their purity. These reagents are marked with an asterisk in Table 2.1, which also contains details about all reagents used in the syntheses described in this chapter.

Table 2.1 Purity and supplier of reagents. An asterisk denotes that the reagent was stored in a nitrogen atmosphere glovebox.

Reagent	Supplier	Purity
*La_2O_3	Avocado	99.9%
Mn	Avocado	99+%
Co	Fisons	
*Co	Alfa-Aesar	99.8%
Ni	Hopkins & Williams	
Zn	Alfa-Aesar	99.9%
S	Aldrich	99.98%
Se	Alfa-Aesar	99.999%
Sn	Goodfellow	99.75%
*BaS	Alfa-Aesar	99.7%
*BaSe	Alfa-Aesar	99.5%
*SrS	Alfa-Aesar	99.9%
*SrSe	Alfa-Aesar	99.5%
*Sm_2O_3	BDH	99.9%
*Y_2O_3	Aldrich	99.99%
CuO	Fluka	>99%
$CoCl_2.6H_2O$	Aldrich	
Fe_2O_3	Avondale Laboratories	
$Mn(C_3H_5O).4H_2O$	Aldrich	99+%

2.1.1 $La_2O_3M_2X_2$ (M = Mn, Fe, Co, Ni; X = S, Se)

The known phases $La_2O_3Fe_2X_2$ (X = S, Se)[1] were synthesised as preliminary experiments to ascertain whether the synthetic technique reported in the literature could be reproduced. The resulting samples were characterised by X-ray powder diffraction and found to be very pure. Using similar synthetic conditions, the $La_2O_3M_2X_2$ compounds (M = Mn, Co, Ni; X = S, Se) were investigated. Syntheses performed between 600 and 1100 °C showed that higher temperatures produced more crystalline and less impure samples, typified by NDW324, shown in Figure 2.1. However, heating the sealed quartz ampoules to 1100 °C and above proved to greatly increase the chance of the ampoules exploding. This meant that a final synthesis temperature of 1000 °C was employed for all compounds discussed in Chapter 3. Table 2.2 summarises the results of these syntheses, with a tick indicating a pure sample was prepared.

Table 2.2 Summary of synthetic results.

M \ *X*	S	Se
Mn		✓
Fe	✓	✓
Co		✓
Ni		

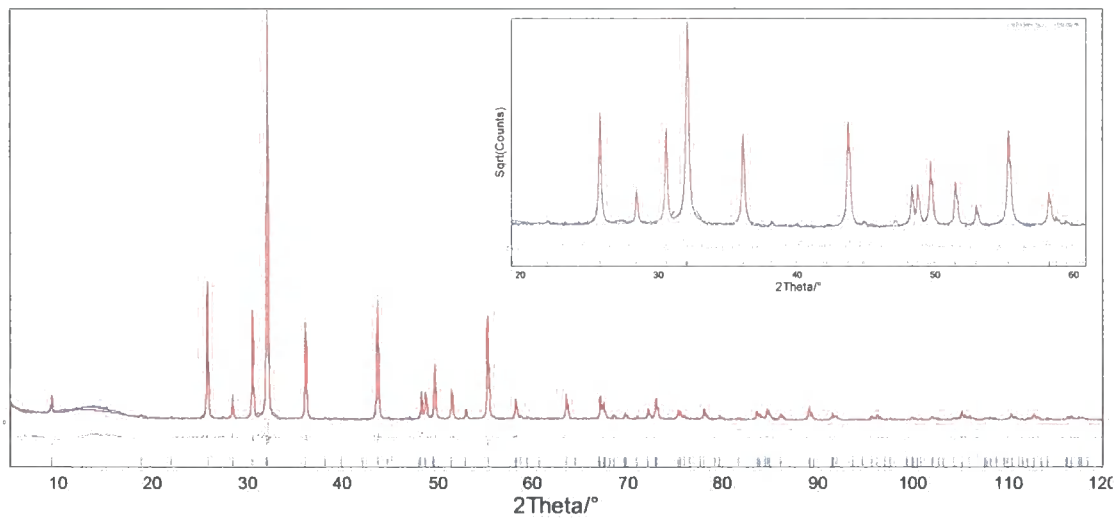

Figure 2.1 Rietveld refinement of $La_2O_3Mn_2Se_2$. Observed pattern in blue, calculated in red, difference in grey. Tick marks show predicted peak positions for $La_2O_3Mn_2Se_2$. Inset shows 20 – 60 2θ region with a square roots (counts) scale to emphasise weaker features in the pattern.

Samples of $La_2O_3M_2X_2$ (M = Mn, Co, Ni; X = S, Se) were all synthesised using stoichiometric amounts of La_2O_3, M and X (purity and supplier shown in Table 2.1). All reagents were tested for phase purity by X-ray diffraction before use. Before use the La_2O_3 was heated to 800 °C to remove any absorbed moisture or CO_2 and then kept in a nitrogen atmosphere Vacuum-Atmospheres glovebox. In a typical synthesis reagents were weighed out to ± 0.0001 g and

intimately ground together in an agate mortar and pestle; specific reagent masses are in Table 2.4. The resultant light grey mixtures were transferred to a pellet die and pressed into 13 mm pellets with a force of ~4 tonnes using a pellet press. It was ensured that the reagents (particularly the hygroscopic La_2O_3) were exposed to air for no more than the time taken to weigh them, typically less than 5 minutes. The pellets (broken in half to fit in the 9 mm inner diameter quartz ampoules) were then flame-sealed in quartz ampoules under a dynamic vacuum of $\leq 1 \times 10^{-1}$ mbar, after having been evacuated for >10 minutes to ensure as much air/moisture had been removed as possible. The sealed quartz ampoules were then placed in furnaces and heated to 1000 °C. Preliminary experiments had demonstrated that careful heating regimes were necessary to avoid the ampoules exploding; as a result samples were first heated at 1 °C min^{-1} to 600 °C and kept at that temperature for twelve hours. They were then slowly heated (0.5 °C min^{-1}) to 800 °C and again held at that temperature for one hour. The final synthesis temperature of 1000 °C was reached at a rate of 1 °C min^{-1}. After 12 hours the furnace was allowed to cool and the sample removed at ≤ 500 °C. When the ampoules had cooled to room temperature in air, they were broken open with a hammer and the pellets removed with tweezers. The pellets were then ground in an agate mortar and pestle and prepared for analysis by X-ray diffraction.

Samples of $La_2O_3Mn_2Se_2$ and $La_2O_3Co_2Se_2$ with purity and crystallinity approaching that of the *M* = Fe phases were obtained. They were found to be isostructural with the Fe analogues, but with slightly differing cell parameters and atomic positions. This was confirmed using the Total Pattern Analysis Suite[2] (TOPAS) to perform Rietveld refinement (Section 2.2.2 below) on a suitable starting model of the structure. The $La_2O_3Mn_2Se_2$ sample formed was a green powder; however, the surface of the pellets was often a pinkish white colour, indicating that a reaction with the quartz ampoule had occurred. $La_2O_3Co_2Se_2$ was a very dark grey colour and the pellets again showed some surface reaction. The purity of the final products was improved by using larger pellets (which reduced the surface area to volume ratio of the samples) and carefully removing the surface of the pellets with a scalpel.

For the neutron diffraction experiments large and high purity samples were required. In order to achieve this, the masses of the reagents in a standard synthesis were scaled up by a factor of ten. 13 mm pellets of approximately 5 mm thickness were sealed in a ~20 mm inner diameter quartz ampoule after 30 minutes of evacuation at 10^{-2} mbar. The surface of the pellets was carefully removed with a scalpel and retained for analysis. Figure 2.2 shows the difference in purity between the surface and bulk of a pellet. Due to high crystallinity and purity of the samples and the need to remove a portion of the sample (the surface) it was decided that repeating the grinding, pelleting and heating process would only decrease the amount of pure sample and was not undertaken.

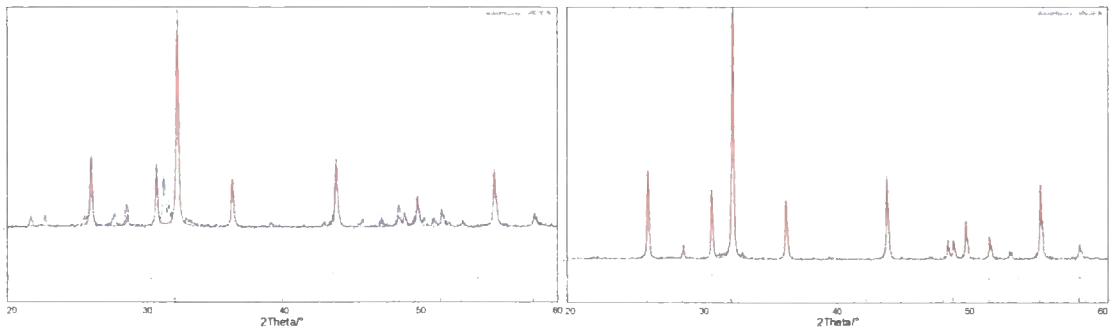

Figure 2.2 Powder patterns of the surface of a pellet (L) and the bulk of a pellet (R). observed points in blue, calculated in red, difference in grey.

Simple 1 hr powder X-ray diffraction experiments were enough to show that the X = S containing compounds had not been successively synthesised. Synthesis temperatures every 100 °C from 600 °C to 1200 °C were attempted and the same result found. The majority product was identified in each case as being La_2O_2S by searching the Powder Diffraction File[3] (PDF) in the X-ray Evaluation program of the DiffracBasic Plus software suite. This was confirmed by Rietveld refinement (Figure 2.3).

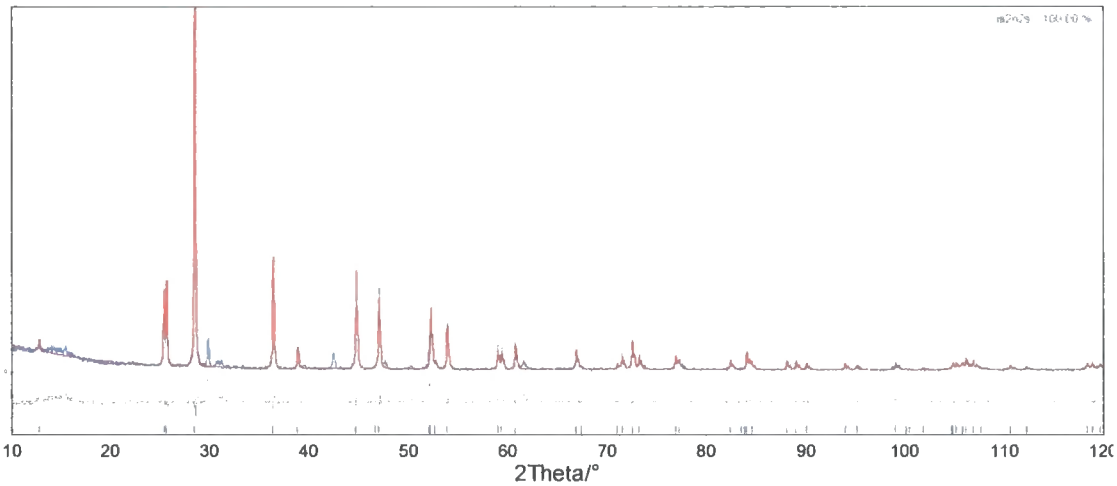

Figure 2.3 Rietveld refinement of sample NDW62, showing La_2O_2S to be majority product. Observed pattern in blue, calculated in red, difference in grey. Tick marks show expected peak positions for La_2O_2S.

Despite three experiments, at varying temperatures and with varying synthesis times, no M = Ni compounds were synthesised. The resulting samples mainly consisted of La_2NiO_4.

2.1.2 $A_2MCu_2O_2X_2$ (A = Sr, Ba; M = Mn, Fe, Co, Ni, Zn; X = S, Se)

The $A_2MCu_2O_2X_2$ compounds discussed in Chapter 4 were all synthesised using stoichiometric amounts of AX, M and CuO (see Table 2.1 for suppliers and purity of reagents). All reagents were tested for phase purity by X-ray diffraction before use. The AX reagents were stored in a nitrogen atmosphere Vacuum-Atmospheres glovebox to prevent oxidation or

hydrolysis. Stoichiometric molar ratios of the reagents were weighed out to ± 0.0001 g and intimately ground together in an agate mortar and pestle. The resultant mixtures were transferred to a pellet die and pressed into 5 or 13 mm pellets with a force of ~2 or ~4 tonnes respectively using a pellet press. This protocol used ensured that the reagents (particularly the mildly air sensitive *AX* reagents) were exposed to air for no more than the time taken to weigh them, typically less than 5 minutes. The pellets (broken in half in the case of 13 mm pellets to fit in the 9 mm inner diameter quartz ampoules) were then flame-sealed in quartz ampoules under a dynamic vacuum of ≤ 1 x 10^{-1} mbar, after having been evacuated for >10 minutes to ensure all air/moisture had been removed. The quartz ampoules were placed in a furnace and heated to the final synthesis temperature (750 – 850 °C) at a rate of 3 °C min^{-1}. After 12/72 hours the furnace was allowed to cool and the sample removed at ≤ 500 °C. When the ampoules had cooled to room temperature in air, they were broken open with a hammer and the pellets removed with tweezers. The pellets were then ground in an agate mortar and pestle and prepared for analysis by X-ray diffraction. Table 2.5 gives compound specific masses and temperatures.

From Table 2.3 it can also be seen which of the compounds were successfully synthesised. In the unsuccessful cases (notably all *M* = Fe containing compounds), the products ranged from the unreacted starting materials to a target compound with many impurities. $BaSO_4$, $BaCu_2S_2$, ZnO, Cu_2SrO_2 (Figure 2.4) were frequently observed as impurities.

Table 2.3 Summary of synthetic results.

M \ *AX*	BaS	BaSe	SrS	SrSe
Mn		✓		✓
Fe				
Co	✓	✓	✓	✓
Ni		✓		✓
Zn			✓	✓

For some experiments (conductivity and some magnetic measurements) 5 mm pellets were required. To ensure the pellets used for these experiments were pure 3 or 4 pellets were pressed from the same batch of ground reagents, and sealed in the same quartz ampoule. In this way, one pellet could be ground up and analysed by X-ray diffraction and the others saved for physical property measurements. Some 5 mm pellets were prepared from samples which had already been synthesised (most often in 13 mm pellet form); again several 5 mm pellets were pressed from the same sample and sealed in the same ampoule and one checked for purity. The samples that were made from re-pelleted samples are highlighted accordingly in Table 2.5.

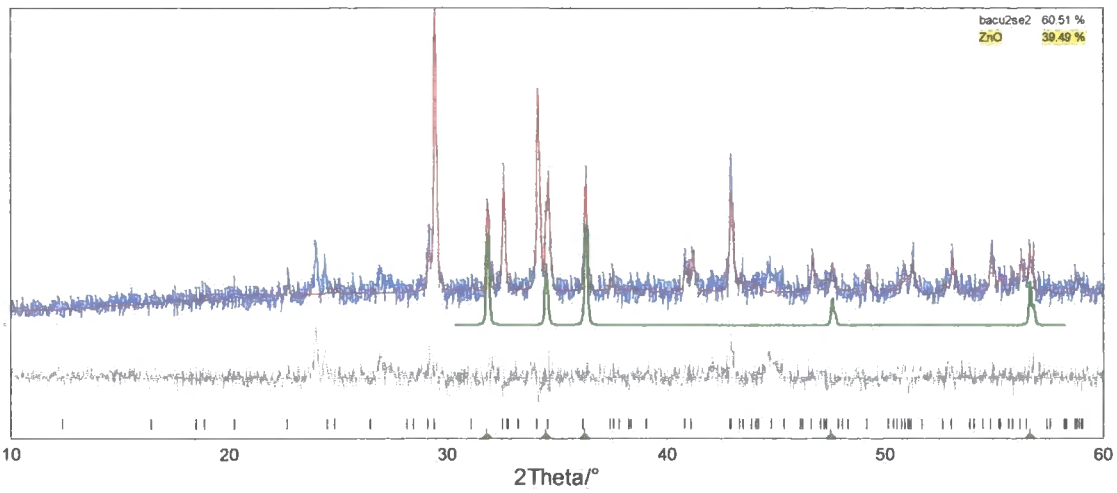

Figure 2.4 Powder X-ray diffaction pattern of sample NDW228, which shows $BaCu_2Se_2$ and ZnO as main products with no $Ba_2ZnCu_2O_2Se_2$ present. Observed pattern in blue, calculated in red, difference in grey and ZnO calculated pattern in green. Tick marks are predicted peak positions for $BaCu_2Se_2$ and ZnO from top to bottom respectively.

2.1.3 $A_2MO_2Ln_2O_2X_2$ (A = Sr, Ba; M = Mn, Fe, Co; Ln = La, Gd, Y; X = S, Se)

Attempts to synthesise the target $A_2MO_2Ln_2O_2X_2$ compounds discussed in Chapter 5 were made using stoichiometric amounts of AX, Ln_2O_3, M_xO_y and M (see Table 2.1 for suppliers and purity of reagents). All reagents were tested for phase purity by X-ray diffraction before use. The Ln_2O_3 reagents had been heated to 800 °C to remove any absorbed moisture or CO_2 and then kept in a nitrogen atmosphere Vacuum-Atmospheres glovebox; the AX reagents were stored in the same glovebox. The reagents were weighed out to ± 0.0001 g and intimately ground in an agate mortar and pestle. The resultant mixtures were pressed into 13 mm pellets with a force of ~4 tonnes using a pellet press. This protocol adopted ensured that the reagents (particularly the mildly air sensitive AX reagents and hygroscopic Ln_2O_3) were exposed to air for no more than the time taken to weigh them, typically less than 5 minutes. The pellets were broken in half and then flame-sealed in a quartz ampoule under a vacuum of $<1 \times 10^{-1}$ mbar, having been evacuated for 10 – 15 min.

The masses used in a typical synthesis were 0.1000g (3.096×10^{-4} mol) La_2O_3, 0.0163g (1.023×10^{-4} mol) Fe_2O_3, 0.1029g (6.139×10^{-4} mol) SrSe, 0.0057g (1.023×10^{-4} mol) Fe. This gives 6.139×10^{-4} mol of Sr, La and Se, 3.069×10^{-4} mol Fe and 12.28×10^{-4} mol O.

The M_xO_y reagents were typically prepared by heating a convenient metal salt in air at ~800 – 1000 °C to decompose them to oxides. $CoCl_2.6H_2O$ was decomposed to CoO and Co_3O_4 by heating at 8 °C min^{-1} to 1000 °C and holding at that temperature for 12 hours. Hydrated manganese acetate was decomposed to Mn_3O_4 by heating at 10 °C min^{-1} to 1100 °C and being held at that temperature for 12 hours. To ensure the Fe_2O_3 did not contain any

absorbed water or other iron oxides it was heated at 5 °C min^{-1} to 1000 °C and left overnight. In cases where a mixture of different oxides were formed, *e.g.* CoO and Co_3O_4 the overall composition of the reagent was ascertained by Rietveld refinement (see Figure 2.5) and in the syntheses the desired molar ratios were achieved by addition of the pure metal.

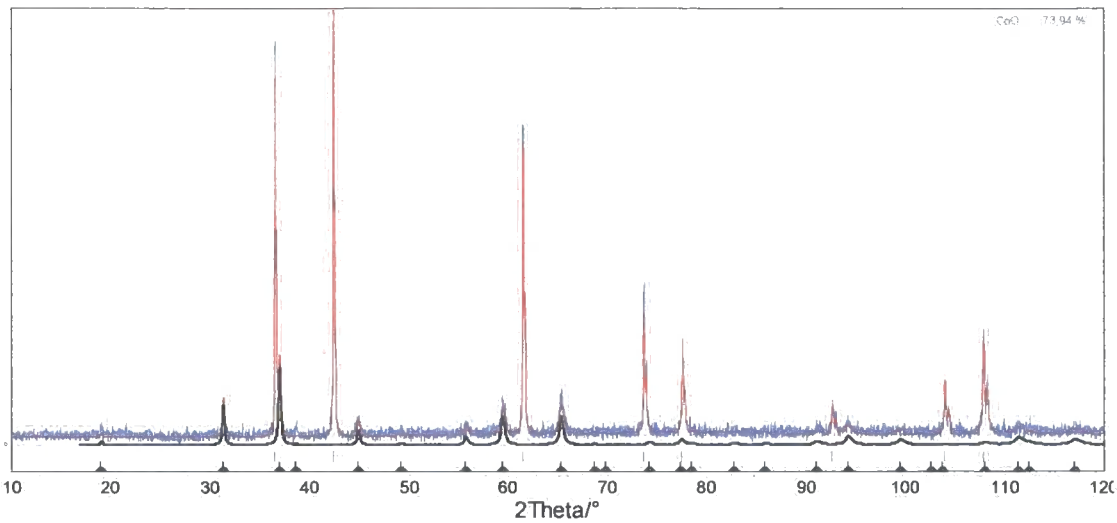

Figure 2.5 Powder pattern of Co_xO_y reagent. Observed pattern in blue, calculated for CoO and Co_3O_4 in red, calculated pattern for Co_3O_4 only in black.

For *X* = S the ampoules were heated using the following regime: heat at 1 °C min^{-1} to 400 °C, hold for 12 hours, heat at 0.5 °C min^{-1} to 600 °C; hold for 1 hour; heat at 1 °C min^{-1} to the final temperature (800, 1000 or 1100 °C) and hold for 12 hours; slow cool to room temperature or removed at ≤ 500 °C. When the ampoules had cooled to room temperature in air, they were broken open with a hammer and the pellets removed with tweezers. The pellets were then ground in an agate mortar and pestle and prepared for analysis by X-ray diffraction.

For *X* = Se, the same regime was used, but the samples were held at 600 and 800 °C before reaching the final temperature.

A number of samples were subjected to a second heat treatment by re-pressing into 13 mm pellets with a force of ~4 tonnes, sealing in a quartz ampoule and heating at 2 °C min^{-1} to 1000 °C and held for 12 hours. An example of this is NDW118, the original products of which were Y_2O_3, BaS and CoO. On re-heating little change in the sample composition was observed.

Attempts to synthesise the $A_2MO_2Ln_2O_2X_2$ materials were unsuccessful; details are outlined in Chapter 5.

Table 2.4 Synthetic details for $La_2O_3M_2X_2$ compounds.

Compound	Sample ID	Mass/g			Pellet size/mm	Temperature/°C	Final dwell time/h	Colour
		La_2O_3	*M*	Se				
$La_2O_3Mn_2Se_2$	324	1.9943	0.6726	0.9789	13	1000	12	Olive green
$La_2O_3Mn_2Se_2$	320	1.0729	0.3618	0.5266	13	1000	12	Olive green
$La_2O_3Co_2Se_2$	328	2.0475	0.7407	1.0050	13	1000	12	Light grey
$La_2O_3Co_2Se_2$	321	0.1315	0.0476	0.0645	5	1000	12	Light grey

Table 2.5 Synthetic details for $A_2MCu_2O_2X_2$ compounds.

Compound	Sample ID	Mass/g			Pellet size/mm	Temperature/°C	Heating rate/°C min^{-1}	Final dwell time/h	Sample re-pelleted from:	Colour
		AX	*M*	CuO						
$Ba_2CoCu_2O_2S_2$	251	0.1830	0.0318	0.0859	5	800	3	12		Dark grey/black
$Ba_2CoCu_2O_2Se_2$	252	0.2255	0.0307	0.8290	5	800	3	12		Dark grey/black
$Sr_2CoCu_2O_2S_2$	255	0.0984	0.0242	0.0654	5	800	3	12		Dark grey/black
$Sr_2CoCu_2O_2Se_2$	256	0.0832	0.0147	0.0397	5	800	3	12		Grey
$Ba_2MnCu_2O_2Se_2$	325	0.1354	0.0172	0.0498	13	800	3	72	287	Dark grey/black
$Sr_2MnCu_2O_2Se_2$	326	0.1264	0.0208	0.0604	13	850	3	12	297	Dark grey/black
$Ba_2NiCu_2O_2Se_2$	334	0.2287	0.0310	0.0841	13	750	3	12		Black
$Sr_2NiCu_2O_2Se_2$	250	0.2078	0.0366	0.0992	13	800	3	12	243	Light grey
$Sr_2ZnCu_2O_2S_2$	301	0.3200	0.0874	0.2127	13	800	3	12		Olive green
$Sr_2ZnCu_2O_2Se_2$	302	0.0909	0.0178	0.0434	13	800	3	12		Dark red/brown

2.2 Diffraction Methods

2.2.1 X-ray diffraction

X-ray diffraction is one of the most important methods for characterising the structures of crystalline materials as it allows almost unparalleled determination of the absolute fractional coordinates of the constituent atoms. This is crucial information to any kind of insight into the properties of a material and to fully understand its behaviour on a macroscopic scale. In addition to structural coordinates, a lot of extra and more subtle information can be gathered: sample texture; crystallite size and strain; the thermal behaviour of the atoms; and, from variable temperature/time experiments, kinetic information such as mechanistic pathways and activation energies. Quantitative phase analysis is routine and even full structure solution is becoming increasingly common with advancing diffraction technology, computing power and the development of better techniques for structure solution.

In a typical laboratory set-up X-rays are generated by a beam of electrons emitted from a heated tungsten filament in a vacuum tube which are typically accelerated through 40 kV and strike a copper target with enough energy to remove a 1*s* electron. An electron changing from the 2*p* to the 1*s* orbital releases a photon with a wavelength of 1.5404 or 1.5443 Å, depending on its spin state in the 2*p* orbital. This radiation is known as Cu $K\alpha_1$ and $K\alpha_2$ radiation respectively and the narrow range of wavelength make them ideal for X-ray diffraction, as the criterion for diffraction of any wave is that the structure producing the diffraction effects must have a size comparable to the wavelength. In a typical X-ray tube, the X-rays leave through beryllium "windows", Be being one of the least absorbing materials to X-rays. During this process "white" radiation across all wavelengths, known as "*bremmstrahlung*", and $K\beta$, produced from other electronic transitions, are also produced. In most diffraction experiments a monochromator is employed to select the $K\alpha$ radiation or a Ni filter used to remove $K\beta$ lines.

When X-rays interact with atoms, the atoms act as secondary point sources and re-radiate X-rays in all directions. It is only when atoms are in a regular, periodic array (*i.e.* are crystalline) that the constructive and destructive interference phenomenon known as diffraction occurs. This phenomenon is most easily described using the Bragg's law approach which, whilst perhaps oversimplifying the physics of the diffraction process is more easily understood than other, more rigorous, treatments.

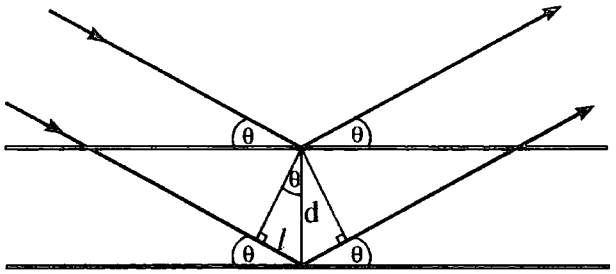

Figure 2.6 The path difference of $2l$ for two reflected beams at angle θ.

W. L. Bragg showed that every diffracted beam can be regarded as if it were a reflection from sets of parallel planes of lattice points. This is analogous to reflection by a mirror in that the angles of incidence and reflection must be equal and co-planar with each other and with the normal to the reflecting plane. The beams reflected by adjacent planes give interference effects equivalent to those employed in the more rigorous Laue equations, as to define a plane three integers are required to specify its orientation with respect to the unit cell edges; these are the *hkl* indices. The spacing between successive planes is determined by the lattice geometry and thus d_{hkl} is a function of the unit cell parameters.

It can be seen from Figure 2.6 that the path difference, $2l$, between two reflected beams is $2d \sin\theta$. For constructive interference to occur this path difference must be equal to an integer number of wavelengths, $n\lambda$. This gives the Bragg equation (Equation 2.1).

$$2d \sin \theta = n \lambda \qquad \text{Equation 2.1}$$

It is common to use n = 1 for all reflections when employing Bragg's law and to consider planes with smaller d spacing, *i.e.* instead of n = 2, the d spacing is halved.

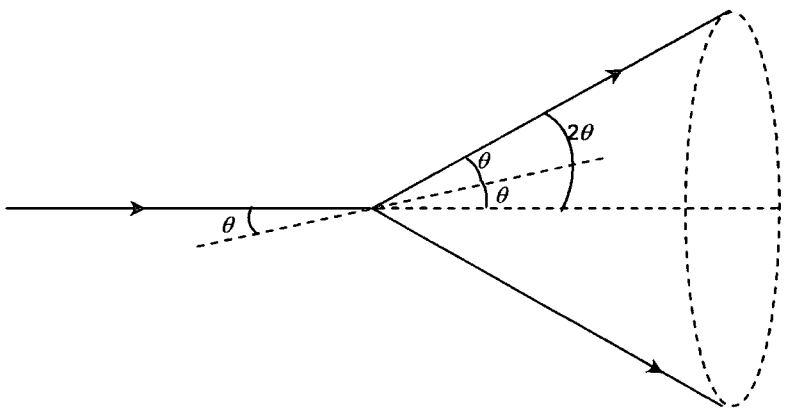

Figure 2.7 Formation of cones of diffracted radiation in powder diffraction.

The principle assumption of powder diffraction is that the sample consists of an infinite number of infinitesimally small crystals (or crystallites) arranged totally randomly. This will

present each set of lattice planes in every possible orientation, meaning that at least some of every set of planes will be at the Bragg angle to the incident beam giving rise to diffraction for those planes. This creates a series of cones, as illustrated in Figure 2.7. The detector in a normal diffractometer will scan across such cones to produce a one dimensional pattern.

The powder diffraction experiment used for all X-ray data sets in this thesis uses convergent X-ray beams in order to get higher resolution and intensity compared to *e.g.* Debye-Scherrer cameras. The X-ray beams are made to converge by making use of the geometric properties of a circle. If the X-ray source, sample and detector all lie on the circumference of a circle (see Figure 2.8) the divergent beam produced by the source will re-focus at the detector. This is because any angles subtended on the circumference of a circle by an arc of that circle will be equal. However, the circle must be sufficiently large that the non-curvature of the sample does not affect the focussing significantly.

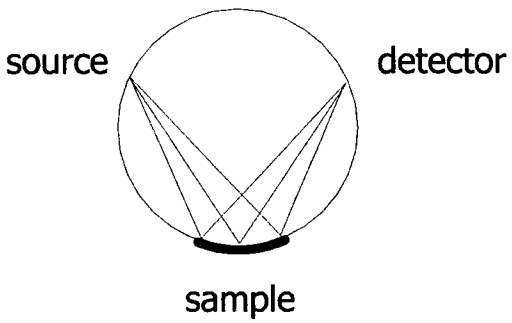

Figure 2.8 Arrangement of X-ray source, sample and detector to focus divergent beam.

2.2.2 Rietveld Refinement

Rietveld refinement is a least-squares refinement method for obtaining the best fit between a structural model and experimental powder diffraction data. This is done by comparing a powder pattern calculated from a model to the pattern recorded experimentally. The calculated pattern is generated from a number of parameters which model characteristics of both the sample and instrument. Sample parameters include unit cell parameters and atomic fractional coordinates; instrument parameters include zero point error, background function and absorption/polarisation corrections. Every point in the profile is treated as an intensity measurement and compared to its counterpart in the calculated profile, and every parameter is refined simultaneously to give the best agreement.

The residual factor (*R* factor) minimised in the Rietveld method is ${}_wR_p$, defined in Equation 2.2, where $y_i(obs)$ is the observed intensity at point *i*, $y_i(calc)$ the calculated intensity at point *i*, and w_i, the weight.

$$ {}_{w}R_{p} = \left(\frac{\sum_{i} w_{i}\left(y_{i}(obs) - y_{i}(calc)\right)^{2}}{\sum_{i} w_{i}\left(y_{i}(obs)\right)^{2}} \right)^{1/2} \qquad \text{Equation 2.2} $$

A statistically best expected R value, R_{exp}, defined in Equation 2.3 (N is the number of observations and P the number of parameters) can be used to assess both the refinement and the quality of the data used, as ${}_{w}R_{p}$ should approach R_{exp} for a good refinement. χ^2, the ratio of ${}_{w}R_{p}$ and R_{exp} (Equation 2.4) is often used to describe the goodness of a fit.

$$ R_{\exp} = \left(\frac{(N-P)}{\sum_{i}^{N} w_{i} y_{i}(obs)^{2}} \right)^{1/2} \qquad \text{Equation 2.3} $$

$$ \chi^{2} = \frac{{}_{w}R_{p}}{R_{\exp}} \qquad \text{Equation 2.4} $$

However, χ^2 can be misleading as it depends on the data collection time. A very long scan will greatly reduce R_{exp}, making χ^2 artificially large, whereas a shorter scan will increase R_{exp} and make χ^2 very small, possibly even less than one. A more reliable R factor, and one more directly comparable to that quoted in single crystal work, is the Bragg R factor, R_{Bragg}, defined in Equation 2.5, where $I_{hkl} = mF_{hkl}^2$ (m = multiplicity).

$$ R_{Bragg} = \frac{\sum_{hkl} \left| I_{hkl}(obs) - I_{hkl}(calc) \right|}{\sum_{hkl} \left| I_{hkl}(obs) \right|} \qquad \text{Equation 2.5} $$

2.2.3 Siemens D5000 diffractometer

Routine sample characterisation, purity checks and longer scans for Rietveld refinement were carried out on a Siemens D5000 X-ray diffractometer. The diffractometer used a Cu Kα radiation source (wavelength average between Kα_1/α_2 =1.5418 Å) passing through a Soller slit and either a variable divergence slit (6 mm or 20 mm of sample illumination; "V6" or "V20") or a fixed 1 degree slit, onto the sample on a plastic slide mounted *via* the automated sample changer. The diffracted radiation then passes through another Soller onto a pyrolitic graphite (001) monochromator and a fixed 0.2 mm receiving slit before entering the scintillation counter. A personal microcomputer using the Bruker Diffrac Plus (version 4.0)[4] suite of programs controls the diffractometer.

Samples were either packed in bulk into a plastic container and the surface smoothed with a glass microscope slide, or sprinkled onto a Vaseline coated glass disc if the volume of sample was not sufficient to fill the container. While this sprinkling method may not give a perfectly smooth surface and gives a larger background (due to the amorphous nature of the glass) it greatly reduces the amount of sample required, allowing smaller sample sizes.

2.2.4 Bruker AXS D8 Advance diffractometer

The laboratory is equipped with a Bruker D8 Advance powder X-ray diffractometer, which can be used for temperature dependent investigations from 15 to 300 K using the PheniX ccr cryostat (see Section 2.2.5), 77 to 723 K using an Anton Paar TTK450 cryostat, and from 300 to 1473 K using an Anton Paar HTK1200 oven-camera. Using the HTK1200 furnace, studies of powders either under vacuum, air or inert gas can be performed. The X-ray generator typically operates at 40 kV and 40 mA and the D8 uses Ge (111)-monochromated Cu $K\alpha_1$ radiation (λ = 1.540598 Å). In normal flat-plate reflection mode (also when the furnace or cryostats are attached), the monochromatic X-rays pass through a 6 mm aperture slit and an anti-scatter tube to a fixed Soller slit and a 1 ° divergence slit. The role of the Soller slit is to decrease axial divergence and therefore minimise peak shifts and asymmetric broadening. With the furnace present, the powdered sample is mounted on a 17 mm revolving alumina crucible. In regular flat-plate mode, powdered specimens are packed into 25 mm plastic holders and spun at 30 revolutions per minute, however in the cryostats samples are normally sprinkled on Al plates. A radial Soller precedes a Braun PSD-50M linear Position Sensitive Detector (PSD) which collects the diffracted X-rays. A Dell Pentium III PC using Bruker *Diffrac+ v4.0*[4] software controls the diffractometer.

The diffractometer can also be used in transmission mode, both using a flat plate stage and capillary geometries. In capillary mode the set up consists of only the copper source, germanium (111) monochromator, an extended "nose cone" to reduce air scatter before the sample and a set radial Soller slits preceding the PSD counter. 0.5 or 1 mm glass capillaries are loaded with sample before being flame sealed and fixed to a goniometer head with beeswax to allow for alignment. Capillaries are spun during data collection.

2.2.5 PheniX CCR cryostat

The Oxford Cryosystem PheniX closed circuit refrigerator (ccr) cryostat allows the D8 diffractometer to measure diffraction patterns from 300 K down to 15 K. Samples are sprinkled on to a Vaseline coated flat Al plate, which screws into the base of the PheniX. The sample is cooled by conduction from the base of the sample holder, which is surrounded by an inner heat shield assembly that is cooled to 50 K, while the sample holder is cooled to

base temperature. This dual cooling means that the thermocouple and the sample experience very similar temperatures.

The PheniX is controlled independently from the diffractometer by the PheniX CryoPad software. DiffracPlus software is used to control the diffractometer as normal data are collected in user-defined time intervals as the sample is warmed or cooled. In most cases many "excess" measurements were programmed, to allow several powder patterns at the end temperature to be recorded. Summation resulted in good quality data sets being recorded at the two temperature extremes. The CryoPad software allows the temperature to be logged as a function of time at 60 s intervals and the average temperature for each diffraction pattern was calculated using the FORTRAN routine *phenixlogfile*.[5]

2.2.6 MultiTOPAS methodology

Variable temperature X-ray diffraction experiments generate a large amount of data in the form of many powder patterns. To refine all of these by "hand" to abstract useful information would take a long time. Instead, *multitopas*, a FORTRAN routine for generating a DOS based batch program, is used to control Rietveld refinements in Topas. This starts with a "seed" refinement, done "by hand" and copies the output to a new file, which is refined against the next data set. This process continues until the last file has been refined. Using the structural model from a refinement at a temperature differing by only 10 – 15 K significantly reduces convergence time and reduces the possibility of the refinement falling into a false minimum. It allows many refinements (typically 40 – 50 in these PheniX experiments) to be performed in a few minutes. The refined parameters of interest are automatically written to a summary file after each refinement, allowing trends to be studied easily and quickly.

In order to investigate the possibility of the refinements becoming stuck in a false minimum, a few *multitopas* processes were performed using a "simulated annealing" approach as well as in the manner described above. After a cycle of refinement had converged the parameter values were randomised and then re-refined. This process was typically repeated tens of thousands of times and the best model kept. The parameters of interest were automatically written to a summary file and the next data set refined in the same way. Analysis of the summary files for both refinements performed with and without simulated annealing revealed no difference between them, indicating false minima were not being encountered. Further data sets were analysed without simulated annealing. A sample *multitopas* seed input file is shown in Appendix 2.

Table 2.6 summarises the PheniX experiments discussed in this thesis, including the samples used, the experiment RAW files, the heating/cooling rates and the length and number of scans performed.

Table 2.6 Summary of PheniX experiments.

Compound	Sample id	Raw file	Ramp rate / K hr^{-1}	Time per scan / min	Cooling/ Heating	No of scans at final T
$Ba_2CoCu_2O_2Se_2$	NDW252	d8_02272	17	30	Cooling	7
		d8_02273	17	30	Heating	5
$Sr_2CoCu_2O_2Se_2$	NDW256	d8_02293	17	30	Cooling	8
		d8_02294	17	30	Heating	14
$La_2O_3Mn_2Se_2$	NDW84	d8_02296	17	30	Cooling	11
		d8_02297	17	30	Heating	8
$La_2O_3Co_2Se_2$	NDW81	d8_02299	17	30	Cooling	8
		d8_02300	17	30	Heating	10
$Sr_2CoCu_2O_2S_2$	NDW255	d8_02302	17	30	Cooling	1
		d8_02303	17	30	Heating	5
$Sr_2NiCu_2O_2Se_2$	NDW240	d8_02305	17	30	Cooling	6
		d8_02306	17	30	Heating	10
$Ba_2MnCu_2O_2Se_2$	NDW287	d8_02308	17	30	Cooling	15
		d8_02309	5	60	Heating	10
$Sr_2NiCu_2O_2Se_2$	NDW240	d8_02440	8	60	Cooling	11
		d8_02441	10	60	Heating	2
$Sr_2MnCu_2O_2Se_2$	NDW297	d8_02443	14	30	Cooling	7
		d8_02444	17	30	Heating	6
$Ba_2NiCu_2O_2Se_2$	NDW334	d8_02451	8	45	Cooling	9
		d8_02452	16	30	Heating	3
$Sr_2ZnCu_2O_2S_2$	NDW301	d8_02454	8	45	Cooling	21
		d8_02455	16	30	Heating	17
$Sr_2ZnCu_2O_2Se_2$	NDW302	d8_02457	10	45	Cooling	3
		d8_02458	8	60	Heating	5
$Ba_2CoCu_2O_2S_2$	NDW251	d8_02460	12	45	Cooling	7
		d8_02461	8	60	Heating	5

2.2.7 Neutron diffraction

In X-ray scattering the incident beam is scattered by the electrons of the atoms, making the scattering power proportional to the atomic number. The relative sizes of the electron cloud and wavelength of the X-rays gives rise to a reduction in scattering factor as a function of diffraction angle, 2θ. Neutrons are scattered by the nuclei of atoms and there is no simple dependence of the scattering power on atomic number. This means that the information gained from neutron diffraction is able both to differentiate better between atoms that are close in atomic number and to investigate lighter atoms in the presence of heavier ones. This

is obviously of great benefit when studying the structures of various metal oxides (or oxychalcogenides).

Pulsed neutron sources are created by high energy protons from a particle accelerator bombarding a heavy metal target. This spallation process yields around 30 neutrons per proton, giving the very high neutron flux required (as neutrons only weakly interact with matter) for diffraction experiments. In time of flight (TOF) neutron diffraction experiments the entire neutron spectrum (variable wavelength) is used with a fixed diffraction angle θ. The wavelength depends on the speed of the neutrons as described by the de Broglie relationship (Equation 2.6) where h is Planck's constant and m is the mass of the neutron, 1.675 x 10^{-27} kg.

$$\lambda = h/mv \qquad \text{Equation 2.6}$$

Hence, the diffracted radiation arriving at the detector is separated according to its time of flight (the time taken for the neutron to travel from the source to the detector) and therefore wavelength. Bragg's law, $n\lambda = 2d \sin\theta$, holds, with λ and d varying and θ fixed. This is compared to X-ray diffraction in which d and θ vary and the wavelength is fixed. TOF gives a high neutron flux allowing for rapid data collection. The fixed sample geometry also facilitates the use of complex sample environments, as shown in Figure 2.9.

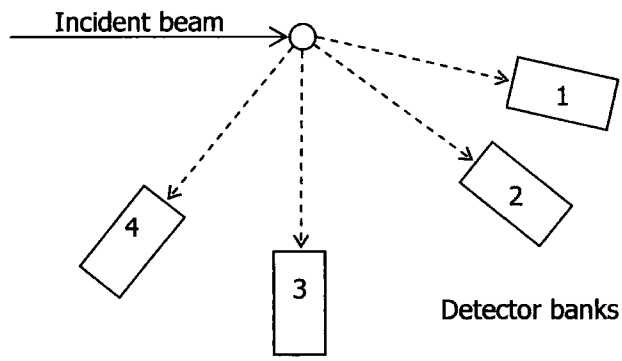

Figure 2.9 TOF neutron experiment set up showing fixed sample and detectors.

Neutrons have a magnetic dipole moment and thus also interact with unpaired electrons as well as with nuclei. As a consequence they are scattered by any unpaired electrons in a sample as well as the atomic nuclei present. As magnetic properties are dependent on unpaired electrons neutron diffraction can reveal ordering of magnetic moments in crystal structures. If long range order exists in the magnetic moments of a sample, Bragg peaks will occur in exactly the same way as for long range order of atomic nuclei. If the magnetic unit cell coincides with the atomic unit cell, these peaks will be at d-spacings already predicted.

Alternatively, the magnetic unit cell could be a supercell of the atomic cell. The Bragg peaks arising from this will appear in much the same way as they would from atomic supercells.

2.3 SQUID magnetometry[6]

The Quantum Design Magnetic Property Measurement System (MPMS) used to collect the data discussed in succeeding chapters contains four superconducting components that allow it to make exceptionally sensitive measurements. These are: the detecting coil, the superconducting quantum interference device (SQUID), the magnetic shield and the magnetic coil.

The sample to be measured is on the end of a rod in a 9 mm diameter sample chamber which is maintained at a low pressure with helium gas from the liquid helium bath in the dewar. The detecting coil is a second order gradiometer and is positioned outside this sample space such that the magnetic field from the sample couples inductively to the coils as the sample is moved through them.

The coil is connected to the SQUID *via* superconducting wires. These allow the current from the coils to inductively couple to the SQUID sensor. The output voltage is strictly proportional to the current flowing in the SQUID input coil, making it a highly sensitive current-to-voltage converter. As the sample moves in the coils the magnetic moment of the sample induces an electric current in the detection coils. The detection coils, wires and SQUID form a closed superconducting loop; any change of magnetic flux in the detection coils produces a change in the persistent current in the detecting circuit, which is proportional to the change in flux. Thus the output voltage of the SQUID is proportional to the current of the detecting coils which is itself proportional to the magnetic moment of the sample, making the output voltage of the SQUID proportional to the magnetic moment of the sample. The set up of the SQUID is shown in Figure 2.10.

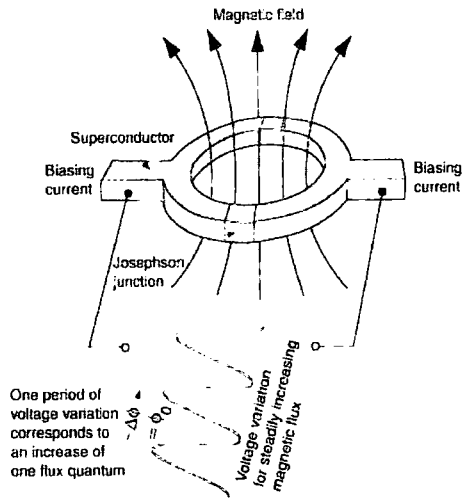

Figure 2.10 Schematic diagram of a SQUID.

A superconducting shield, or superinsulator, is required to shield the SQUID sensor from both the magnetic flux present in the lab and the large magnetic fields produced by the superconducting magnet. This superconducting shielding provides a volume of relatively low magnetic field in which the SQUID (and its coupling transformers) are located. It is not necessarily an extremely low magnetic field that is required, but that the field should be extremely stable. The SQUID sensitivity is such that it can detect the magnetic flux produced by a small sample, around 1/1000 of a flux quanta (2.07×10^{-7} Gm^{-2}) and thus needs to be protected from the magnetic field of the Earth; the magnetic flux through a 1 cm^2 area of which is around 2 million flux quanta.

The superconducting magnetic coil is a completely closed superconducting loop which can be charged up to a specific current then operated in "persistent" mode without external current source or power supply. To charge it up the loop must be opened by heating a small section of the loop to above the T_c. A power supply can then be attached to either side of the gap and the magnet charged. Current fluctuations from the power supply can make the field noisy, meaning measurements are taken in persistent mode, and also after the magnetic field has become stable.

There are two modes in which the magnetic coil was operated: oscillate and hysteresis modes. In the former, the magnetic field alternately over- and under-shoots the desired field with decreasing amplitude each cycle. This minimises the amount of magnetic flux "settling", characteristic of a field change in any superconducting magnet, and allows highly sensitive measurements to be run more quickly. In hysteresis mode the persistent current switch is left on at all times, meaning the magnet is not run in persistent mode and the power supply is a continual part of the magnetic circuit. This is useful for rapid magnetisation (*M*) *vs.* applied field (*H*), but requires a sample with large ($>10^{-5}$ emu) magnetisation.

Samples were mounted in one of two different ways. One method was to glue a small fragment of a 5 mm pellet to the inside of a gelatine capsule. Once the glue had dried the capsule was closed with a hole in it to allow air/moisture to escape on evaporation. The other way was to load loose powder into half a capsule and use the other half to fix the powder in place. The two capsule halves were then glued together. In both these techniques the capsule was then glued to the inside of a plastic straw in a position to keep the sample as close to the middle of the straw as possible, to minimise environment anisotropy. The glue used was a mixture of "G" varnish and solvent (10:1 ethanol: toluene)

Typical experiments performed consisted of magnetisation *vs.* applied field at room temperature and magnetisation *vs.* temperature. In the *M vs. T* experiments the sample was typically cooled to 10 K and the magnetisation measured at 10 K intervals to 290 K. In zero-field cooled (ZFC) experiments, there was no applied field during the initial cooling; in field-cooled (FC) experiments, there was (typically 100 Oe). This was to investigate whether the presence of a magnetic field had any effect on the magnetisation of a sample during cooling.

Table 2.7 summarises the samples used for SQUID magnetometry experiments, including the masses of sample used and the method used for preparing them.

Table 2.7 Summary of SQUID magnetometry experiments.

Compound	Sample ID	MASS	Method	Interval/K	Expts
$Sr_2MnCu_2O_2Se_2$	326	0.0124	Pellet	5	ZFC, FC, M vs H
$Ba_2MnCu_2O_2Se_2$	325	0.0091	Pellet	5	ZFC, FC
$Sr_2CoCu_2O_2S_2$	255b	0.0100	Pellet	10	ZFC, FC, M vs H
$Sr_2CoCu_2O_2Se_2$	256b	0.0022	Pellet	10	ZFC, FC, M vs H
$Sr_2CoCu_2O_2Se_2$	323	0.0076	Powder	n/a	M vs H (10, 100, 200, 290 K)
$Ba_2CoCu_2O_2S_2$	251b	0.0025	Pellet	10	ZFC, FC, M vs H
$Ba_2CoCu_2O_2Se_2$	252a	0.0183	Pellet	5	ZFC, FC, M vs H
$Sr_2NiCu_2O_2Se_2$	250b	0.0036	Pellet	10	ZFC, FC, M vs H
$Ba_2NiCu_2O_2Se_2$	334	0.0161	Powder	5	ZFC, FC, M vs H
$La_2O_3Co_2Se_2$	247a	0.0118	Pellet	10	ZFC, FC, M vs H
$La_2O_3Co_2Se_2$	321b	0.0079	Pellet	5	ZFC, FC
$La_2O_3Mn_2Se_2$	246a	0.0232	Pellet	5	ZFC, FC, M vs H
$La_2O_3Mn_2Se_2$	320	0.0212	Powder	5	ZFC, FC

2.4 Conductivity measurements

2.4.1 Contacts

In order to investigate the temperature dependence of the conductivity of the compounds synthesised it was necessary to press them into 5 mm pellets and anneal them at 800 – 1000 °C in a vacuum sealed quartz ampoule. These pellets then had to have contacts deposited on them in order that they be connected to the electrometer. Either aluminium or gold was used. Aluminium was evaporated onto both sides of the pellets using a standard Edwards coating unit. Quick drying silver paint was then used to protect the aluminium from oxidation in the air. Copper wires were then soldered to the silver paint and the current/voltage (*I-V*) characteristics examined to ensure the contacts were ohmic. Alternatively, gold was evaporated onto both sides of the pellets and copper wires attached with quick drying silver paint. The *I-V* characteristics were again tested to ensure ohmic behaviour.

2.4.2 *R vs. T* measurements

The copper wires attached to the samples were soldered to two of the pins of the sample holder connected to a Keithley Instruments electrometer *via* coaxial cables. The resistance between the sample holder's pins was measured to be ~1 x 10^{11} Ω, therefore reliable measurements could be taken up to 1 x 10^{10} Ω with a current leakage of <10%.

This sample holder was placed in an Oxford Instruments cryostat controlled by an Oxford Instruments temperature controller. This controlled the temperature by resistive heaters embedded in a heat exchanger block attached to the sample chamber. Liquid nitrogen from an isolated reservoir was passed around the sample chamber to cool the sample. The temperature resulting from this interplay was measured by a platinum resistance thermometer. A second platinum resistance thermometer linked to the temperature controller was placed beneath the sample to more accurately measure the sample temperature.

The sample chamber was evacuated with a rotary pump to remove air, moisture and dust and then refilled with helium gas. This was repeated three or more times and the sample chamber left filled with helium to enable good heat exchange.

Both the electrometer and temperature controller were connected to a PC and the measurements automated *via* a Visual Basic 6.0 program.[7] This made sure a steady temperature had been reached in two ways: firstly, by ensuring that both thermometer readings were stable and in close agreement and secondly by waiting for the resistance reading to stabilise before writing to the data file. Two readings were taken nine seconds apart and if they were within 1 %, the measurement was recorded. This consisted of the average of 20 readings taken in ~2 s. As the resistance typically changes with temperature this helps ensure that the sample was in thermal equilibrium with its environment.

Table 2.8 summarises the samples used for conductivity experiments, including the type of contacts used and the temperature interval readings were recorded at. The area of evaporated metal contact was determined by the mask used, which had holes of 4 mm radius.

Table 2.8 Summary of conductivity experiments.

Expt No.	Sample	Sample no.	Interval/K	Contact	Thickness /mm
jsoe015	$Sr_2NiCu_2O_2Se_2$	NDW250a	5	Al, Ag paint, solder	0.88
jsoe024	$Ba_2CoCu_2O_2S_2$	NDW251c	10	Al, Ag paint, solder	1.48
jsoe034	$Sr_2CoCu_2O_2Se_2$	NDW256a	10	Al, Ag paint, solder	0.72
jsoe040	$Ba_2CoCu_2O_2Se_2$	NDW268b	10	Al, Ag paint, solder	1.08
jsoe054	$La_2O_3Co_2Se_2$	NDW321d	5	Au, Ag paint	0.80
jsoe073	$La_2O_3Mn_2Se_2$	NDW331b	5	Au, Ag paint	0.60

2.5 References

(1) Mayer, J. M.; Schneemeyer, L. F.; Siegrist, T.; Waszczak, J. V. and Vandover, B. *Angew. Chem.-Int. Edit. Engl.*, **1992**, *31*, 1645-1647.

(2) Coelho, A. A., *TOPAS v2.13 General Profile and Structure Analysis Software for Powder Diffraction Data*, Bruker AXS, Karlsruhe, 2000.

(3) *Powder Diffraction File*, International Center for Diffraction Data, Pennsylvannia, 1998.

(4) *DiffracPlus*, Bruker AXS, Karlsruhe, 1998.

(5) Evans, J. S. O., *phenixlogfile - a Fortran routine for extracting average temperatures from PheniX logfiles.*, 2000.

(6) McElfresh, M. *Fundamentals of Magnetism and Magnetic Measurements*; Quantum Design: San Diego, 1994.

(7) Schmidt, R., *Production and performance of thin and thick film NTCR thermistors based on* $NiMn_2O_{4+\delta}$, Ph.D. Thesis, University of Durham, Durham, 2003.

Chapter 3 $La_2O_3M_2X_2$ compounds (M = Mn, Fe, Co, Ni; X = S, Se)

3.1 Introduction

This chapter discusses the properties of the $La_2O_3M_2X_2$ (M = Mn, Fe, Co, Ni; X = S, Se) series of compounds; their structures, magnetic properties and conductivity. Structures were investigated using powder X-ray and neutron diffraction, magnetic properties by SQUID magnetometry and conductivity by 2-probe measurements. Summary sheets with key results to aid the reader, containing the results of each experimental technique for both compounds, can be found in Appendices 1.1 and 1.2.

The $La_2O_3M_2X_2$ family of materials crystallise in the *I4/mmm* spacegroup (*no.* 139) with an *a* cell parameter between 4.0408 and 4.1389 Å and *c* between 17.8985 and 18.8498 Å. The basic structure is shown in Figure 3.1 and consists of layers stacked along the *c* axis in the order $M_2O/X/La/O/La/X/M_2O$. The M_2O layers feature oxygen in a square-planar environment coordinated by metal atoms, while the metal is octahedrally coordinated by 4 chalcogen atoms and the 2 oxygen atoms. The key La_2O_2 layer, featured in many other oxychalcogenides (Section 1.2.1), is made up of oxygen centred edge-sharing La_4O tetrahedra. The La is in a square anti-prismatic coordination with O(1) and X atoms and there are two of these layers in between each $M_2O(2)$ layer. Typical atomic coordinates are given in Table 3.1.

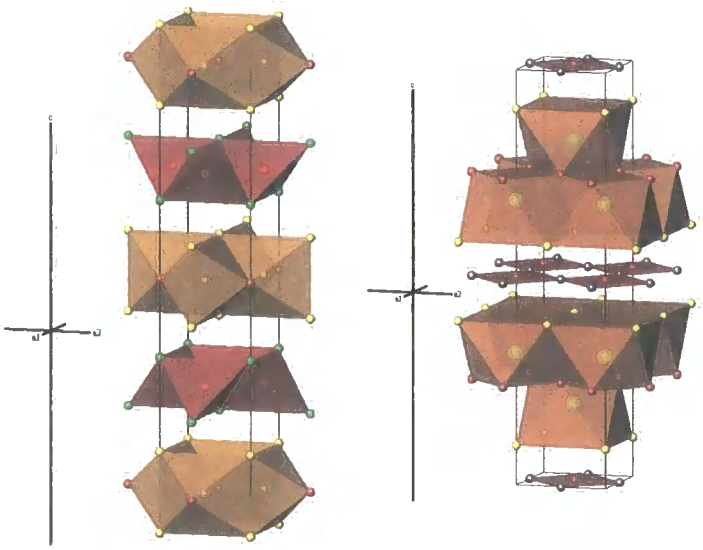

Figure 3.1 Structure of $La_2O_3M_2X_2$. La atoms in green, O atoms in red, M atoms in grey and X atoms in yellow. Left shows La_4O tetrahedra in red and MO_2X_4 octahedra in orange, right LaO_4X_4 square anti-prisms in orange, and square planar M_2O in red.

Table 3.1 Atomic fractional coordinates and multiplicity (N_p) for $La_2O_3M_2X_2$ compounds.

Site	N_p	x/a	y/b	z/c
La	4	½	½	~0.18
M	4	½	0	0
X	4	0	0	~0.09
O(1)	4	½	0	¼
O(2)	2	½	½	0

The aim of this work was to synthesise the oxysulfide and oxyselenides of the different transition metals using the synthesis of $La_2O_3Fe_2X_2$ (X = S, Se) as a starting point. These have been reported[1] as showing semi-conducting properties with possible anti-ferromagnetic behaviour at low temperatures. Table 3.2 summarises the results of the various syntheses outlined in Chapter 2.1.1. It is notable that none of the M = Ni phases could be prepared and that a X = S compound could only be prepared for M = Fe.

Table 3.2 Summary of synthetic results. A ✓ means that the sample was prepared with good phase purity.

M \ *X*	S	Se
Mn		✓
Fe	✓	✓
Co		✓
Ni		

3.2 $La_2O_3Mn_2Se_2$

3.2.1 Room temperature X-ray diffraction

$La_2O_3Mn_2Se_2$ was synthesised from stoichiometric amounts of La_2O_3, Mn and Se at 1000 °C as discussed in Chapter 2.1.1. The resulting olive green powder was characterised by powder X-ray diffraction using a Siemens D5000 diffractometer (Chapter 2.2.3) and its structure confirmed by Rietveld refinement, as shown in Figure 3.2. The relatively large amorphous background visible between 10 and 20 ° 2θ in Figure 3.2 is due to the sample being sprinkled on a Vaseline covered glass disc held within the plastic sample holder. Thirty six parameters were refined: an 18th order Chebychev polynomial function was used to fit the background radiation, 2 instrument corrections (the sample height displacement and a simple axial model to describe low angle peak asymmetry), 1 scale factor for the phase, 6 pseudo Voigt peak shape parameters, 2 lattice parameters (a and c), 2 atomic positions (La and Se z coordinates) and 5 atomic displacement parameters. The $_wR_p$ for the refinement was 11.32 %, χ^2 1.76 and R_{Bragg} for the phase was 2.95 %. Details of the important parameters from this refinement are given in Table 3.3.

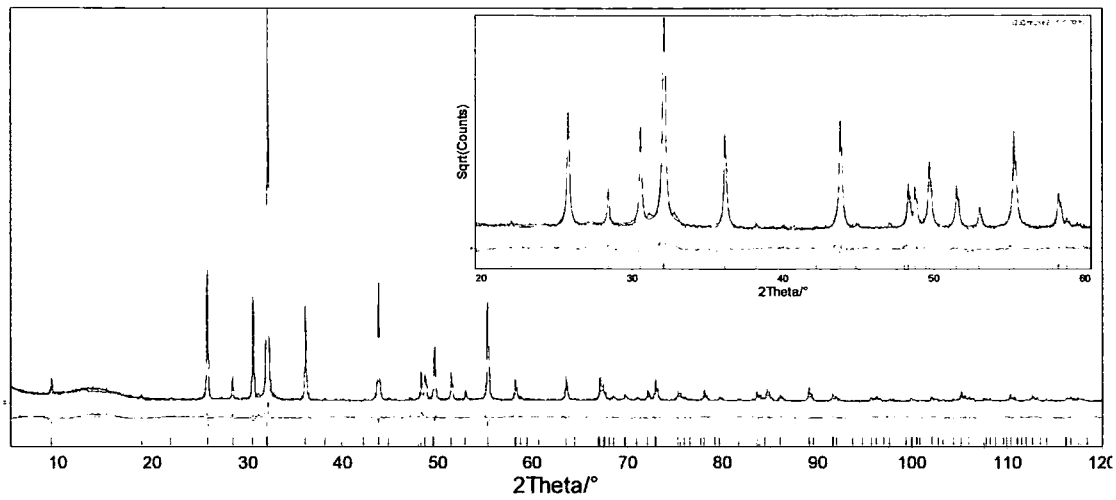

Figure 3.2 Rietveld refinement of $La_2O_3Mn_2Se_2$. Observed pattern in blue, calculated in red and difference in grey. The vertical tick marks show predicted peak positions and the inset shows 20 – 60 ° 2θ region on a square root (counts) scale to emphasise weaker features in the pattern.

Table 3.3 Results of room temperature Rietveld refinement for $La_2O_3Mn_2Se_2$.

$La_2O_3Mn_2Se_2$	NDW324
Spacegroup	*I4/mmm*
a cell parameter*/Å	4.13891(3)
c cell parameter*/Å	18.84976(28)
La *z* coordinate/*c*	0.18620(8)
Se *z* coordinate/*c*	0.0995(1)
La B_{iso}/Å^2	1.77(4)
Mn B_{iso}/Å^2	2.03(9)
Se B_{iso}/Å^2	1.53(6)
O(1) B_{iso}/Å^2	1.96(32)
O(2) B_{iso}/Å^2	2.32(53)
$_wR_p$/%	11.32
R_{Bragg}/%	2.95
χ^2	1.76
No. parameters	36

* Cell parameters are from Si standardised experiment, details below.

In order to accurately determine the unit cell parameters a sample was prepared for Rietveld analysis containing a Si standard. Using the intensities of the strongest peaks in similar diffraction patterns to decide on a suitable ratio, 0.1955 g Si was combined with 0.4400 g $La_2O_3Mn_2Se_2$. A portion of this was packed into a 12 mm sample holder and its powder pattern recorded on a Siemens D5000 diffractometer from 5 – 120 ° 2θ with a step size of 0.02 ° and a count time of ~6.5 s per step. The total scan time was 17.5 hours and variable slits giving a constant 6 mm illumination on the sample were used. The resulting pattern is shown in Figure 3.3. The Si cell parameter was fixed at 5.4311946 Å (the value for NIST sample 640c)[2] during refinement and a 3-term polynomial calibration curve applied to the data to correct observed peak positions in the pattern. This resulted in an *a* cell parameter of 4.13891(3) Å and *c* = 18.84976(28) Å for $La_2O_3Mn_2Se_2$.

A total of forty five parameters were included in the refinement: a 16 order Chebychev polynomial function to fit the background (fewer terms were required because of the reduced background given by a bulk, rather than glass mounted, sample), sample height correction, simple axial model and 3 terms in the calibration curve; 6 peak shape coefficients, 1 scale factor, 2 cell parameters, 2 atomic positions and 5 B_{iso} thermal parameters for the $La_2O_3Mn_2Se_2$ phase; 6 peak shape parameters, 1 scale factor and 1 B_{iso} thermal factor for the Si phase.

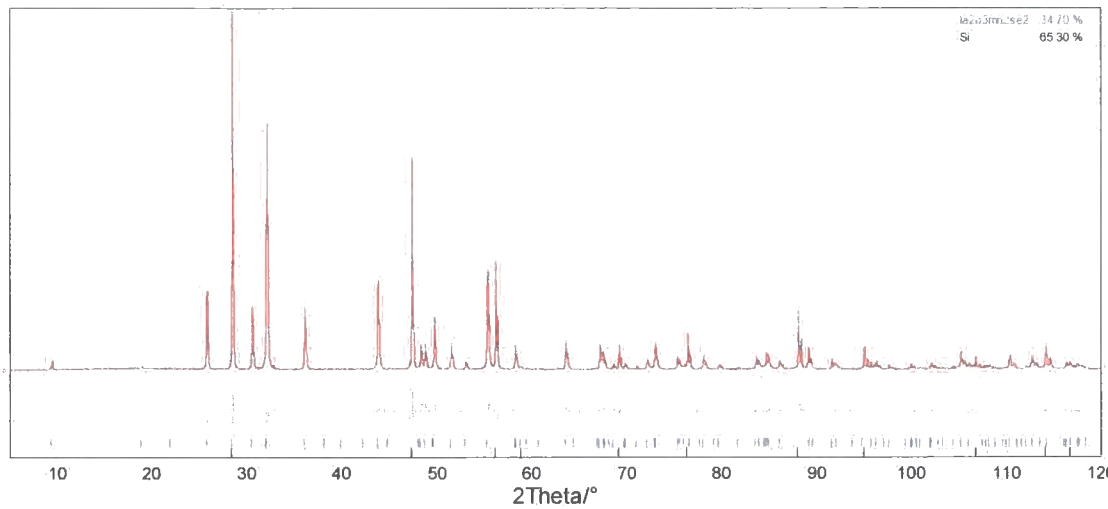

Figure 3.3 Two phase Rietveld refinement of $La_2O_3Mn_2Se_2$ and Si to accurately determine cell parameters. Observed pattern in blue, calculated in red and difference in grey. The vertical tick marks show predicted peak positions for $La_2O_3Mn_2Se_2$ and Si from top to bottom respectively.

3.2.2 Variable temperature powder X-ray diffraction

Variable temperature powder X-ray diffraction experiments were performed on this compound using a Bruker D8 diffractometer with PheniX He ccr attachment (Chapter 2.2.5). The sample NDW84 was studied in experiments d8_02296 and d8_02297. In experiment number d8_02296 it was cooled at 17 K hr^{-1} and data collected over a 5 – 120 ° 2θ range in 30 minute time slices. Eleven 30 minute scans were performed at the base temperature, and summed together giving the equivalent of one 5.5 hr data collection. In experiment d8_02297 the sample was then heated at 17 K hr^{-1} to 300 K and data collected using the same range and time as experiment d8_02296. Eight 30 minute scans were performed at 300 K and summed together. Average temperatures for each pattern were extracted from the experimental logfile using the FORTRAN routine *phenixlogfile*.[3]

The data were analysed using the *multitopas* methodology described in Chapter 2.2.6. The summed scans from 300 K were used to fit a suitable calibration curve to the data using the fixed cell parameters determined with a Si standard. At lower temperatures the parameters for the calibration curve were fixed and the cell parameter allowed to refine as normal. The cell parameters determined with and without this calibration process were reassuringly

different by less than one standard deviation (4.13891(3) and 4.13897(4) Å with and without calibration respectively). For consistency between various X-ray and neutron studies all measurements were calibrated relative to the Si standardised values.

Figure 3.4 shows the variation of the *a* cell parameter with temperature and Figure 3.5 shows the *c* cell parameter. A simple model of the thermal expansion has been least-squares fitted to these data, and is shown in these figures as a solid grey line. The expression used is shown in Equation 3.1, where *a* is the cell parameter, a_0 the ideal cell parameter at 0 K, *T* the temperature, θ_i the *i*th Einstein temperature and C_i a "refinable" quantity. These curves, whilst derived from a physically meaningful model, are intended primarily as "guides to the eye" and to highlight any deviations from smooth behaviour.

$$\ln\left(\frac{a}{a_0}\right) = \frac{C_1}{\exp\left(\frac{\theta_1}{T}\right)-1} + \frac{C_2}{\exp\left(\frac{\theta_2}{T}\right)-1} \qquad \text{Equation 3.1}$$

As the sample holder in the PheniX ccr is an anodised aluminium plate it gives large peaks in the diffraction pattern and has been included in the refinements as a model independent Pawley fit. In this way it also acts as an internal standard to verify that observed trends are not artefacts of the refinement procedure. The variation of the Al cell parameter (space group *Fm*3*m* [number 225], a = 4.04992 Å at 300 K) is shown in Figure 3.8. A model of the thermal expansion was least-squares fitted to the data for a perfect Al crystal quoted by Wang and Reeber,[4] again using Equation 3.1. The values produced by this fit are shown in Table 3.4. This ideal thermal expansion curve is then superimposed on experimental data in Figure 3.8 and subsequent figures with fixed C_n and θ_n values. Due to slight differences between the anodised aluminium plate and a perfect aluminium crystal the term a_0 was refined for each experiment. The value of a_0 for this experiment is given in Table 3.4.

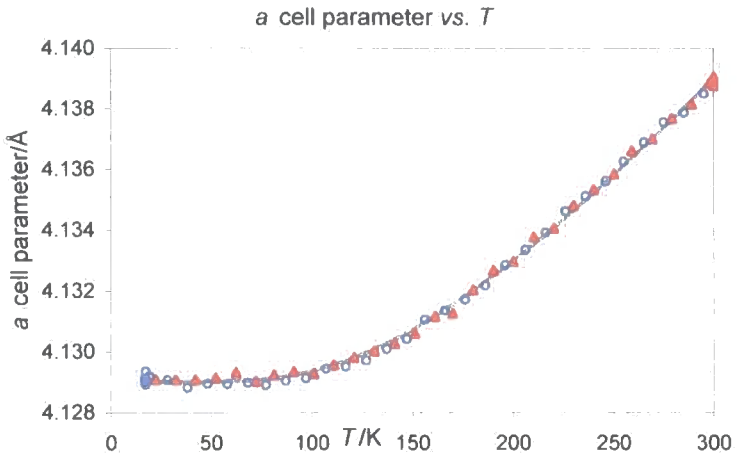

Figure 3.4 $La_2O_3Mn_2Se_2$ *a* cell parameter against temperature. Cooling data are open blue circles, heating filled red triangles, fit to the experimental data using Equation 3.1 and the values in Table 3.4 in grey. Size of error bars comparable to size of points, so omitted from this and following figures for clarity.

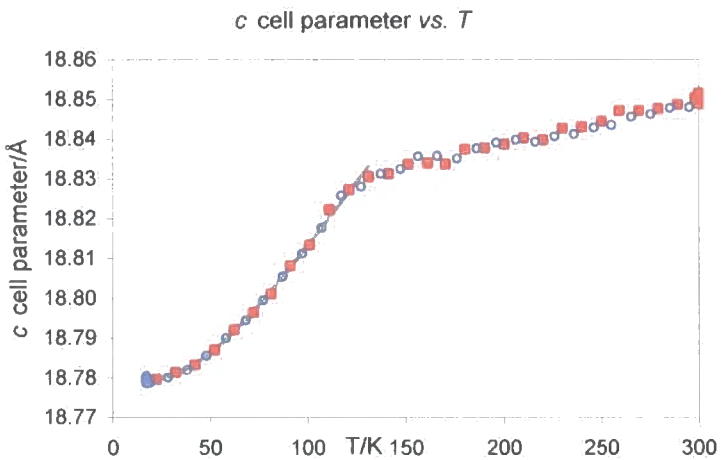

Figure 3.5 $La_2O_3Mn_2Se_2$ *c* cell parameter against temperature. Cooling data are open blue circles, heating filled red triangles, fit to the experimental data using Equation 3.1 and the values in Table 3.4 in grey.

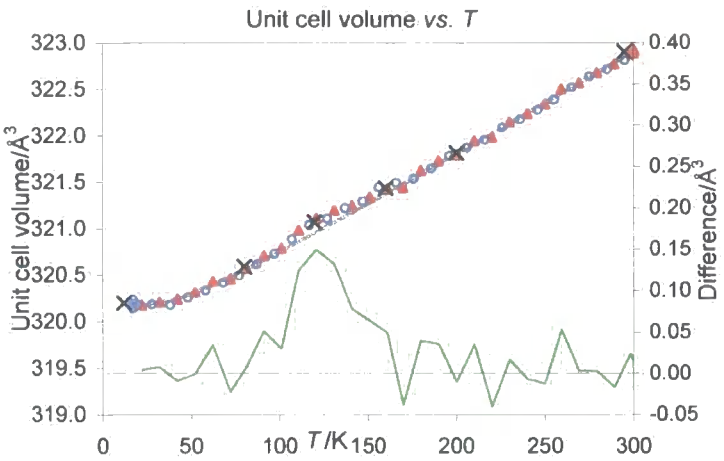

Figure 3.6 $La_2O_3Mn_2Se_2$ unit cell volume against temperature. Cooling data are open blue circles, heating filled red triangles, fit to the experimental data using Equation 3.1 and the values in Table 3.4 in grey, difference in green.

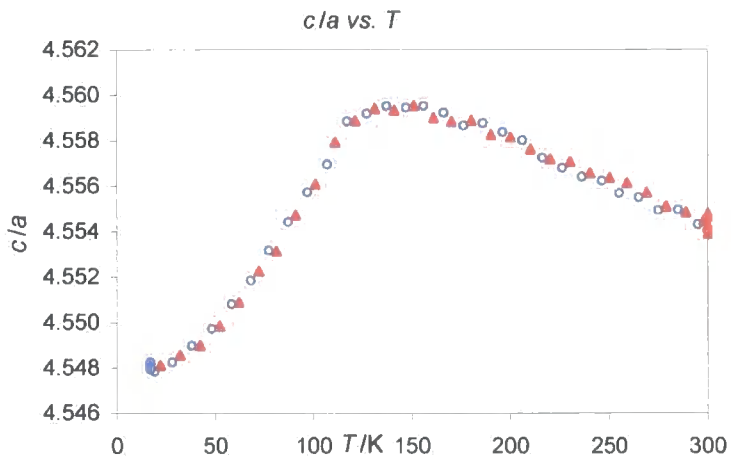

Figure 3.7 $La_2O_3Mn_2Se_2$ *c/a* ratio against temperature. Cooling data are open blue circles, heating filled red triangles.

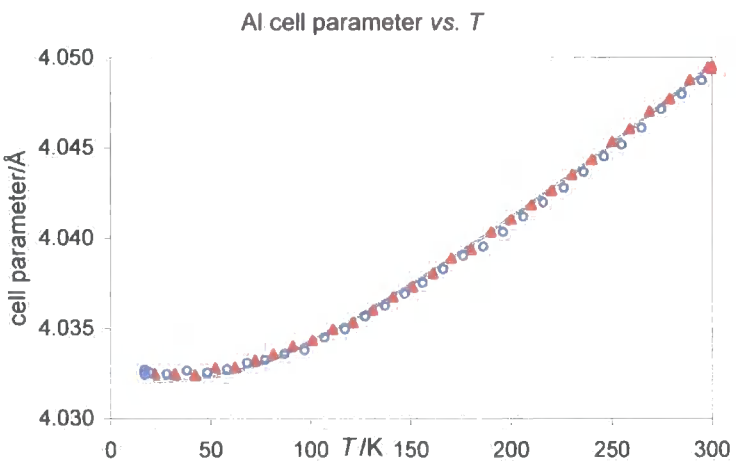

Figure 3.8 Aluminium cell parameter against temperature. Cooling data are open blue circles, heating filled red triangles, Wang and Reeber's theoretical data in grey.

Figure 3.4 shows that the *a* cell parameter expands smoothly on heating and that the data points very closely match the fitted expansion expression, with the parameters determined by a least-squares fit shown in Table 3.4. Thermal expansion coefficients $\alpha_{(300\text{-}15K)}$, as defined in Equation 3.2 (where *a* is the cell parameter at temperature *T*, a_0 the cell parameter at temperature T_0), are also quoted. Figure 3.5 shows that the *c* cell parameter shows a significant change in behaviour at around 120 K. Below this temperature it fits the expansion model well, and the parameters for this are given in Table 3.4. Above 120 K the *c* cell parameter expansion is considerably reduced.

$$\alpha_1 = \frac{\left[\frac{(a - a_0)}{a_0}\right]}{T - T_0} \qquad \text{Equation 3.2}$$

Table 3.4 Thermal expansion data from PheniX experiments on $La_2O_3Mn_2Se_2$.

	a_0/Å	θ_1/K	$C_1/10^{-6}$	θ_2/K	$C_2/10^{-6}$	$\alpha_{(300\text{-}15K)}$ / 10^{-6} K^{-1}
a	4.12903(3)	471(8)	19.5(3)			8.5(2)
c	18.7794(2)	137(5)	39(1)			32.2(9)
v	320.172(7)	121(4)	34.9(2)			30.0(3)
Al	4.03211(4)*	231(31)†	21(2)†	1459(200)†	13(1)†	15(2)†

* Refined against experimental data.
† Calculated from data for perfect Al crystal from Wang and Reeber.

Figure 3.7 shows the variation in *c/a* ratio with temperature which clearly shows the change in behaviour between 120 and 150 K.

A change in the thermal expansion properties such as those indicated by *e.g.* Figure 3.7 is often an indication of a structural phase transition. Figure 3.9 and Figure 3.10 show plots of all powder patterns for the 20 – 120 ° 2θ and 25 – 60 ° 2θ regions respectively and there are no visible changes in peak intensities or widths which would indicate a significant structural change.

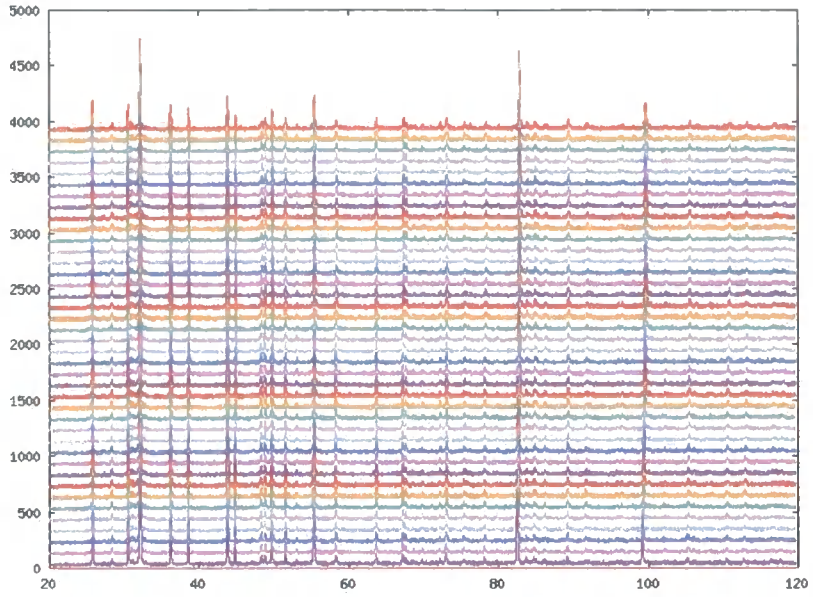

Figure 3.9 Powder patterns from d8_02296 (300 – 17 K) for $La_2O_3Mn_2Se_2$, showing the 20 – 120 ° 2θ region. Highest temperature at bottom, *y* offset of 100 counts per 8.5 K used for presentation.

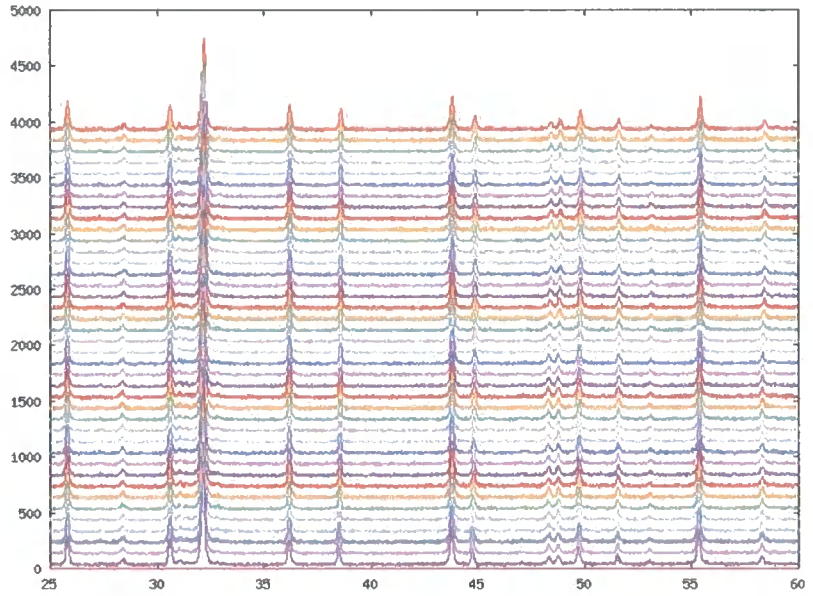

Figure 3.10 Powder patterns from d8_02296 (300 – 17 K) for $La_2O_3Mn_2Se_2$, showing the 25 – 60 ° 2θ region. Highest temperature at bottom, *y* offset of 100 counts per 8.5 K used for presentation.

The Rietveld refinement performed on the summed data set at 17 K is shown in Figure 3.11 (the *y* scale is a square root (counts) scale because the pattern is dominated by the scatter from the Al sample holder). The calculated patterns show a good fit to the observed with the following cell parameters: a = 4.12904(4) Å c = 18.77894(33) Å. The *R*-factors were ${}_wR_p$ = 6.55 and 7.00 %, χ^2 1.50 and 1.38 and R_{Bragg} 2.13 and 1.85 % for 17 and 300 K respectively. Other important structural least-squares parameters are summarised in Table 3.5 for the refinements performed on the long scans at 17 and 300 K.

Table 3.5 Atomic fractional coordinates values for $La_2O_3Mn_2Se_2$ at 17 and 300 K.

Site	*z/c* (17 K)	*z/c* (300 K)
La	0.18619(8)	0.18640(9)
Mn	0	0
Se	0.1003(1)	0.1008(2)
O(1)	0.25	0.25
O(2)	0	0

Within experimental error, there is almost no difference between the *z* coordinates at 17 and 300 K of either the La or Se atoms (the only two atomic coordinates in the structure which are not fixed by symmetry). They are also very similar to the values from the room temperature d5000 Rietveld refinements given in Table 3.3. B_{iso} values from these refinements are not quoted as the sample preparation method invariably leads to a significant sample surface roughness; values from neutron refinements (below) are more reliable.

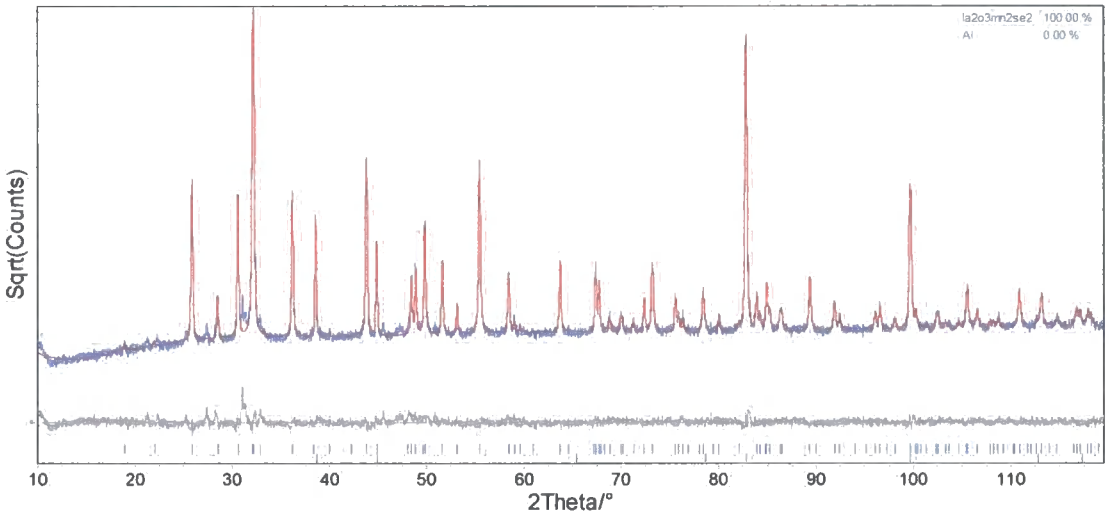

Figure 3.11 17 K refinement of $La_2O_3Mn_2Se_2$. Observed pattern in blue, calculated in red, difference in grey. Tick marks show predicted peak positions for $La_2O_3Mn_2Se_2$ and Al from top to bottom respectively.

3.2.3 SQUID magnetometry

A portion of sample NDW320 was loaded into a gelatine capsule and magnetically characterised by SQUID magnetometry using the sample preparation and experiment technique described in Chapter 2.3. Zero field cooled (ZFC) and field cooled (FC) experiments were conducted on this sample in a field of 100 Oe with measurements taken at 5 K steps from 10 – 290 K and the results shown in Figure 3.12. A magnetisation *vs.* applied field (*M vs. H*) experiment was also performed at 290 K on this sample, and the results are shown in Figure 3.13. This is straight line crossing the origin indicating paramagnetic behaviour at room temperature.

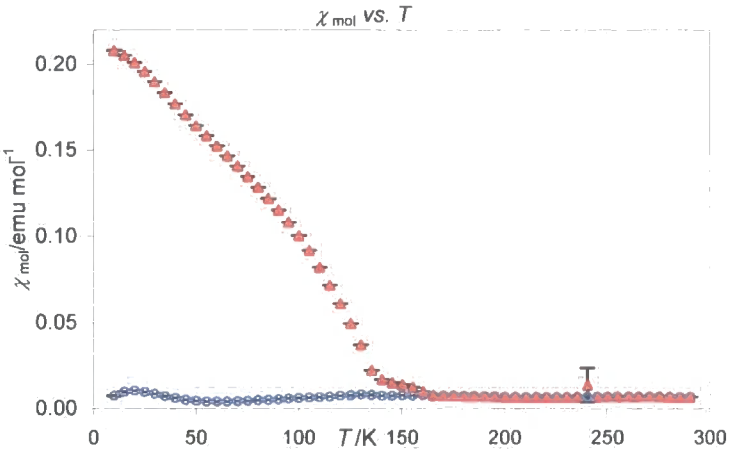

Figure 3.12 ZFC (open blue circles) and FC (filled red triangles) data for $La_2O_3Mn_2Se_2$.

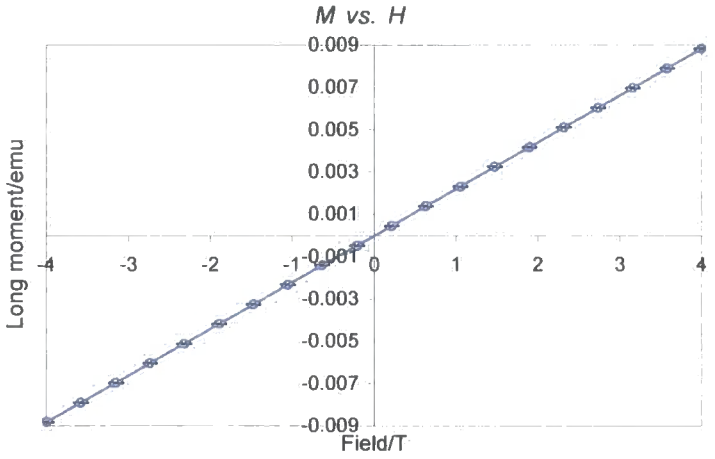

Figure 3.13 Magnetisation against applied field for $La_2O_3Mn_2Se_2$.

Figure 3.12 shows that the ZFC and FC data are the same above 160 – 170 K. Below this temperature the FC data are considerably greater than the ZFC; in the absence of an applied field no long range ferromagnetic ordering occurs.

3.2.4 Variable temperature neutron diffraction

Powder neutron diffraction patterns were collected at 12, 80, 120, 160, 200 and 295 K on the SEPD diffractometer at the Intense Pulsed Neutron Source (IPNS) at the Argonne National Laboratory, USA. These points were chosen to be representative of the areas above and below the possible phase transition at 120 – 130 K observed in the X-ray experiments described above. The following banks of data were collected and will hereafter be referred to by their histogram number; histogram 1 = 145 ° (backscatter), histogram 2 = 90 °, histogram 3 = 44 °, histogram 4 = 22 °. All refinements discussed in this section were performed in the General Structure Analysis Suite (GSAS)[5] and a crystallographic information file (*c.i.f.*) for

refinements at each temperature is included in the electronic appendix on the CD attached to this thesis.

An initial refinement was performed against the 295 K data set (histograms 1 – 3) and a d5000 scan (recorded at room temperature) for reference. The lattice parameters were fixed at the value determined using a Si standard in order to refine appropriate instrument parameters and absorption corrections. These were *dif*$_c$, *dif*$_a$, *zero* for the neutron histograms and a zero point error for the d5000 data. A total of 69 variables were refined. The following were refined for each histogram: the instrument parameters mentioned above, 3 peak shape parameters (*sig*1, *sig*2, *gam*1 for the neutron data histograms; *GW*, *LY*, *asym* for the X-ray data), a 9 term Chebychev polynomial to fit the background, an absorption correction factor and scale factor. Two atomic coordinates and 11 anisotropic thermal factors were refined for the $La_2O_3Mn_2Se_2$ phase. This resulted in a good fit, shown in Figure 3.14, and a $_wR_P$ of 4.93 %, $R(F^2)$ of 11.42 % and a χ^2 of 1.771. The instrument parameters are summarised in Table 3.6.

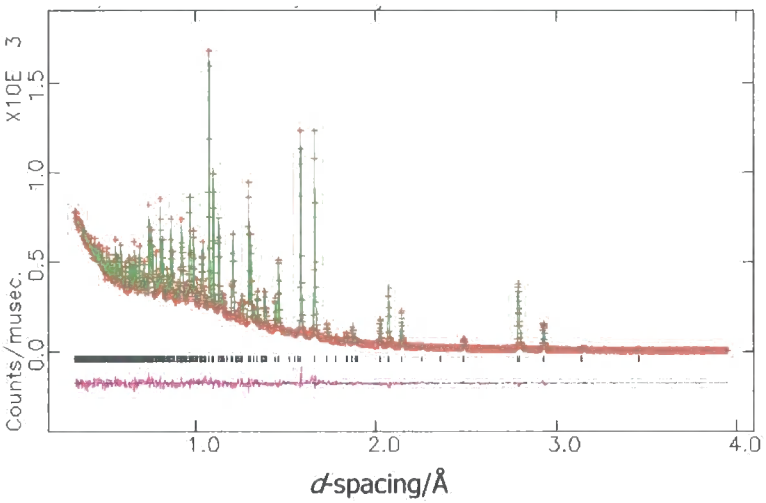

Figure 3.14 Rietveld refinement of histogram 1 (145 °) of $La_2O_3Mn_2Se_2$ neutron data at 295 K. Observed points in red, calculated in green, difference in pink.

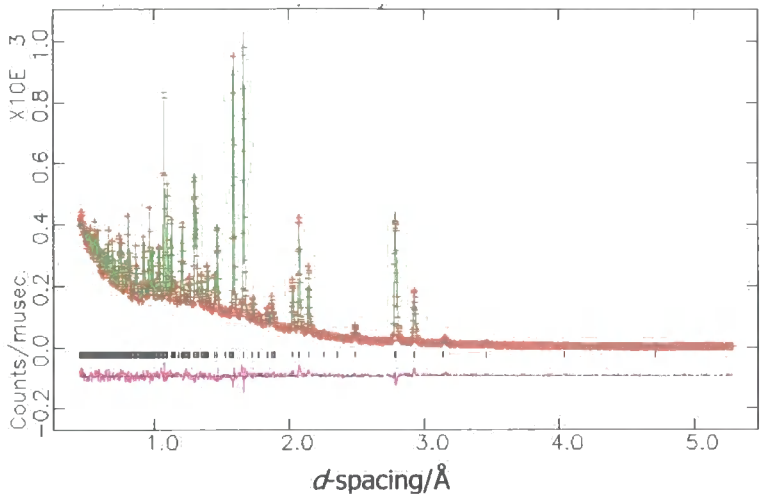

Figure 3.15 Rietveld refinement of histogram 2 (90 °) of $La_2O_3Mn_2Se_2$ neutron data at 295 K. Observed points in red, calculated in green, difference in pink.

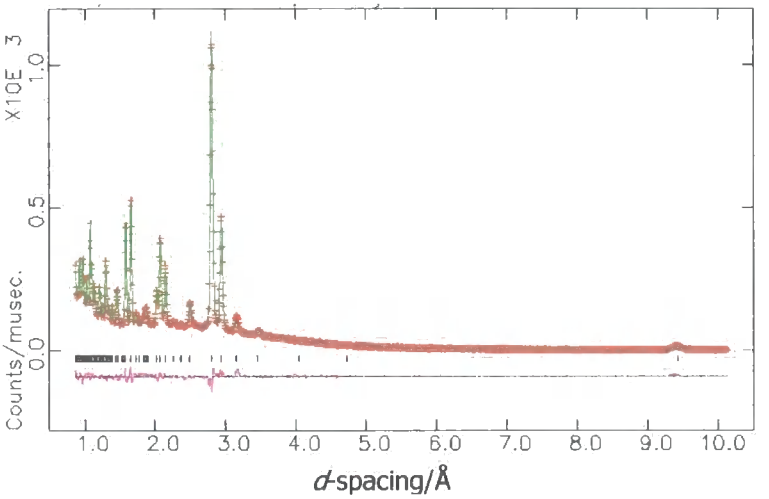

Figure 3.16 Rietveld refinement of histogram 3 (44 °) of $La_2O_3Mn_2Se_2$ neutron data at 295 K. Observed points in red, calculated in green, difference in pink.

Table 3.6 Instrument parameters for $La_2O_3Mn_2Se_2$ neutron refinements.

Histogram	dif_c	dif_a	*zero*	Absorption
1	7474.51	-1.54	-4.41	0.14153
2	5582.21	0.04	-1.11	0.15190
3	2898.77	1.17	-0.55	0.12285

This refinement was then used as a template for refinement of data collected at other temperatures. The dif_c, dif_a, *zero* and absorption parameters were fixed at the values given in Table 3.6 and the cell parameters allowed to refine. This resulted in a χ^2 of 2.079, 2.570, 5.268, 7.150 and 9.229 for 200, 160, 120, 80 and 12 K datasets respectively. An examination of the 12 K data (Figure 3.17) shows that the decrease in goodness of fit between 160 and 120 K is due to the presence of extra peaks at ~3.5 and 4 Å *d*-spacing at lower temperatures. The observation that these peaks occur at temperatures below the magnetic phase transition, and that they are observed only for relatively large *d*-spacings, suggest that they are magnetic in origin.

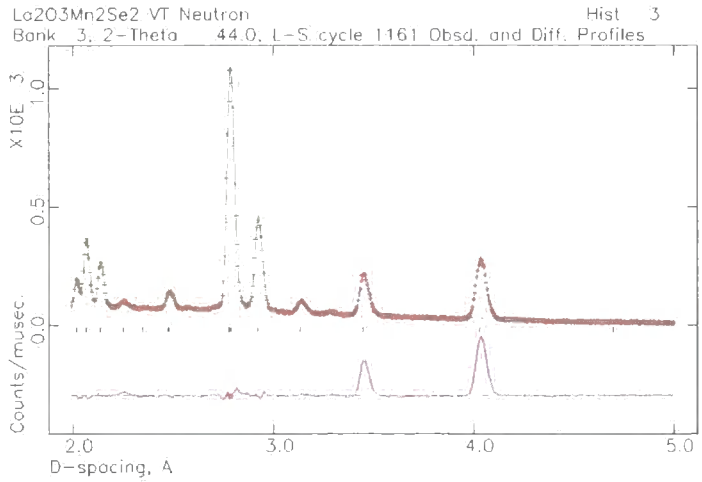

Figure 3.17 Rietveld refinement of histogram 3 of $La_2O_3Mn_2Se_2$ neutron data between 2 and 5 Å *d*-spacing at 12 K showing magnetic peaks not fitted. Observed points in red, calculated in green, difference in pink.

Successful refinement of the magnetic structure of $La_2O_3Mn_2Se_2$ was achieved in Shubnikov space group *I4'/mm'm*. The inclusion of magnetic scattering in the refinement improved the combined ${}_wR_p$ from 12.18 to 6.12 % for the 12 K dataset, as shown in Figure 3.18. Table 3.7 shows the Mn M_z and ${}_wR_p$ factors before and after including the magnetic scattering in the refinements.

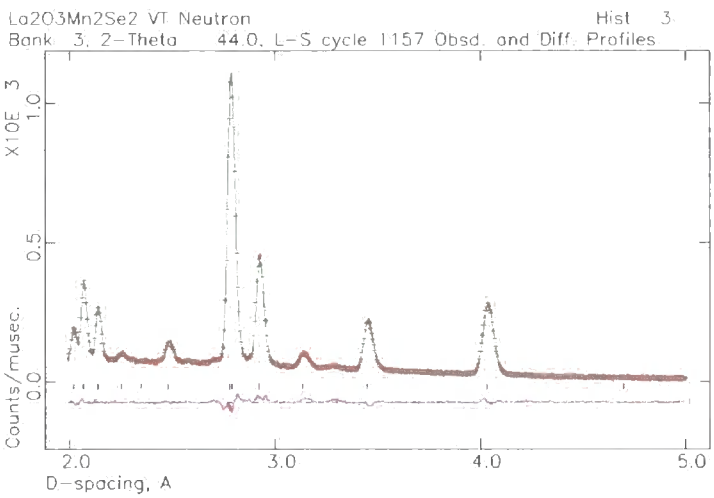

Figure 3.18 Rietveld refinement of histogram 3 of $La_2O_3Mn_2Se_2$ neutron data between 2 and 5 Å *d*-spacing at 12 K showing magnetic peaks fitted. Observed points in red, calculated in green, difference in pink.

Table 3.7 Magnetic moment on Mn atom and ${}_wR_p$ for refinements on $La_2O_3Mn_2Se_2$ neutron data with and without magnetic moment included.

T/K	Mn M_z	${}_wR_p$ with M_z /%	${}_wR_p$ without M_z /%	Δ_wR_p
12	4.38(1)	6.12	12.18	-6.06
80	3.84(1)	5.75	10.55	-4.80
120	3.26(1)	5.63	9.00	-3.37
160	1.82(2)	5.54	6.29	-0.75
200	0.55(4)	5.58	5.69	-0.15
295	0.2(1)	5.38	5.38	0

The validity of this magnetic model was verified using the more rigorous representational analysis approach as coded in the program SARAh. [6] The magnetic model obtained in space group *P*1 was essentially identical to that obtained *via* the Shubnikov approach. The arrangement of spins is anti-ferromagnetic and is shown in Figure 3.19. The spins of Mn–O–Mn units separated by an oxygen atom with a 180° bond angle are coupled ferromagnetically, while those at 90° are coupled anti-ferromagnetically. The former is not predicted by the Goodenough rules[7] for superexchange between two d^5 ions (anti-ferromagnetic coupling is predicted), but the latter is. In the closely related rock-salt MnO the 180° interactions are anti-ferromagnetic and the 90° interactions are a mixture of ferro- and anti-ferromagnetic, meaning that the 180° interactions dominate. However, the Mn atoms in $La_2O_3Mn_2Se_2$ only have two 180° Mn–O–Mn interactions whereas in MnO they have six. This is perhaps the reason why the 90° interactions dominate in $La_2O_3Mn_2Se_2$.

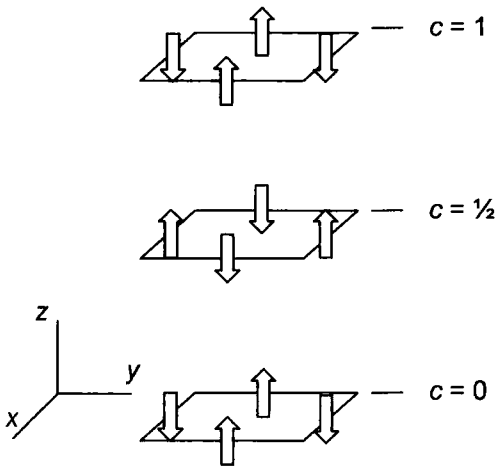

Figure 3.19 Arrangement of magnetic moments on Mn atoms (Mn M_z) in $La_2O_3Mn_2Se_2$.

Figure 3.20 and Figure 3.21 show the variation of the cell parameters from the neutron diffraction experiments superimposed on the data from the PheniX X-ray diffraction experiments. It can be seen that the cell parameters and volume (Figure 3.22) determined from the neutron data closely match those determined from X-ray data, with the exception of the *a* and *c* cell parameters at 12 K. These are larger and smaller respectively than the X-ray data. The *c* cell parameter determined from the neutron data exactly mirrors the phase transition at ~130 K determined from the X-ray data. The cell volume at 135 K determined from neutron diffraction closely matches that determined from X-ray data in its deviation from the least-squares fit line.

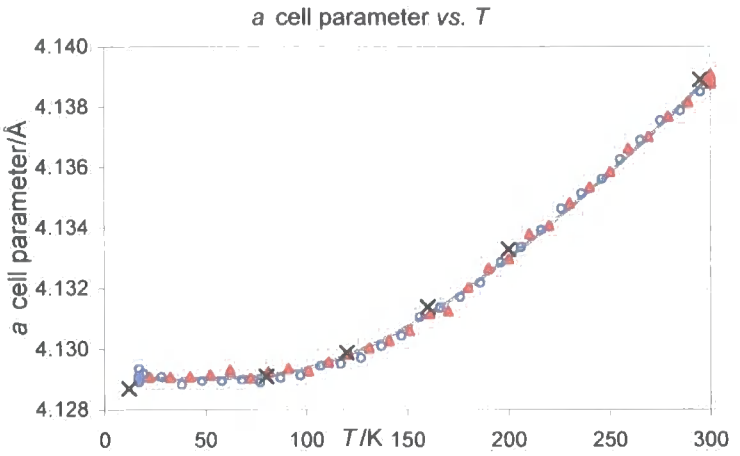

Figure 3.20 $La_2O_3Mn_2Se_2$ *a* cell parameter against temperature. Cooling data are open blue circles, heating filled red triangles, fit to the experimental data using Equation 3.1 and the values in Table 3.4 in grey, values from neutron data in black crosses.

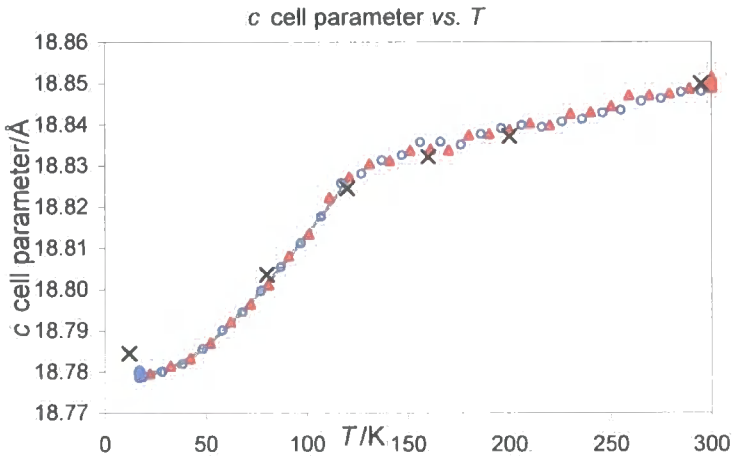

Figure 3.21 $La_2O_3Mn_2Se_2$ *c* cell parameter against temperature. Cooling data are open blue circles, heating filled red triangles, fit to the experimental data using Equation 3.1 and the values in Table 3.4 in grey, values from neutron data in black crosses.

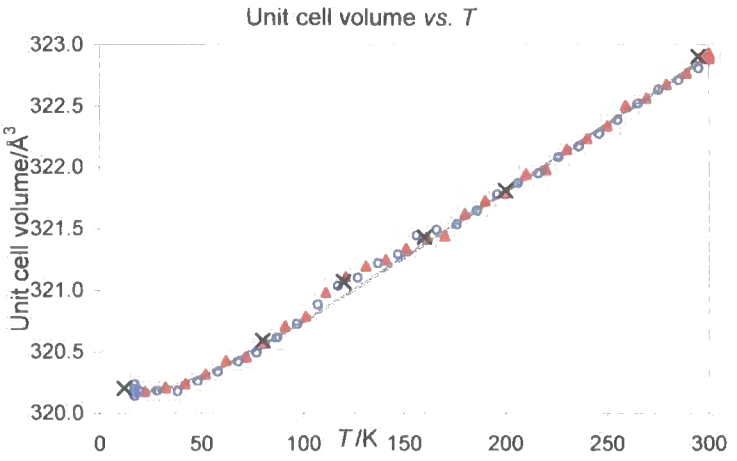

Figure 3.22 $La_2O_3Mn_2Se_2$ unit cell volume against temperature. Cooling data are open blue circles, heating filled red triangles, fit to the experimental data using Equation 3.1 and the values in Table 3.4 in grey, values from neutron data in black crosses.

Table 3.8 summarises the important structural parameters from the refinements performed using the data from the neutron diffraction experiments. The U_{eq} values are generated from the anisotropic temperature factors employed in the refinements. The U_{iso} values increase with temperature, as expected.

Table 3.8 Results from neutron diffraction refinements for $La_2O_3Mn_2Se_2$.

T/K	z/c		100 x U_{eq}/Å^2					Mn M_z	$_wR_p$	χ^2	a/Å	c/Å
	La	Se	La	Mn	Se	O(1)	O(2)					
12	0.18636(4)	0.10009(5)	0.43	0.54	0.63	0.55	2.74	4.38(1)	6.12	2.281	4.128704(25)	18.78452(21)
80	0.18638(4)	0.10002(5)	0.48	0.67	0.61	0.53	2.47	3.84(1)	5.75	2.073	4.129108(24)	18.80354(19)
120	0.18639(4)	0.10002(5)	0.5	0.79	0.64	0.56	2.02	3.26(1)	5.63	2.017	4.129889(24)	18.82446(19)
160	0.18652(4)	0.10013(5)	0.6	0.94	0.74	0.59	2.19	1.82(2)	5.54	1.955	4.131379(24)	18.83216(19)
200	0.18655(4)	0.10015(5)	0.66	1.08	0.87	0.65	2.42	0.55(4)	5.58	1.966	4.133285(24)	18.83711(20)
295	0.18660(4)	0.10012(5)	0.83	1.39	1.07	0.78	2.82	0.2(1)	5.38	1.919	4.138890(25)	18.84982(21)

It is apparent from Table 3.8 that O(2) has a U_{eq} value that is significantly larger than other atoms. Inspection of the individual U_{ij} values shows that this is essentially due to an elongation of ellipsoids perpendicular to the M_2O planes at low temperatures, as shown in Figure 3.23. This behaviour is further evidenced by Figure 3.24 and Figure 3.25 which show the temperature dependence of U_{11} (in plane) and U_{33} (perpendicular to the plane) values for each atom. U_{33} for O(2) is significantly larger than all other U_{ij} values and shows an initial apparent decrease in magnitude as the temperature is increased from 12 to 120 K. Above this temperature (which is also the temperature of the cell parameter discontinuity) a normal increase with temperature is observed. This suggests that there may be local structural distortions of the M_2O layers away from planarity at low temperatures and that the large U_{33} values are modelling this presumably static disorder. The neutron data show no evidence for any superstructure reflections, suggesting that any deviations from planarity do not have long range order.

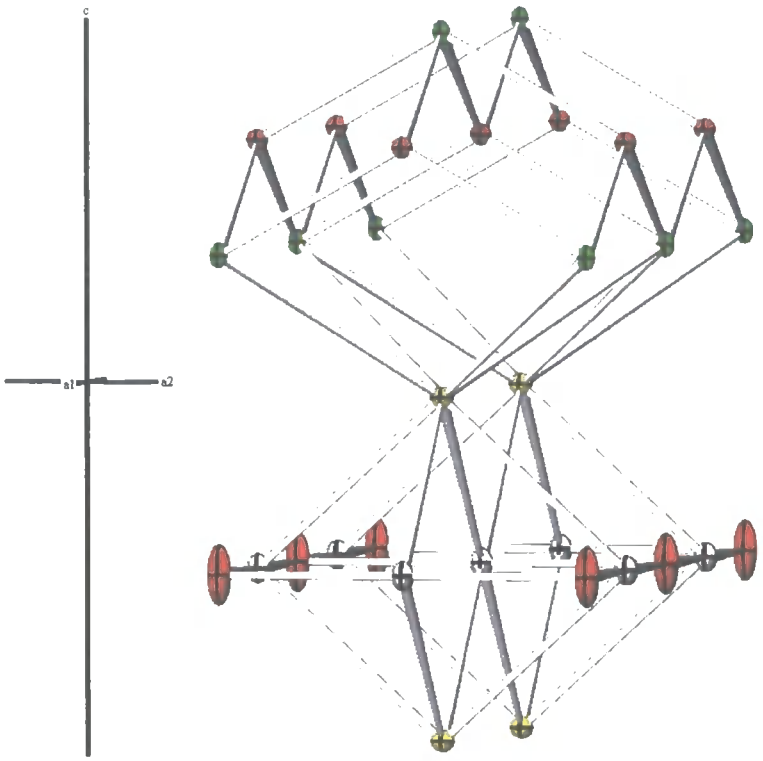

Figure 3.23 Structure of $La_2O_3Mn_2Se_2$ showing elongated thermal ellipsoids for O(2). La in green, Mn in grey, Se in yellow, O in red.

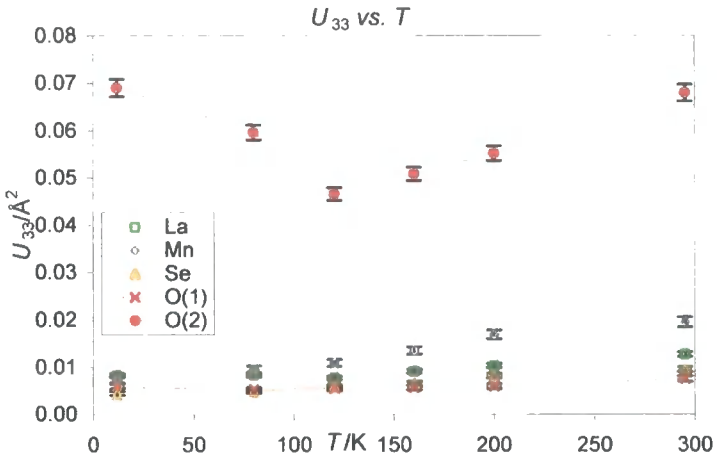

Figure 3.24 Graph of U_{33} against T from $La_2O_3Mn_2Se_2$ neutron data. La in green squares, Mn in grey diamonds, Se in yellow triangles, O(1) in red crosses and O(2) in filled red circles.

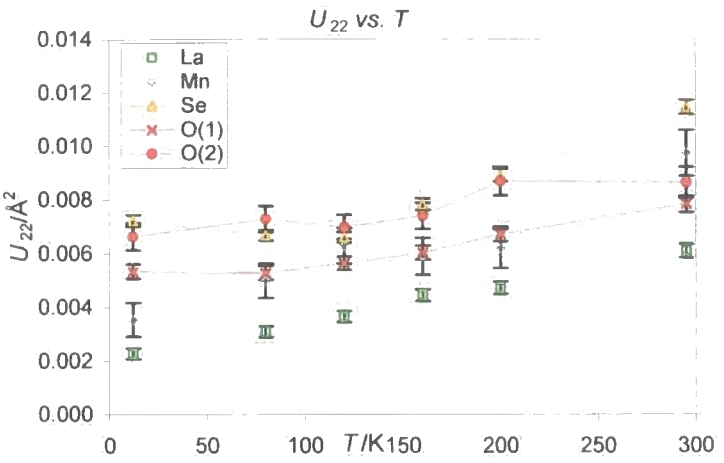

Figure 3.25 Graph of U_{22} against T from $La_2O_3Mn_2Se_2$ neutron data. La in green squares, Mn in grey diamonds, Se in yellow triangles, O(1) in red crosses and O(2) in filled red circles.

Calculating inter-layer distances as a function of temperature (Table 3.9) shows some interesting behaviour, especially for the $Mn_2O(2)$ – Se and Se – La distances, as shown in Figure 3.26 and Figure 3.27, which quite well mirror the change in the *c* axis (*e.g.* Figure 3.21). However, the inter-layer distances, for La – O(1), shown in Figure 3.28, does not change in the same way. From Figure 3.29, which shows the $\Delta d/d$ (separation at T – separation at 12 K/separation at 12 K) for all the interlayer spacings, it can be seen that the La – O(1) distance has least effect on the overall expansion of the material and that it is the layers involving Se that contribute most to the expansion in the *c* direction.

Table 3.9 Interlayer distances for $La_2O_3Mn_2Se_2$ from 12 - 300 K.

T/K	Distance/Å		
	$Mn_2O(2)$ – Se	**Se – La**	**La – O(1)**
12	1.8802(5)	1.6206(7)	1.1954(2)
80	1.8808(5)	1.6238(7)	1.1963(2)
120	1.8829(5)	1.6258(7)	1.1974(2)
160	1.8856(5)	1.6269(7)	1.1955(2)
200	1.8866(5)	1.6275(8)	1.1952(2)
295	1.8873(5)	1.6301(7)	1.1951(2)

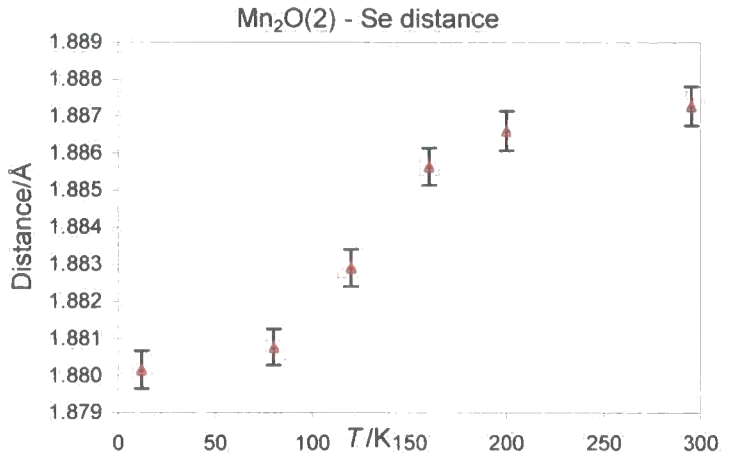

Figure 3.26 $Mn_2O(2)$ – Se interlayer distance against temperature for $La_2O_3Mn_2Se_2$.

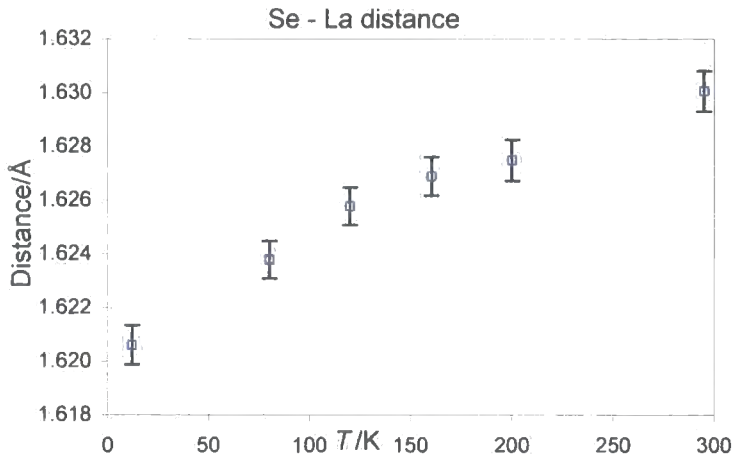

Figure 3.27 Se – La interlayer distance against temperature for $La_2O_3Mn_2Se_2$.

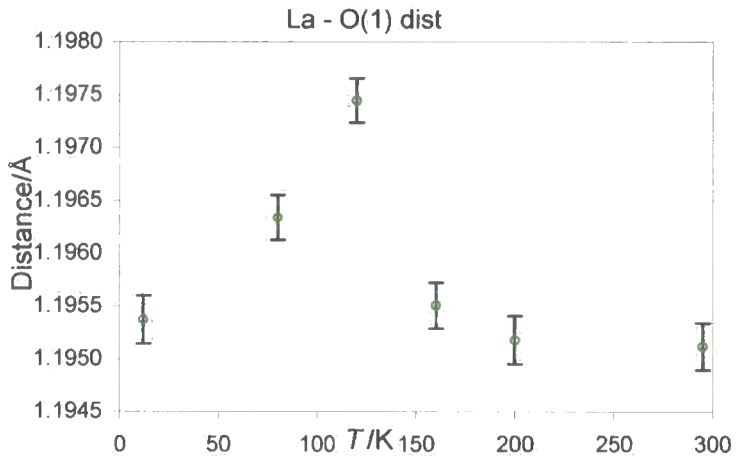

Figure 3.28 La – O(1) interlayer distance against temperature for $La_2O_3Mn_2Se_2$.

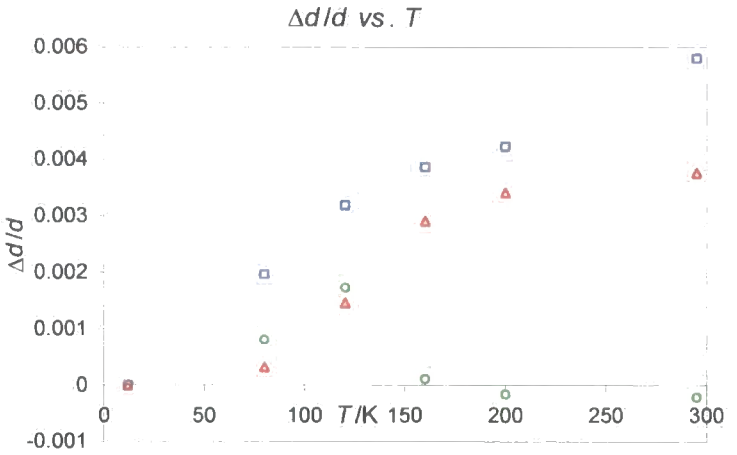

Figure 3.29 $\Delta d/d$ for $Mn_2O(2)$ - Se (red triangles), Se - La (blue squares) and La - O(1) (green circles) layers.

Figure 3.30 superimposes the values of the moment on the Mn atom (M_z) on the ZFC magnetisation data from the SQUID experiments. These show similar behaviour, with the susceptibility and moment both rising at around 200 K. While the moment continues this rise down to 12 K, the susceptibility starts to fall at around 130 K. This is possibly due to small impurities dominating the bulk susceptibility, which would not be included in the Rietveld phase.

The large increase in the FC data at ~140 K (Figure 3.31) showing ferromagnetic ordering must only come about due to the applied field, implying that the mechanism behind the anti-ferromagnetic ordering is very weak, and that spins are readily realigned by an applied field.

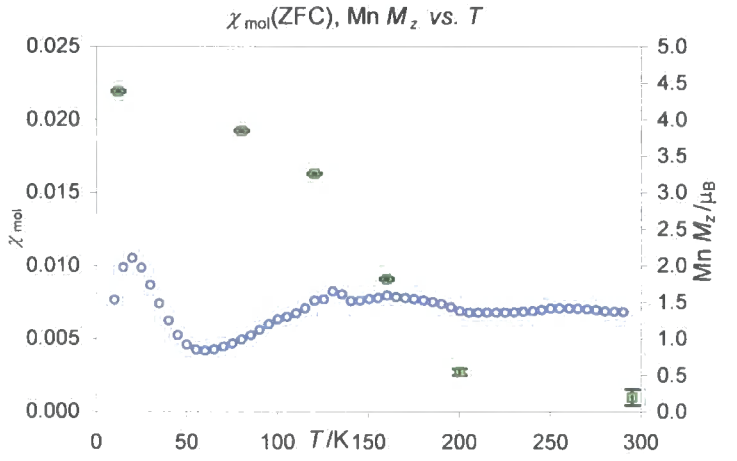

Figure 3.30 Graph of χ_{mol}(ZFC) and Mn M_z *vs.* T for $La_2O_3Mn_2Se_2$. Zero field cooled χ_{mol} data are open blue circles, Mn M_z data in green squares and line.

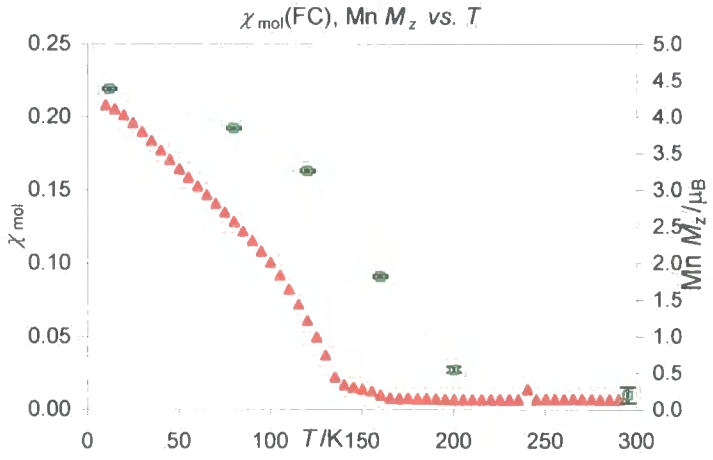

Figure 3.31 Graph of χ_{mol} (FC) and Mn M_z *vs.* T for $La_2O_3Mn_2Se_2$. Field cooled χ_{mol} data are filled red triangles, Mn M_z data in green squares and line.

3.2.5 Conductivity measurements

Conductivity measurements were performed on pellet NDW331b according to the method described in Chapter 2.4. The contacts used were sputtered gold with copper wires connected with silver paint and then soldered to the electrometer. The pellet was cooled to 80 K in the cryostat with resistance readings taken in 5 K steps. The pellet was then warmed to 300 K and resistance readings taken in 5 K intervals. The entire experiment of 300 – 80 – 300 K was then repeated to ensure the behaviour was reproducible. The results are shown in Figure 3.32, which shows the resistivity (ρ) increases significantly on cooling from ~3 x 10^4 Ω cm to ~3 x 10^{11} Ω cm at around 100 K. At this point the resistance of the sample is greater than the limit of the electrometer and the reading levels out. This exponential increase on cooling suggests semiconducting behaviour.

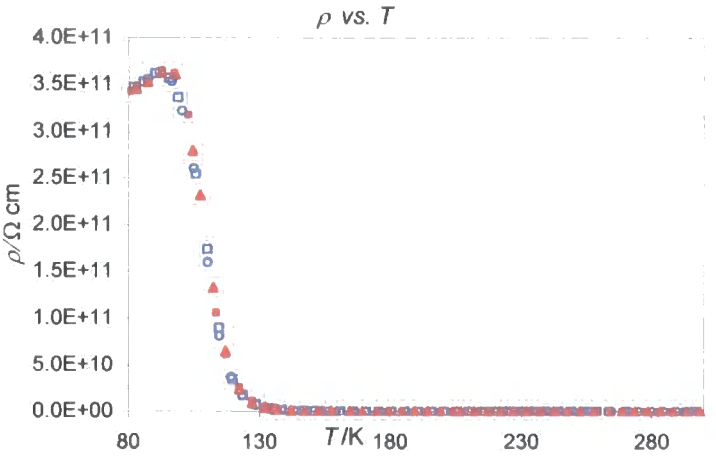

Figure 3.32 Resistivity versus temperature for $La_2O_3Mn_2Se_2$. Cooling data are open blue points, heating filled red points.

The exponential behaviour of ρ with cooling is confirmed by plotting ln ρ against $1/T$, as shown in Figure 3.33 which shows a straight line until ~0.01 K^{-1}. Fitting this linear behaviour to an Arrenhius equation (Equation 3.3, where ρ is the resistivity, ρ_0 the resistivity at 0 K, E_a the activation energy, k_B the Boltzmann constant {1.3806503 × 10^{-23} m^2 kg s^{-2} K^{-1}} and T the temperature) as shown as a black line in Figure 3.33 gives an activation energy, E_a = 23.22(7) kJ mol^{-1} or 0.2406(7) eV. This value is within the 0.2 – 2.2 eV for most intrinsic semiconductors; PbSe has an energy gap of 0.5 eV and PbTe 0.22 eV.[8]

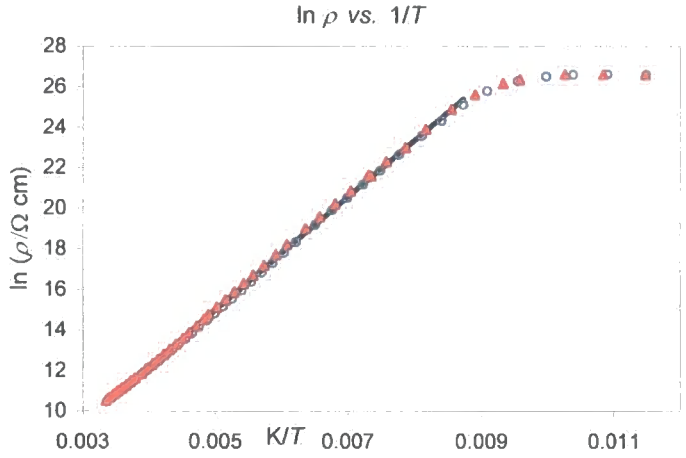

Figure 3.33 ln ρ versus $1/T$ for $La_2O_3Mn_2Se_2$. Cooling data are open blue points, heating filled red points, Arrhenius fit in black.

$$\rho = \rho_0 \exp\left[\frac{E_a}{k_B T}\right] \qquad \text{Equation 3.3}$$

3.2.6 Conclusion

In summary, $La_2O_3Mn_2Se_2$ has been synthesised with high phase purity and its structure and physical properties examined as a function of temperature. It has been shown to order anti-ferromagnetically below 200 K in the absence of a field and the magnetic structure has been elucidated by neutron diffraction. When cooled in a field, the sample orders ferromagnetically below 140 K, at which temperature there are deviations in the behaviour of the c cell parameter, the O(2) U_{33} adp and the L–O interlayer distance. This points to a possible phase transition at 140 K. However, no change can be seen in the diffraction patterns (or the conductivity) suggesting that the detailed study of the phase transition are beyond the limits of the instrumentation used in this study

3.3 $La_2O_3Co_2Se_2$

3.3.1 Room temperature X-ray diffraction

$La_2O_3Co_2Se_2$ was synthesised from stoichiometric amounts of La_2O_3, Co and Se at 1000 °C as discussed in Chapter 2.1.1. The resulting light grey powder was characterised by powder X-ray diffraction using a Siemens D5000 diffractometer (Chapter 2.2.3) and its structure confirmed by Rietveld refinement, as shown in Figure 3.34. The relatively large amorphous background visible between 10 and 20 ° 2θ in Figure 3.34 is due to the sample being sprinkled on a Vaseline covered glass disc held within the plastic sample holder. The ${}_wR_p$ for the refinement was 14.01 %, χ^2 1.84 and R_{Bragg} for the phase was 2.98 %. Details of the important parameters from this refinement are given in Table 3.10.

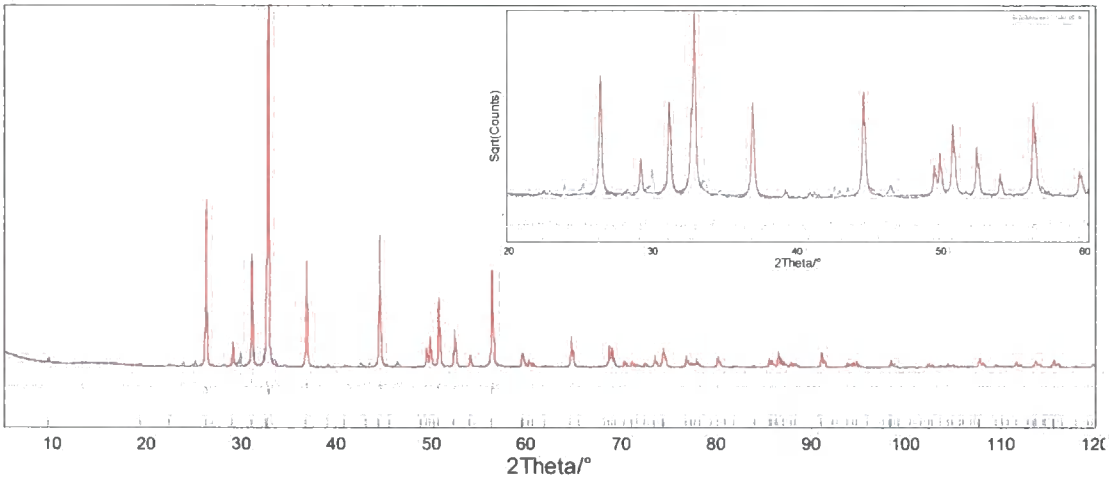

Figure 3.34 Rietveld refinement of $La_2O_3Co_2Se_2$. Observed pattern in blue, calculated in red and difference in grey. The vertical tick marks show predicted peak positions and the inset shows 20 – 60 ° 2θ region on a square root(counts) scale to emphasise weaker features in the pattern.

Table 3.10 Results of room temperature Rietveld refinement for $La_2O_3Co_2Se_2$.

$La_2O_3Co_2Se_2$	NDW328
Spacegroup	*I4/mmm*
a cell parameter*/Å	4.07114(4)
c cell parameter*/Å	18.42700(30)
La *z* coordinate/*c*	0.18343(18)
Se *z* coordinate/*c*	0.09491(29)
La B_{iso}/Å^2	1.24(14)
Mn B_{iso}/Å^2	0.99(29)
Se B_{iso}/Å^2	0.65(24)
O(1) B_{iso}/Å^2	4.0(12)
O(2) B_{iso}/Å^2	3.7(16)
${}_wR_p$/%	15.27
R_{Bragg}/%	2.98
χ^2	1.84
No. parameters	36

* Cell parameters are from Si standardised experiment, details below.

In order to accurately confirm the cell parameters, a sample was prepared for Rietveld analysis containing a Si standard. 0.1416 g Si was combined with 0.4389 g $La_2O_3Co_2Se_2$ and a portion of this was packed into a 12 mm sample holder and its powder pattern recorded on a Siemens D5000 diffractometer from 5 – 120 ° 2θ with a step size of 0.02 ° and a count time of ~6.5 s per step. The total scan time was 17.5 hours and variable 6mm slits were used. The resulting pattern is shown in Figure 3.3. The Si cell parameter was fixed at 5.4311946 Å (the value for NIST sample 640c[2]) during refinement and a calibration curve applied as for $La_2O_3Mn_2Se_2$. This resulted in an *a* cell parameter of 4.07114(4) Å and *c* = 18.42700(30) Å for $La_2O_3Co_2Se_2$.

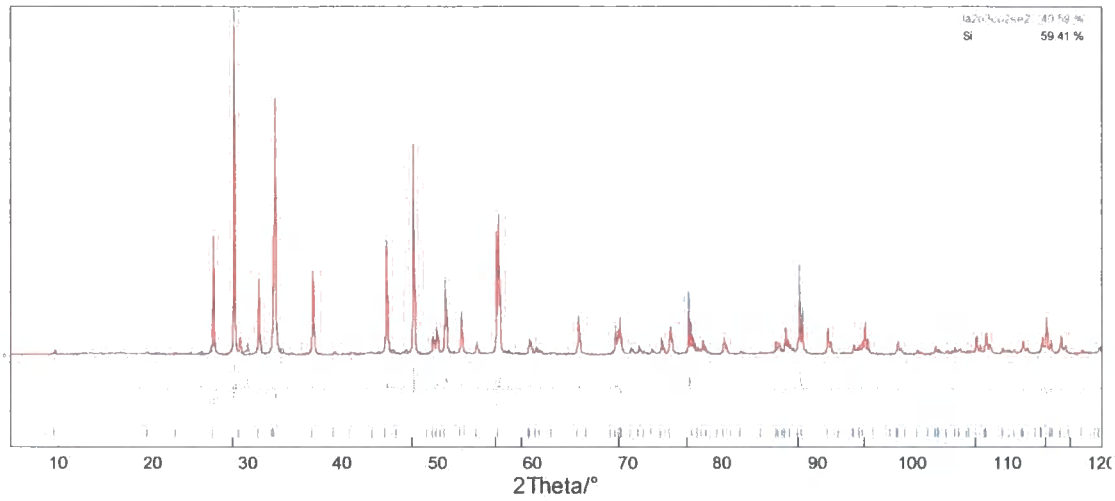

Figure 3.35 Two phase Rietveld refinement of $La_2O_3Co_2Se_2$. Observed pattern in blue, calculated in red and difference in grey. The vertical tick marks show predicted peak positions for $La_2O_3Co_2Se_2$ and Si from top to bottom respectively.

3.3.2 Variable temperature powder X-ray diffraction

Variable temperature powder X-ray diffraction experiments were performed on this compound using a Bruker D8 diffractometer with PheniX He ccr attachment (Chapter 2.2.5). The sample NDW81 was studied in experiments d8_02299 and d8_02300. In experiment number d8_02299 it was cooled at 17 K hr^{-1} and data collected over a 5 – 120 ° 2θ range in 30 minute time slices. Eight 30 minute scans were performed at the base temperature and summed together giving the equivalent of one 4 hr data collection. In experiment d8_02300 the sample was then heated at 17 K hr^{-1} to 300 K and data collected using the same range and scan time as experiment d8_02299. Ten 30 minute scans were performed at 300 K and summed together.

The data were analysed using the *multitopas* methodology described in Section 2.2.6. The summed scan from 300 K was again used to fit a calibration curve to the data using the cell parameters ascertained with a Si standard. In the *multitopas* procedure, these parameters for the calibration curve were fixed and the cell parameter allowed to refine as normal.

Figure 3.36 shows the variation of the *a* cell parameter with temperature and Figure 3.37 shows the *c* cell parameter. Both these figures include a least-squares fitted model as a grey line, calculated from Equation 3.1. The variation of the Al cell parameter is shown in Figure 3.40 together with Wang and Reeber's data[4] as a grey line, which both cooling and heating data closely match with an a_0 refined to 4.03277(4) Å.

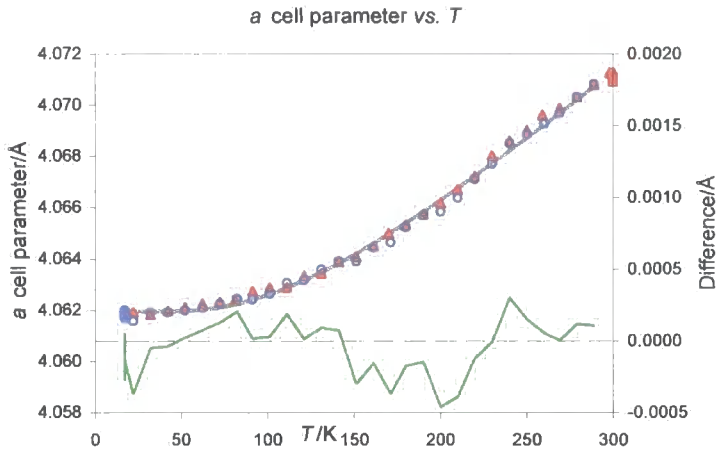

Figure 3.36 $La_2O_3Co_2Se_2$ *a* cell parameter against temperature. Cooling data are open blue circles, heating filled red triangles, fit to the experimental data using Equation 3.1 and the values in Table 3.11 in grey and difference in green.

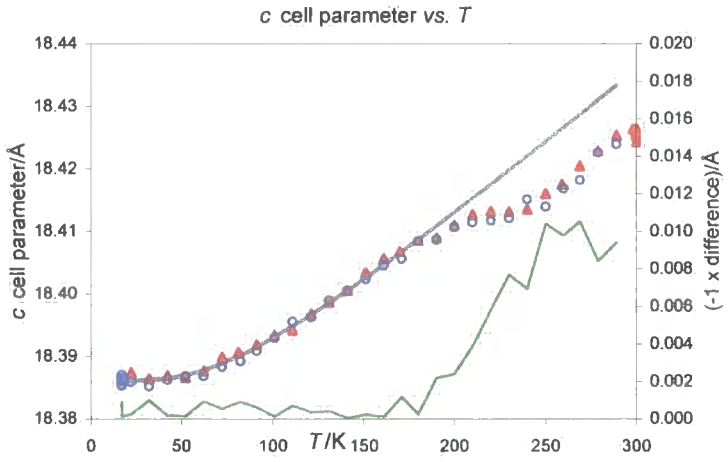

Figure 3.37 $La_2O_3Co_2Se_2$ *c* cell parameter against temperature. Cooling data are open blue circles, heating filled red triangles, fit to the experimental data using Equation 3.1 and the values in Table 3.11 in grey and difference in green.

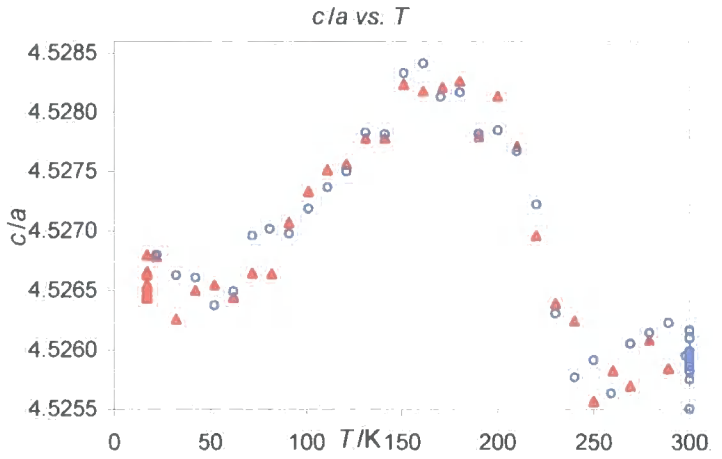

Figure 3.38 $La_2O_3Co_2Se_2$ *c/a* ratio against temperature. Cooling data are open blue circles, heating filled red triangles.

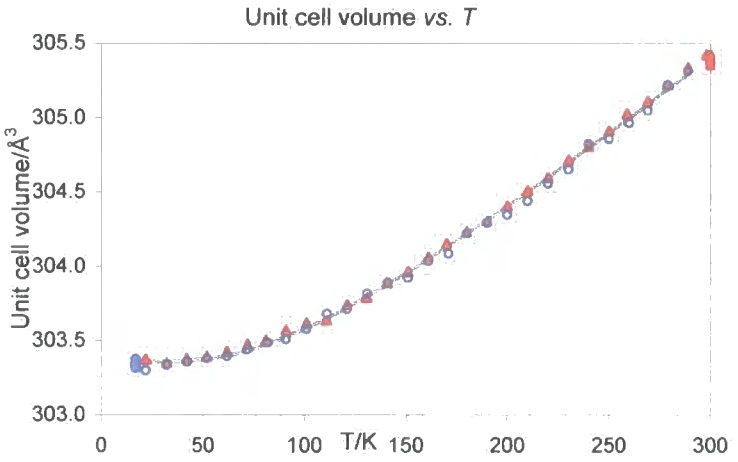

Figure 3.39 $La_2O_3Co_2Se_2$ unit cell volume against temperature. Cooling data are open blue circles, heating filled red triangles, fit to the experimental data using Equation 3.1 and the values in Table 3.11 in grey.

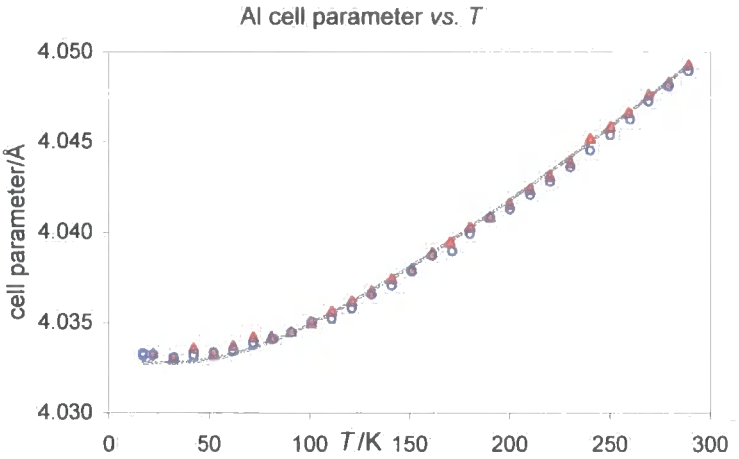

Figure 3.40 Aluminium cell parameter against temperature. Cooling data are open blue circles, heating filled red triangles, Wang and Reeber's data in grey.

Figure 3.36 shows that the *a* cell parameter expands smoothly on heating and that the data very closely match the fitted expansion expression, with the parameters determined by a least-squares fit shown in Table 3.11. There is a slight deviation between around 150 and 200 K, which is highlighted by the difference curve in Figure 3.36. Figure 3.37 shows that the *c* cell parameter shows a significant change in behaviour at around 180 K. Below this temperature it fits the simple expansion model well, and the parameters for this are given in Table 3.11. Above this temperature it shows more complex behaviour, levelling out before expanding again at 250 K. These changes at ~180 and 250 K are mirrored in the *c/a* plot in Figure 3.38 which shows marked changes at those temperatures. Figure 3.39 shows the change in unit cell volume with temperature which shows a smooth variation.

Table 3.11 Thermal expansion coefficients from PheniX experiments on $La_2O_3Co_2Se_2$.

	a_0/Å	θ_1/K	$C_1/10^{-6}$	$\alpha_{(300\text{-}15K)}/10^{-6}$ K^{-1}
a	4.06195(4)	350(10)	14.5(3)	8.1(2)
c	18.3861(2)	218(11)	13.2(5)	9.5(4)
v	303.358(6)	266(6)	36.1(4)	23.7(4)

The Rietveld refinement performed on the summed data set from 17 K is shown in Figure 3.41 (the *y* scale is a square root (counts) scale because the pattern is dominated by the scatter from the Al sample holder). The calculated patterns show a good fit to the observed and give the following cell parameters: *a* = 4.06181(5) Å *c* = 18.38601(34) Å at 17 K and *a* = 4.07114(4) Å and *c* = 18.42700(30) Å at 300 K. The *R*-factors were $_wR_p$ = 5.07 and 7.04 %, χ^2 = 1.462 and 1.500 and R_{Bragg} 1.51 and 1.92 % for 17 and 300 K respectively. Other important structural least-squares parameters are summarised in Table 3.12 for the refinements performed on the long scans at 17 and 300 K.

Table 3.12 Atomic fractional coordinates and displacement parameter values for $La_2O_3Co_2Se_2$ at 17 and 300 K.

Site	*z/c* (17 K)	*z/c* (300 K)	B_{iso}/Å^2 (17 K)	B_{iso}/Å^2 (300 K)
La	0.1831(1)	0.1833(1)	-1.79(6)	-1.37(6)
Mn	0	0	-1.59(11)	-0.95(12)
Se	0.0951(2)	0.0952(2)	-1.81(9)	-1.31(9)
O(1)	0.25	0.25	-1.61(39)	-1.88(38)
O(2)	0	0	-0.47(71)	-0.21(75)

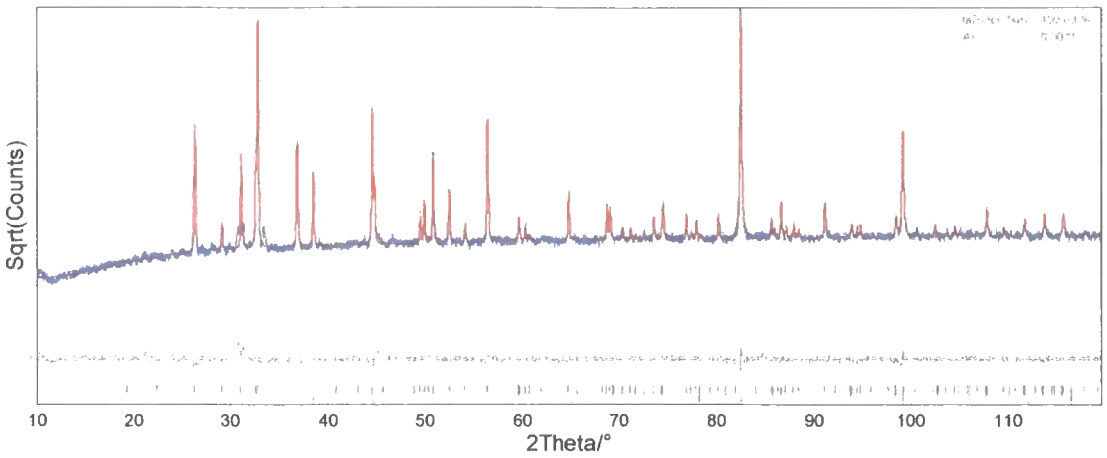

Figure 3.41 17 K refinement of $La_2O_3Co_2Se_2$. Observed pattern in blue, calculated in red, difference in grey. Tick marks show predicted peak positions for $La_2O_3Co_2Se_2$ and Al from top to bottom respectively.

Within experimental error, there is no difference between the *z* coordinates at 17 and 300 K of either the La or Se atoms (the only two atomic coordinates in the structure which are not fixed by symmetry). They are also the same (within experimental error) as the values from the room temperature d5000 Rietveld refinements given in Table 3.10. B_{iso} values from these refinements are not quoted as the sample preparations method invariably leads to a sizeable sample surface roughness; values from neutron refinements (below) are more reliable.

3.3.3 SQUID magnetometry

A small part of a pellet of sample number NDW321b was characterised by SQUID magnetometry using the sample preparation and experiment technique described in Chapter 2.3. Zero field cooled (ZFC) and field cooled (FC) experiments were conducted on this sample in a field of 100 Oe with measurements taken at 5 K steps from 10 – 290 K and the results shown in Figure 3.42. A magnetisation *vs.* applied field (*M vs. H*) experiment was also performed at 290 K on this sample, and the results are shown in Figure 3.43. This is clearly a straight line crossing the origin.

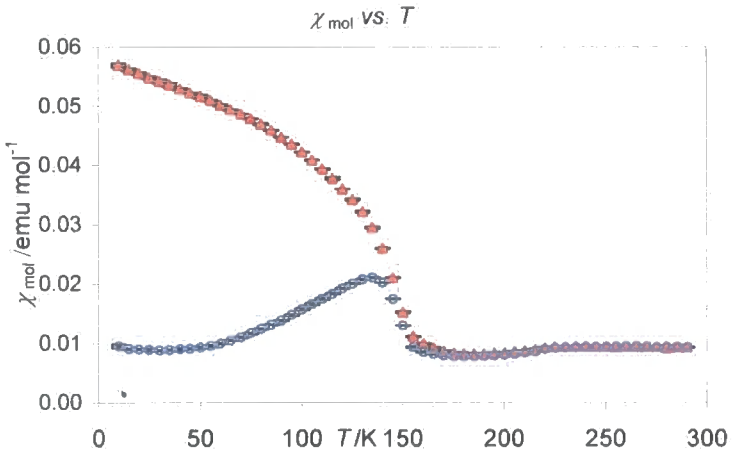

Figure 3.42 ZFC (open blue circles) and FC (filled red triangles) data for $La_2O_3Co_2Se_2$.

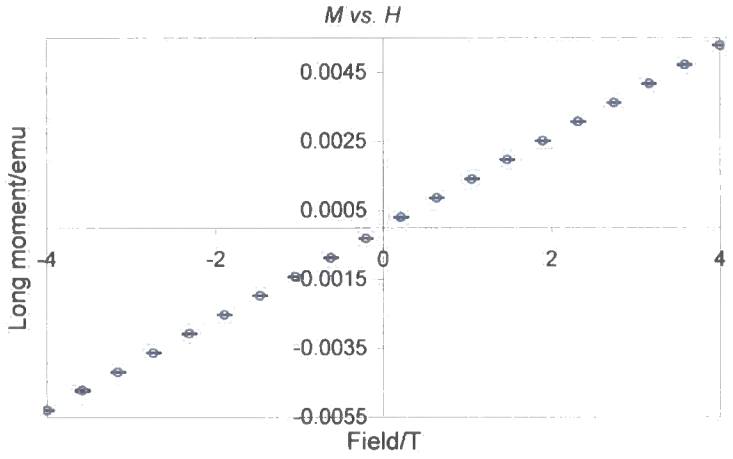

Figure 3.43 Magnetisation against applied field for $La_2O_3Co_2Se_2$

Figure 3.42 shows similar behaviour to $La_2O_3Mn_2Se_2$. It is worth noting that the susceptibility in the ZFC experiment increases on heating until around 130 K, when it is, at ~0.020 emu mol^{-1}, almost the same value as the FC data. Above this temperature it falls until ~150 K; above this temperature it is more constant.

3.3.4 Variable temperature neutron diffraction

Neutron diffraction patterns were recorded at 12, 100, 135, 165, 200 and 295 K on the SEPD diffractometer at the IPNS at the Argonne National Laboratory, USA. These points were chosen to be representative of the areas above and below the discontinuities in unit cell and magnetic data described above.

An initial refinement was performed against the 295 K data set (histograms 1 – 3) and a d5000 scan (recorded at room temperature) for reference. The lattice parameters were fixed at the value determined using a Si standard in order to refine appropriate instrument

parameters and absorption corrections. These were *dif*$_c$, *dif*$_a$, *zero* for the neutron histograms and a zero point error for the d5000 data. A total of 69 variables were refined. The following were refined for each histogram: 3 instrument parameters, 3 peak shape parameters (*sig*1, *sig*2, *gam*1 for the neutron data histograms; *GW*, *LY*, *asym* for the X-ray data), a 9 term Chebychev polynomial to fit the background, an absorption correction factor and scale factor. Two atomic coordinates and 11 non symmetry equivalent thermal factors were refined for the $La_2O_3Co_2Se_2$ phase. This resulted in a good fit, shown in Figure 3.44, and a $_wR_P$ of 8.04 % and a χ^2 of 3.754. The instrument parameters are summarised in Table 3.13.

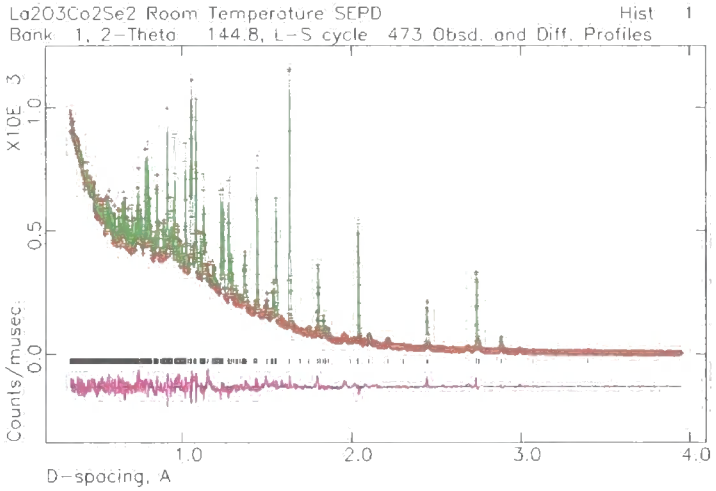

Figure 3.44 Rietveld refinement of histogram 1 (145 °) of $La_2O_3Co_2Se_2$ neutron data at 295 K. Observed points in red, calculated in green, difference in pink.

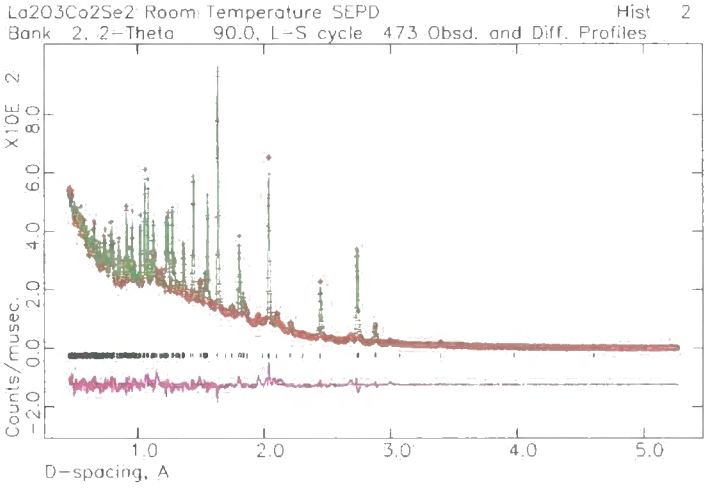

Figure 3.45 Rietveld refinement of histogram 2 (90 °) of $La_2O_3Co_2Se_2$ neutron data at 295 K. Observed points in red, calculated in green, difference in pink.

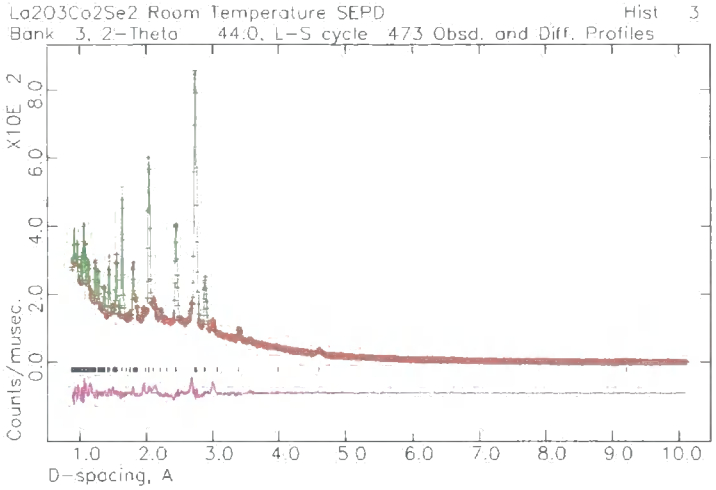

Figure 3.46 Rietveld refinement of histogram 3 (44 °) of $La_2O_3Co_2Se_2$ neutron data at 295 K. Observed points in red, calculated in green, difference in pink.

Table 3.13 Instrument parameters for $La_2O_3Co_2Se_2$ neutron refinements.

Histogram	dif_c	dif_a	*zero*	Absorption
1	7477.35	-1.84	-9.95	0.17578
2	5585.33	-0.18	-7.97	0.17808
3	2899.54	1.66	-7.2	0.13100

This refinement was then used as a template for the refinements of data collected at other temperatures. The dif_c, dif_a, *zero* and absorption parameters were fixed at the values determined above and the cell parameters allowed to refine. An examination of the data from histogram 3 at 12 K (Figure 3.47) shows the presence of extra peaks, not fitted by the structural model. They appear below the magnetic phase transition observed by SQUID magnetometry and are at high *d*-spacings (3 – 6 Å), suggesting that $La_2O_3Co_2Se_2$ has long range magnetic ordering at low temperature.

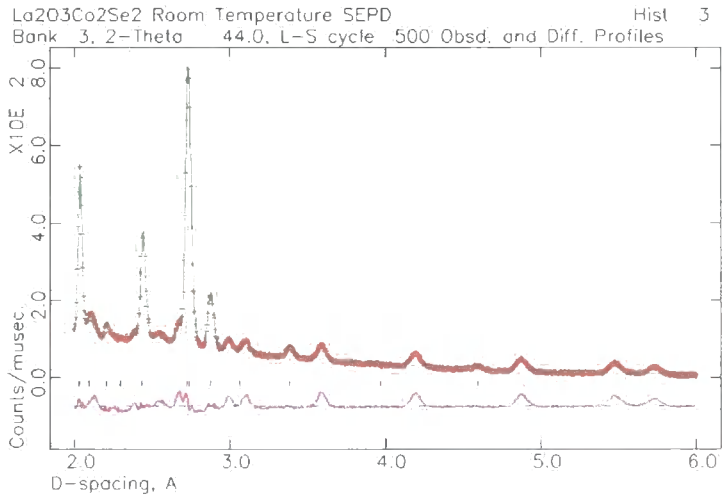

Figure 3.47 Rietveld refinement of histogram 3 of $La_2O_3Co_2Se_2$ neutron data between 2 and 6 Å d-spacing at 12 K showing magnetic peaks not fitted. Observed points in red, calculated in green, difference in pink.

Successful refinement of this magnetic structure was achieved using SARAh with a *P4/mmm* space group and irreducible representations generated by a propagation vector k = (0.5, 0.5, 0). Figure 3.48 shows the refinement using this model, with a doubled *a/b* cell parameter of a = 8.12560 Å at 12 K. Table 3.14 gives the fractional occupancy (*Frac*) and thus magnetic moment (2 x *Frac*) for the Co atoms, together with the nuclear and magnetic unit cell parameters and the $_wR_p$ factors for the refinements before and after including the magnetic phase.

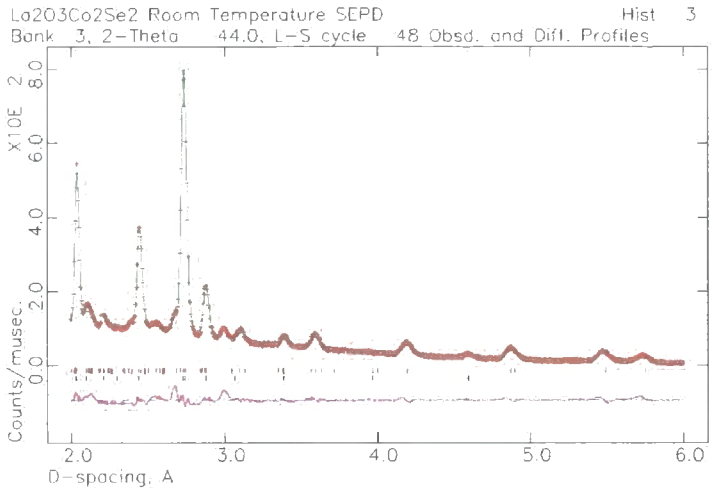

Figure 3.48 Rietveld refinement of histogram 3 of $La_2O_3Co_2Se_2$ neutron data between 2 and 6 Å d-spacing at 12 K showing magnetic peaks fitted. Observed points in red, calculated in green, difference in pink. Unfitted peak < 3 Å due to minor impurity phase.

Table 3.14 *Frac* and magnetic moment on Co atom, nuclear and magnetic unit cell parameters and wRp for refinements on $La_2O_3Co_2Se_2$ neutron data.

T/K	Co *Frac*	Co mom.	a_{nuc}/Å	a_{mag}/Å	*c*/Å	$_wR_p$ after	$_wR_p$ before
12	2.407(16)	4.814	4.06264(4)	8.125284	18.38825(33)	7.25	8.83
100	2.412(16)	4.824	4.06354(4)	8.127084	18.39556(33)	7.04	8.56
135	2.382(16)	4.764	4.06439(4)	8.128772	18.40147(33)	7.02	8.40
165	2.323(16)	4.646	4.06529(4)	8.139568	18.40743(33)	7.00	8.16
200	2.045(17)	4.09	4.06677(4)	8.133538	18.41285(33)	6.94	7.51
295	0.870(32)	0.174	4.07162(5)	8.143152	18.4282(4)	8.32	8.04

The arrangement of magnetic moments is shown in Figure 3.49. The spins of Co atoms separated by an oxygen atom at 180° are coupled anti-ferromagnetically, as predicted by the Goodenough rules for superexchange between two d^7 ions.[7]

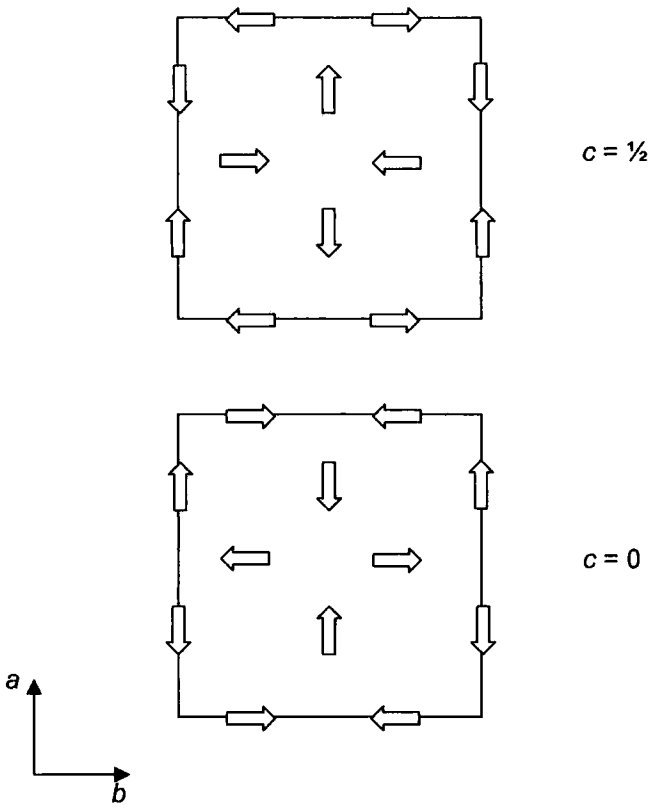

Figure 3.49 Arrangement of magnetic moments on Co atoms in $La_2O_3Co_2Se_2$.

Figure 3.50 and Figure 3.51 show the variation of the cell parameters from the neutron diffraction experiments superimposed on the plots from the PheniX X-ray diffraction experiments. The *a* cell parameter determined from neutron diffraction data is larger than from the d8/PheniX X-ray experiments, but follows roughly the same trend. The *c* cell parameter is also slightly larger for the neutron data (less noticeable due to the larger scale of the graph) and also very closely follows the unusual behaviour seen in the X-ray data. The cell volume (Figure 3.52) is also slightly larger for the neutron data, but follows the same behaviour as the X-ray data.

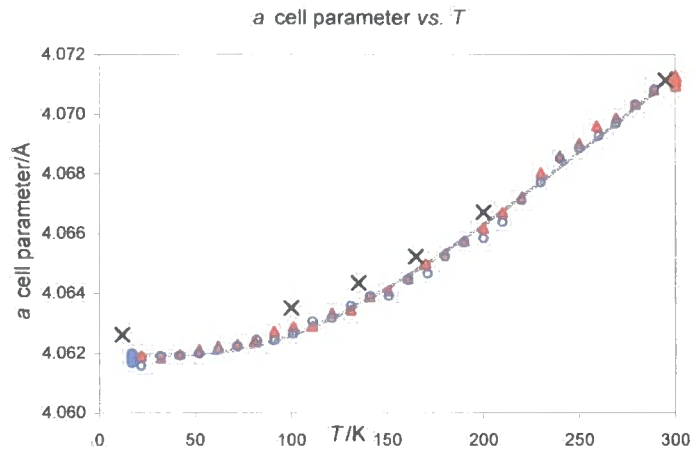

Figure 3.50 $La_2O_3Co_2Se_2$ *a* cell parameter against temperature. Cooling data are open blue circles, heating filled red triangles, fit to the experimental data using Equation 3.1 and the values in Table 3.11 in grey, values from neutron data in black crosses.

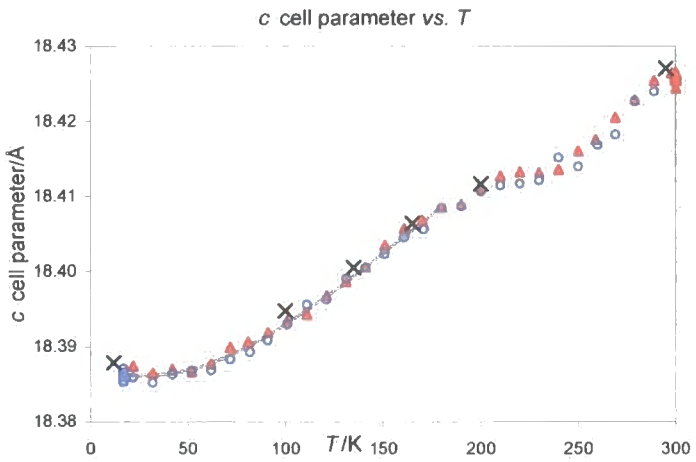

Figure 3.51 $La_2O_3Co_2Se_2$ *c* cell parameter against temperature. Cooling data are open blue circles, heating filled red triangles, fit to the experimental data using Equation 3.1 and the values in Table 3.8 in grey, values from neutron data in black crosses.

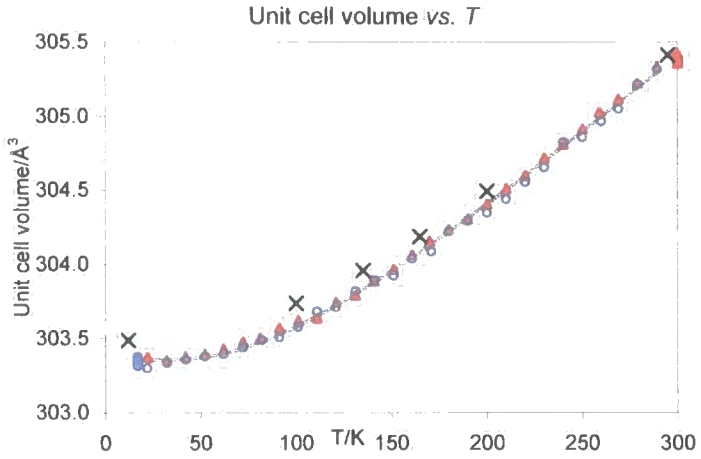

Figure 3.52 $La_2O_3Co_2Se_2$ unit cell volume against temperature. Cooling data are open blue circles, heating filled red triangles, fit to the experimental data using Equation 3.1 and the values in Table 3.8 in grey, values from neutron data in black crosses.

Table 3.15 summarises the important phase parameters from the neutron refinements. The U_{eq} values have been generated from the anisotropic temperature factors employed in the refinements. The U_{eq} values increase with temperature, as expected, and the z coordinates of the La and Se atoms do not greatly change.

Table 3.15 Results from neutron diffraction refinements for $La_2O_3Co_2Se_2$.

T/K	z/c		100 x U_{eq}/Å^2					Co Frac	$_wR_p$	χ^2	a/Å	c/Å
	La	Se	La	Co	Se	O(1)	O(2)					
12	0.18335(7)	0.09525(8)	0.48	0.52	0.47	0.38	1.19	2.407(16)	7.25	3.680	4.06264(4)	18.38825(33)
100	0.18340(7)	0.09529(8)	0.62	0.63	0.59	0.43	1.39	2.412(16)	7.04	3.523	4.06354(4)	18.39556(33)
135	0.18347(7)	0.09528(8)	0.66	0.73	0.65	0.45	1.56	2.382(16)	7.02	3.514	4.06439(4)	18.40147(33)
165	0.18341(7)	0.09531(8)	0.69	0.79	0.74	0.5	1.68	2.323(16)	7.00	3.512	4.06529(4)	18.40743(33)
200	0.18346(7)	0.09522(8)	0.79	0.85	0.83	0.54	1.87	2.045(17)	6.94	3.420	4.06677(4)	18.41285(33)
295	0.18337(5)	0.09511(7)	1.1	1.39	1.19	0.66	2.51	0.870(32)	8.32	5.487	4.07162(5)	18.4282(4)

As for $La_2O_3Mn_2Se_2$, the O(2) U_{33} term is significantly larger than other U_{ij} terms, as illustrated in Figure 3.53 and Figure 3.54. However, its temperature dependence is, in contrast to the Mn material, normal and it increases gradually with temperature. This, together with the temperature dependence of the c parameter suggests that no long range structural change occurs on cooling.

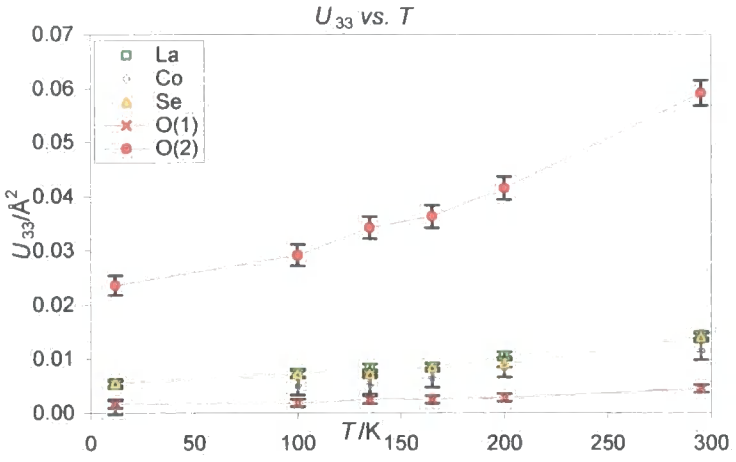

Figure 3.53 Graph of U_{33} against T from $La_2O_3Mn_2Se_2$ neutron data. La in green squares, Co in grey diamonds, Se in yellow triangles, O(1) in red crosses and O(2) in filled red circles.

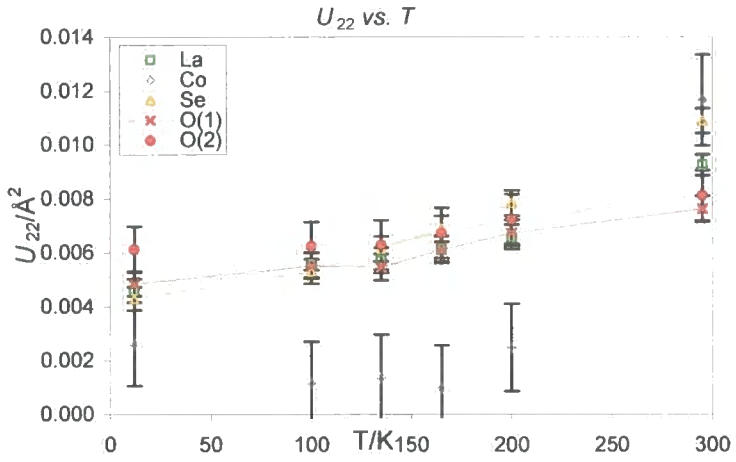

Figure 3.54 Graph of U_{22} against T from $La_2O_3Co_2Se_2$ neutron data. La in green squares, Co in grey diamonds, Se in yellow triangles, O(1) in red crosses and O(2) in filled red circles.

The interlayer distances are shown in Table 3.16 and Figure 3.55 to Figure 3.57. These show quite different behaviour to those for $La_2O_3Mn_2Se_2$, with none of the interlayer differences obviously mirroring the temperature dependence of the unit cell parameter.

Table 3.16 Interlayer distances from 12 - 300 K for $La_2O_3Co_2Se_2$.

T/K	Distance/Å		
	$Co_2O(2)$ – Se	Se – La	La – O(1)
12	1.7515(8)	1.6199(12)	1.2256(4)
100	1.7529(9)	1.6207(13)	1.2251(4)
135	1.7532(9)	1.6227(13)	1.2243(4)
165	1.7544(9)	1.6215(12)	1.2257(4)
200	1.7531(8)	1.6247(12)	1.2251(4)
295	1.7525(7)	1.6265(10)	1.2278(3)

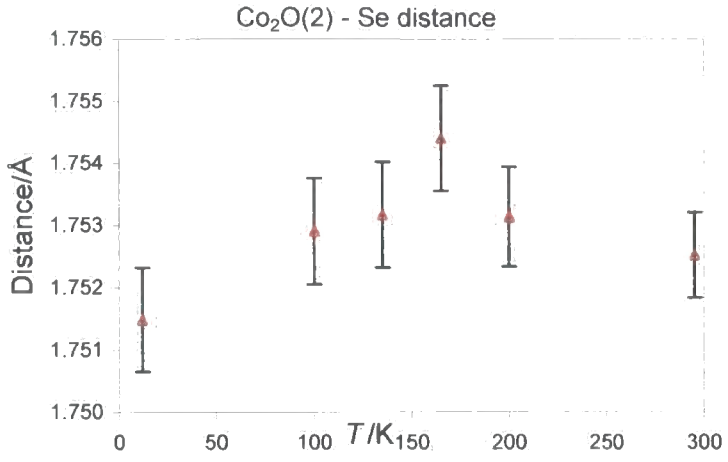

Figure 3.55 $Co_2O(2)$ – Se interlayer distance against temperature for $La_2O_3Co_2Se_2$.

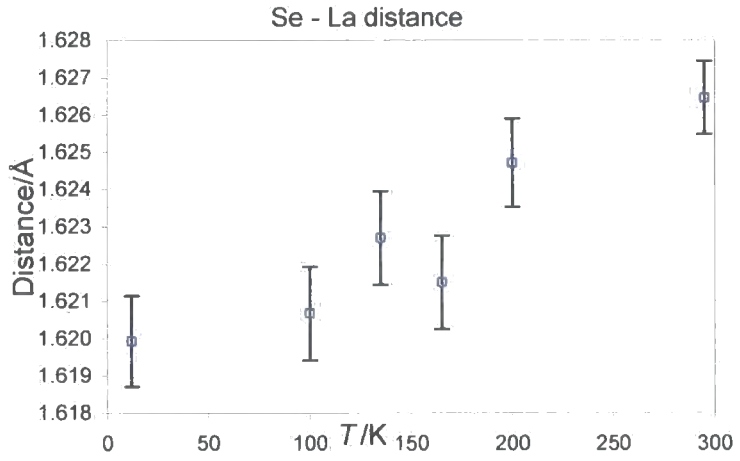

Figure 3.56 Se – La interlayer distance against temperature for $La_2O_3Co_2Se_2$.

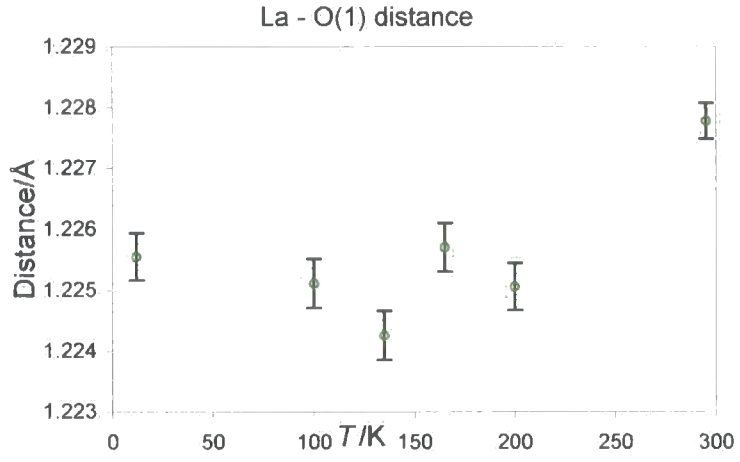

Figure 3.57 La – O(1) interlayer distance against temperature for $La_2O_3Co_2Se_2$.

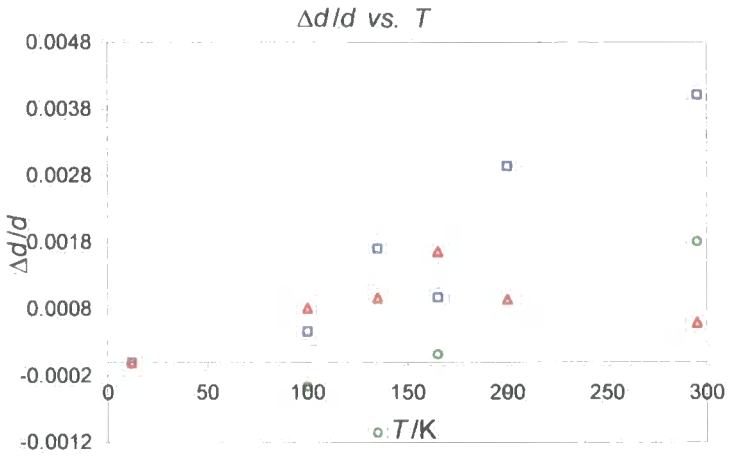

Figure 3.58 $\Delta d/d$ for $Co_2O(2)$ - Se (red triangles), Se - La (blue squares) and La - O(1) (green circles) layers.

Figure 3.59 superimposes the values of the moment on the Co atom on the ZFC magnetisation data from the SQUID experiments. The small change seen in the SQUID data at ~220 K, below which the magnetisation falls indicating anti-ferromagnetic ordering, matches the increase in moment, seen on cooling between 300 and 200 K from the neutron data. The large increase in the magnetisation in the SQUID data at ~150 K, indicating ferromagnetic ordering, implies that in the presence of a magnetic field, the magnetic ground state is ferromagnetic, not antiferromagnetic as in the absence of a field (e.g. as when the neutron diffraction patterns were recorded).

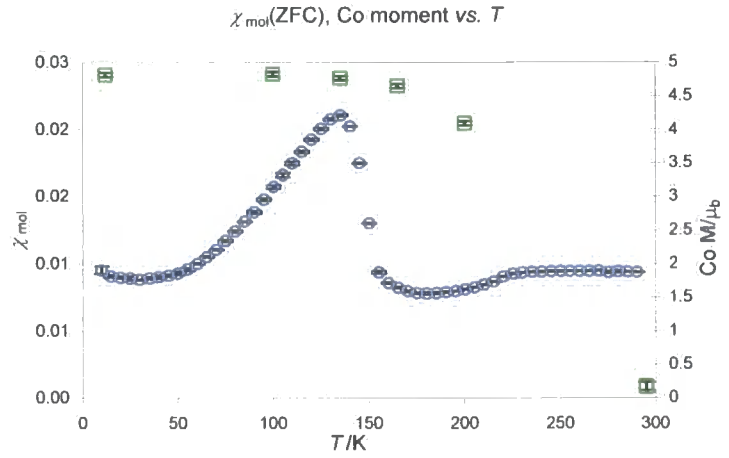

Figure 3.59 Graph of χ_{mol}(ZFC) and Co M *vs.* T for $La_2O_3Co_2Se_2$. Zero field cooled cmol data are open blue circles, Co M data in green squares.

3.3.5 Conductivity measurements

Conductivity measurements were performed on pellet NDW256a according to the method described in chapter 2.4. The contacts used were sputtered aluminium protected against oxidation with silver paint and then connected to the electrometer with soldered copper wires.

The pellet was cooled to 80 K in the cryostat and resistance readings taken every 5 K on cooling. The pellet was then warmed to 300 K and resistance readings taken every 5 K. This 300 – 80 – 300 K experiment was repeated three times to ensure the results were reproducible. The results are shown in Figure 3.32. This shows the resistivity increasing exponentially on cooling from ~1 x 10^7 Ω cm to a maximum of ~3 x 10^{10} Ω cm at around 180 K. At this point the resistance of the sample is greater than the limit of the electrometer and the reading levels out. This exponential increase on cooling suggests semiconducting behaviour and is confirmed by plotting ln ρ against $1/T$, as shown in Figure 3.61 which shows a straight line until ~0.005 K^{-1}. Fitting these data to an Arrhenius equation (Equation 3.3) as shown as a black line in Figure 3.61 gave E_a = 33.6(5) kJ mol^{-1} or 0.348(5) eV, again within the expected range of a semiconductor.

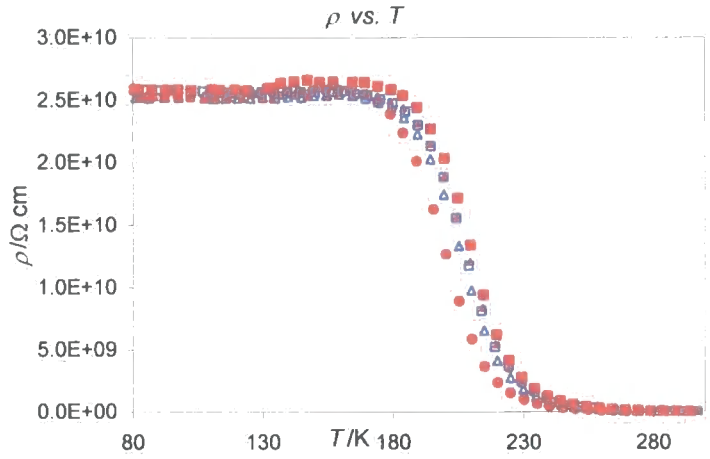

Figure 3.60 Resistance versus temperature for $La_2O_3Co_2Se_2$. Cooling data are open blue points, heating filled red points.

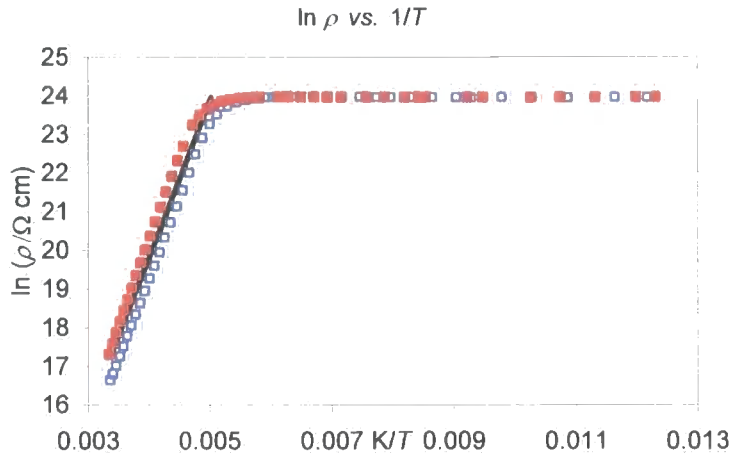

Figure 3.61 ln ρ versus $1/T$ for $La_2O_3Co_2Se_2$. Cooling data are open blue points, heating filled red points, Arrhenius fit in black.

3.3.6 Conclusion

$La_2O_3Co_2Se_2$ has been synthesised and its structure and physical properties examined as a function of temperature. It has been shown to order anti-ferromagnetically below 200 K and the magnetic structure has been characterised by neutron diffraction. Similarly to $La_2O_3Mn_2Se_2$ when the sample is cooled in a field it orders ferromagnetically below around 150 K. The deviation in the ratio of *c* to *a* cell parameter (*c*/*a*) suggests a structural change, rather then the presence of a ferromagnetic impurity. Again, the subtle nature of this phase transition means no evidence in the form of peak-splitting or extra peaks could be observed in the low temperature powder patterns.

3.4 Conclusions

Both the $La_2O_3M_2Se_2$ samples show anti-ferromagnetic ordering in the absence of a field, as shown by both SQUID magnetometry and variable temperature neutron diffraction data. The spin ordering has been characterized by the neutron data. For both samples (*M* = Mn, Co) anti-ferromagnetic ordering occurs below at T_N of around 200 K, as can be seen from the change in magnetic moment obtained by Rietveld refinement (Figure 3.62). It is also suggested by minor changes in the bulk magnetisation from ZFC SQUID data at around that temperature. In the case of Co a clear discontinuity can also be seen in the thermal expansion at this temperature.

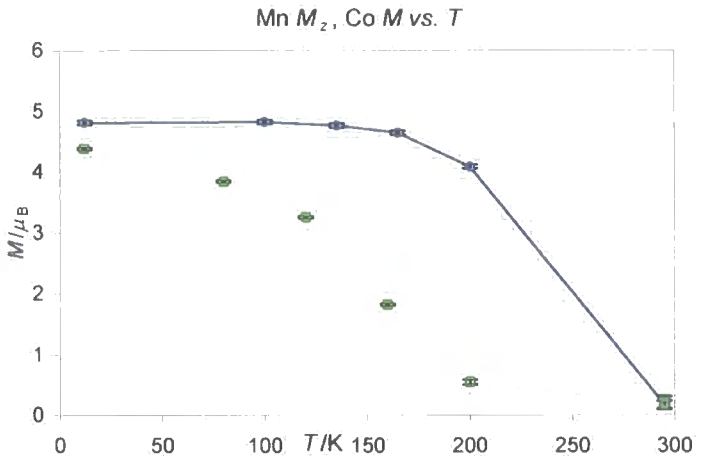

Figure 3.62 Magnetic moment *vs.* *T* for $La_2O_3M_2Se_2$ (*M* = Mn (green), Co (blue)).

SQUID data show that both samples appear to order ferromagnetically in an applied magnetic field below a T_C of around 150 K (Co) and 130 K (Mn) (Figure 3.63). This is not seen in the neutron diffraction data, presumably because the data were not recorded in an applied field. This could either be due to a ferromagnetic impurity present in both samples, or to the compounds themselves showing ferromagnetic ordering in a field. The presence of events around these temperatures in the behaviour of other structural parameters suggests that the

latter is the case. The clear discontinuity in the behaviour of the U_{33} parameter for O(2) in the M = Mn sample is perhaps the clearest evidence. The $La_2O_3Mn_2Se_2$ c cell parameter also has a clear discontinuity around this point. For M = Co the c/a ratio shows a large change at this point. The La–O distance for $La_2O_3Mn_2Se_2$ shows a large discontinuity at 130 K, giving further evidence for a subtle phase transition at this temperature.

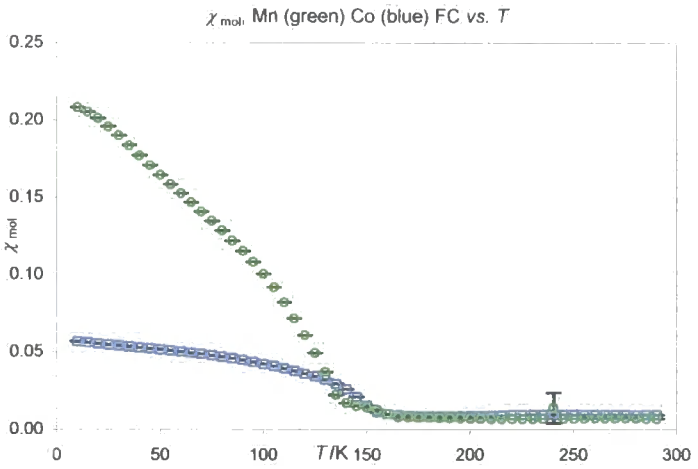

Figure 3.63 FC χ_{mol} for $La_2O_3M_2Se_2$ (M = Mn (green), Co (blue))

This phase transition must be relatively subtle as no extra peaks (indicating either a superstructure or loss of symmetry) or peak-splitting can seen in the low temperature neutron or X-ray diffraction patterns. The effect is still significant, however, as above this temperature the compounds do not exhibit ferromagnetic ordering, even in an applied field. Clearly there is a complex interplay between structural and magnetic properties in these materials.

3.5 References

(1) Mayer, J. M.; Schneemeyer, L. F.; Siegrist, T.; Waszczak, J. V. and Vandover, B. *Angew. Chem.-Int. Edit. Engl.*, **1992**, *31*, 1645-1647.

(2) In;; NIST Specification Certificate for Silicon (SRM640c), http://patapasco.nist.gov/srmcatalog/common/view_cert.cfm?srm=640c.

(3) Evans, J. S. O., *phenixlogfile - a Fortran routine for extracting average temperatures from PheniX logfiles.*, 2000.

(4) Wang, K. and Reeber, R. R. *Philos. Mag. A-Phys. Condens. Matter Struct. Defect Mech. Prop.*, **2000**, *80*, 1629-1643.

(5) Larson, A. C. and von Dreele, R. B., *GSAS - General Structure Analysis System, powder data refinement program for UNIX systems*, Los Alamos National Laboratory, Los Alamos, NM, USA, 1998.

(6) Wills, A. S. *Physica B*, **2000**, *276*, 680-681.

(7) Goodenough, J. B. *Magnetism and the Chemical Bond*; John Wiley and Sons: New York-London, 1963.

(8) Kittel, C. *Introduction to Solid State Physics*; 3rd ed.; John Wiley and Sons, Inc.: London.

Chapter 4 $A_2MCu_2O_2X_2$ compounds (A = Sr, Ba; M = Mn, Fe, Co, Ni, Zn; X = S, Se)

4.1 Introduction

This chapter discusses the properties of the $A_2MCu_2O_2X_2$ (A = Sr, Ba; M = Mn, Fe, Co, Ni, Zn; X = S, Se) family of compounds as investigated by variable temperature powder X-ray diffraction, SQUID magnetometry and conductivity. The experimental techniques and equipment used, together with synthetic methods, are described in Chapter 2. Summary sheets to aid the reader, containing the results of each experimental technique for each compound, can be found in Appendices 1.3 – 1.12. Also, many of the results are tabulated in the conclusions in Section 4.6 below.

The $A_2MCu_2O_2X_2$ compounds mentioned above are all isostructural. Their structures have spacegroup *I4/mmm* (*no.* 139) with an *a* cell parameter between 3.989 and 4.190 Å and *c* between 17.740 and 19.653 Å. The structure is shown in Figure 4.1 and can be described as consisting of three different types of layers; square planar layers of M and O with MO_2 stoichiometry, layers of anti-PbO-type Cu_2X_2 and a separating layer of A^{2+} cations. Figure 4.1 shows a ball and stick model on the left and a polyhedral view on the right. The polyhedral view well illustrates the Cu_2X_2 tetrahedra and MO_2 square planar layers, separated by A^{2+} cations. The structure is described in terms of atomic coordinates and site multiplicity in Table 4.1. The unusual MO_2 square planar layer is presumably stabilised by the rigidity of the Cu_2X_2 layer, which is observed in many other compounds (*e.g.* LaOCuS,[1] BiOCuSe[2]).

Table 4.1 Atomic fractional coordinates and multiplicity (N_p) for $A_2MCu_2O_2X_2$ compounds.

Site	N_p	x/a	y/b	z/c
A	4	½	½	~0.09
Cu	4	½	0	¼
M	2	0	0	0
X	4	0	0	~0.17
O	4	½	0	0

The target of this work was to synthesise the Sr and Ba compounds of different transition metal oxysulfides and oxyselenides. Table 4.2 summarises the results of the syntheses which are described in Section 2.1.2; which compounds were synthesised with the necessary purity to carry out rigorous physical property measurement experiments (marked with a "✓") and which were not. This also shows which compounds have been reported in the literature (see Section 1.2.3 and also the relevant sections in this chapter for more information). It is notable that no M = Fe containing compounds were synthesised with even reasonable purity, despite the stability of $La_2O_3Fe_2X_2$ (X = S, Se).

Table 4.2 Summary of synthetic results, E = existing compound, ✓ = synthesised.

M \ *AX*	BaS	BaSe	SrS	SrSe
Mn		✓	E^3	✓
Fe				
Co	E^4 ✓	✓	E^4 ✓	✓
Ni		✓	E^5	✓
Zn			E^3 ✓	✓

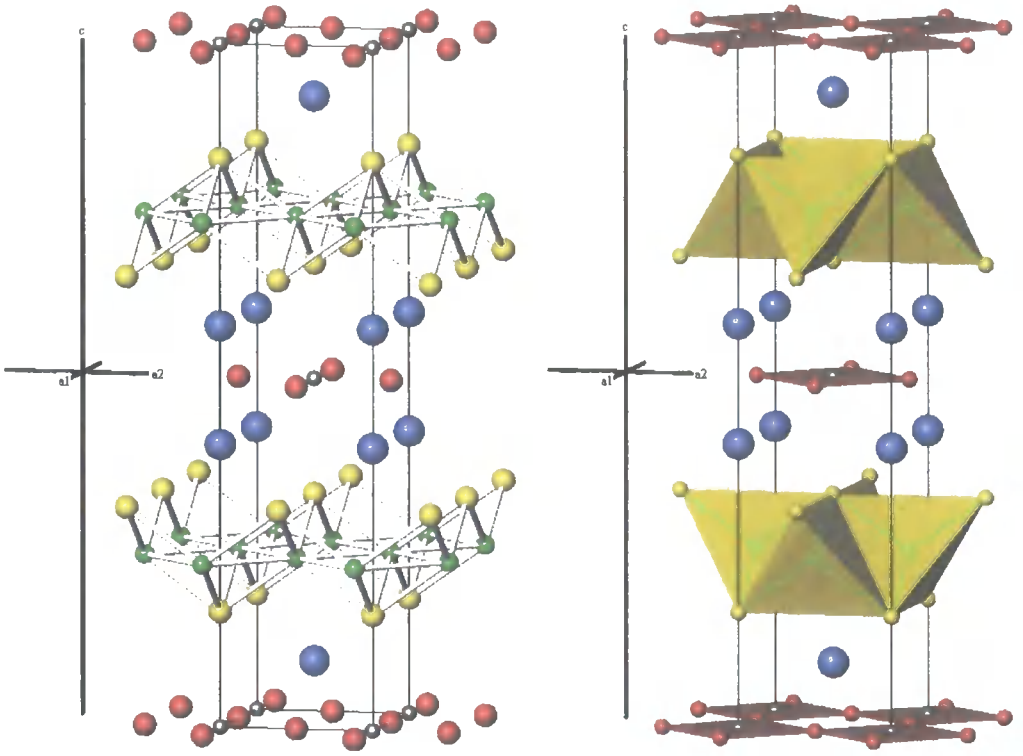

Figure 4.1 Structure of $A_2MCu_2O_2X_2$. *A* atoms in grey, *M* atoms in blue, Cu atoms in green, O atoms in red and *X* atoms in yellow. Ball and stick view on left, polyhedra on right. Polyhedra are coloured according to metal atom contained.

As Chapter 3 shows, layered oxychalcogenide compounds can show interesting structural, magnetic and conducting behaviour as a function of temperature. In order to fully characterise the structures and physical properties of the materials highlighted in Table 4.2 the following experiments were undertaken: Rietveld refinements performed on room temperature powder X-ray diffraction data, PheniX variable temperature (typically 17 – 300 K) powder X-ray diffraction experiments, variable temperature zero- and field-cooled SQUID (typically 10 – 290 K) experiments and variable temperature (typically 80 – 300 K) conductivity experiments. No magnetic experiments were performed on the *M* = Zn containing compounds as they were expected to show no interesting behaviour due to Zn^{2+} being a d^{10} ion with a closed valence shell. The experiments performed are summarised in Table 4.3 and described in the Experimental chapter, sections 2.2 – 2.4.

Table 4.3 Summary of experiments discussed in this chapter.

Compound	RT Rietveld	PheniX	SQUID	Conductivity
$Sr_2MnCu_2O_2Se_2$	✓	✓	✓	
$Ba_2MnCu_2O_2Se_2$	✓	✓	✓	
$Sr_2CoCu_2O_2S_2$	✓	✓	✓	
$Sr_2CoCu_2O_2Se_2$	✓	✓	✓	✓
$Ba_2CoCu_2O_2S_2$	✓	✓	✓	✓
$Ba_2CoCu_2O_2Se_2$	✓	✓	✓	✓
$Sr_2NiCu_2O_2Se_2$	✓	✓	✓	✓
$Ba_2NiCu_2O_2Se_2$	✓	✓	✓	
$Sr_2ZnCu_2O_2S_2$	✓	✓		
$Sr_2ZnCu_2O_2Se_2$	✓	✓		

This chapter is ordered in terms of the different compounds studied rather than experimental technique in order to more clearly discuss the properties of each compound. However, there is discussion in the conclusion (section 4.6) of this chapter in terms of the different properties investigated. The chapter is ordered first in terms of the transition metal *M*, then the cation *A*, then the anion *X*.

4.2 Mn containing phases

The synthesis of $A_2MCu_2O_2X_2$ phases with *M* = Mn; *A* = Sr, Ba; *X* = S, Se was attempted. The *X* = Se containing compounds were synthesised with high purity and physical properties were measured. The results for these are presented and discussed in Sections 4.2.1 and 4.2.2 below. The *X* = S compounds contained many different impurities, such as the starting reagent, *AX* and oxides such as MnO, or $Ba(SO_4)$. While the percentage values from the refinement shown in Figure 4.2 are from a short purity-checking scan (~1 hour) and not fully quantitative, they do show that the sample was very impure and give a rough estimate of the high levels of impurity present.

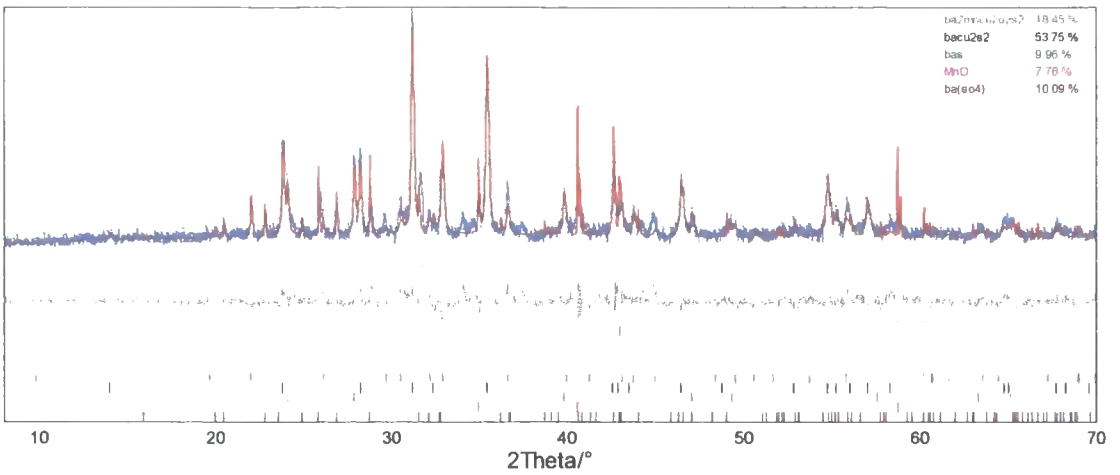

Figure 4.2 A powder X-ray diffraction pattern of $Ba_2MnCu_2O_2S_2$ showing the impurities present. Observed pattern in blue, calculated in red and difference in grey. Tick marks are predicted peak positions for $Ba_2MnCu_2O_2S_2$, $BaCu_2S_2$, BaS, MnO and $Ba(SO_4)$ from top to bottom respectively.

4.2.1 $Sr_2MnCu_2O_2Se_2$

$Sr_2MnCu_2O_2Se_2$ was synthesised as discussed in Section 2.1.2, with the difference from the "standard" synthesis being that it was heated to 850 °C rather than 800 °C as the majority of the $A_2MCu_2O_2X_2$ compounds were. It was a very dark grey to black colour when synthesised and was made by two cycles of pressing into pellets and heating. It was characterised by powder X-ray diffraction using the Siemens D5000 diffractometer and its structure confirmed by Rietveld refinement, as shown in Figure 4.3. There are a number of small impurity peaks present, notably around 25 ° 2θ and one around 12 ° 2θ, but these are only minor. From experience of more impure samples (*e.g.* Figure 4.2) this unknown impurity is estimated to be in the $\leq$ 5 % range. The relatively large amorphous background visible between 10 and 20 ° 2θ in Figure 4.3 (and throughout this chapter in the other figures presenting data from the D5000) is due to the sample being sprinkled on a Vaseline covered glass disc held within the plastic sample holder. Thirty six parameters were refined for these Rietveld refinements: an 18 order Chebychev polynomial function was used to fit the background radiation, 2 instrument corrections (the sample height displacement and a simple axial model), 1 scale factor for the phase, 6 pseudo Voigt peak shape parameters, 2 lattice parameters (*a* and *c*), 2 atomic positions (Sr and Se *z* coordinates) and 5 atomic displacement parameters (B_{iso}). The ${}_wR_p$ for the refinement was 9.87 %, χ^2 2.34 and R_{Bragg} for the phase was 5.10 %. Details of refined parameters are given in Table 4.4.

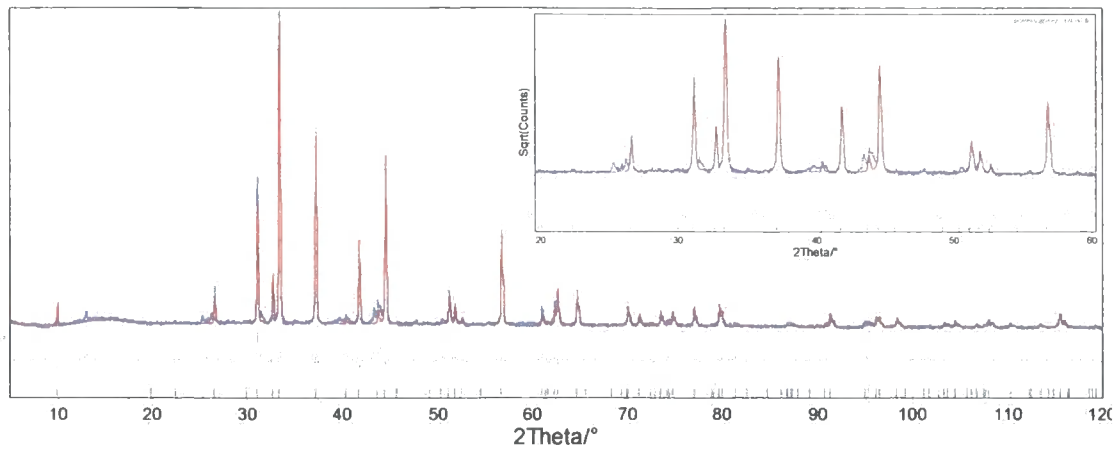

Figure 4.3 Rietveld refinement of $Sr_2MnCu_2O_2Se_2$. Observed pattern in blue, calculated in red and difference in grey. The vertical tick marks show predicted peak positions and the inset shows 20 – 60 ° 2θ region on a square root (counts) scale to emphasise weaker features in the pattern.

It was suggested by Zhu and Hor[4] that some of these compounds might be copper deficient. To test this possibility the occupancy of the Cu site was refined with the displacement parameters (B_{iso}) of all atoms constrained to be the same value. This improved the ${}_wR_p$ to 8.55 % and the R_{Bragg} to 2.75 % with two fewer parameters refined; only 34, with the Cu site occupancy falling to 0.747(5) atoms per site. The constrained B_{iso} for all atoms refined to 1.001(42). As this makes only a small difference to the structural model used in refinements, a Cu site occupancy of one was used in the refinements discussed in the following sections. However, further discussion about this copper deficiency can be found in the concluding part of this chapter (Section 4.6), together with *R*-factors and refined parameters for the other compounds.

Table 4.4 Results of room temperature Rietveld refinement for $Sr_2MnCu_2O_2Se_2$.

$Sr_2MnCu_2O_2Se_2$	NDW313
Spacegroup	*I4/mmm*
a cell parameter/Å	4.073165(81)
c cell parameter/Å	17.88003(54)
Sr *z* coordinate/*c*	0.0928(1)
Se *z* coordinate/*c*	0.1672(2)
Sr B_{iso}/Å^2	0.57(9)
Cu B_{iso}/Å^2	6.02(20)
Mn B_{iso}/Å^2	1.49(20)
Se B_{iso}/Å^2	0.77(10)
O B_{iso}/Å^2	-1.43(35)
${}_wR_p$/%	9.87
R_{Bragg}/%	5.10
χ^2	4.22
No. of parameters	31

As can be seen from Table 4.4 the atomic displacement parameter (B_{iso}) for Cu is very large (6.02(20) Å^2) and negative for O (-1.43(35) Å^2) indicative of problems with the refinement.

However, the possible Cu deficiency, the sprinkled nature of the sample (not providing the smooth surface required for accurate thermal parameter determination) and the fewer electrons in oxygen compared to other, heavier elements will affect these. Similar effects can be seen in the room temperature B_{iso} values for the other compounds discussed in this chapter.

Variable temperature powder X-ray diffraction experiments were performed on this compound using a Bruker D8 diffractometer with PheniX He ccr attachment (Section 2.2.5). Sample NDW297 was studied in experiments d8_02444 and d8_02446. In experiment number d8_02444 it was cooled at 14 K hr^{-1} and data collected over a 5 – 120 ° 2θ range in 30 minute time slices. Seven 30 minute scans were performed at the base temperature and summed together, giving the equivalent of one 3.5 hour data collection. In experiment d8_02446 the sample was then heated at 17 K hr^{-1} to 300 K and data collected using the same range and collection time as experiment d8_02444. Six 30 minute scans were performed at 300 K and summed together.

The data were analysed using the *multitopas* methodology described in Section 2.2.6. Figure 4.4 shows the variation of the *a* cell parameter with temperature and Figure 4.5 shows the *c* cell parameter. A simple model of the thermal expansion has been fitted to these data, and is shown in the figures as a solid grey line. The expression used is shown in Equation 4.1, where *a* is the cell parameter, a_0 the ideal cell parameter at 0 K, *T* the temperature, θ_i the *i*th Einstein temperature and C_i the *i*th Gruneisen parameter. A satisfactory fit to the data could be obtained without the second term (*i.e.* with $C_2 = 0$) for the phases studied. The second term was, however, required to fit the thermal expansion of the aluminium sample holder (see below). These curves are intended primarily as "guides to the eye" and to highlight any marked deviations from smooth behaviour. While the various terms have a physical origin highly accurate parameters of, for example, the Einstein temperature, are not expected from these data.

$$\ln\left(\frac{a}{a_0}\right) = \frac{C_1}{\exp\left(\frac{\theta_1}{T}\right)-1} + \frac{C_2}{\exp\left(\frac{\theta_2}{T}\right)-1} \qquad \text{Equation 4.1}$$

As the sample holder in the PheniX ccr is an anodised aluminium plate it gives large peaks in the diffraction pattern and has been included in the refinements as a structure-less Pawley fit. In this way it also acts as an internal standard to verify the true cryostat temperature. The variation of the Al cell parameter (space group *Fm*3*m* {number 225}, a = 4.04992 Å at 300 K) is shown in Figure 4.6. A model of the thermal expansion was least-squares fitted to the data for a perfect Al crystal quoted by Wang and Reeber,[6] again using Equation 4.1. The values produced by this fit are shown in Table 4.5. This ideal thermal expansion curve is then

superimposed on experimental data in Figure 4.6 and subsequent figures with fixed C_n and θ_n values. Due to slight differences between the anodised aluminium plate and a perfect aluminium crystal the term a_0 was refined for each experiment; the values are tabulated at the end of this chapter in Section 4.6.2.

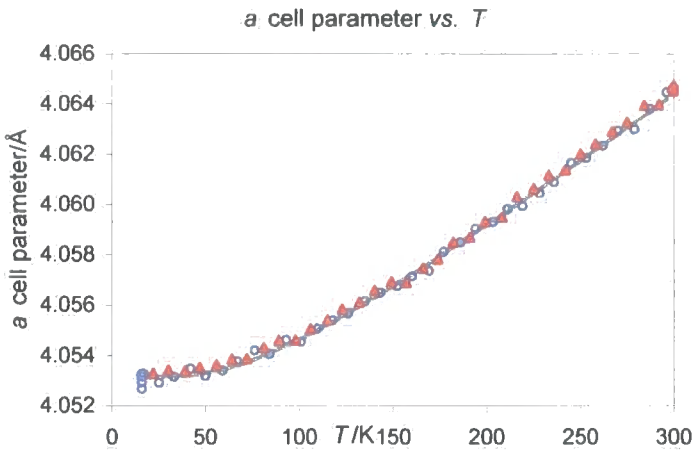

Figure 4.4 $Sr_2MnCu_2O_2Se_2$ *a* cell parameter against temperature. Cooling data are open blue circles, heating filled red triangles, fit to the experimental data using Equation 4.1 and the values in Table 4.5 in grey.

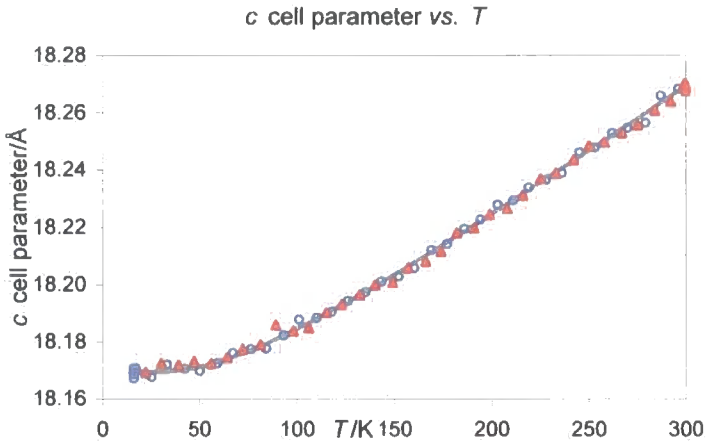

Figure 4.5 $Sr_2MnCu_2O_2Se_2$ *c* cell parameter against temperature. Cooling data are open blue circles, heating filled red triangles, fit to the experimental data using Equation 4.1 and the values in Table 4.5 in grey.

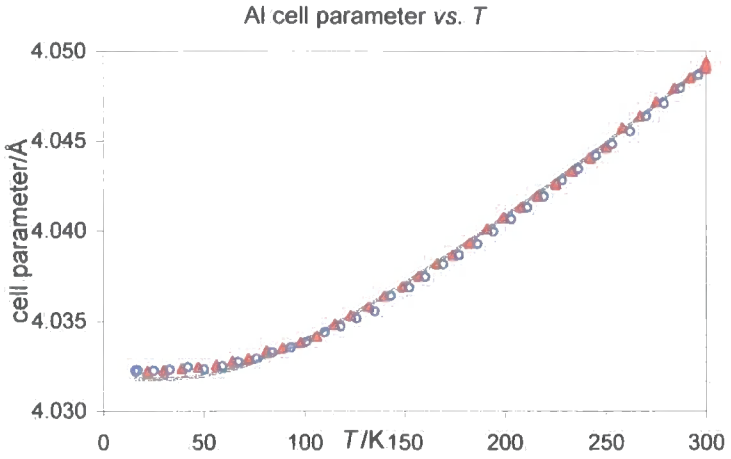

Figure 4.6 Aluminium cell parameter against temperature. Cooling data are open blue circles, heating filled red triangles, Wang and Reeber's data in grey.

The cell parameter plots show that the unit cell expands smoothly on heating and that there is no evidence for any phase transitions. The data points very closely match the fitted expansion expression, with the parameters determined by a least-squares fit shown in Table 4.5. together with α, as defined in Equation 4.2 where a is the cell parameter at temperature T and a_0 the cell parameter at temperature T_0.

$$\alpha_1 = \frac{\left[\frac{(a-a_0)}{a_0}\right]}{T-T_0} \qquad \text{Equation 4.2}$$

Table 4.5 Thermal expansion data from PheniX experiments on $Sr_2MnCu_2O_2Se_2$.

	a_0/Å	θ_1/K	$C_1/10^{-6}$	θ_2/K	$C_2/10^{-6}$	$\alpha_{(300\text{-}15K)}/10^{-6}$ K^{-1}
a	4.05315(5)	223(9)	13. 7(3)			9.7(3)
c	18.16950(43)	196(8)	25.8(4)			19.3(4)
Al	4.03229(26)	231(31)	21(2)	1459(200)	13(1)	15(2)

The Rietveld refinement performed on the summed data set from 17 K is shown in Figure 4.7 (the *y* scale is a square root (counts) scale because the pattern is dominated by the scatter from the Al sample holder. The other figures showing Rietveld refinements from PheniX data in this chapter also use either a square root (counts) or ln (counts) scale). The calculated patterns show a good fit to the observed and give the following cell parameters: a = 4.05314(9) Å c = 18.16891(60) Å at 17 K and a = 4.06469(10) Å and c = 18.26874(62) Å at 300 K. The *R*-factors were ${}_wR_p$ = 16.58 and 16.27 % and R_{Bragg} 9.68 and 9.81 % at 17 and 300 K respectively. Other important structural least-squares parameters are summarised in Table 4.6 for the refinements performed on the long scans at 17 and 300 K.

Table 4.6 Atomic fractional coordinates for $Sr_2MnCu_2O_2Se_2$ at 17 and 300 K.

Site	*z/c* (17 K)	*z/c* (300 K)
Sr	0.0921(2)	0.0922(2)
Cu	0.25	0.25
Mn	0	0
Se	0.1671(2)	0.1672(2)
O	0	0

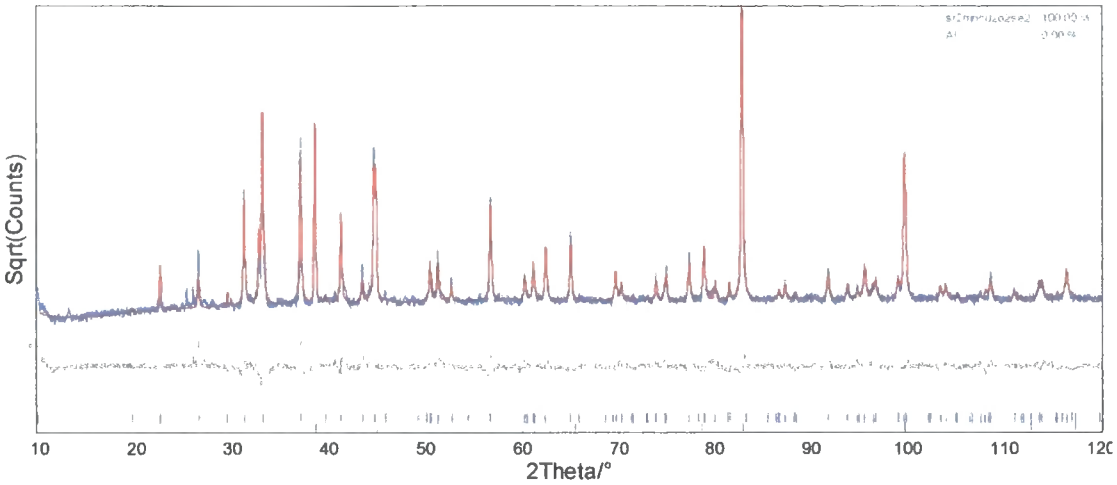

Figure 4.7 Rietveld refinement at 17 K of $Sr_2MnCu_2O_2Se_2$. Observed pattern in blue, calculated in red, difference in grey. Tick marks show predicted peak positions for $Sr_2MnCu_2O_2Se_2$ and Al from top to bottom respectively.

Within experimental error, there is no difference between the *z* coordinates at 17 and 300 K of either the Sr or Se atoms (the only two atomic coordinates in the structure which are not fixed by symmetry). They are also very similar (only differing in the 4th decimal place) to the values from the room temperature d5000 Rietveld refinements given in Table 4.4. Together with the smooth change in lattice parameters this is an indication that there is no significant structural change beyond normal thermal expansion between 17 and 300 K.

Part of a pellet of sample number NDW326 was magnetically characterised by SQUID magnetometry using the sample preparation and experimental technique described in Section 2.3. Zero field cooled (ZFC) and field cooled (FC) experiments were conducted on this sample in a field of 100 Oe with measurements taken in 5 K steps from 10 – 290 K and the results are shown in Figure 4.8. A magnetisation *vs.* applied field experiment was also performed at 290 K, and the results are shown in Figure 4.9. It is a straight line, going through the origin, indicating that the compound is paramagnetic with no significant ferromagnetic impurities.

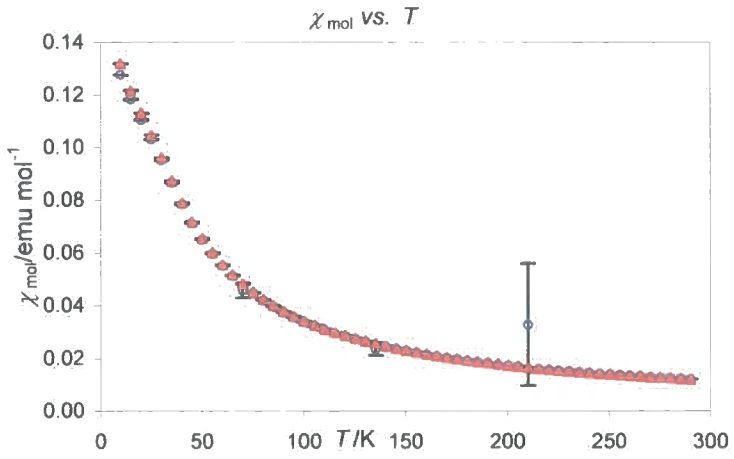

Figure 4.8 ZFC (open blue circles) and FC (filled red triangles) data for $Sr_2MnCu_2O_2Se_2$. The point at 210 K can be considered to follow the observed trend due to its associated error.

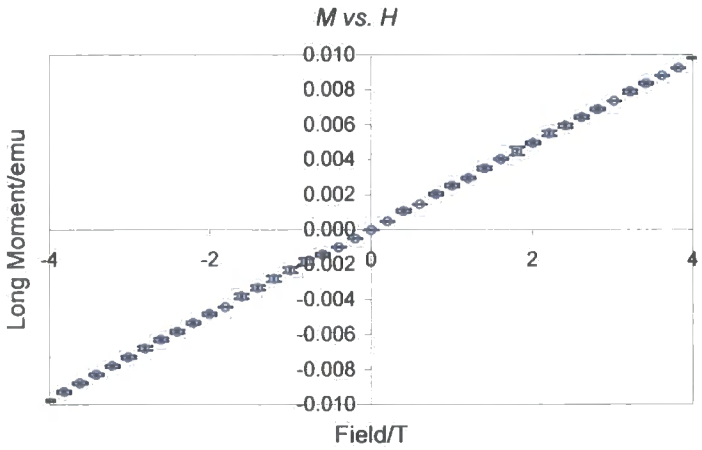

Figure 4.9 Magnetisation against applied field for $Sr_2MnCu_2O_2Se_2$.

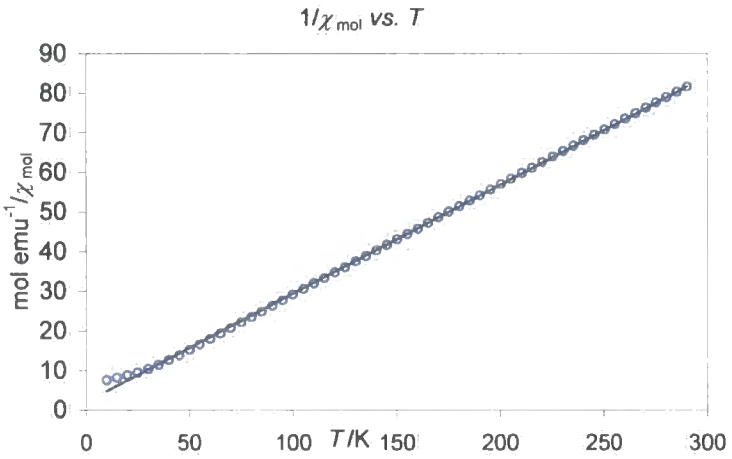

Figure 4.10 Graph of $1/\chi_{mol}$ (open blue circles) for $Sr_2MnCu_2O_2Se_2$ Curie-Weiss fit in black.

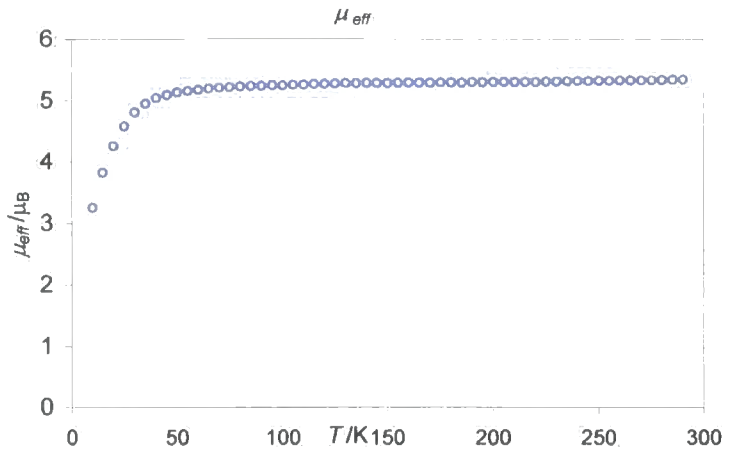

Figure 4.11 μ_{eff} for $Sr_2MnCu_2O_2Se_2$.

Figure 4.8 shows that both FC and ZFC sets of data closely match and appear to follow Curie-Weiss law behaviour. This is described by Equation 4.3, where χ is the susceptibility, C the Curie constant, T the temperature, θ the Curie temperature and χ_{TIP} and χ_{DIA} are the temperature-independent and diamagnetic components of the susceptibility respectively. There is some suggestion from the plot (Figure 4.10) of $1/\chi_{mol}$ against T that the susceptibility departs from the Curie-Weiss behaviour at very low temperature. A few of the lower temperature points of the ZFC data appear to be slightly lower than the FC values at the same temperatures. This could be due to a small amount of ordering occurring in the field-cooled experiment at these very low temperatures.

$$\chi = \frac{C}{T-\theta} + \chi_{TIP} + \chi_{DIA} \qquad \text{Equation 4.3}$$

A least squares fit to Equation 4.3 of the data from 300 to 30 K is shown in Figure 4.10 and gives μ_{eff} = 5.369(2) μ_B, θ = -4.92(9) K and the temperature independent correction (χ_{TIP} + χ_{DIA}) = -1.16(3) x 10^{-4} emu mol^{-1}. Figure 4.11 shows μ_{eff} against temperature, which is nearly constant until ~50 K, below which it falls. The value of 5.369(2) μ_B is less than the ideal value of 5.9 μ_B for a Mn^{2+} ion.

4.2.2 $Ba_2MnCu_2O_2Se_2$

$Ba_2MnCu_2O_2Se_2$ was synthesised as discussed in Section 2.1.2, from re-heating a pellet of previously synthesised sample to 800 °C. The resulting dark grey to black powder was characterised by powder X-ray diffraction using the Siemens D5000 diffractometer and its structure confirmed by Rietveld refinement, as shown in Figure 4.12. There are a few small impurity peaks present, notably around 24 ° 2θ, but these are only minor (< 5 %). The

refinement resulted in a ${}_wR_p$ of 8.45 %, χ^2 1.56 and R_{Bragg} of 2.45 %. Details of the important parameters from this refinement are given in Table 4.7.

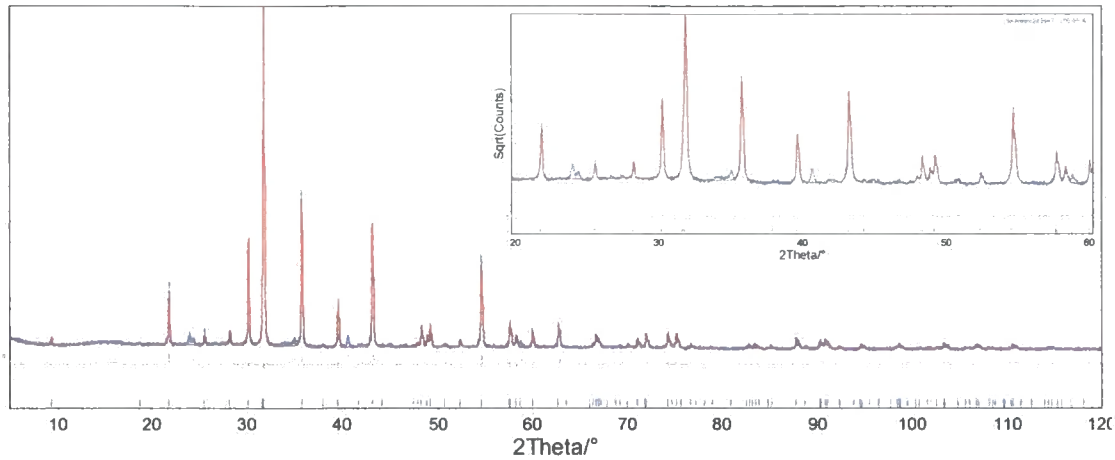

Figure 4.12 Rietveld refinement of $Ba_2MnCu_2O_2Se_2$. Observed pattern in blue, calculated in red and difference in grey. The vertical tick marks show predicted peak positions and the inset shows 20 – 60 ° 2θ region on a square root (counts) scale to emphasise weaker features.

Table 4.7 Results of room temperature Rietveld refinement for $Ba_2MnCu_2O_2Se_2$.

$Ba_2MnCu_2O_2Se_2$	NDW325
Spacegroup	*I4/mmm*
a cell parameter/Å	4.189509(72)
c cell parameter/Å	18.99183(46)
Ba *z* coordinate/*c*	0.09267(9)
Se *z* coordinate/*c*	0.1749(2)
Ba B_{iso}/Å^2	1.17(5)
Cu B_{iso}/Å^2	2.12(12)
Mn B_{iso}/Å^2	4.88(23)
Se B_{iso}/Å^2	1.70(9)
O B_{iso}/Å^2	1.63(49)
${}_wR_p$/%	8.45
R_{Bragg}/%	2.45
χ^2	1.56
No. of parameters	36

Variable temperature powder X-ray diffraction experiments were performed on this compound using a Bruker D8 diffractometer with PheniX He ccr attachment (Section 2.2.5). Sample NDW287 was studied in experiments d8_02308 and d8_02309. In experiment d8_02308 it was cooled at 17 K hr^{-1} and data collected over a 5 – 120 ° 2θ range in 30 minute time slices. Fifteen 30 minute scans were performed at base temperature and summed together, giving the equivalent of one 7.5 hour data collection. In experiment d8_02309 the sample was then heated at 5 K hr^{-1} to 300K and data collected over the same 2θ range in 60 minute time slices. Ten 1 hour scans were performed at 300 K and summed together.

The data were analysed using the *multitopas* methodology described in Section 2.2.6. Figure 4.13 shows the variation of the *a* cell parameter with temperature and Figure 4.14 shows the *c* cell parameter. The variation of the Al cell parameter is shown in Figure 4.15 together with

the fit to Wang and Reeber's data[6] as a grey line, which both cooling and heating data closely match.

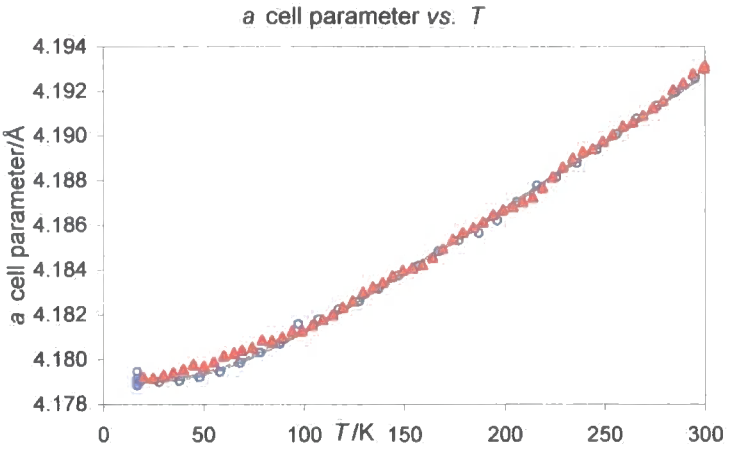

Figure 4.13 $Ba_2MnCu_2O_2Se_2$ *a* cell parameter against temperature. Cooling data are open blue circles, heating filled red triangles, fit to the experimental data using Equation 4.1 and the values in Table 4.8 in grey.

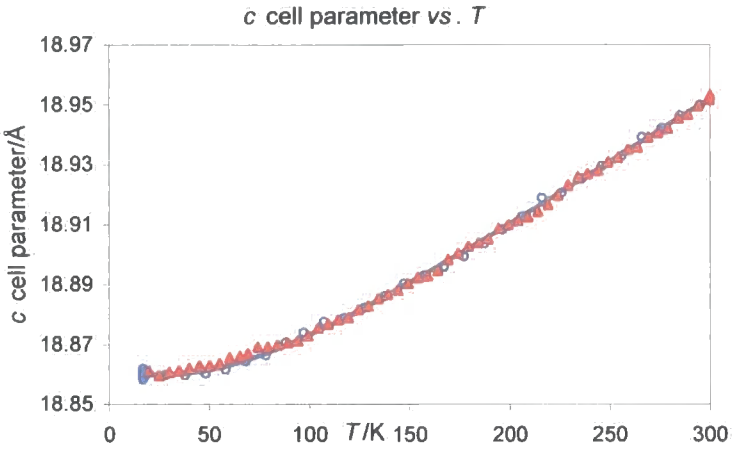

Figure 4.14 $Ba_2MnCu_2O_2Se_2$ *c* cell parameter against temperature. Cooling data are open blue circles, heating filled red triangles, fit to the experimental data using Equation 4.1 and the values in Table 4.8 in grey.

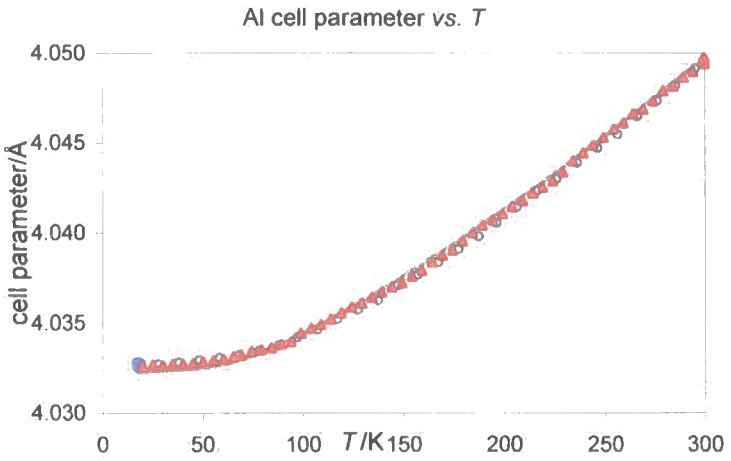

Figure 4.15 Aluminium cell parameter against temperature. Cooling data are open blue circles, heating filled red triangles, Wang and Reeber's data in grey.

The cell parameter plots show that the unit cell expands smoothly on heating and that no phase transitions are visible. The data points very closely match the fitted expansion expression, with parameters used in the least-squares fit shown in Table 4.8. There is perhaps some suggestion that the *a* cell parameter obtained on warming is a slightly higher than on cooling between ~20 and 100 K, but discrepancies are small.

Table 4.8 Thermal expansion data from PheniX experiments on $Ba_2MnCu_2O_2Se_2$.

	a_0/Å	θ_1/K	$C_1/10^{-6}$	$\alpha_{(300\text{-}15K)}/10^{-6}$ K^{-1}
a	4.17905(4)	181(6)	15.0(2)	11.5(2)
c	18.85997(23)	206(6)	23.4(3)	17.2(3)

The Rietveld refinements performed on the summed data sets at 17 K are shown in Figure 4.16. The Rietveld refinements at 17 and 300 K show a good fit to the observed data and give the following cell parameters: a = 4.17908(5) Å, c = 18.86014(31) Å at 17 K; a = 4.19300(5) Å, c = 18.95165(32) Å at 300 K. The *R*-factors were ${}_wR_p$ = 10.067 and 9.72 % and R_{Bragg} 3.64 and 3.31 % at 17 and 300 K respectively. Other important structural least-squares parameters are summarised in Table 4.9 for the refinements performed on the long scans at 17 and 300 K.

Table 4.9 Atomic fractional coordinates and displacement parameter values for $Ba_2MnCu_2O_2Se_2$ at 17 and 300 K.

Site	z/c (17 K)	z/c (300 K)	B_{iso}/Å^2 (17 K)	B_{iso}/Å^2 (300 K)
Ba	0.09374(8)	0.09358(8)	-1.47(4)	-0.80(5)
Cu	0.25	0.25	-1.27(9)	0.34(11)
Mn	0	0	1.48(19)	2.40(21)
Se	0.1747(3)	0.1747(1)	-1.55(7)	-0.85(8)
O	0	0	-0.81(38)	-1.33(36)

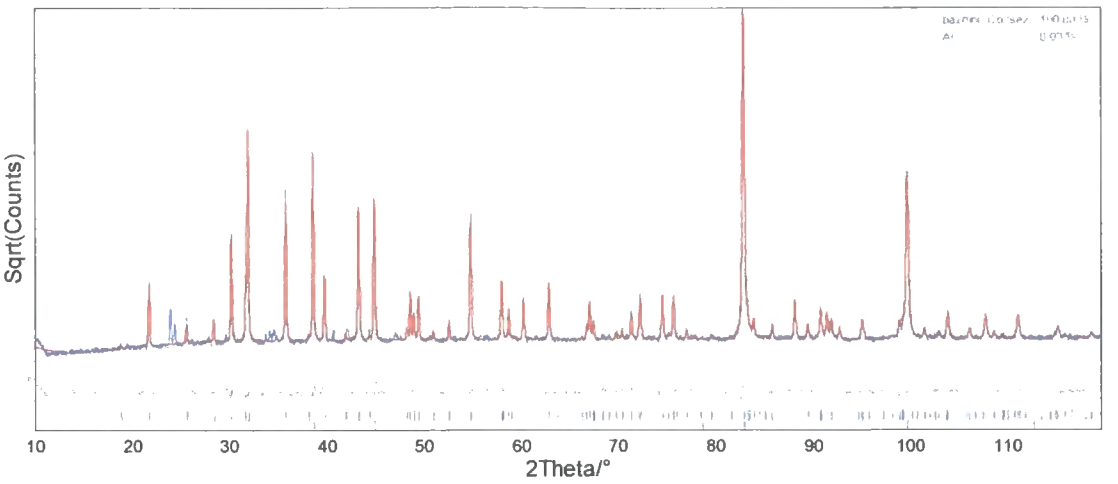

Figure 4.16 Rietveld refinement at 17 K of $Ba_2MnCu_2O_2Se_2$. Observed pattern in blue, calculated in red, difference in grey. Tick marks show predicted peak positions for $Ba_2MnCu_2O_2Se_2$ and Al from top to bottom respectively.

Within experimental error, there is very little difference between the *z* coordinates at 17 and 300 K of either the Ba or Se atoms. They are also very similar (again only differing in the 4th decimal place) to the values from the room temperature d5000 Rietveld refinements given in Table 4.7. Together with the smooth change in lattice parameters this is an indication that there is no significant structural change beyond normal thermal expansion between 17 and 300 K.

Part of a pellet of sample number NDW325 was magnetically characterised by SQUID magnetometry using the sample preparation and experimental technique described in Section 2.3. Zero field cooled (ZFC) and field cooled (FC) experiments were conducted on this sample in a field of 100 Oe with measurements taken at 5 K steps from 10 – 290 K and the results shown in Figure 4.17. The lowest temperature point of the ZFC data appears to be significantly lower than the FC value at the same temperature, but inspection shows a significant error bar on this point, which shows that within experimental error it has a similar value. By comparison, the error bars of the measurements at all other temperatures are smaller than the points on the graph.

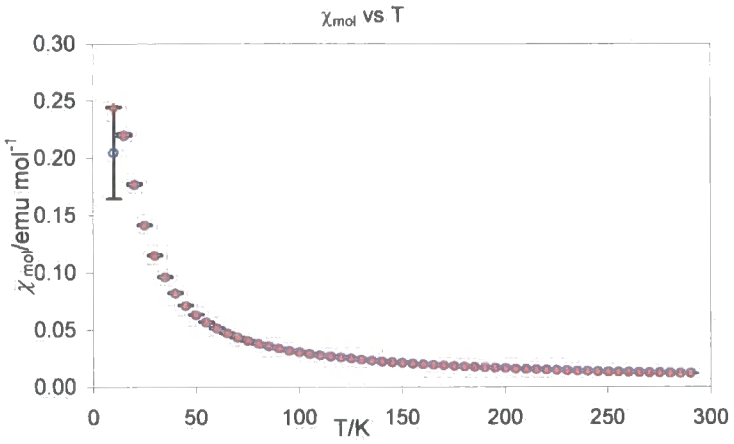

Figure 4.17 ZFC (open blue circles) and FC (filled red triangles) data for $Ba_2MnCu_2O_2Se_2$.

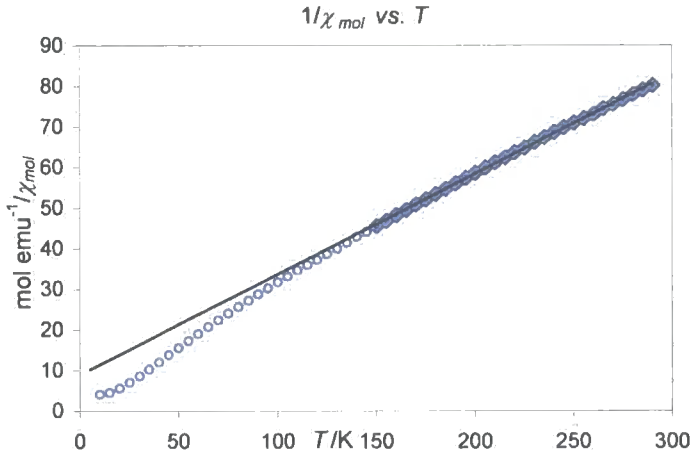

Figure 4.18 A graph of $1/\chi_{mol}$ for $Ba_2MnCu_2O_2Se_2$ observed points in blue, Curie Weiss fit in black.

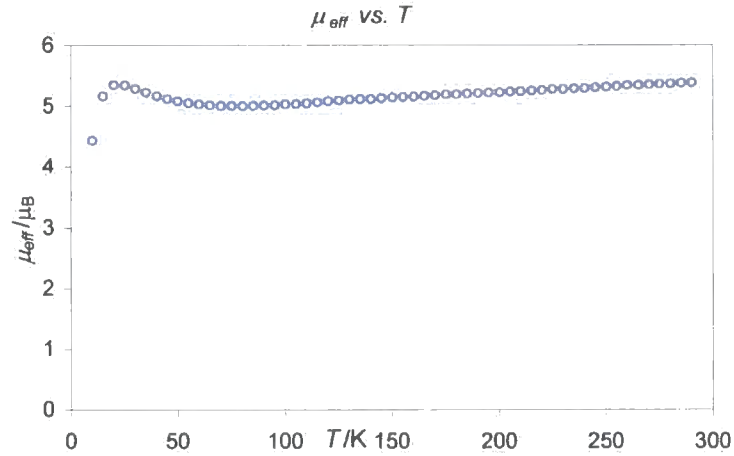

Figure 4.19 A graph of μ_{eff} *vs.* T for $Ba_2MnCu_2O_2Se_2$.

Figure 4.17 shows that both sets of data closely match and appear to follow Curie-Weiss law behaviour. However, a plot (Figure 4.18) of $1/\chi_{mol}$ against T with a least-squares fit to

Equation 4.3 indicates that, while this is true above ~100 K, there is perhaps some deviation below this temperature. The fit gives μ_{eff} = 5.23(3) μ_B, θ = -0.642(1.280) K and temperature independent correction = -6.01(4) x 10^{-4} emu mol^{-1}. Figure 4.19 shows μ_{eff} against temperature. The value of 5.23(3) μ_B is less than the ideal value of 5.9 μ_B for a Mn^{2+} ion.

4.2.3 *M* = Mn conclusions

In summary, $Sr_2MnCu_2O_2Se_2$ and $Ba_2MnCu_2O_2Se_2$ have been synthesised with high phase purity and their structural and magnetic properties examined as a function of temperature by powder X-ray diffraction and SQUID magnetometry. No phase changes have been observed between 10 and 300 K. The thermal expansion expressions give an Einstein temperature of between around 180 and 220 K for both *a* and *c* parameters of both compounds. The thermal expansion parameters α are 9.7(3) and 11.5(2) x 10^{-6} K^{-1}, and 19.3(4) and 17.2(3) x 10^{-6} K^{-1} for *a* and *c* parameters of both compounds respectively. The materials appear to be paramagnetic with μ_{eff} 5.369(2) and 5.23(3) μ_B for the two compounds and θ = -4.92(9) and -1(2) K for *M* = Sr and Ba respectively. The value of ~5 μ_B for both compounds is lower than expected for Mn^{2+} as a d^5 high spin ion. The copper deficiency of these materials, discussed in Sections 4.2.1 and 4.6.1, which would have the effect of increasing the average oxidation of the Mn ions (and thus making some d^4 instead of d^5 ions), is a likely reason for this reduction.

4.3 Co containing phases

All the *A* = Sr, Ba, *X* = S, Se containing members of the *M* = Co $A_2MCu_2O_2X_2$ materials were prepared, although some problems with minor impurities persisted. They were all made at 800 °C as 5 mm pellets, whereas the purest of the other, *M* ≠ Co, compounds were made using 13 mm pellets. All the *M* = Co samples were a dark grey to black colour, apart from $Sr_2CoCu_2O_2Se_2$, which was pale grey.

4.3.1 $Sr_2CoCu_2O_2S_2$

$Sr_2CoCu_2O_2S_2$ was synthesised as discussed in Section 2.1.2, characterised by powder X-ray diffraction using the Siemens D5000 diffractometer and its structure confirmed by Rietveld refinement, as shown in Figure 4.20. The ${}_wR_p$ for the refinement was 6.66 %, χ^2 1.26 and R_{Bragg} for the phase was 2.45 %. Details of the important parameters from this refinement are given in Table 4.10.

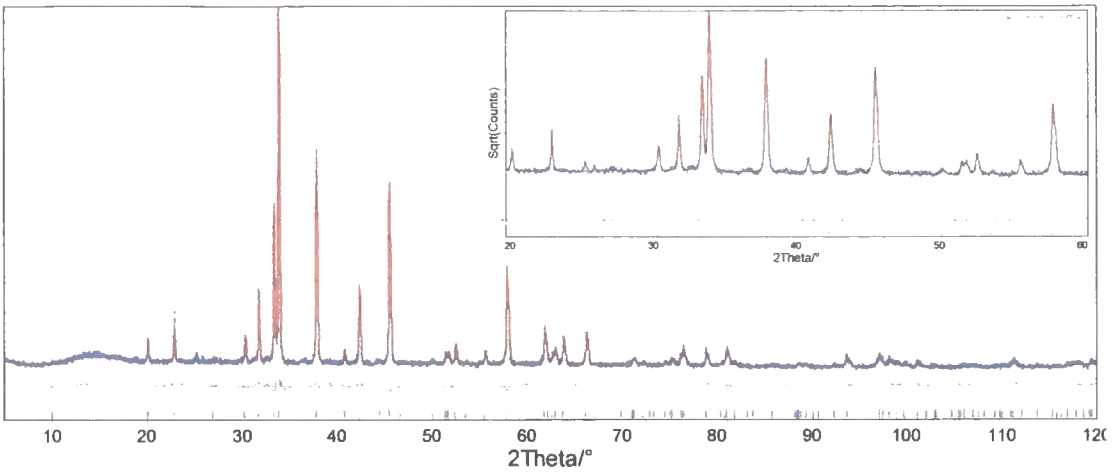

Figure 4.20 Rietveld refinement of $Sr_2CoCu_2O_2S_2$. Observed pattern in blue, calculated in red and difference in grey. The vertical tick marks show predicted peak positions and the inset shows 20 – 60 ° 2θ region on a square root (counts) scale to emphasise weaker features in the pattern.

Table 4.10 Results of room temperature Rietveld refinement for $Sr_2CoCu_2O_2S_2$.

$Sr_2CoCu_2O_2S_2$	NDW255
Spacegroup	*I4/mmm*
a cell parameter/Å	3.989105(90)
c cell parameter/Å	17.70326(55)
Sr *z* coordinate/*c*	0.09250(10)
S *z* coordinate/*c*	0.1720(2)
Sr B_{iso}/Å^2	3.41(6)
Cu B_{iso}/Å^2	4.91(8)
Co B_{iso}/Å^2	3.41(1)
S B_{iso}/Å^2	3.71(15)
O B_{iso}/Å^2	3.79(3)
$_wR_p$/%	6.66
R_{Bragg}/%	2.45
χ^2	1.26
No. of parameters	36

Variable temperature powder X-ray diffraction experiments were performed on this compound using a Bruker D8 diffractometer with PheniX He ccr attachment (Section 2.2.5). Sample NDW255 was studied in experiments d8_02302 and d8_02303. In experiment number d8_02302 it was cooled at 17 K hr^{-1} and data collected over a 5 – 120 ° 2θ range in 30 minute time slices. Only one 30 minute scan was performed at the base temperature. In experiment d8_02303 the sample was then heated at 17 K hr^{-1} to 300 K and data collected using the same range and collection time as experiment d8_02302. Five 30 minute scans were performed at 300 K and summed together.

Data were analysed using the *multitopas* methodology described in Section 2.2.6. Figure 4.21 shows the variation of the *a* cell parameter with temperature and Figure 4.22 shows the *c* cell parameter The variation of the Al cell parameter is shown in Figure 4.23. The heating data are, however, clearly systematically higher than the cooling, but both are close to the

curve showing the literature data. It is not known what has caused this behaviour. One possibility is that the Al sample holder was not tightly screwed into the PheniX stage, allowing a slight movement between the cooling and heating experiments. It is not an artefact of the seeded refinement procedure, as many attempts at using different starting models (*i.e.* from the last scan in the cooling experiment, from the summed scans at low temperature on cooling *etc*) have given exactly the same result. As the sample showed no evidence of unusual trends in all parameters with *T* this discrepancy was not investigated further.

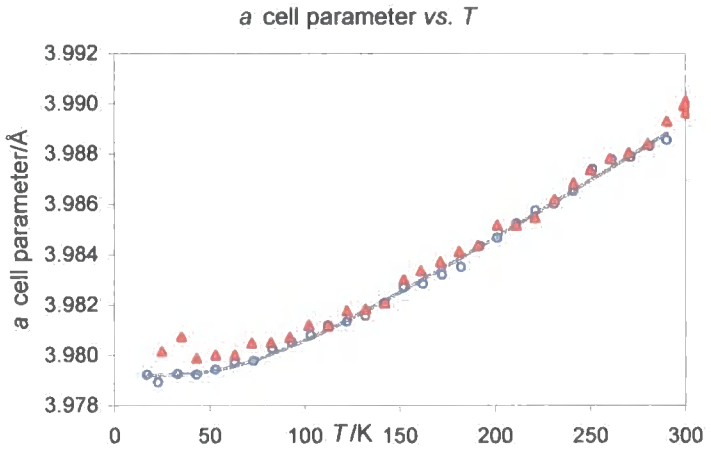

Figure 4.21 $Sr_2CoCu_2O_2S_2$ *a* cell parameter against temperature. Cooling data are open blue circles, heating filled red triangles, fit to the experimental data using Equation 4.1 and the values in Table 4.11 in grey.

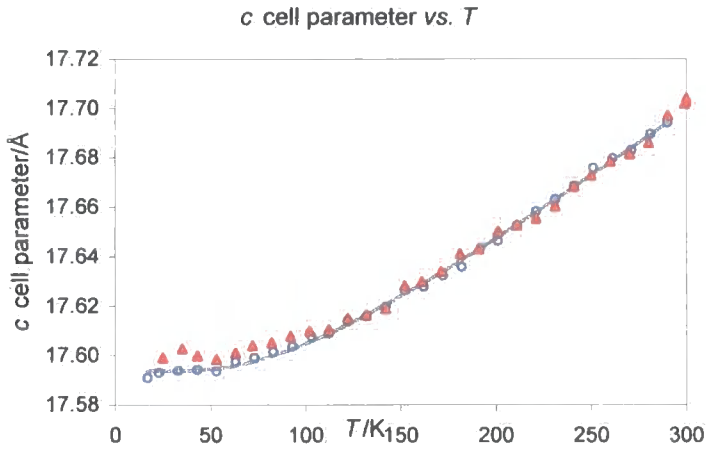

Figure 4.22 $Sr_2CoCu_2O_2S_2$ *c* cell parameter against temperature. Cooling data are open blue circles, heating filled red triangles, fit to the experimental data using Equation 4.1 and the values in Table 4.11 in grey.

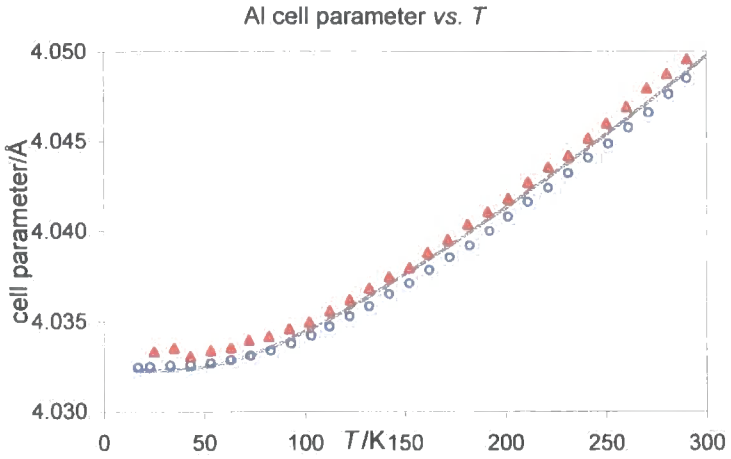

Figure 4.23 Aluminium cell parameter against temperature. Cooling data are open blue circles, heating filled red triangles, Wang and Reeber's data in grey.

This discrepancy is mirrored slightly in the *a* and *c* cell parameters of the sample which at low temperatures are higher for the heating data than for the cooling. Presumably, it is the same effect causing these anomalies and they can be assumed to be an artefact of the experiment or refinement procedure.

Table 4.11 Thermal expansion data from PheniX experiments on $Sr_2CoCu_2O_2S_2$.

	a_0/Å	θ_1/K	$C_1/10^{-6}$	$\alpha_{(300\text{-}15K)}/10^{-6}$ K^{-1}
a	3.97922(9)	217(14)	12.4(3)	8.9(4)
c	17.59383(60)	273(11)	32.6(7)	21.1(7)

The Rietveld refinement performed on the single data set at 17 K is shown in Figure 4.24. The calculated patterns show a good fit to the observed and give the following cell parameters: *a* = 3.97925(20) Å *c* = 17.59104(119) Å at 17 K and *a* = 3.98975(14) Å and *c* = 17.70172(83) Å at 300 K. The *R*-factors were $_wR_p$ = 10.08 and 7.47 % and R_{Bragg} 1.90 and 2.11 % at 17 and 300 K respectively. Other important structural least-squares parameters are summarised in Table 4.12 for the refinements performed on the scans at 17 and 300 K.

Table 4.12 Atomic fractional coordinates and displacement parameter values for $Sr_2CoCu_2O_2S_2$ at 17 and 300 K.

Site	*z*/*c* (17 K)	*z*/*c* (300 K)	B_{iso}/Å^2 (17 K)	B_{iso}/Å^2 (300 K)
Sr	0.0926(3)	0.9073(2)	-0.29(16)	0.37(14)
Cu	0.25	0.25	0.97(22)	2.00(19)
Co	0	0	0.28(32)	0.28(25)
S	0.1732(6)	0.1722(4)	-0.32(39)	-0.62(29)
O	0	0	1.91(97)	2.50(77)

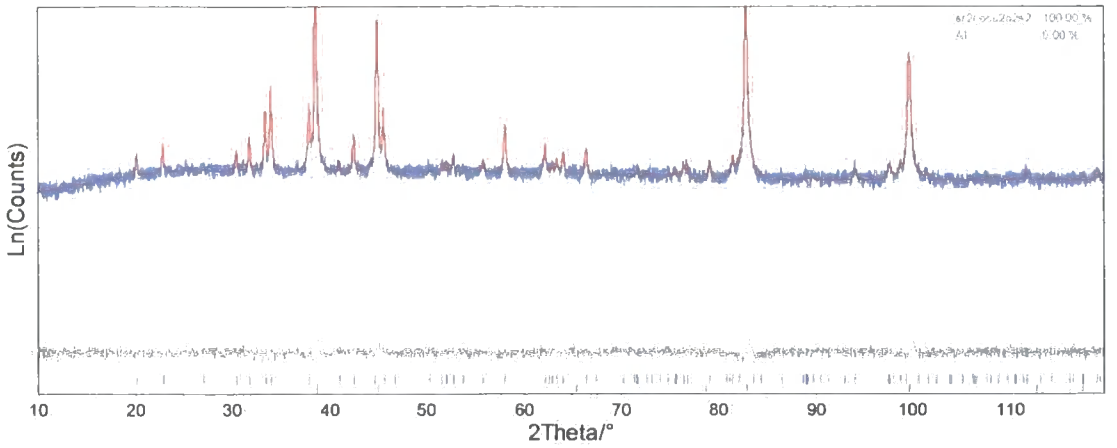

Figure 4.24 Rietveld refinement at 17 K of $Sr_2CoCu_2O_2S_2$. Observed pattern in blue, calculated in red, difference in grey. Tick marks show predicted peak positions for $Sr_2CoCu_2O_2S_2$ and Al from top to bottom respectively.

Within experimental error, there is very little difference between the *z* coordinates at 17 and 300 K of either the Sr or S atoms. They are also very similar to the values from the room temperature d5000 Rietveld refinements given in Table 4.10. Together with the smooth change in lattice parameters this is an indication that there is no significant structural change beyond normal thermal expansion between 17 and 300 K. While the B_{iso} values in Table 4.12 are better than (less negative) for other PheniX experiments, they still show a fairly large *e.s.d.* which is again due to the relatively short data collection times.

Part of a pellet of sample number NDW255b was magnetically characterised by SQUID magnetometry using the sample preparation and experimental technique described in Section 2.3. Zero field cooled (ZFC) and field cooled (FC) experiments were conducted on this sample in a field of 5000 Oe with measurements taken at 10 K steps from 10 – 290 K and the results shown in Figure 4.25. A magnetisation *vs.* applied field experiment was also performed at 290 K, and the results are shown in Figure 4.26

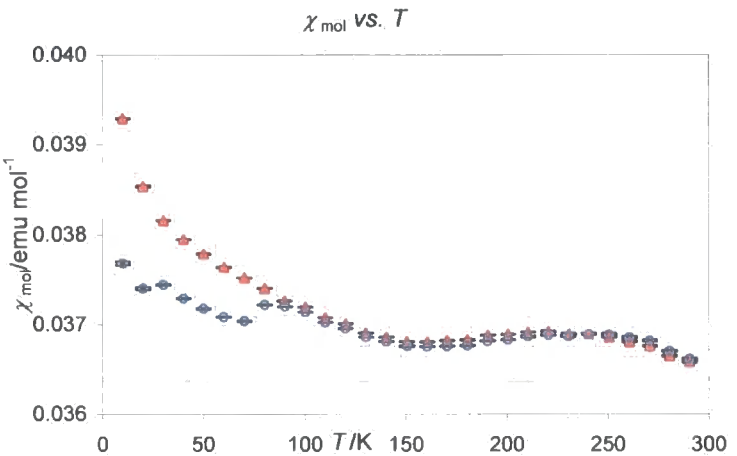

Figure 4.25 ZFC (open blue circles) and FC (filled red triangles) data for $Sr_2CoCu_2O_2S_2$.

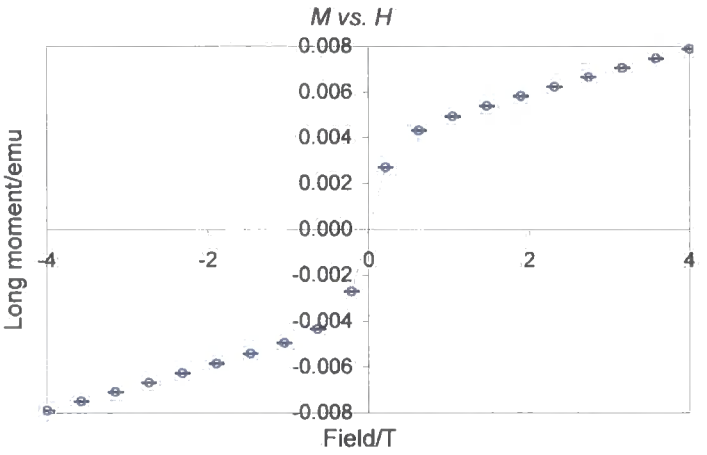

Figure 4.26 Magnetisation against applied field for $Sr_2CoCu_2O_2S_2$.

Figure 4.25 shows that both FC and ZFC sets of data closely match until around 90 K. Below this temperature the ZFC data are clearly lower than the FC data, possibly indicating some spin-glass type behaviour. There is a broad hump around 240 K in both ZFC and FC data also. Zhu *et al.* [4] stated that:

"In addition to two broad transitions at about 100 and 200 K, a crossover, possibly antiferromagnetic to ferrimagnetic transition, takes place at about 80 K as indicated in the FC data. The difference observed between FC and ZFC susceptibilities beginning at this temperature suggests spin-glass freezing of ferromagnetic clusters. At temperatures below 30 K the FC susceptibility is enhanced, while that of ZFC again exhibits a freezing behaviour. The magnetic behaviours of these compounds above 80 K are similar to that of La_2CoO_4 (Yamada, K., Phys Rev B **1989**, *39*, 2336-2342) which also shows successive antiferromagnetic transitions."

Due to the minor impurities present and the lack of any structural anomalies from the variable temperature X-ray diffraction studies little more can be concluded without further magnetic measurement or low temperature neutron diffraction studies.

4.3.2 $Sr_2CoCu_2O_2Se_2$

$Sr_2CoCu_2O_2Se_2$ was synthesised as discussed in Section 2.1.2, characterised by powder X-ray diffraction using the Siemens D5000 diffractometer and its structure confirmed by Rietveld refinement, as shown in Figure 4.27. The ${}_wR_p$ for the refinement was 6.75 %, χ^2 1.45 and R_{Bragg} for the phase was 1.35 %. Details of the important parameters from this refinement are given in Table 4.13.

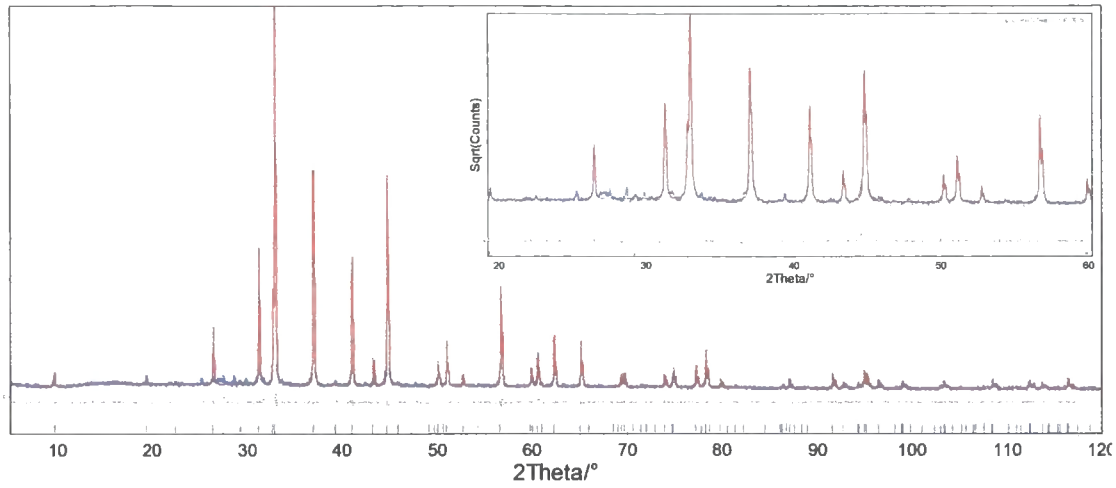

Figure 4.27 Rietveld refinement of $Sr_2CoCu_2O_2Se_2$. Observed pattern in blue, calculated in red and difference in grey. The vertical tick marks show predicted peak positions and the inset shows 20 – 60 ° 2θ region on a square root (counts) scale to emphasise weaker features in the pattern.

Table 4.13 Results of room temperature Rietveld refinement for $Sr_2CoCu_2O_2Se_2$.

$Sr_2CoCu_2O_2Se_2$	NDW323
Spacegroup	*I4/mmm*
a cell parameter/Å	4.052322(35)
c cell parameter/Å	18.34531(21)
Sr *z* coordinate/*c*	0.08804(8)
Se *z* coordinate/*c*	0.16757(9)
Sr B_{iso}/Å^2	1.53(5)
Cu B_{iso}/Å^2	2.43(8)
Co B_{iso}/Å^2	1.39(1)
Se B_{iso}/Å^2	1.53(6)
O B_{iso}/Å^2	0.30(25)
$_wR_p$/%	6.75
R_{Bragg}/%	1.35
χ^2	1.45
No. of parameters	36

Variable temperature measurements were performed on sample NDW256 in experiments d8_02293 and d8_02294. In experiment number d8_02293 it was cooled at 17 K hr^{-1} and data collected over a 5 – 120 ° 2θ range in 30 minute time slices. Eight 30 minute scans were performed at the base temperature and summed together giving the equivalent of one 4 hour data collection. In experiment d8_02294 the sample was then heated at 17 K hr^{-1} to 300 K and data collected over using the same range and collection time as experiment d8_02293. Fourteen 30 minute scans were performed at 300 K and summed together.

The data were analysed using the *multitopas* methodology described in Section 2.2.6. Figure 4.28 shows the variation of the *a* cell parameter with temperature and Figure 4.29 shows the *c* cell parameter. The variation of the Al cell parameter is shown in Figure 4.30 together with the fit to Wang and Reeber's data[6] as a grey line, which both cooling and heating data closely match.

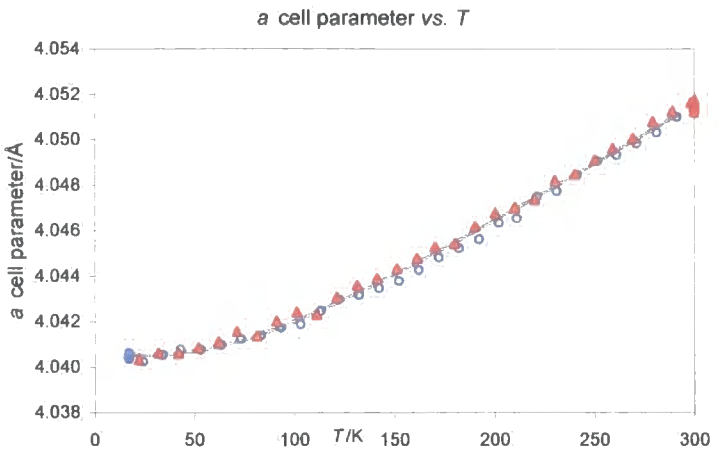

Figure 4.28 $Sr_2CoCu_2O_2Se_2$ *a* cell parameter against temperature. Cooling data are open blue circles, heating filled red triangles, fit to the experimental data using Equation 4.1 and the values in Table 4.14 in grey.

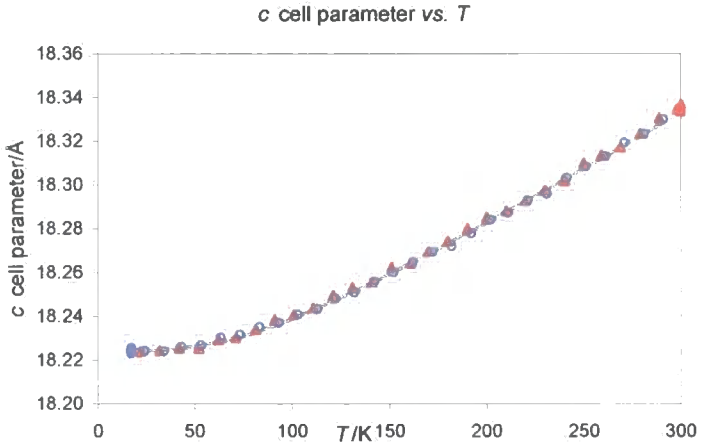

Figure 4.29 $Sr_2CoCu_2O_2Se_2$ *c* cell parameter against temperature. Cooling data are open blue circles, heating filled red triangles, fit to the experimental data using Equation 4.1 and the values in Table 4.14 in grey.

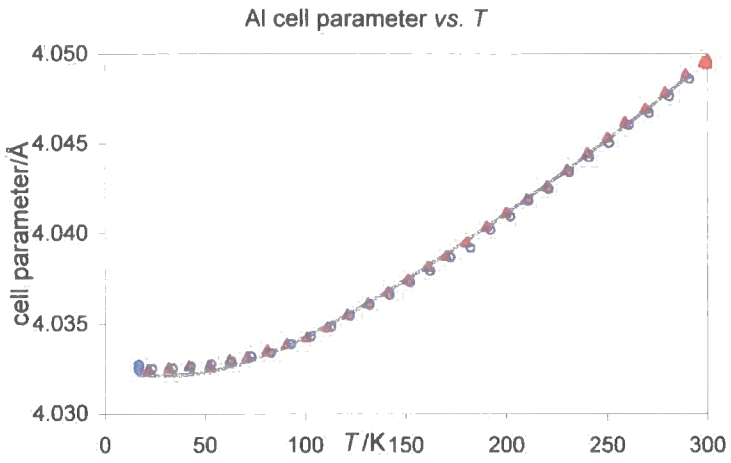

Figure 4.30 Aluminium cell parameter against temperature. Cooling data are open blue circles, heating filled red triangles, Wang and Reeber's data in grey.

The cell parameter plots show that the unit cell expands smoothly on heating and that no phase transitions are visible. The data points very closely match the fitted expansion expression, with the parameters determined by a least-squares fit shown in Table 4.14.

Table 4.14 Thermal expansion data from PheniX experiments on $Sr_2CoCu_2O_2Se_2$.

	a_0/Å	θ_i/K	$C/10^{-6}$	$\alpha_{(300\text{-}15K)}/10^{-6}$ K^{-1}
a	4.04054(5)	223(8)	13.4(2)	9.5(2)
c	18.22487(31)	226(6)	29.4(4)	20.8(4)

The Rietveld refinement performed on the summed data set from 17 K is shown in Figure 4.31. The calculated patterns show a good fit to the observed and give the following cell parameters: a = 4.04045(18) Å c = 18.22442(107) Å at 17 K and a = 4.05146(16) Å and c = 18.33554(99) Å at 300 K. The R-factors were $_wR_p$ = 9.83 and 8.61 % and R_{Bragg} 2.91 and 2.12 % at 17 and 300 K respectively. Other important structural least-squares parameters are summarised in Table 4.15 for the refinements performed on the long scans at 17 and 300 K.

Table 4.15 Atomic fractional coordinates and displacement parameter values for $Sr_2CoCu_2O_2Se_2$ at 17 and 300 K.

Site	z/c (17 K)	z/c (300 K)	B_{iso}/Å^2 (17 K)	B_{iso}/Å^2 (300 K)
Sr	0.0872(3)	0.0873(2)	-0.82(16)	0.07(19)
Cu	0.25	0.25	0.80(25)	2.36(29)
Co	0	0	2.11(49)	1.56(46)
Se	0.1702(3)	0.1701(3)	-0.26(20)	0.39(20)
O	0	0	6.34(1.66)	3.55(1.34)

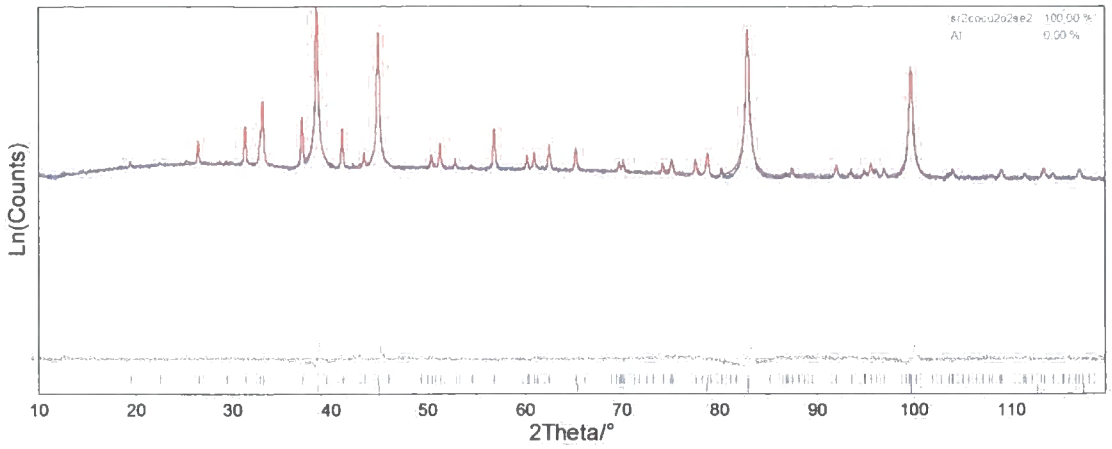

Figure 4.31 Rietveld refinement at 17 K of $Sr_2CoCu_2O_2Se_2$. Observed pattern in blue, calculated in red, difference in grey. Tick marks show predicted peak positions for $Sr_2CoCu_2O_2Se_2$ and Al from top to bottom respectively.

Within experimental error, there is no difference between the *z* coordinates at 17 and 300 K of either the Sr or Se atoms. The Sr coordinates are also quite similar (differing in the 3rd decimal place) to the values from the room temperature d5000 Rietveld refinements given in Table 4.13. There is, however, a larger difference for the Se *z* coordinate, but they are still close. Together with the smooth change in lattice parameters this is an indication that there is no significant structural change beyond normal thermal expansion between 17 and 300 K.

Part of a pellet of sample number NDW256b was magnetically characterised by SQUID magnetometry using the sample preparation and experimental technique described in Section 2.3. Zero field cooled (ZFC) and field cooled (FC) experiments were conducted on this sample with measurements taken at 10 K steps from 10 – 290 K and the results shown in Figure 4.32. A magnetisation *vs.* applied field (*M vs. H*) experiment was also performed at 290 K on this sample, and the results are shown in Figure 4.33. This shows that the magnetisation saturates at a magnetisation of ~ 0.0015 emu in a field of around 1 T. There is no hysteresis around $H = 0$ T. However, the relatively large error bars (believed to be caused by an anisotropic sample environment due to the shape of the pellet) make detailed analysis difficult.

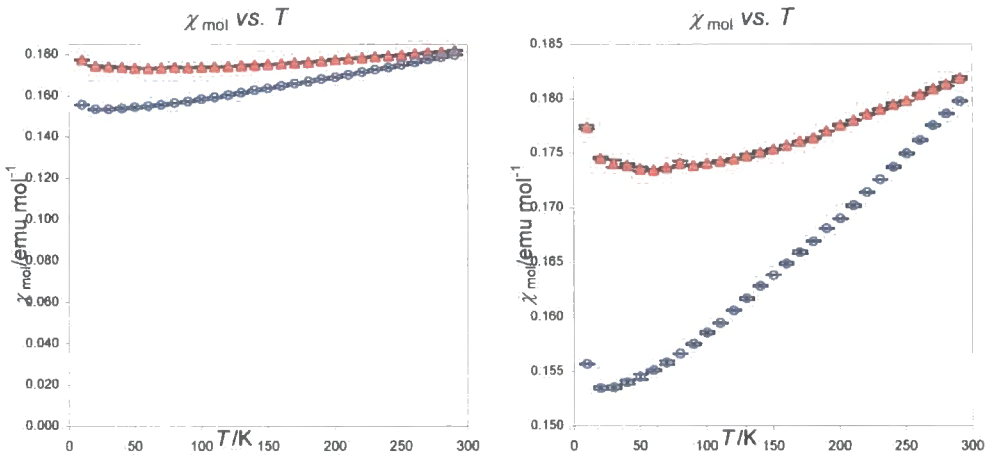

Figure 4.32 ZFC (open blue circles) and FC (filled red triangles) data for $Sr_2CoCu_2O_2Se_2$ data shown on different scales for clarity.

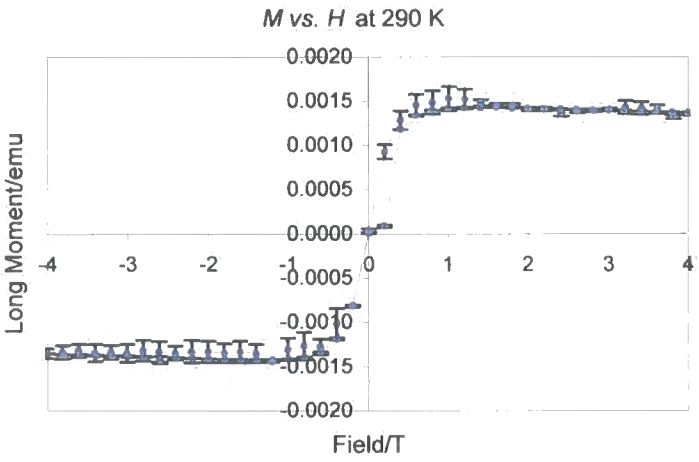

Figure 4.33 Magnetisation against applied field for $Sr_2CoCu_2O_2Se_2$.

Figure 4.32 shows that the susceptibility falls with decreasing temperature, for both the ZFC and FC data, indicative of anti-ferromagnetic behaviour. However, there is a considerable difference between the two sets of data, with a higher susceptibility clear for the data recorded after cooling the sample in a field.

Conductivity measurements were performed on pellet NDW256a according to the method described in Section 2.4. The contacts used were sputtered aluminium protected against oxidation with silver paint and then connected to the electrometer with soldered copper wires. The pellet was cooled to 130 K in the cryostat and resistance readings taken every 10 K on cooling. The pellet was then warmed to 300 K and resistance readings taken every 10 K. The results are shown in Figure 4.34. This shows that ρ increases from 150 to 200 Ω cm with decreasing temperature, implying a semi-conducting mechanism for this conduction. There are notable discontinuities in the data both on cooling and heating at 210 and 170 K respectively. These are believed to be artefacts of the experimental apparatus and are only

around 10 – 30 Ω cm, quite small when viewed in perspective of the range of resistances measured and discussed in this thesis; from 10 to 10^{10} Ω cm.

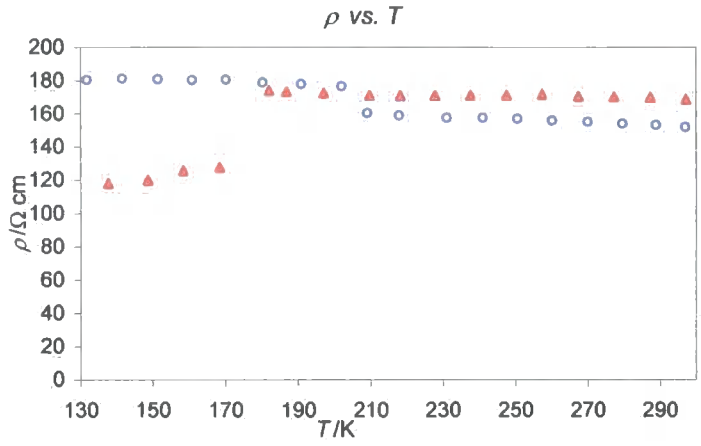

Figure 4.34 Resistance versus temperature for $Sr_2CoCu_2O_2Se_2$. Open blue circles are cooling data, filled red triangles heating.

4.3.3 $Ba_2CoCu_2O_2S_2$

$Ba_2CoCu_2O_2S_2$ was synthesised as discussed in Section 2.1.2, characterised by powder X-ray diffraction using the Siemens D5000 diffractometer and its structure confirmed by Rietveld refinement, as shown in Figure 4.35. There are a number of minor impurity peaks present, with the level of impurity estimated to be around 5 %. The $_wR_p$ for the refinement was 12.29 %, χ^2 1.66 and R_{Bragg} for the main phase was 3.60 %. Details of the important parameters from this refinement are given in Table 4.13.

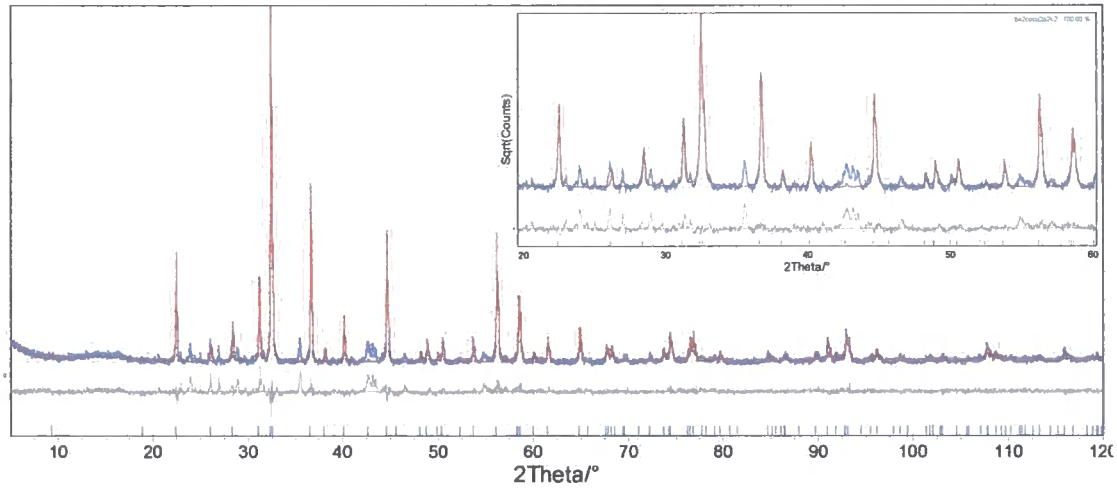

Figure 4.35 Rietveld refinement of $Ba_2CoCu_2O_2S_2$. Observed pattern in blue, calculated in red and difference in grey. The vertical tick marks show predicted peak positions and the inset shows 20 – 60 ° 2θ region on a square root (counts) scale to emphasise weaker features in the pattern.

Table 4.16 Results of room temperature Rietveld refinement for $Ba_2CoCu_2O_2S_2$.

$Ba_2CoCu_2O_2S_2$	NDW251
Spacegroup	*I4/mmm*
a cell parameter/Å	4.064064(84)
c cell parameter/Å	18.88696(58)
Ba *z* coordinate/*c*	0.9037(1)
S *z* coordinate/*c*	0.1768(5)
Ba B_{iso}/Å^2	-0.50(6)
Cu B_{iso}/Å^2	0.96(15)
Co B_{iso}/Å^2	-0.61(16)
S B_{iso}/Å^2	0.16(22)
O B_{iso}/Å^2	1.27(67)
$_wR_p$/%	12.29
R_{Bragg}/%	3.60
χ^2	1.66
No. of parameters	36

Variable temperature powder X-ray diffraction experiments were performed on sample NDW251 in experiments d8_02460 and d8_02461. In experiment number d8_02460 it was cooled at 12 K hr^{-1} and data collected over a 5 – 120 ° 2θ range in 45 minute time slices. Seven 45 minute scans were performed at the base temperature and summed together giving the equivalent of one 5.25 hour data collection. In experiment d8_02461 the sample was then heated at 8 K hr^{-1} to 300 K and data collected over the same 2θ range as experiment d8_02460 in 60 minute time slices. Five 1 hour scans were performed at 300 K and summed together.

The data were analysed using the *multitopas* methodology described in Section 2.2.6. Figure 4.36 shows the variation of the *a* cell parameter with temperature and Figure 4.37 shows the *c* cell parameter. The variation of the Al cell parameter is shown in Figure 4.39 together with the fit to Wang and Reeber's data[6] as a grey line, which both cooling and heating data closely match, apart from at low temperatures (< 60 K) indicating that the actual cryostat temperature was perhaps not as cold as the set point for this experiment.

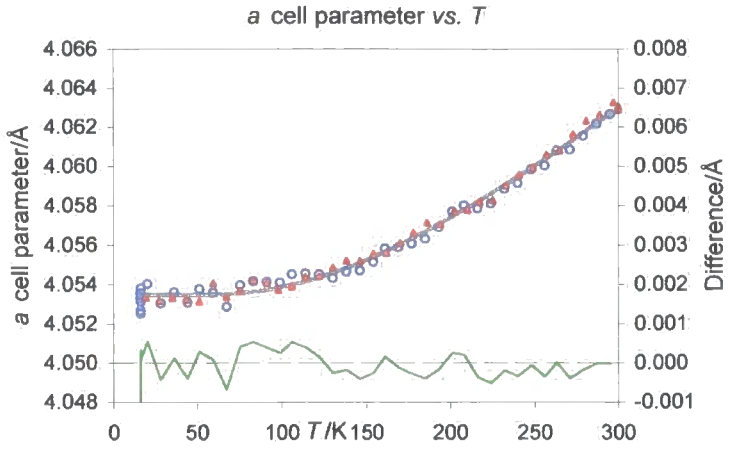

Figure 4.36 $Ba_2CoCu_2O_2S_2$ *a* cell parameter against temperature. Cooling data are open blue circles, heating filled red triangles, fit to the experimental data using Equation 4.1 and the values in Table 4.17 in grey and difference in green.

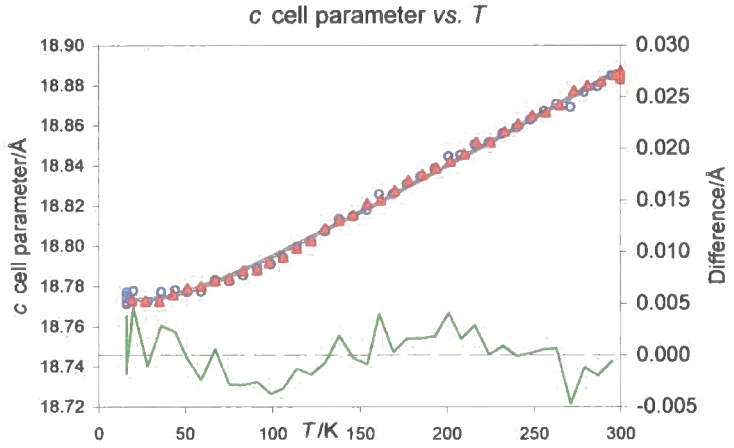

Figure 4.37 $Ba_2CoCu_2O_2S_2$ *c* cell parameter against temperature. Cooling data are open blue circles, heating filled red triangles, fit to the experimental data using Equation 4.1 and the values in Table 4.17 in grey and difference in green.

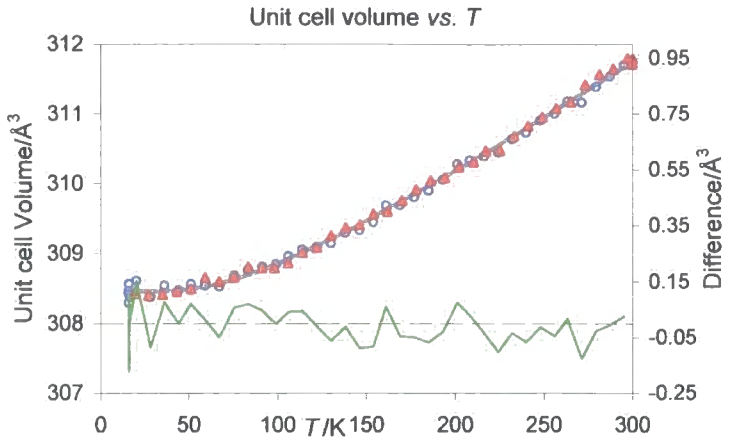

Figure 4.38 $Ba_2CoCu_2O_2S_2$ unit cell volume against temperature. Cooling data are open blue circles, heating filled red triangles, fit to the experimental data using Equation 4.1 and the values in Table 4.17 in grey and difference in green.

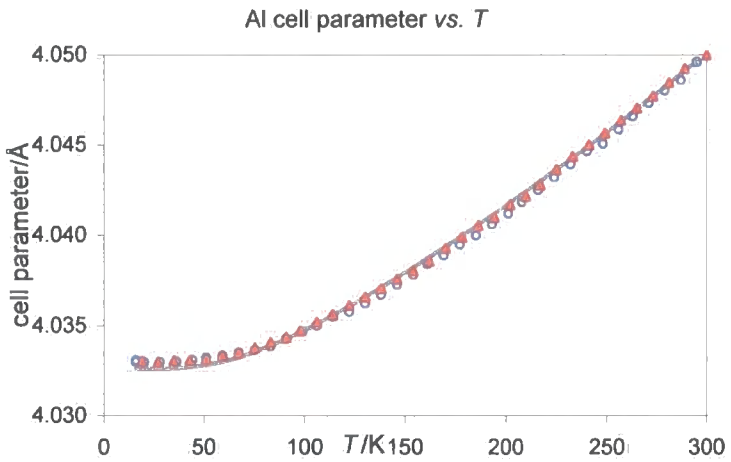

Figure 4.39 Aluminium cell parameter against temperature. Cooling data are open blue circles, heating filled red triangles, Wang and Reeber's data in grey.

The *a* cell parameter plots varies smoothly with temperature and the data points roughly match the fitted expansion expression, with the parameters determined by a least-squares fit shown in Table 4.14. There is some scatter in these points, but it is still clear that they follow a smooth trend. There is some indication that the *c* axis departs from the fitted curve between ~130 and 250 K which suggest a non phonon contribution to thermal expansion similar to that discussed for $La_2O_3Mn_2Se_2$ in chapter 3. Firm conclusions on this subtle effect are difficult given the data quality. A plot of the cell volume *vs.* temperature (Figure 4.38) shows smoother behaviour.

Table 4.17 Thermal expansion data from PheniX experiments on $Ba_2CoCu_2O_2S_2$.

	a_0/Å	θ_1/K	$C_1/10^{-6}$	$\alpha_{(300\text{-}15K)}/10^{-6}$ K^{-1}
a	4.05347(6)	442(18)	17.8(7)	8.2(5
c	18.77306(58)	142(7)	26.0(3)	21.5(4)

The Rietveld refinement performed on the summed data set from 17 K is shown in Figure 4.40. The calculated patterns show a good fit to the observed and give the following cell parameters: a = 4.05382(18) Å c = 18.77220(13) Å at 17 K and a = 4.06305(10) Å and c = 18.88354(70) Å at 300 K. The R-factors were ${}_wR_p$ = 10.46 and 9.05 % and R_{Bragg} 4.44 and 5.03 % at 17 and 300 K respectively. Other important structural least-squares parameters are summarised in Table 4.18 for the refinements performed on the long scans at 17 and 300 K. The particularly large uncertainty in the displacement parameter for the oxygen atom is understandable considering both the presence of barium atoms (atomic number 56, compared to oxygen, 8) and the pattern being dominated by aluminium from the sample holder.

Table 4.18 Atomic fractional coordinates and displacement parameter values for $Ba_2CoCu_2O_2S_2$ at 17 and 300 K.

Site	z/c (17 K)	z/c (300 K)	B_{iso}/Å^2 (17 K)	B_{iso}/Å^2 (300 K)
Ba	0.0966(2)	0.0960(2)	-3.06(8)	-2.46(8)
Cu	0.25	0.25	-2.7(2)	-0.7(2)
Co	0	0	-2.4(3)	-2.4(2)
S	0.1756(8)	0.1761(6)	-2.8(3)	-1.5(3)
O	0	0	2(1)	0.2(8)

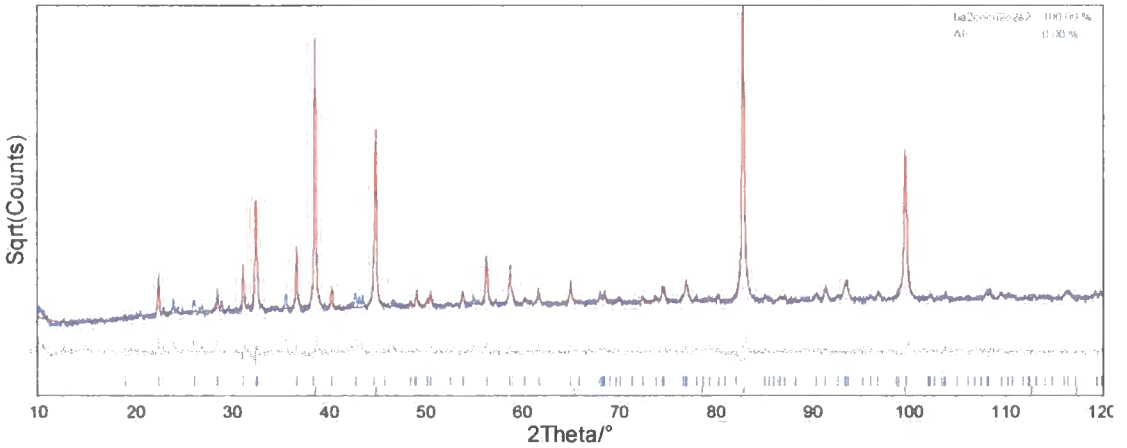

Figure 4.40 Rietveld refinement at 17 K of $Ba_2CoCu_2O_2S_2$. Observed pattern in blue, calculated in red, difference in grey. Tick marks show predicted peak positions for $Ba_2CoCu_2O_2S_2$ and Al from top to bottom respectively.

Within experimental error, there is no difference between the z coordinates at 17 and 300 K of either the Ba or S atoms. The S coordinates are also the same (within experimental error) as the values from the room temperature d5000 Rietveld refinements given in Table 4.16. There is, however, a larger difference for the Ba z coordinate, but they are still close. Together with the smooth change in lattice parameters this is an indication that there is no significant structural change beyond normal thermal expansion between 17 and 300 K.

Part of a pellet of sample number NDW251b was magnetically characterised by SQUID magnetometry using the sample preparation and experimental technique described in Section

2.3. Zero field cooled (ZFC) and field cooled (FC) experiments were conducted on this sample in a field of 5000 Oe with measurements taken at 10 K steps from 10 – 290 K and the results shown in Figure 4.41. A magnetisation *vs.* applied field experiment was also performed at 290 K, and the results are shown in Figure 4.42. This is clearly a straight line crossing the origin indicating that the sample is paramagnetic.

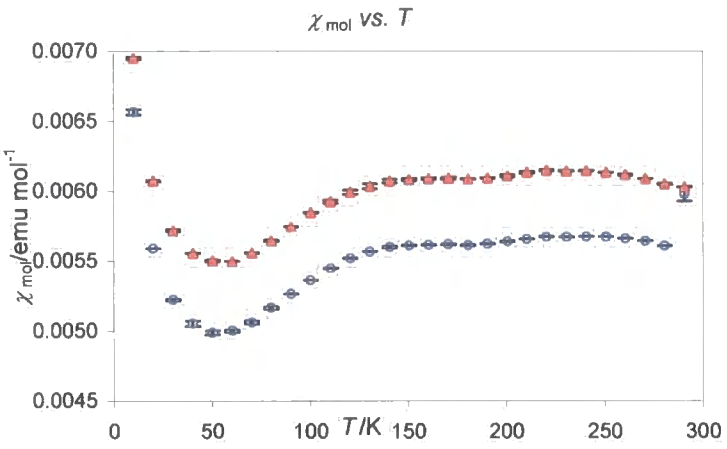

Figure 4.41 ZFC (open blue circles) and FC (filled red triangles) data for $Ba_2CoCu_2O_2S_2$.

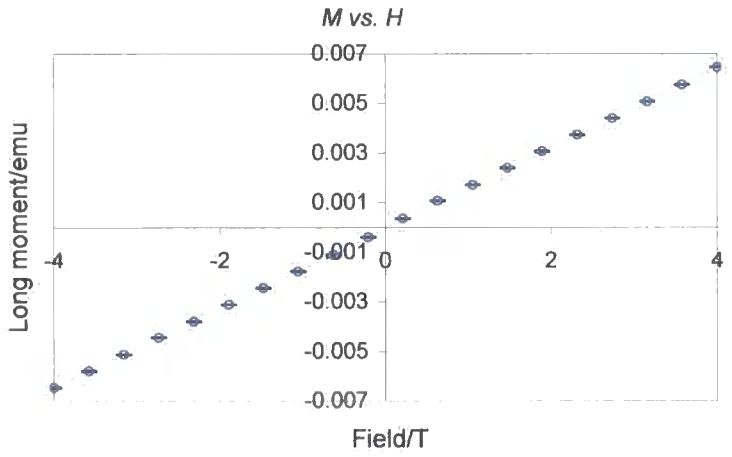

Figure 4.42 Magnetisation against applied field for $Ba_2CoCu_2O_2S_2$.

Figure 4.41 shows that there is a broad hump in the susceptibility at around 240 K, below which temperature the susceptibility falls away until 50 K. At this point the susceptibility steeply rises. This behaviour could be caused by small impurities dominating at lower temperatures. This roughly mirrors the "0 – 50 – 150 – 250 K" regions shown in the difference plots for the *c* cell parameter (Figure 4.37). Similar data have been reported by Zhu *et al.* [4]

Conductivity measurements were performed on pellet NDW251c according to the method described in Section 2.4. The contacts used were sputtered aluminium protected against

oxidation with silver paint and then connected to the electrometer with soldered copper wires. The pellet was cooled to 80 K in the cryostat and resistance readings taking every 10 K on cooling (apart from a few points missing due to software failure between 200 and 180 K). The pellet was then warmed to 300 K and resistance readings taken every 10 K. The results are shown in Figure 4.43. The resistivity increases gradually on cooling from ~1.5 x 10^3 to ~5.5 x 10^4 Ω cm indicating semi conducting behaviour. This is matched almost exactly on heating until there is a discontinuity in the data at 180 K, believed to be due to the instability of the Keithley electrometer.

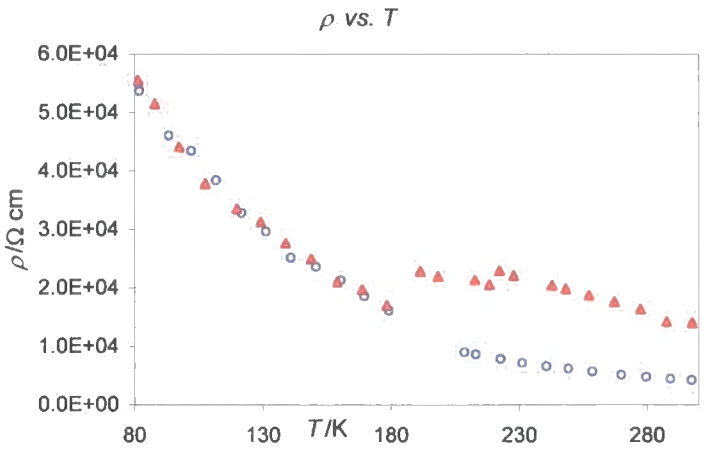

Figure 4.43 Resistivity versus temperature for $Ba_2CoCu_2O_2S_2$. Open blue circles are cooling data, filled red triangles heating.

4.3.4 $Ba_2CoCu_2O_2Se_2$

$Ba_2CoCu_2O_2Se_2$ was synthesised as discussed in Section 2.1.2, characterised by powder X-ray diffraction using the Siemens D5000 diffractometer and its structure confirmed by Rietveld refinement, as shown in Figure 4.35. The ${}_wR_p$ for the refinement was 10.19 %. χ^2 1.77 and R_{Bragg} for the phase was 1.97%. Details of the important parameters from this refinement are given in Table 4.19.

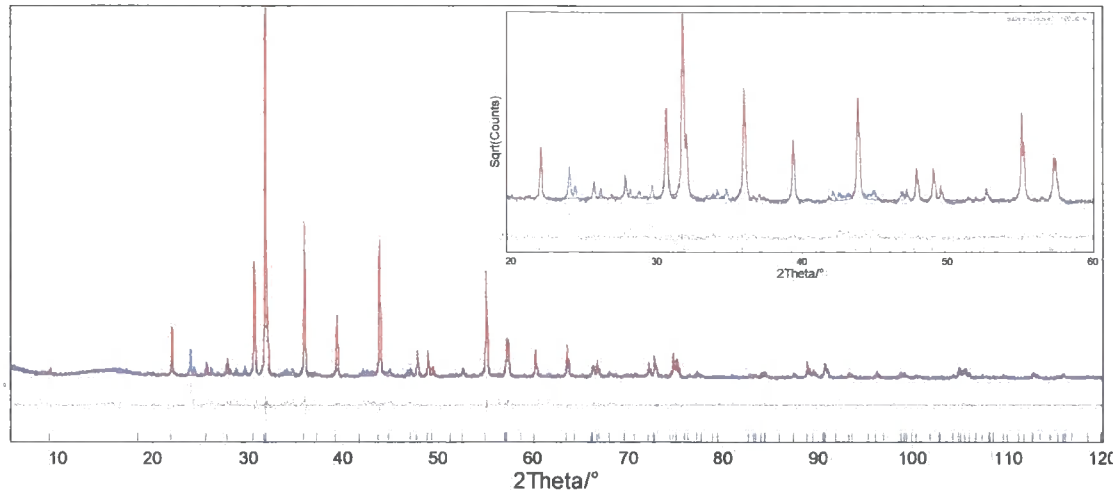

Figure 4.44 Rietveld refinement of $Ba_2CoCu_2O_2Se_2$. Observed pattern in blue, calculated in red and difference in grey. The vertical tick marks show predicted peak positions and the inset shows 20 – 60 ° 2θ region on a square root (counts) scale to emphasise weaker features in the pattern.

Table 4.19 Results of room temperature Rietveld refinement for $Ba_2CoCu_2O_2Se_2$.

$Ba_2CoCu_2O_2Se_2$	NDW322
Spacegroup	*I4/mmm*
a cell parameter/Å	4.140761(62)
c cell parameter/Å	19.29302(42)
Ba *z* coordinate/*c*	0.0924(1)
Se *z* coordinate/*c*	0.1744(2)
Ba B_{iso}/Å^2	0.86(6)
Cu B_{iso}/Å^2	1.83(13)
Co B_{iso}/Å^2	1.71(19)
Se B_{iso}/Å^2	1.36(11)
O B_{iso}/Å^2	2.87(68)
$_wR_p$/%	10.19
R_{Bragg}/%	1.97
χ^2	1.77
No. of parameters	36

Variable temperature powder X-ray diffraction experiments were performed on sample NDW252 experiments d8_02272 and d8_02273. In experiment number d8_02272 it was cooled at 17 K hr^{-1} and data collected over a 5 – 120 ° 2θ range in 30 minute time slices. Seven 30 minute scans were performed at base temperature and summed together giving the equivalent of one 3.5 hour data collection. In experiment d8_02273 the sample was then heated at 17 K hr^{-1} to 300 K and data collected using the same range and collection time as experiment d8_02272. Five 30 minute scans were performed at 300 K and summed together.

The data were analysed using the *multitopas* methodology described in Section 2.2.6. Figure 4.45 shows the variation of the *a* cell parameter with temperature and Figure 4.46 shows the *c* cell parameter. The variation of the Al cell parameter is shown in Figure 4.47 together with the fit to Wang and Reeber's data[6] as a grey line, which both cooling and heating data are systematically less than for temperatures above 60 K.

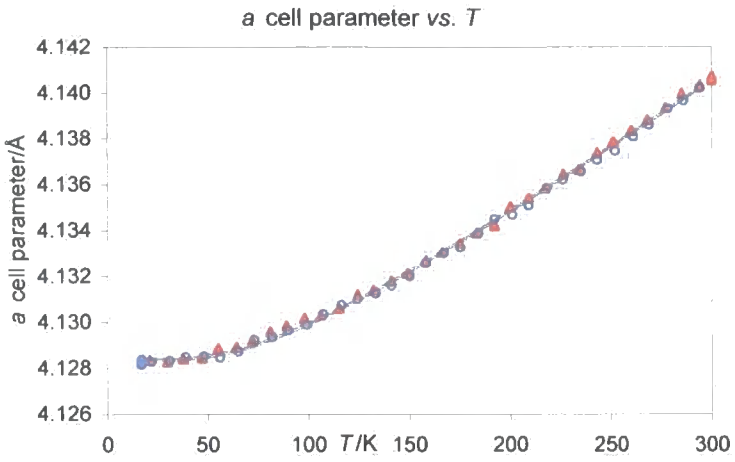

Figure 4.45 $Ba_2CoCu_2O_2Se_2$ *a* cell parameter against temperature. Cooling data are open blue circles, heating filled red triangles, fit to the experimental data using Equation 4.1 and the values in Table 4.20 in grey.

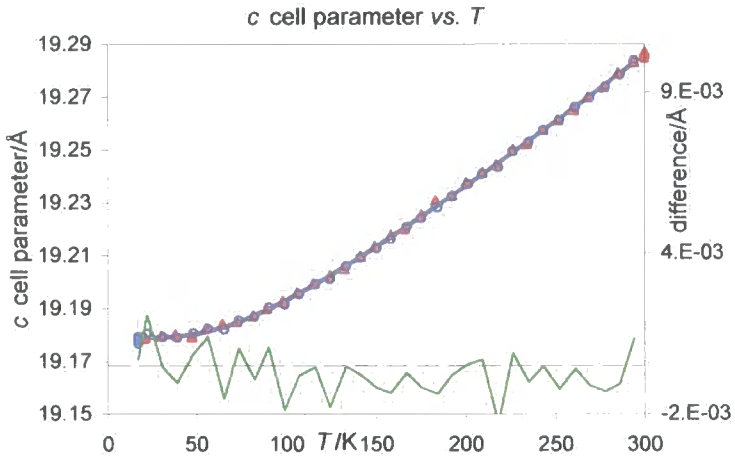

Figure 4.46 $Ba_2CoCu_2O_2Se_2$ *c* cell parameter against temperature. Cooling data are open blue circles, heating filled red triangles, fit to the experimental data using Equation 4.1 and the values in Table 4.20 in grey.

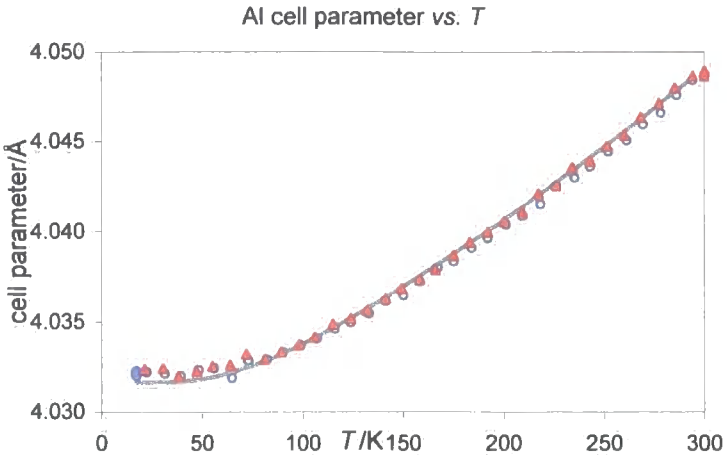

Figure 4.47 Aluminium cell parameter against temperature. Cooling data are open blue circles, heating filled red triangles, Wang and Reeber's data in grey.

Both *a* and *c* cell parameters vary smoothly with temperature. Thermal expansion parameters determined by a least-squares fit are shown in Table 4.20. The systematic error in aluminium cell parameter compared to the literature values could indicate that the temperature in the cryostat was less than recorded above 60 K. However, this would only subtly shift the cell parameters and would not affect the smooth behaviour.

Table 4.20 Thermal expansion data from PheniX experiments on $Ba_2CoCu_2O_2Se_2$.

	a_0/Å	θ_i/K	$C_i/10^{-6}$	$\alpha_{(300\text{-}15K)}/10^{-6}$ K^{-1}
a	4.12838(4)	230(6)	14.8(2)	10.3(2)
c	19.17908(19)	224(3)	27.5(2)	19.5(2)

The Rietveld refinement performed on the summed data set from 17 K is shown in Figure 4.48. The calculated patterns show a good fit to the observed and give the following cell parameters: *a* = 4.12827(6) Å *c* = 19.17866(41) Å at 17 K and *a* = 4.14059(6) Å and *c* = 19.28608(43) Å at 300 K. The *R*-factors were $_wR_p$ = 9.31 and 9.81 % and R_{Bragg} 2.79 and 2.58 % at 17 and 300 K respectively. Other important structural least-squares parameters are summarised in Table 4.21 for the refinements performed on the long scans at 17 and 300 K.

Table 4.21 Atomic fractional coordinates and displacement parameter values for $Ba_2CoCu_2O_2Se_2$ at 17 and 300 K.

Site	z/c (17 K)	z/c (300 K)	B_{iso}/Å^2 (17 K)	B_{iso}/Å^2 (300 K)
Ba	0.0922(1)	0.0921(1)	-2.35(6)	-1.83(7)
Cu	0.25	0.25	-2.29(11)	-0.91(15)
Co	0	0	-1.70(18)	-0.78(22)
Se	0.1745(2)	0.1746(2)	-2.04(10)	-1.49(12)
O	0	0	-1.02(60)	-1.96(60)

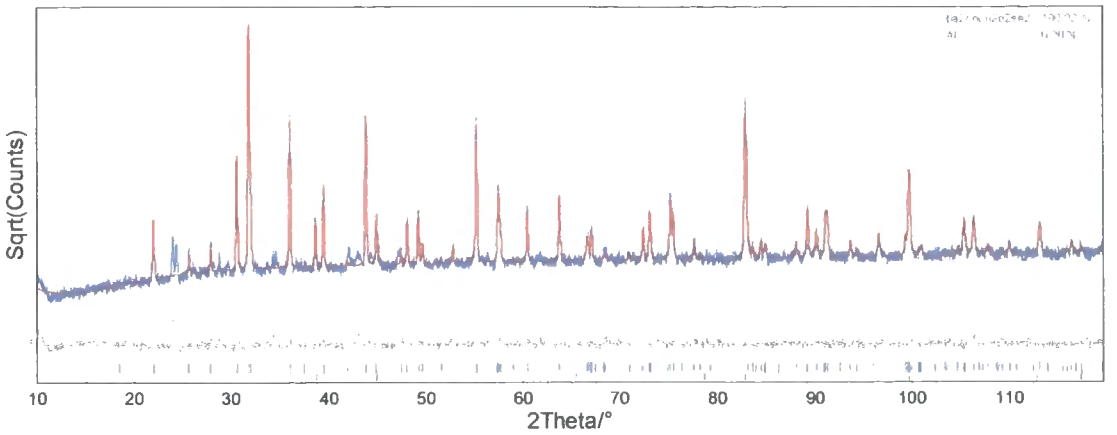

Figure 4.48 Rietveld refinement at 17 K of $Ba_2CoCu_2O_2Se_2$. Observed pattern in blue, calculated in red, difference in grey. Tick marks show predicted peak positions for $Ba_2CoCu_2O_2Se_2$ and Al from top to bottom respectively.

Within experimental error, there is no difference between the *z* coordinates at 17 and 300 K of either the Ba or Se atoms. They are also the same (within experimental error) as the values from the room temperature d5000 Rietveld refinements given in Table 4.19. Together with the smooth change in lattice parameters this is an indication that there is no significant structural change beyond normal thermal expansion between 17 and 300 K.

Part of a pellet of sample number NDW252a was magnetically characterised by SQUID magnetometry. Zero field cooled (ZFC) and field cooled (FC) experiments were conducted on this sample in a field of 100 Oe with measurements taken at 5 K steps from 10 – 290 K and the results shown in Figure 4.49. A magnetisation *vs.* applied field experiment was also performed at 290 K, and the results are shown in Figure 4.50. This is clearly a straight line crossing the origin indicating that the sample is paramagnetic.

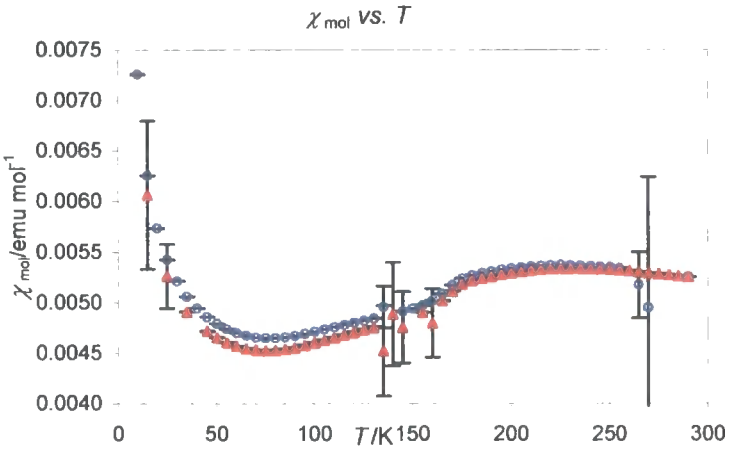

Figure 4.49 ZFC (open blue circles) and FC (filled red triangles) data for $Ba_2CoCu_2O_2Se_2$. Large error bars an artefact of the experimental apparatus.

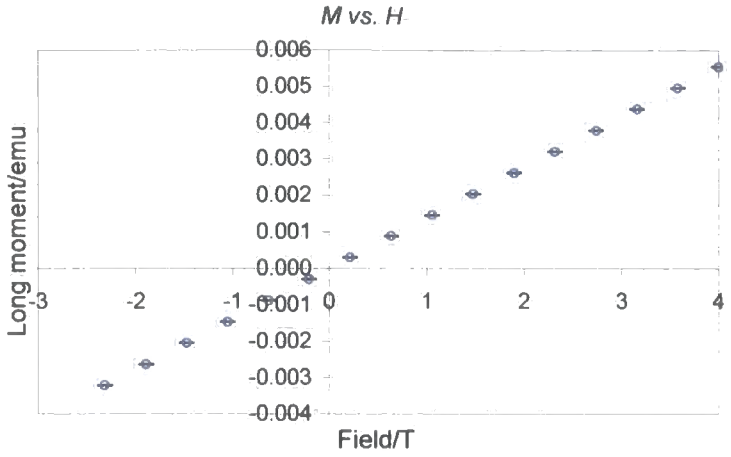

Figure 4.50 Magnetisation against applied field for $Ba_2CoCu_2O_2Se_2$.

Figure 4.49 shows behaviour quite similar to that in the X = S analogue, with a similar broad hump in the susceptibility at around 200 K, below which temperature the susceptibility falls away until rising at 50 K. For this compound there is much less difference between the ZFC and the FC data and above around 170 K the two sets of data are identical within experimental error. This similarity in magnetic behaviour does not extend to a similarity in the c cell parameter, as Figure 4.46 fits the least-squares determined equation very well.

Conductivity measurements were performed on pellet NDW268b using sputtered aluminium contacts protected against oxidation with silver paint and then attached to the electrometer with soldered copper wires. The pellet was cooled to 80 K in the cryostat and resistance readings taken every 5 K on cooling. The pellet was then warmed to 230 K with readings taken every 5 K, data were also recorded over the temperature range 300 – 80 – 300 K, with readings taken every 5 K. The results are shown in Figure 4.51. This shows the resistivity increasing from ~500 to 800 Ω cm from 300 to 80 K suggesting a semi-conducting mechanism. While there are various discontinuities in the data at various points in the two experiments, the overall trend is still clear.

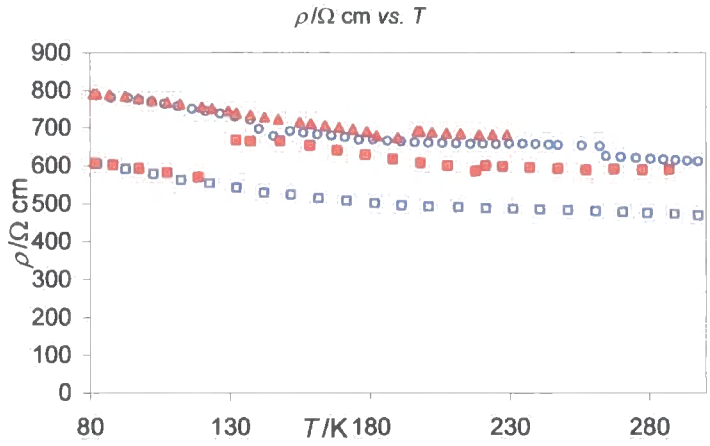

Figure 4.51 Resistivity versus temperature for $Ba_2CoCu_2O_2Se_2$. Open blue points are taken on cooling, filled red points on heating.

4.3.5 *M* = Co conclusions

All *A* = Sr, Ba and *X* = S, Se members of the *M* = Co series have been synthesised and shown to be isostructural. Their structures have been studied from 16 – 300 K and all show similar expansion behaviour over that temperature range. Both *A* = Ba compounds show very similar magnetic behaviour, while the *A* = Sr compounds are quite different. $Sr_2CoCu_2O_2Se_2$ shows broadly anti ferromagnetic behaviour while $Sr_2CoCu_2O_2S_2$ shows more complex behaviour. The three members whose electrical properties were examined show semi conductor type resistance and temperature dependant behaviour; the *X* = Se members are more conducting than the *X* = S, due to the more polarisable nature of the larger anion.

4.4 Ni containing phases

As was the case for the *M* = Mn compounds, the *X* = Se compounds were both synthesised with high phase purity and their physical properties measured, the results of which are presented and discussed in section 4.4.1 and 4.4.2. $Ba_2NiCu_2O_2Se_2$ was a black powder when synthesised and $Sr_2NiCu_2O_2Se_2$ light grey. Neither of the *X* = S containing materials were synthesised with the necessary purity to perform physical property measurements discussed for the other compounds. The predominant products were $BaSO_4$ and SrS with no evidence of the target phase.

4.4.1 $Sr_2NiCu_2O_2Se_2$

$Sr_2NiCu_2O_2Se_2$ was synthesised as discussed in Section 2.1.2, characterised by powder X-ray diffraction using the Siemens D5000 diffractometer and its structure confirmed by Rietveld refinement, as shown in Figure 4.52. The ${}_wR_p$ for the refinement was 8.89 %, χ^2 2.38 and

R_{Bragg} for the phase was 4.69 %. Details of the important parameters from this refinement are given in Table 4.22.

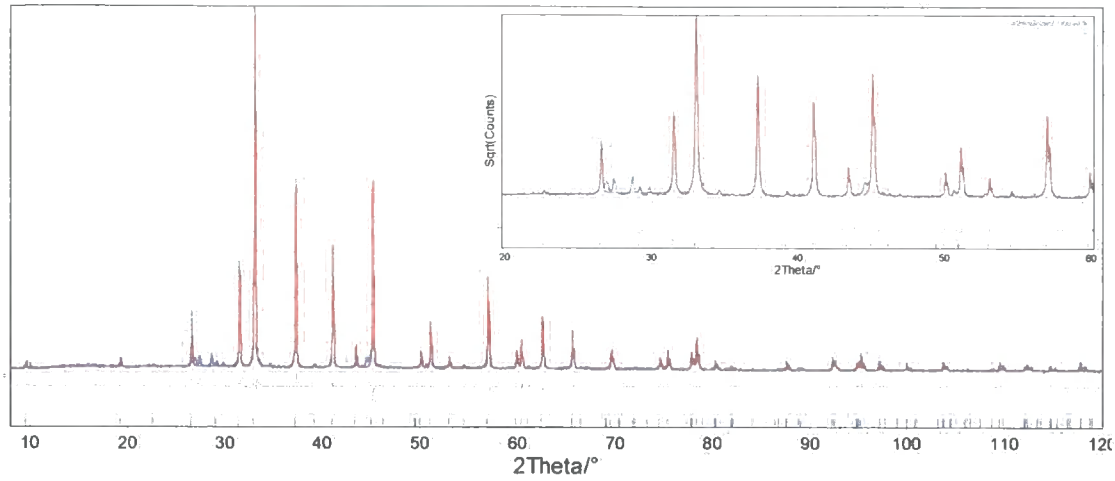

Figure 4.52 Rietveld refinement of $Sr_2NiCu_2O_2Se_2$. Observed pattern in blue, calculated in red and difference in grey. The vertical tick marks show predicted peak positions and the inset shows 20 – 60 ° 2θ region on a square root (counts) scale to emphasise weaker features in the pattern.

Table 4.22 Results of room temperature Rietveld refinement for $Sr_2NiCu_2O_2Se_2$.

$Sr_2NiCu_2O_2Se_2$	NDW303
Spacegroup	*I4/mmm*
a cell parameter/Å	4.024351(48)
c cell parameter/Å	18.40436(28)
Sr *z* coordinate/*c*	0.08680(10)
Se *z* coordinate/*c*	0.16759(12)
Sr B_{iso}/Å^2	3.86(5)
Cu B_{iso}/Å^2	5.26(9)
Ni B_{iso}/Å^2	5.87(15)
Se B_{iso}/Å^2	4.55(7)
O B_{iso}/Å^2	9.70(57)
$_wR_p$/%	8.89
R_{Bragg}/%	4.69
χ^2	2.38
No. of parameters	36

Variable temperature powder X-ray diffraction experiments were performed on sample NDW240 in experiments d8_02305 and d8_02306. In experiment number d8_02305 it was cooled at 17 K hr^{-1} and data collected over a 5 – 120 ° 2θ range in 30 minute time slices. Six 30 minute scans were performed at the base temperature and summed together giving the equivalent of one 3 hour data collection. In experiment d8_02306 the sample was then heated at 17 K hr^{-1} to 300 K and data collected using the same range and collection time as experiment d8_02441. Ten 30 minute scans were performed at 300 K and summed together.

Due to the unusual behaviour observed in this experiment another two experiments were performed on the same sample (NDW240); d8_02440 and d8_02441. A longer scan time and slower heating/cooling rate was used in order to improve the signal:noise ratio and in

order to obtain more experimental points. In experiment number d8_02440 it was cooled at 8 K hr^{-1} and data collected over a 5 – 120 ° 2θ range in 60 minute time slices. Eleven 60 minute scans were performed at base temperature and summed together giving the equivalent of one 11 hour data collection. In experiment d8_02441 the sample was then heated at 10 K hr^{-1} to 300 K and data collected over the same 2θ range as experiment d8_02441 in 60 minute time slices. Two 1 hour scans were performed at 300 K and summed together.

The data were analysed using the *multitopas* methodology described in Section 2.2.6. Figure 4.53 and Figure 4.54 show the variation of the *a* cell parameter with temperature and Figure 4.55 and Figure 4.56 show the *c* cell parameter. All of these figures include a least-squares fitted model as a grey line, calculated from Equation 4.1. The variation of the Al cell parameter from the two experiments is shown in Figure 4.60 and Figure 4.61 together with the fit to Wang and Reeber's data[6] as a grey line, which both sets of cooling and heating data match well.

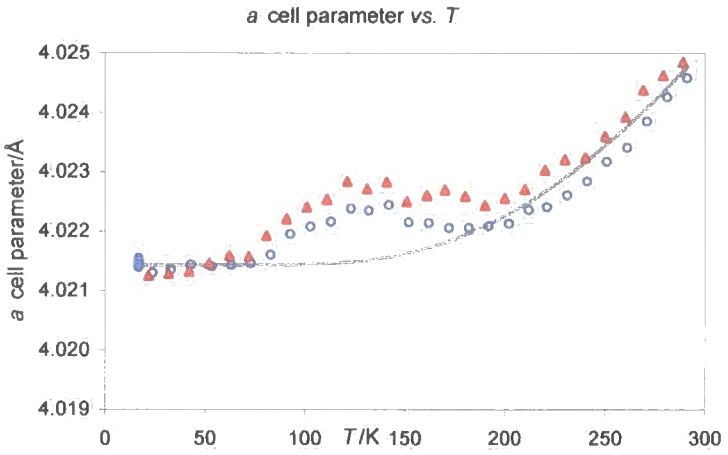

Figure 4.53 $Sr_2NiCu_2O_2Se_2$ *a* cell parameter against temperature from d8_02305/6. Cooling data are open blue circles, heating filled red triangles, fit to the experimental data using Equation 4.1 and the values in Table 4.23 in grey.

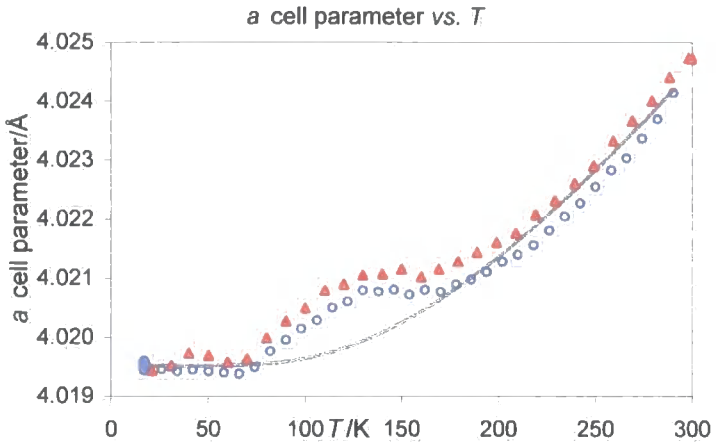

Figure 4.54 $Sr_2NiCu_2O_2Se_2$ *a* cell parameter against temperature from d8_02440/1. Cooling data are open blue circles, heating filled red triangles, fit to the experimental data using Equation 4.1 and the values in Table 4.23 in grey.

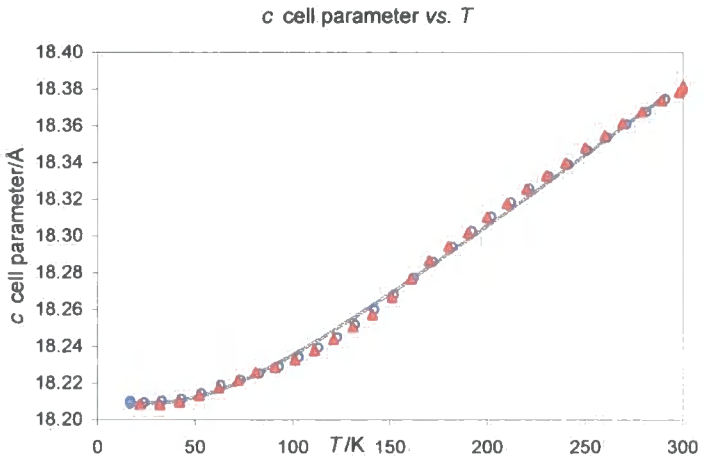

Figure 4.55 $Sr_2NiCu_2O_2Se_2$ c cell parameter against temperature from d8_02305/6. Cooling data are open blue circles, heating filled red triangles, fit to the experimental data using Equation 4.1 and the values in Table 4.23 in grey.

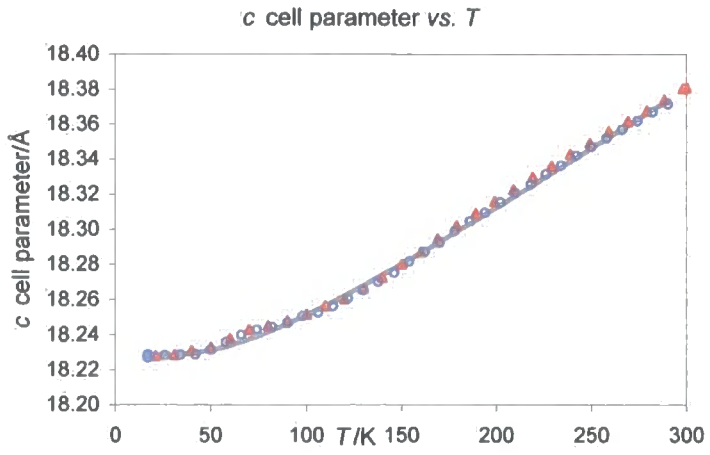

Figure 4.56 $Sr_2NiCu_2O_2Se_2$ *c* cell parameter against temperature from d8_02440/1. Cooling data are open blue circles, heating filled red triangles, fit to the experimental data using Equation 4.1 and the values in Table 4.23 in grey.

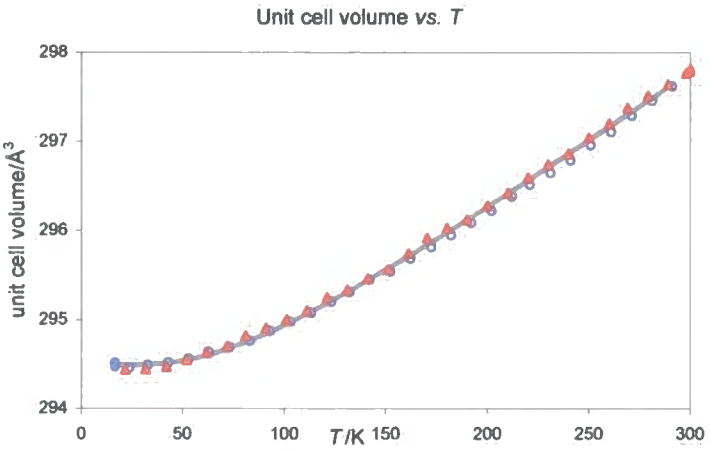

Figure 4.57 $Sr_2NiCu_2O_2Se_2$ unit cell volume against temperature from d8_02305/6. Cooling data are open blue circles, heating filled red triangles, fit to the experimental data using Equation 4.1 and the values in Table 4.23 in grey.

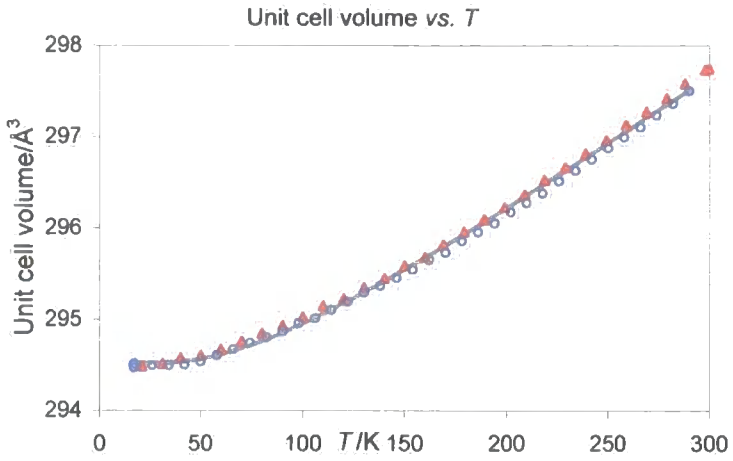

Figure 4.58 $Sr_2NiCu_2O_2Se_2$ unit cell volume against temperature from d8_02440/1. Cooling data are open blue circles, heating filled red triangles, fit to the experimental data using Equation 4.1 and the values in Table 4.23 in grey.

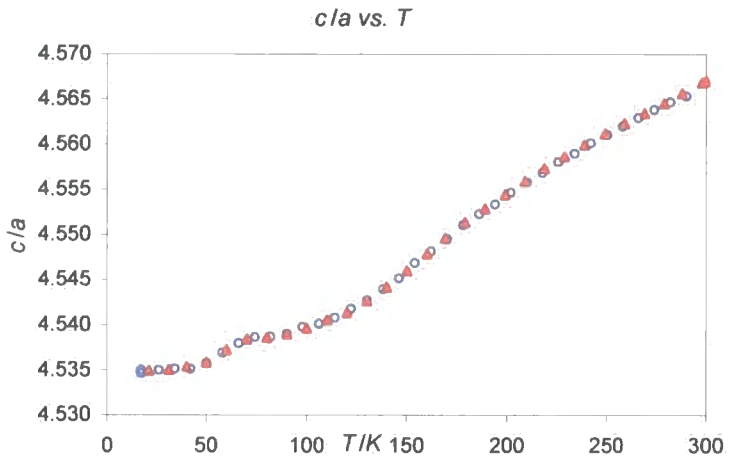

Figure 4.59 Graph of *c*/*a* for $Sr_2NiCu_2O_2Se_2$. Cooling data are open blue circles, heating filled red triangles.

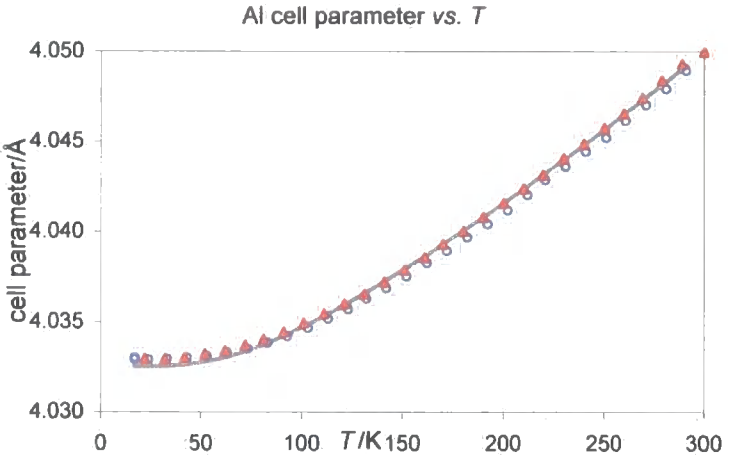

Figure 4.60 Aluminium cell parameter against temperature from d8_02305/6. Cooling data are open blue circles, heating filled red triangles, Wang and Reeber's data in grey.

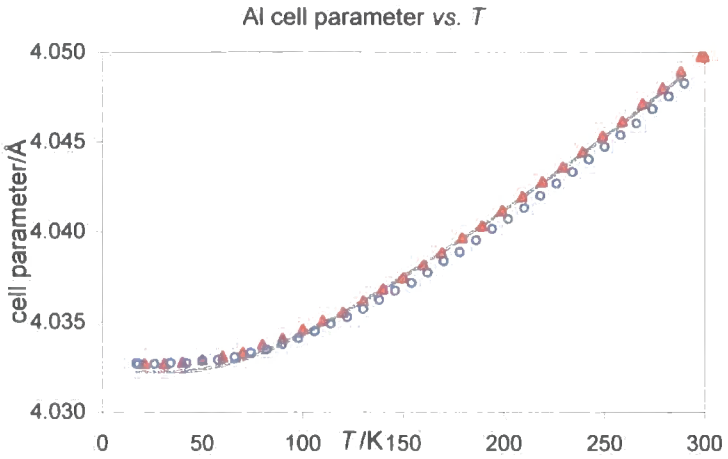

Figure 4.61 Aluminium cell parameter against temperature from d8_02440/1. Cooling data are open blue circles, heating filled red triangles, Wang and Reeber's data in grey.

The *a* cell parameter shows some unusual behaviour and departs from a simple phonon behaviour between 50 and 200 K. Due to the increased data collection time in experiments d8_02440 and d8_02441 compared to d8_02305 and d8_02306 the cell parameter data are less scattered, but show the same behaviour. To a much lesser extent, the *c* cell parameter data show a similar departure from the model thermal expansion behaviour around the same 80 – 160 K region. The *a* cell parameter also does not decrease to the same extent in the first experiment, as can clearly be seen from Figure 4.53 and Figure 4.54. Conversely, the *c* cell parameter in the first experiment decreases more than in the second. This means that the volume plots for both experiments are very similar, far more so than either of the cell parameters.

A plot of the cell volume (Figure 4.58) resembles far more the expected behaviour as the *a* cell parameter deviates above the expected behaviour, and the *c* slightly below. It is possible that this distortion of the unit cell (relative to the values expected at these temperatures) is an artefact of the seeded multi-temperature refinement process, but as it is not seen in any other experiments, nor reflected in the aluminium cell parameter data, this seems unlikely. It is further shown to be real behaviour by examination of plots of the other parameters included in the refinement shown in Appendix 3. The unusual features shown in the above figures are in no way mirrored by any of the other parameters, showing that the cell parameters are not becoming correlated to any of them. Also, using the simulated annealing *multitopas* approach discussed in Section 2.2.6 gave exactly the same cell parameters indicating that the refinement is not falling into false minima.

Table 4.23 Thermal expansion data from PheniX experiments on $Sr_2NiCu_2O_2Se_2$.

		a_0/Å	θ_1/K	$C_1/10^{-6}$	$\alpha_{(300\text{-}15K)}/10^{-6}$ K^{-1}
2441/2	a	4.01952(5)	533(29)	11.5(8)	4.4(4)
	c	18.22829(35)	197(4)	39.3(4)	29.4(4)
	v	294.52(1)	216(7)	51.8(8)	37.4(8)
2305/6	a	4.02143(4)	867(47)	18(2)	3.2(5)
	c	18.20891(78)	195(7)	44.8(5)	33.7(6)
	v	294.49(1)	217((5)	54.4(5)	39.2(6)

The Rietveld refinement performed on the summed data set from 17 K in experiment d8_02305 is shown in Figure 4.62. The calculated patterns show a good fit to the observed and give the following cell parameters: a = 4.02149(5) Å c = 18.20955(33) Å at 17 K and a = 4.02510(3) Å and c = 18.38071(23) Å at 300 K. The R-factors were $_wR_p$ = 17.26 and 14.64 % and R_{Bragg} 6.64 and 5.73 % at 17 and 300 K respectively. Other important structural least-squares parameters are summarised in Table 4.24 for the refinements performed on the long scans at 17 and 300 K.

Table 4.24 Atomic fractional coordinates and displacement parameter values for $Sr_2NiCu_2O_2Se_2$ at 17 and 300 K from d8_02305/6.

Site	z/c (17 K)	z/c (300 K)	B_{iso}/Å^2 (17 K)	B_{iso}/Å^2 (300 K)
Sr	0.0873(1)	0.0870(1)	-1.20(5)	-0.72(4)
Cu	0.25	0.25	-0.81(7)	0.45(7)
Ni	0	0	0.21(12)	0.39(11)
Se	0.1681(1)	0.1679(1)	-1.17(5)	-0.47(5)
O	0	0	0.07(32)	0.23(31)

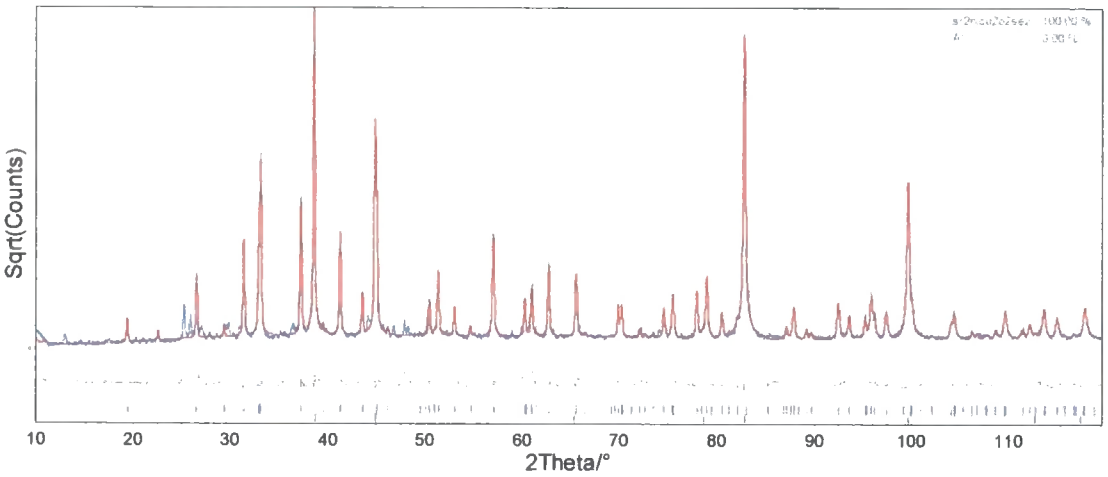

Figure 4.62 Rietveld refinement at 17 K of $Sr_2NiCu_2O_2Se_2$ from d8_02305. Observed pattern in blue, calculated in red, difference in grey. Tick marks show predicted peak positions for $Sr_2NiCu_2O_2Se_2$ and Al from top to bottom respectively.

Within experimental error, there is almost no difference between the z coordinates at 17 and 300 K of either the Sr or Se atoms. They are also very similar (differing in the 3rd or 4th

decimal place respectively) to the values from the room temperature d5000 Rietveld refinements given in Table 4.22.

Part of a pellet of sample number NDW250b was magnetically characterised by SQUID magnetometry using the sample preparation and experimental technique described in Section 2.3. Zero field cooled (ZFC) and field cooled (FC) experiments were conducted on this sample in a field of 100 Oe with measurements taken in 10 K steps from 10 – 290 K and the results shown in Figure 4.63. A magnetisation *vs.* applied field experiment was also performed at 290 K, and the results are shown in Figure 4.64. This shows a straight line crossing the origin indicating that the sample is paramagnetic.

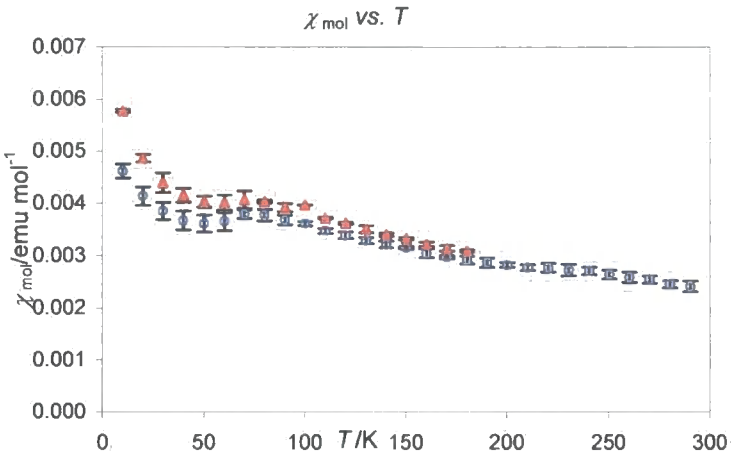

Figure 4.63 ZFC (open blue circles) and FC (filled red triangles) data for $Sr_2NiCu_2O_2Se_2$.

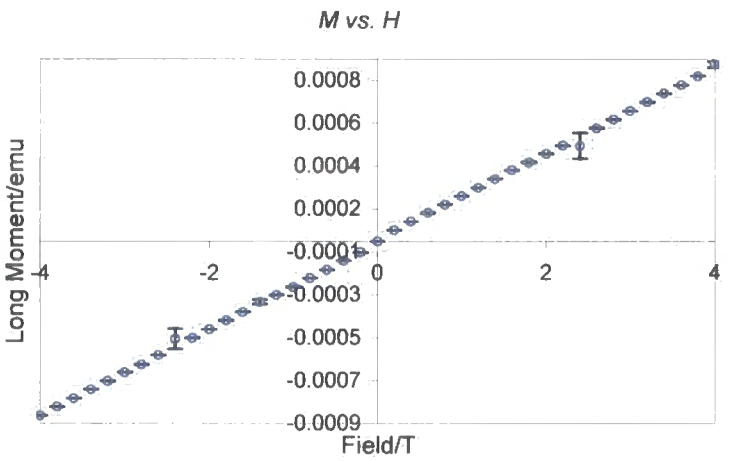

Figure 4.64 Magnetisation against applied field for $Sr_2NiCu_2O_2Se_2$, large error bars on points at +/- 2.2 T are artefacts of the experimental apparatus.

Figure 4.63 shows that both FC and ZFC sets of data closely match above 160 K. Below this point the ZFC data are clearly less than the FC data, possibly indicating some spin-glass type behaviour. However, both sets of data show that the increase in susceptibility stops at around 80 K. Below this point, the susceptibility decreases until around 40 K, suggesting

short range antiferromagnetic ordering. At low temperature a rise in susceptibility is observed. The possibility of small impurities causing this behaviour cannot be ruled out. The errors associated with these data are rather high, unfortunately more so at the lower temperatures where interesting behaviour can be observed. However, these do not obscure the fact that there is a clear difference between the two sets of data and that this unusual behaviour occurs at a similar temperature, 160 K, to the deviation in the *a* cell parameter.

Conductivity measurements were performed on pellet NDW268b according to the method described in Section 2.4. The contacts used were sputtered aluminium protected against oxidation with silver paint and then connected to the electrometer with soldered copper wires. The pellet was cooled to 80 K in the cryostat and resistance readings taking every 10 K. The pellet was then warmed to 300 K, with readings every 10 K. However, the software crashed between 90 and 170 K meaning there were no data recorded between these two temperatures. The results are shown in Figure 4.65. This shows that $Sr_2NiCu_2O_2Se_2$ is quite conducting with *R* changing from ~0.2 to ~0.13 Ω cm between 300 and 80 K respectively. The decrease is roughly linear over this temperature range and the fact that it decreases indicates metallic behaviour, which would agree with the low resistance values measured throughout. There is quite a lot of scatter in the data points which is believed to be due to the behaviour of the Keithley electrometer. However, this scatter, typically between 0.01 – 0.02 Ω cm, is again very small in the context of the range of resistances measured and discussed in this thesis; from 1 x 10^1 to 1 x 10^{10} Ω cm.

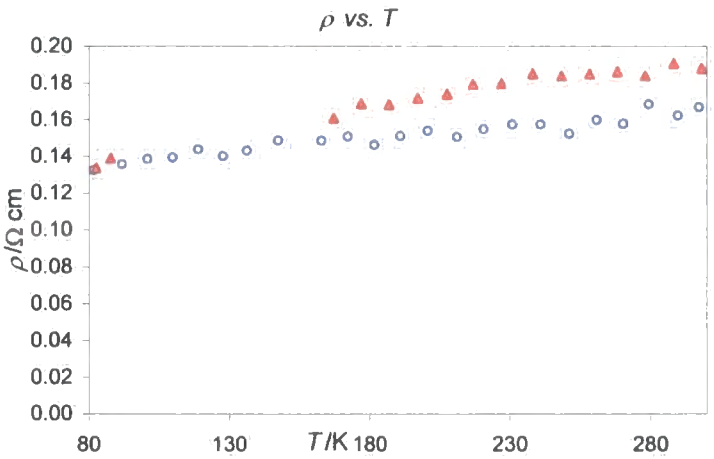

Figure 4.65 Resistivity versus temperature for $Sr_2NiCu_2O_2Se_2$. Open blue points are cooling data, filled red points heating.

4.4.2 $Ba_2NiCu_2O_2Se_2$

$Ba_2NiCu_2O_2Se_2$ was synthesised at a lower temperature than all the other $A_2MCu_2O_2X_2$ compounds; 750 °C rather than 800 °C. This was because attempts at 800 °C resulted in the pellet melting and nothing could be recovered from the quartz ampoule. The resultant black

powder was characterised by powder X-ray diffraction using the Siemens D5000 diffractometer and its structure confirmed by Rietveld refinement, as shown in Figure 4.66. The ${}_wR_p$ for the refinement was 9.47 %, χ^2 1.82 and R_{Bragg} for the phase was 4.70 %. Details of the important parameters from this refinement are given in Table 4.25.

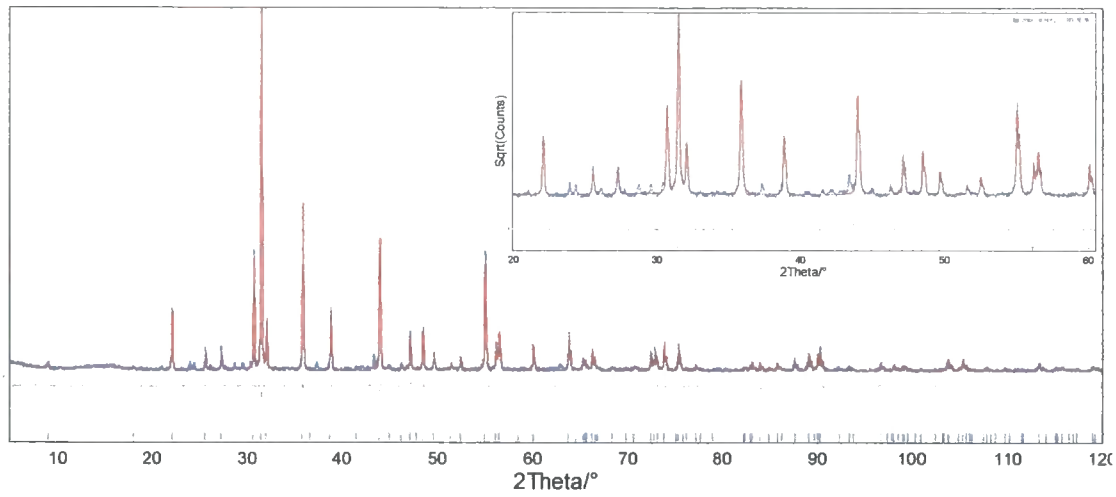

Figure 4.66 Rietveld refinement of $Ba_2NiCu_2O_2Se_2$. Observed pattern in blue, calculated in red and difference in grey. The vertical tick marks show predicted peak positions and the inset shows 20 – 60 ° 2θ region on a square root (counts) scale to emphasise weaker features in the pattern.

Table 4.25 Results of room temperature Rietveld refinement for $Ba_2NiCu_2O_2Se_2$.

$Ba_2NiCu_2O_2Se_2$	NDW334
Spacegroup	*I4/mmm*
a cell parameter/Å	4.123459(52)
c cell parameter/Å	19.65059(34)
Ba *z* coordinate/*c*	0.09149(8)
Se *z* coordinate/*c*	0.17488(13)
Ba B_{iso}/Å^2	0.14(5)
Cu B_{iso}/Å^2	1.29(11)
Ni B_{iso}/Å^2	9.90(37)
Se B_{iso}/Å^2	0.23(7)
O B_{iso}/Å^2	5.49(72)
${}_wR_p$/%	9.47
R_{Bragg}/%	4.70
χ^2	1.82
No. of parameters	36

Variable temperature powder X-ray diffraction experiments were performed on sample NDW334 in experiments d8_02451 and d8_02452. In experiment number d8_02451 it was cooled at 8 K hr^{-1} and data collected over a 5 – 120 ° 2θ range in 45 minute time slices. Nine 45 minute scans were performed at the base temperature and summed together giving the equivalent of one 6.75 hour data collection. In experiment d8_02452 the sample was then heated at 16 K hr^{-1} to 300 K and data collected over the same 2θ range as experiment d8_02451 in 30 minute time slices. Three 30 minute scans were performed at 300 K and summed together.

The data were analysed using the *multitopas* methodology described in Section 2.2.6. Figure 4.67 shows the variation of the *a* cell parameter with temperature and Figure 4.68 shows the *c* cell parameter. The variation of the Al cell parameter is shown in Figure 4.69 together with the fit to Wang and Reeber's data[6] as a grey line, which both cooling and heating data closely match.

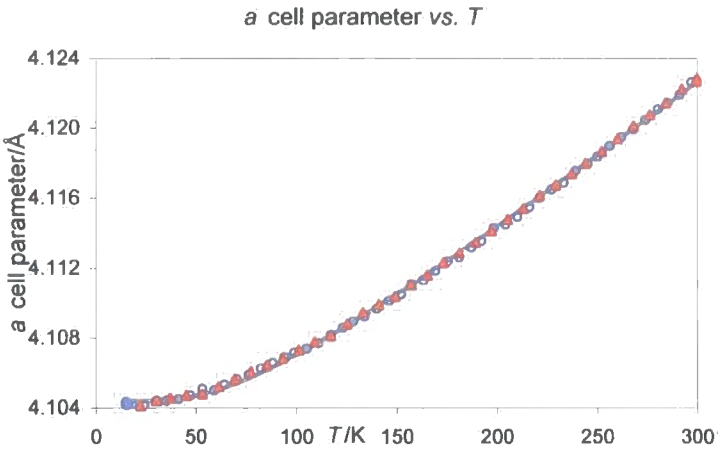

Figure 4.67 $Ba_2NiCu_2O_2Se_2$ *a* cell parameter against temperature. Cooling data are open blue circles, heating filled red triangles, fit to the experimental data using Equation 4.1 and the values in Table 4.26 in grey.

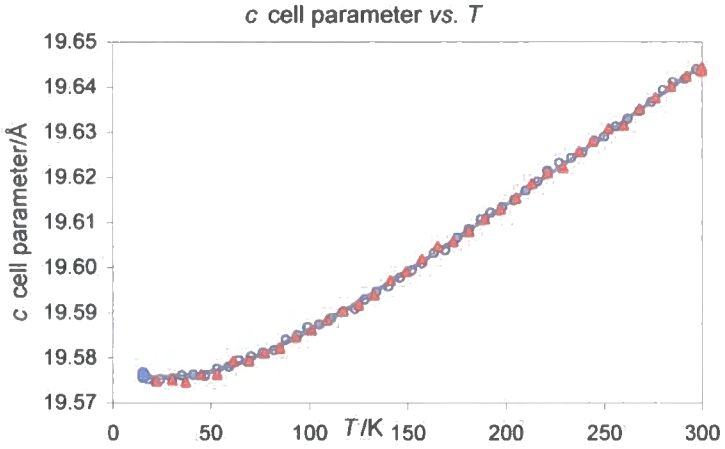

Figure 4.68 $Ba_2NiCu_2O_2Se_2$ *c* cell parameter against temperature from d8_02440/1. Cooling data are open blue circles, heating filled red triangles, fit to the experimental data using Equation 4.1 and the values in Table 4.26 in grey.

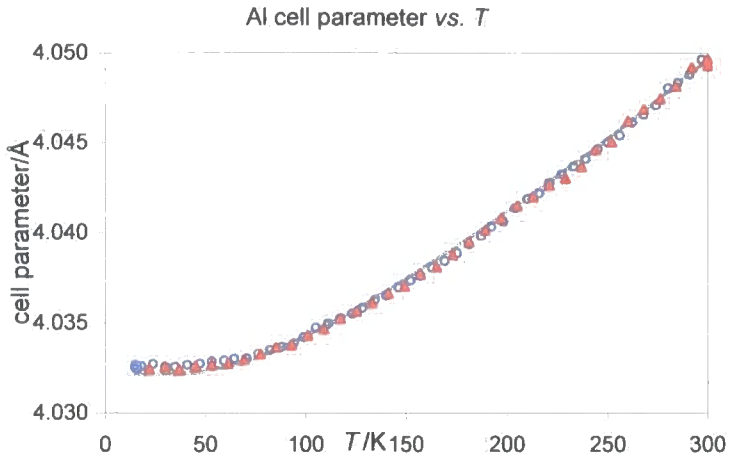

Figure 4.69 Aluminium cell parameter against temperature. Cooling data are open blue circles, heating filled red triangles, Wang and Reeber's data in grey.

Both *a* and *c* cell parameters vary smoothly with temperature and show no evidence of phase transitions. The parameters determined by a least-squares fit are shown in Table 4.26.

Table 4.26 Thermal expansion data from PheniX experiments on $Ba_2NiCu_2O_2Se_2$.

	a_0/Å	θ_1/K	$C_1/10^{-6}$	$\alpha_{(300\text{-}15K)}/10^{-6}$ K^{-1}
a	4.10440(4)	204(3)	21.2(1)	15.6(1)
c	19.57563(13)	195(3)	16.60(10)	12.4(1)

The Rietveld refinement performed on the summed data set from 17 K is shown in Figure 4.70. The calculated patterns show a good fit to the observed and give the following cell parameters: *a* = 4.10423(4) Å *c* = 19.57609(30) Å at 17 K and *a* = 4.12272(6) Å and *c* = 19.64397(41) Å at 300 K. The *R*-factors were $_wR_p$ = 15.06 and 20.63 % and R_{Bragg} 5.03 and 6.23 % at 17 and 300 K respectively. Other important structural least-squares parameters are summarised in Table 4.27 for the refinements performed on the long scans at 17 and 300 K.

Table 4.27 Atomic fractional coordinates and displacement parameter values for $Ba_2NiCu_2O_2Se_2$ at 17 and 300 K.

Site	*z*/*c* (17 K)	*z*/*c* (300 K)	B_{iso}/Å^2 (17 K)	B_{iso}/Å^2 (300 K)
Ba	0.09220(7)	0.0915(1)	-1.52(4)	-1.47(5)
Cu	0.25	0.25	-1.52(7)	-0.85(11)
Ni	0	0	4.57(25)	8.30(47)
Se	0.1755(1)	0.1750(2)	-1.74(5)	-1.58(7)
O	0	0	1.35(47)	6.02(1.05)

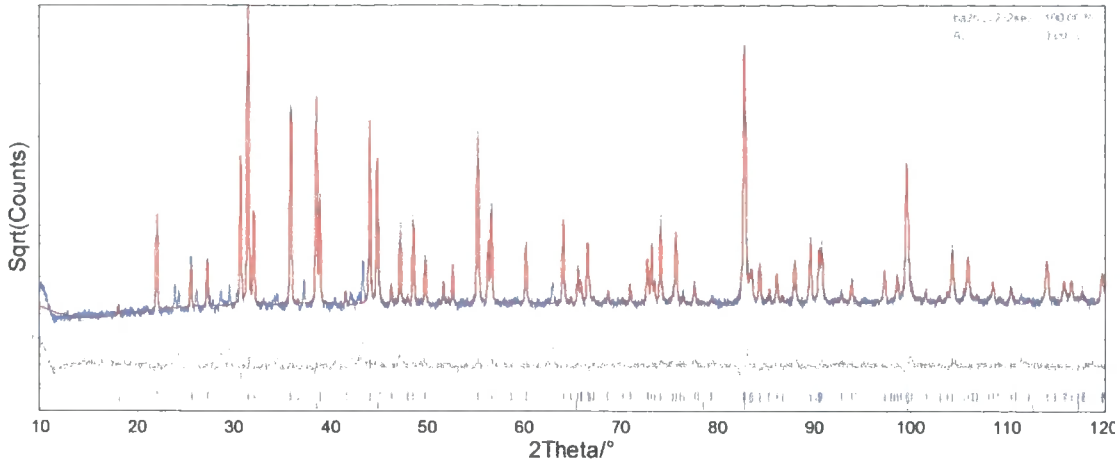

Figure 4.70 Rietveld refinement at 17 K of $Ba_2NiCu_2O_2Se_2$. Observed pattern in blue, calculated in red, difference in grey. Tick marks show predicted peak positions for $Ba_2NiCu_2O_2Se_2$ and Al from top to bottom respectively.

Within experimental error, there is very little difference between the *z* coordinates at 17 and 300 K of either the Ba or Se atoms. They are also very similar (differing in the 3rd or 4th decimal place) to the values from the room temperature d5000 Rietveld refinements given in Table 4.25. Together with the smooth change in lattice parameters this is an indication that there is no significant structural change beyond normal thermal expansion between 17 and 300 K.

Part of sample number NDW334 was loaded into a gelatine capsule as a loose powder and magnetically characterised by SQUID magnetometry using the sample preparation and experimental technique described in Section 2.3. Zero field cooled (ZFC) and field cooled (FC) experiments were conducted on this sample in a field of 100 Oe with measurements taken at 5 K steps from 10 – 290 K and the results shown in Figure 4.71. Magnetisation *vs.* applied field experiments was also performed at 290 and 10 K, and the results are shown in Figure 4.72 and Figure 4.73 respectively. At 290 K the magnetisation saturates in a field of less than 0.5 T at a magnetisation of ~ 0.0035 emu. There is no hysteresis around $H = 0$ T in either the 10 or 290 K sets of data. The magnetisation does not saturate, even at 2 T, in the 10 K experiment.

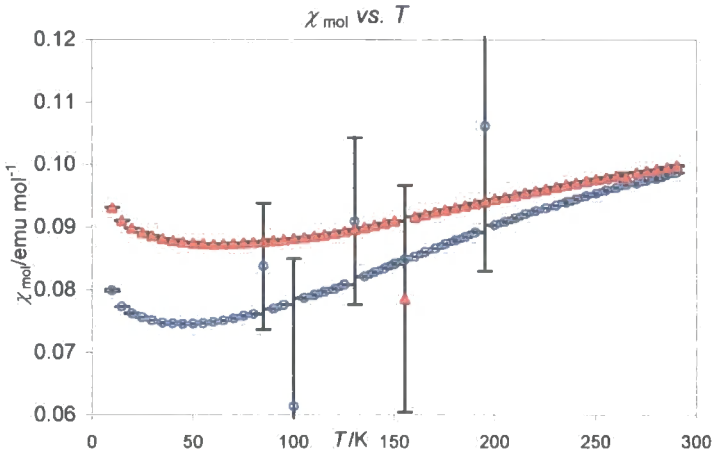

Figure 4.71 ZFC (open blue circles) and FC (filled red triangles) data for $Ba_2NiCu_2O_2Se_2$, large error bars artefacts of the experimental apparatus.

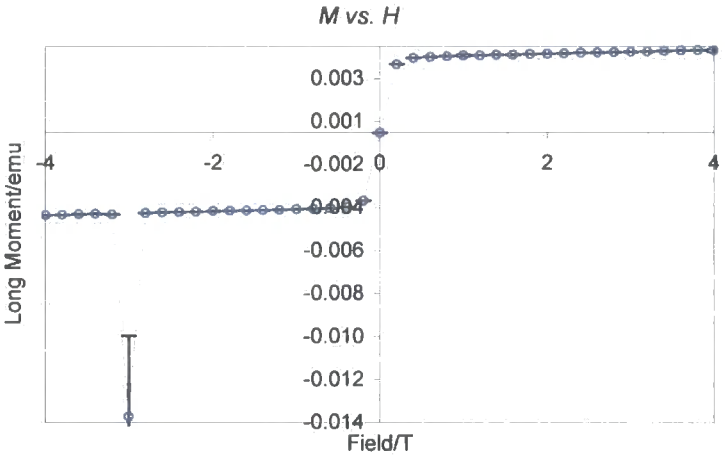

Figure 4.72 Magnetisation against applied field for $Ba_2NiCu_2O_2Se_2$ at 290 K, large error bar artefact of the experimental apparatus.

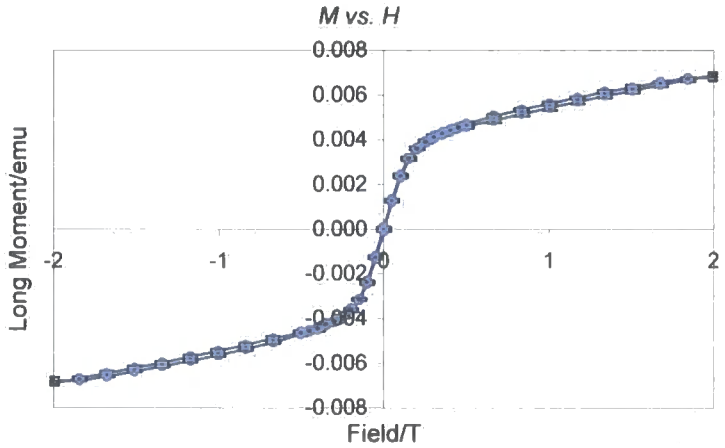

Figure 4.73 Magnetisation against applied field for $Ba_2NiCu_2O_2Se_2$ at 10 K.

Figure 4.71 shows that the susceptibility falls with decreasing temperature, for both the ZFC and FC data, indicative of anti-ferromagnetic behaviour, until around 30 – 40 K below which temperature it increases. This could be due to a paramagnetic impurity dominating the magnetisation at these low temperatures. There is also a considerable difference between the two sets of data, with a higher susceptibility for data recorded after cooling the sample in a field

4.4.3 *M* = Ni conclusions

The *M* = Sr, Ba; *X* = Se containing compounds of this series have been synthesised. They have been found to have very different thermal and magnetic behaviour. The *A* = Ba compound exhibits normal thermal expansion behaviour until around 200 K, above which temperature the cell expands more slowly than expected. The *A* = Sr compound shows extremely unusual behaviour, with the *a* cell axis expanding at a greater rate than expected between 80 and 160 K, but following the expected behaviour outside that temperature range. Interestingly, this unusual behaviour at 80 K corresponds with changes in the magnetic properties. This is considerably different from the *A* = Ba compound which shows antiferromagnetic behaviour above 40 K. The *A* = Sr compound was found to show metallic conductivity, with $\rho_{(300\ K)}$ = 0.273(22) Ω.

4.5 Zn containing phases

In contrast to the *M* = Mn, Ni phases, in the *M* = Zn containing compounds neither of the *A* = Ba members could be synthesised, but both of the *A* = Sr could. In addition to the $BaCu_2X_2$ impurities encountered in previous syntheses, a major impurity phase present in these compounds was ZnO. Both the *A* = Sr members were synthesised with high purity using 13 mm pellets at 800 °C. $Sr_2ZnCu_2O_2S_2$ was an olive green powder when synthesised and $Sr_2ZnCu_2O_2Se_2$ was a dark red to brown colour.

4.5.1 $Sr_2ZnCu_2O_2S_2$

$Sr_2ZnCu_2O_2S_2$ was synthesised as discussed in Section 2.1.2, characterised by powder X-ray diffraction using the Siemens D5000 diffractometer and its structure confirmed by Rietveld refinement, as shown in Figure 4.74. The ${}_wR_p$ for the refinement was 6.11 %, χ^2 1.66 and R_{Bragg} for the phase was 4.73 %. Details of the important parameters from this refinement are given in Table 4.28.

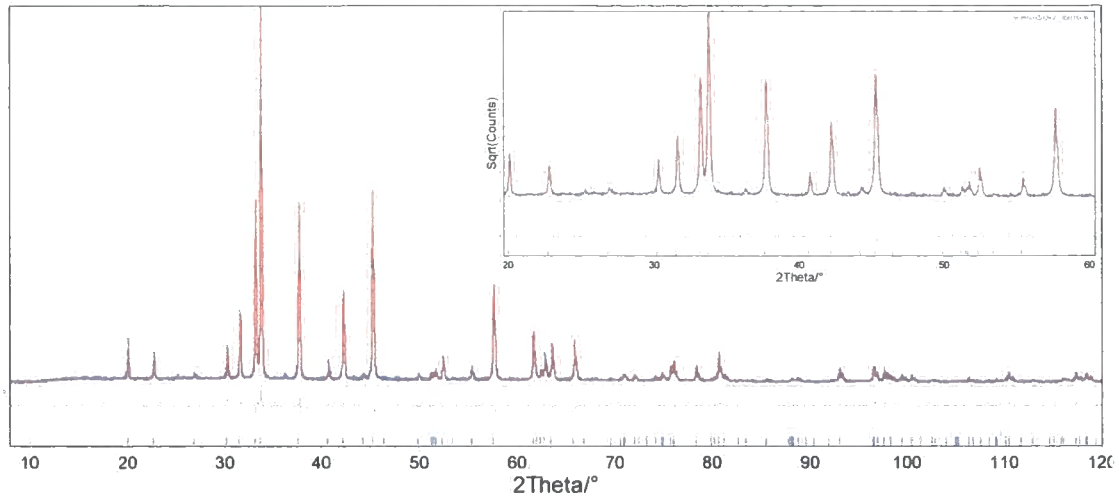

Figure 4.74 Rietveld refinement of $Sr_2ZnCu_2O_2S_2$. Observed pattern in blue, calculated in red and difference in grey. The vertical tick marks show predicted peak positions and the inset shows 20 – 60 ° 2θ region on a square root (counts) scale to emphasise weaker features in the pattern.

Table 4.28 Results of room temperature Rietveld refinement for $Sr_2ZnCu_2O_2S_2$.

$Sr_2ZnCu_2O_2S_2$	NDW301
Spacegroup	*I4/mmm*
a cell parameter/Å	4.010869(42)
c cell parameter/Å	17.74020(26)
Sr *z* coordinate/*c*	0.0911(1)
S *z* coordinate/*c*	0.1735(2)
Sr B_{iso}/Å^2	3.98(4)
Cu B_{iso}/Å^2	4.96(6)
Zn B_{iso}/Å^2	4.33(7)
S B_{iso}/Å^2	4.30(11)
O B_{iso}/Å^2	4.77(23)
$_wR_p$/%	5.43
R_{Bragg}/%	3.00
χ^2	1.66
No. of parameters	36

Variable temperature powder X-ray diffraction experiments were performed on sample NDW301 in experiments d8_02454 and d8_02455. In experiment number d8_02454 it was cooled at 8 K hr^{-1} and data collected over a 5 – 120 ° 2θ range in 45 minute time slices. Twenty-one 45 minute scans were performed at the base temperature and summed together giving the equivalent of one 15.75 hour data collection. In experiment d8_02455 the sample was then heated at 16 K hr^{-1} to 300 K and data collected over the same 2θ range as experiment d8_02455 in 30 minute time slices. Seventeen 30 minute scans were performed at 300 K and summed together.

The data were analysed using the *multitopas* methodology described in Section 2.2.6. Figure 4.75 shows the variation of the *a* cell parameter with temperature and Figure 4.76 shows the *c* cell parameter. The variation of the Al cell parameter is shown in Figure 4.77 together with

the fit to Wang and Reeber's data[6] as a grey line, which both cooling and heating data match quite well, apart from a very small discrepancy at temperatures less than ~60 K.

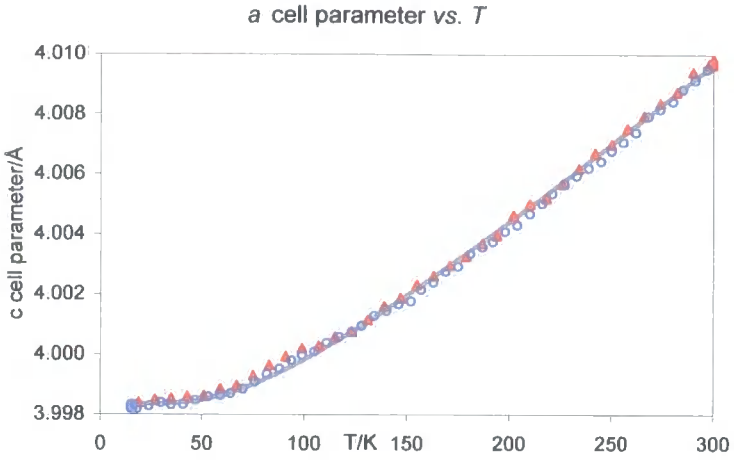

Figure 4.75 $Sr_2ZnCu_2O_2S_2$ *a* cell parameter against temperature. Cooling data are open blue circles, heating filled red triangles, fit to the experimental data using Equation 4.1 and the values in Table 4.29 in grey.

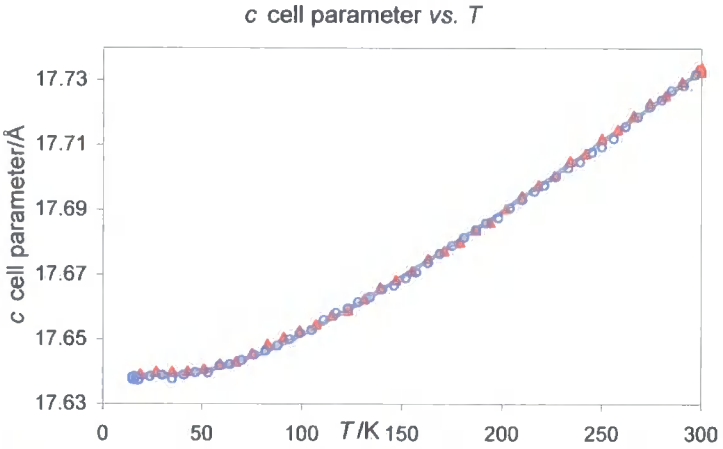

Figure 4.76 $Sr_2ZnCu_2O_2S_2$ *c* cell parameter against temperature. Cooling data are open blue circles, heating filled red triangles, fit to the experimental data using Equation 4.1 and the values in Table 4.29 in grey.

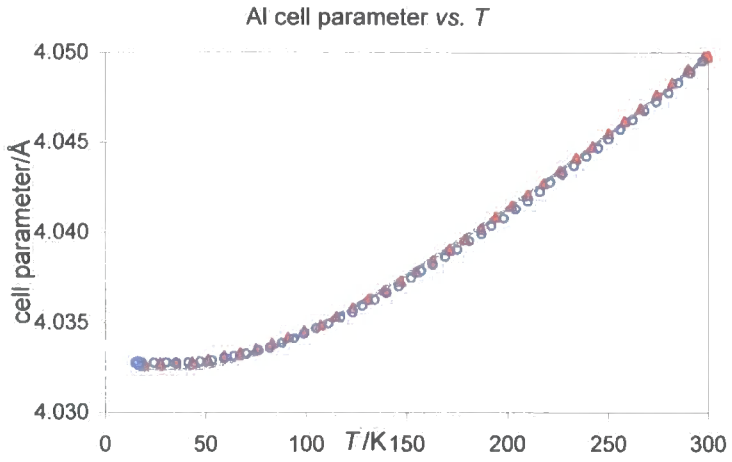

Figure 4.77 Aluminium cell parameter against temperature. Cooling data are open blue circles, heating filled red triangles, Wang and Reeber's data in grey.

Both *a* and *c* cell parameters vary smoothly with temperature and show no evidence for phase transitions. The parameters determined by a least-squares fit are shown in Table 4.29.

Table 4.29 Thermal expansion data from PheniX experiments on $Sr_2ZnCu_2O_2S_2$.

	a_0/Å	θ_1/K	$C_1/10^{-6}$	$\alpha_{(300\text{-}15K)}/10^{-6}$ K^{-1}
a	3.99836(3)	228(6)	14.1(2)	9.9(2)
c	17.63883(18)	221(3)	26.3(1)	18.7(2)

The Rietveld refinement performed on the summed data set from 17 K is shown in Figure 4.78. The calculated patterns show a good fit to the observed and give the following cell parameters: *a* = 3.99834(6) Å *c* = 17.63897(37) Å at 17 K and *a* = 3.99844(8) Å and *c* = 17.63923(50) Å at 300 K. The *R*-factors were $_wR_p$ = 14.36 and 20.52 % and R_{Bragg} 5.66 and 7.50 % at 17 and 300 K respectively. Other important structural least-squares parameters are summarised in Table 4.30 for the refinements performed on the long scans at 17 and 300 K.

Table 4.30 Atomic fractional coordinates and displacement parameter values for $Sr_2ZnCu_2O_2S_2$ at 17 and 300 K.

Site	*z*/*c* (17 K)	*z*/*c* (300 K)	B_{iso}/Å^2 (17 K)	B_{iso}/Å^2 (300 K)
Ba	0.0919(1)	0.0917(2)	-0.33(6)	-0.64(8)
Cu	0.25	0.25	-0.46(7)	-0.69(9)
Ni	0	0	-2.37(8)	-2.49(11)
Se	0.1744(3)	0.1746(4)	-0.76(11)	-1.03(15)
O	0	0	1.24(34)	0.87(49)

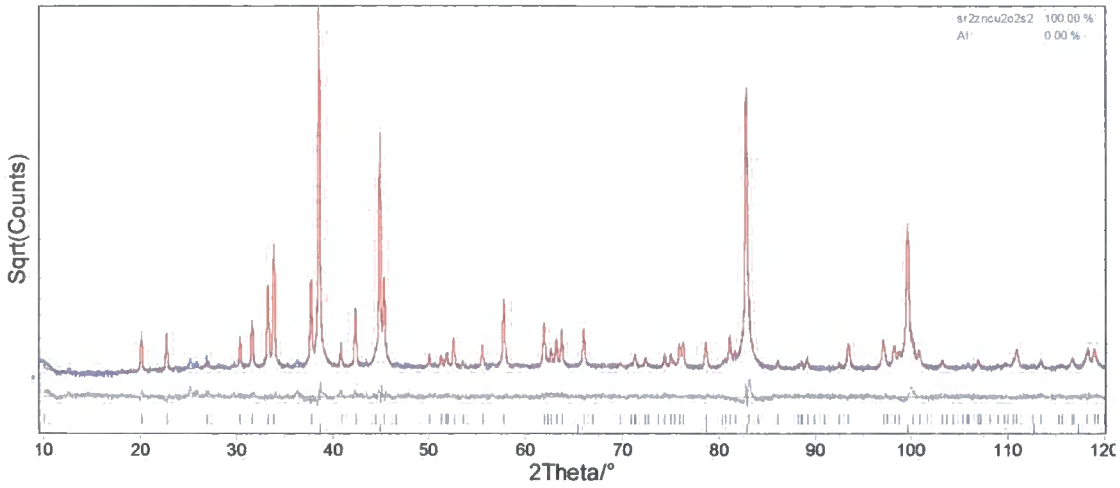

Figure 4.78 Rietveld refinement at 17 K of $Sr_2ZnCu_2O_2S_2$. Observed pattern in blue, calculated in red, difference in grey. Tick marks show predicted peak positions for $Sr_2ZnCu_2O_2S_2$ and Al from top to bottom respectively.

Within experimental error, there is no difference between the *z* coordinates at 17 and 300 K of either the Sr or S atoms. They are also very similar (differing in the 3rd or 4th decimal place) to the values from the room temperature d5000 Rietveld refinements given in Table 4.28. Together with the smooth change in lattice parameters this is an indication that there is no significant structural change beyond normal thermal expansion between 17 and 300 K.

4.5.2 $Sr_2ZnCu_2O_2Se_2$

$Sr_2ZnCu_2O_2Se_2$ was synthesised as discussed in Section 2.1.2, characterised by powder X-ray diffraction using the Siemens D5000 diffractometer and its structure confirmed by Rietveld refinement, as shown in Figure 4.79. The ${}_wR_p$ for the refinement was 8.70 % and R_{Bragg} for the phase was 4.01 %. Details of the important parameters from this refinement are given in Table 4.31.

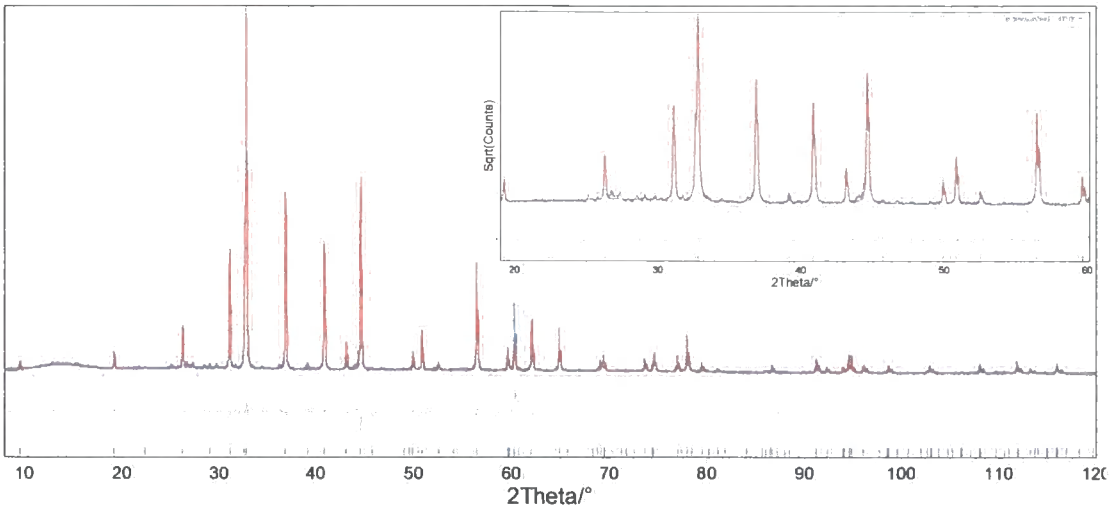

Figure 4.79 Rietveld refinement of $Sr_2ZnCu_2O_2Se_2$. Observed pattern in blue, calculated in red and difference in grey. The vertical tick marks show predicted peak positions and the inset shows 20 – 60 ° 2θ region on a square root (counts) scale to emphasise weaker features in the pattern.

Table 4.31 Results of room temperature Rietveld refinement for $Sr_2ZnCu_2O_2Se_2$.

$Sr_2ZnCu_2O_2Se_2$	NDW301
Spacegroup	*I4/mmm*
a cell parameter/Å	4.062513(37)
c cell parameter/Å	18.40196(23)
Sr *z* coordinate/*c*	0.0872(1)
Se *z* coordinate/*c*	0.1684(1)
Sr B_{iso}/Å^2	1.67(6)
Cu B_{iso}/Å^2	2.37(9)
Zn B_{iso}/Å^2	1.89(12)
Se B_{iso}/Å^2	1.59(6)
O B_{iso}/Å^2	2.04(36)
$_wR_p$/%	8.70
R_{Bragg}/%	4.01
R_{exp}/%	3.74
No. of parameters	31

Variable temperature powder X-ray diffraction experiments were performed on sample NDW302 in experiments d8_02457 and d8_02458. In experiment number d8_02457 it was cooled at 10 K hr^{-1} and data collected over a 5 – 120 ° 2θ range in 45 minute time slices. Three 45 minute scans were performed at the base temperature and summed together giving the equivalent of one 2.25 hour data collection. In experiment d8_02458 the sample was then heated at 8 K hr^{-1} to 300 K and data collected over the same 2θ range as experiment d8_02457 in 60 minute time slices. Five 30 minute scans were performed at 300 K and summed together.

The data were analysed using the *multitopas* methodology described in Section 2.2.6. Figure 4.80 shows the variation of the *a* cell parameter with temperature and Figure 4.81 shows the *c* cell parameter. The variation of the Al cell parameter is shown in Figure 4.82 together with

the fit to Wang and Reeber's data[6] as a grey line, which both cooling and heating data are systematically lower than above temperatures of ~60 K.

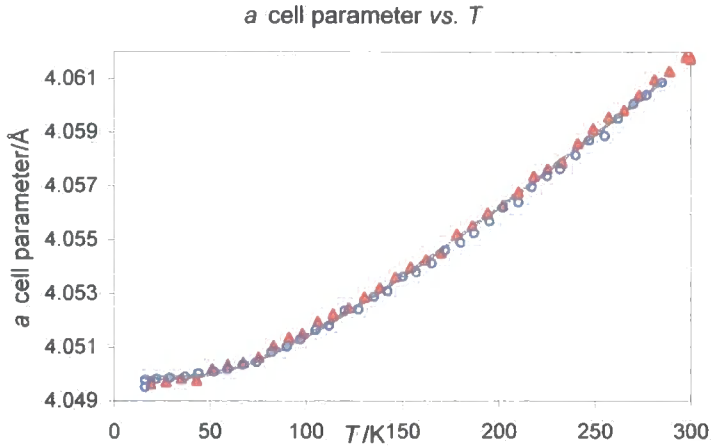

Figure 4.80 $Sr_2ZnCu_2O_2Se_2$ *a* cell parameter against temperature. Cooling data are open blue circles, heating filled red triangles, fit to the experimental data using Equation 4.1 and the values in Table 4.32 in grey.

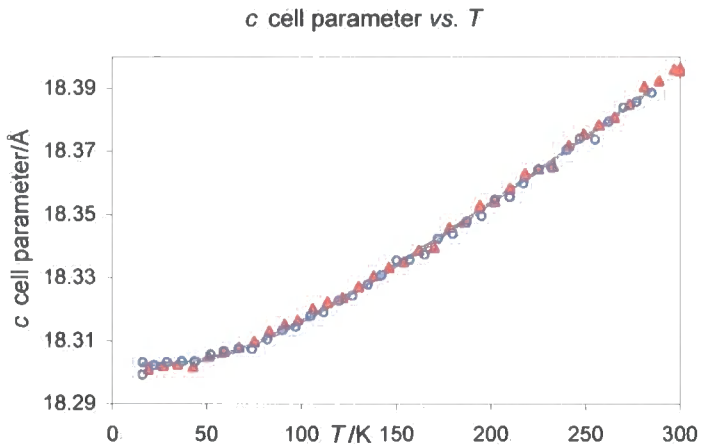

Figure 4.81 $Sr_2ZnCu_2O_2Se_2$ *c* cell parameter against temperature. Cooling data are open blue circles, heating filled red triangles, fit to the experimental data using Equation 4.1 and the values in Table 4.32 in grey.

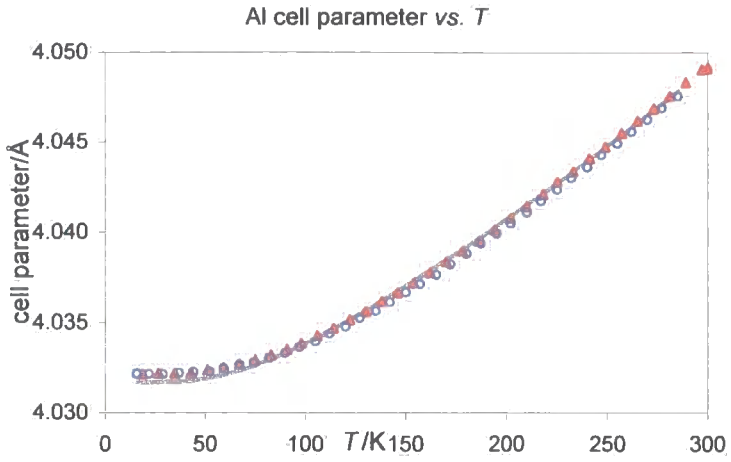

Figure 4.82 Aluminium cell parameter against temperature. Cooling data are open blue circles, heating filled red triangles, Wang and Reeber's data in grey.

Both *a* and *c* cell parameters vary smoothly with temperature and show no phase transitions. As was the case for $Ba_2CoCu_2O_2Se_2$, the aluminium cell parameter is systematically lower than those in the literature. Again, any small change in the recorded temperature would not significantly affect the plots of the cell parameters. The parameters determined by a least-squares fit are shown in Table 4.32.

Table 4.32 Thermal expansion data from PheniX experiments on $Sr_2ZnCu_2O_2Se_2$.

	a_0/Å	θ_1/K	$C_1/10^{-5}$	$\alpha_{(300\text{-}15K)}/10^{-6}$ K^{-1}
a	4.04987(5)	229(6)	14.6(2)	10.3(2)
c	18.30258(37)	204(6)	24.3(3)	17.9(3)

The Rietveld refinement performed on the summed data set from 17 K is shown in Figure 4.83. The calculated patterns show a good fit to the observed and give the following cell parameters: *a* = 4.048148(33) Å *c* = 18.29377(25) Å at 17 K and *a* = 4.060028(35) Å and *c* = 18.38761(26) Å at 300 K. The *R*-factors were $_wR_p$ = 27.82 and 14.83 % and R_{Bragg} 5.78 and 4.68 % at 17 and 300 K respectively. Other important structural least-squares parameters are summarised in Table 4.33 for the refinements performed on the long scans at 17 and 300 K.

Table 4.33 Atomic fractional coordinates and displacement parameter values for $Sr_2ZnCu_2O_2Se_2$ at 17 and 300 K.

Site	z/c (17 K)	z/c (300 K)	B_{iso}/Å^2 (17 K)	B_{iso}/Å^2 (300 K)
Ba	0.0875(1)	0.0874(1)	0.05(5)	0.61(6)
Cu	0.25	0.25	0.17(6)	1.30(8)
Ni	0	0	1.00(10)	1.25(11)
Se	0.1690(1)	0.1688(1)	-0.06(5)	0.41(6)
O	0	0	3.23(42)	2.71(43)

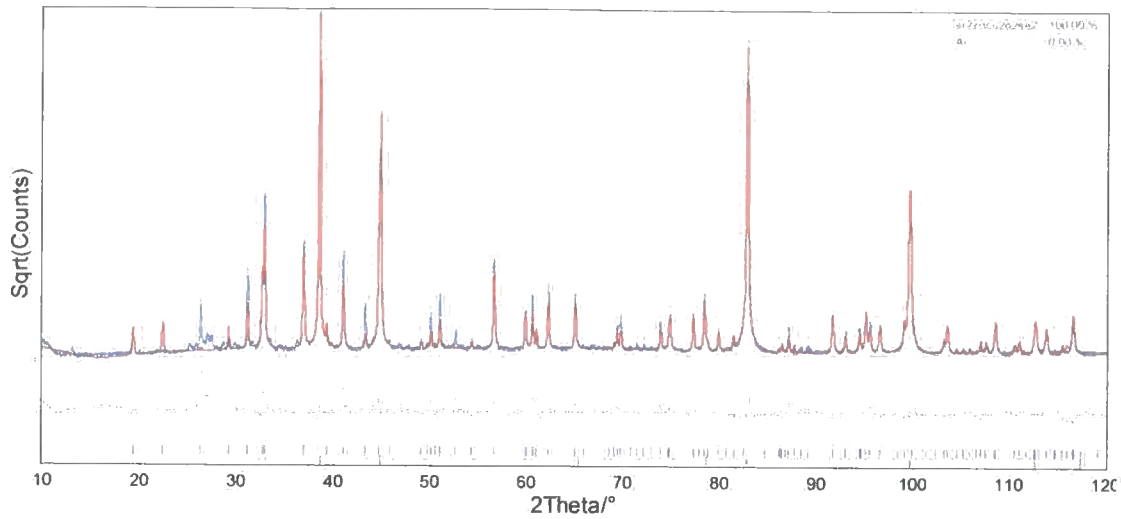

Figure 4.83 Rietveld refinement at 17 K of $Sr_2ZnCu_2O_2Se_2$. Observed pattern in blue, calculated in red, difference in grey. Tick marks show predicted peak positions for $Sr_2ZnCu_2O_2Se_2$ and Al from top to bottom respectively.

Within experimental error, there is no difference between the *z* coordinates at 17 and 300 K of either the Sr or Se atoms. They are also very similar (differing in the 3rd or 4th decimal place) to the values from the room temperature d5000 Rietveld refinements given in Table 4.31. Together with the smooth change in lattice parameters this is an indication that there is no significant structural change beyond normal thermal expansion between 17 and 300 K.

4.5.3 *M* = Zn conclusions

Both *A* = Sr containing members of the $A_2ZnCu_2O_2X_2$ family have been synthesised and their structures characterised by powder X-ray diffraction. Their structures have been studied from 300 – 16 K using variable temperature X-ray diffraction and shown to follow typical thermal expansion properties.

4.6 Overall conclusions

In this section some overall conclusions are drawn. The reader is again referred to Appendices 1.3 – 1.12 for graphical summaries of the various experiments discussed in this chapter.

Table 4.34 summarises the cell parameters and fractional *z* coordinate of the synthesised $A_2MCu_2O_2X_2$ compounds. There is a possibility that the accuracy of these figures is overstated, *i.e.* 0.000001 Å, but the estimated standard uncertainties generated by Rietveld refinement (by Topas/GSAS) have been shown to be fairly believable. However, as this was for extremely well characterised and simple structures (NIST Si and Y_2O_3), rather than the

more complex and less well known structures detailed in Table 4.34 it may be that the actual uncertainty in the figures is greater.

Table 4.34 Cell parameters and non special position atomic coordinates for $A_2MCu_2O_2X_2$.

Compound	a/Å	c/Å	A z/c	X z/c	$_wR_p$/%	R_{Bragg}/%
$Sr_2MnCu_2O_2Se_2$	4.073157(86)	17.88003(58)	0.0931(2)	0.1667(2)	9.87	5.10
$Ba_2MnCu_2O_2Se_2$	4.189527(75)	18.99212(47)	0.09273(9)	0.1747(2)	8.45	2.45
$Sr_2CoCu_2O_2S_2$	3.989105(90)	17.70326(55)	0.09250(10)	0.1720(2)	6.66	2.45
$Sr_2CoCu_2O_2Se_2$	4.052293(36)	18.34518(22)	0.08813(8)	0.16741(9)	6.75	1.35
$Ba_2CoCu_2O_2S_2$	4.064065(86)	18.88718(61)	0.9036(1)	0.1762(5)	12.29	3.60
$Ba_2CoCu_2O_2Se_2$	4.140735(62)	19.29280(40)	0.0924(1)	0.1744(2)	10.19	1.97
$Sr_2NiCu_2O_2Se_2$	4.024369(49)	18.40447(28)	0.086820(9)	0.1676(1)	8.89	4.69
$Ba_2NiCu_2O_2Se_2$	4.122786(53)	19.65312(36)	0.09214(9)	0.1756(1)	9.47	4.70
$Sr_2ZnCu_2O_2S_2$	4.010863(43)	17.74018(26)	0.09111(7)	0.1733(2)	5.43	3.00
$Sr_2ZnCu_2O_2Se_2$	4.062384(50)	18.40154(29)	0.0873(1)	0.1690(1)	8.70	4.01

4.6.1 Cu occupancy

Table 4.35 summarises the results from the refinements before and after the Cu fractional occupancy was included in the refinement, including the value for the occupancy, the *R*-factors, constrained displacement parameter and *A* and *X z* coordinate. Apart from the rather unusual instance of 0.7486(48) atoms per site found for the $Sr_2MnCu_2O_2Se_2$ data, all the others vary between 0.91 and 0.99 atoms per site. It perhaps surprising that for exactly half the compounds, the R_{Bragg} is improved by the inclusion of the Cu occupancy in the refinement, while in the other half it is made worse. The uncertainty in the value of the occupancy is between 0.002 and 0.01 (or 0.2 and 1 %) atom per site, far below the occupancy itself, indicating that it is meaningful to compare these values. The observation that refined occupancies for the majority of phases is > 0.95 suggests that Cu partial occupancy is not a significant phenomenon in these materials. However, investigating effects this subtle with lab powder X-ray diffraction data should be done with caution due to correlation with between structural parameters. For instance, there may be dynamic disorder on the copper sites, rather than partial occupancy. For this to be properly solved more powerful techniques such as neutron or synchrotron X-ray powder diffraction would be required, or single crystals to be studied.

Table 4.35 *R*-factors and atomic parameters for Rietveld refinements before and after including refined Cu occupancies.

Compound		$_wR_p$	R_{Bragg}	*A* z	*X* z	Cu Occ	B_{iso}/Å^2
$Sr_2MnCu_2O_2Se_2$	Before	10.96	5.39	0.0931(2)	0.1667(2)	1	
	After	8.55	2.75	0.0944(1)	0.1680(1)	0.749(5)	1.00(4)
$Ba_2MnCu_2O_2Se_2$	Before	8.82	2.28	0.09273(9)	0.1747(2)	1	
	After	9.00	3.16	0.09322(10)	0.1743(2)	0.984(6)	1.52(4)
$Sr_2CoCu_2O_2S_2$	Before	7.11	2.49	0.09250(10)	0.1720(2)	1	
	After	6.85	1.36	0.09288(9)	0.1706(2)	0.916(4)	0.95(4)
$Sr_2CoCu_2O_2Se_2$	Before	7.52	2.28	0.08813(8)	0.16741(9)	1	
	After	7.27	1.64	0.08850(8)	0.16772(9)	0.925(3)	1.63(3)
$Ba_2CoCu_2O_2S_2$	Before	12.92	3.57	0.9036(1)	0.1762(5)	1	
	After	13.01	3.83	0.9036(1)	0.1775(5)	0.9380(9)	-0.31(5)
$Ba_2CoCu_2O_2Se_2$	Before	10.74	2.31	0.0924(1)	0.1744(2)	1	
	After	10.80	2.53	0.0926(1)	0.1744(2)	0.971(7)	1.14(4)
$Sr_2NiCu_2O_2Se_2$	Before	9.19	5.04	0.08682(10)	0.1676(1)	1	
	After	8.271	2.035	0.08701(9)	0.1672(1)	0.941(4)	1.60(3)
$Ba_2NiCu_2O_2Se_2$	Before	9.97	4.62	0.09214(9)	0.1757(1)	1	
	After	10.68	6.47	0.0925 (1)	0.1741(2)	0.987(7)	0.48(4)
$Sr_2ZnCu_2O_2S_2$	Before	5.43	3.00	0.09111 (7)	0.17330(2)	1	
	After	5.50	2.88	0.09152 (6)	0.1723(1)	0.967(2)	1.36(2)
$Sr_2ZnCu_2O_2Se_2$	Before	9.05	4.22	0.0873(1)	0.1689(1)	1	
	After	9.02	4.34	0.0874(1)	0.1684(1)	0.957(4)	1.72(3)

The Cu deficiency will mean that in order to charge-balance, some of the *M* metal will be in a higher oxidation state, with corresponding effects on the physical properties as is seen in the magnetic behaviour of the *M* = Mn containing compounds.

4.6.2 Thermal expansion

With the exception of $Ba_2CoCu_2O_2S_2$ and $Sr_2NiCu_2O_2Se_2$ all members of the $A_2MCu_2O_2X_2$ family of compounds follow a well modelled thermal expansion profile, fitting Equation 4.1 well. $Ba_2CoCu_2O_2S_2$ subtly deviates from this modelled behaviour with the *c* cell parameter being below and then above the expected value between 50 and 150 K and 150 and 250 K respectively. $Sr_2NiCu_2O_2Se_2$ shows more complex behaviour in the *a* cell parameter with a large departure from expected behaviour between around 80 and 160 K. However, the cell volume for both these exceptions shows much more expected behaviour.

These smoothly changing unit cells and the lack of change in the fractional atomic coordinates show that there are no structural phase transitions present in any of the samples studied, in contrast to those described in Chapter 3.

Table 4.36 summarises the thermal expansion parameters calculated from PheniX experiments on the $A_2MCu_2O_2X_2$ compounds.

Table 4.36 Summary of thermal expansion parameters for $A_2MCu_2O_2X_2$ compounds.

Compound	a_0/Å	θ_1 (a)/K	c_1(a)/10^{-6}	$\alpha_{(300\text{-}15K)}$ (a)/ $10^{-6}K^{-1}$	c_0/Å	θ_1 (c)/K	c_1 (c)/10^{-6}	$\alpha_{(300\text{-}15K)}$ (c)/ 10^{-6} K^{-1}	α_c/α_a	Al a_0/Å
$_2$MnCu$_2$O$_2$Se$_2$	4.05315(5)	223(9)	13. 7(3)	9.7(3)	18.16950(43)	196(8)	25.8(4)	19.3(4)	2.0(1)	4.03179(4)
$_2$MnCu$_2$O$_2$Se$_2$	4.17905(4)	181(6)	15.0(2)	11.5(2)	18.85997(23)	206(6)	23.4(3)	17.2(3)	1.50(5)	4.03232(6)
$_2$CoCu$_2$O$_2$S$_2$	3.97922(9)	217(14)	12.4(3)	8.9(4)	17.59383(60)	273(11)	32.6(7)	21.1(7)	2.4(2)	4.03192(6)
$_2$CoCu$_2$O$_2$Se$_2$	4.04054(5)	223(8)	13.4(2)	9.5(2)	18.22487(31)	226(6)	29.4(4)	20.8(4)	2.19(9)	4.03211(6)
$_2$CoCu$_2$O$_2$S$_2$	4.05347(6)	442(18)	17.8(7)	8.2(5)	18.77306(58)	142(7)	26.0(3)	21.5(4)	2.6(2)	4.03260(3)
$_2$CoCu$_2$O$_2$Se$_2$	4.12838(4)	230(6)	14.8(2)	10.3(2)	19.17908(19)	224(3)	27.5(2)	19.5(2)	1.90(6)	4.03163(4)
NiCu$_2$O$_2$Se$_2$ 2441/2	4.01952(5)	533(29)	11.5(8)	4.4(4)	18.22829(35)	197(4)	39.3(4)	29.4(4)	6.7(7)	4.03254(4)
2305/6	4.02143(4)	867(47)	18(2)	3.2(5)	18.20891(78)	195(7)	44.8(5)	33.7(6)	11(2)	4.03218(5)
$_2$NiCu$_2$O$_2$Se$_2$	4.10440(4)	204(3)	21.2(1)	15.6(1)	19.57563(13)	195(3)	16.60(10)	12.4(1)	0.79(1)	4.03213(3)
ZnCu$_2$O$_2$S$_2$	3.99836(3)	228(6)	14.1(2)	9.9(2)	17.63883(18)	221(3)	26.3(1)	18.7(2)	1.90(6)	4.03232(3)
ZnCu$_2$O$_2$Se$_2$	4.04987(5)	229(6)	14.6(2)	10.3(2)	18.30258(37)	204(6)	24.3(3)	17.9(3)	1.74(6)	4.03169(3)

The value of α_c/α_a is a measure of the isotropy of the expansion and for all bar the M = Ni samples varies from 1.5 – 2.6. The values for the Ni containing compounds are very different, with $Sr_2NiCu_2O_2Se_2$ having a much higher value (6.7(7) and 11(2) for the two experiments) and $Ba_2NiCu_2O_2Se_2$ having a much lower value (0.79(1)).

4.6.3 Magnetic properties

Both M = Mn containing compounds show similar Curie-Weiss behaviour, but the other M = Co, Ni compounds show more complex behaviour. The four different M = Co compounds themselves show quite differing behaviour, with only the two A = Ba compounds showing similar behaviour. The two M = Ni compounds also show quite different behaviour, although these are both quite small effects when viewed on a full scale. This shows that even the subtle change in environment between *e.g.* A = Sr and Ba or X = S and Se has a significant difference on the magnetic properties of the sample, which is mainly determined by the transition metal, M, contained.

4.6.4 Resistivity

Table 4.37 summarises the resistivities of the compounds discussed in this chapter at around 80 and 300 K. The resistivity of $Ba_2CoCu_2O_2X_2$ is much larger for the X = S compound than for the X = Se, as would be expected. For $A_2CoCu_2O_2X_2$, the A = Sr compound is more conducting that the A = Ba, but to much less an extent (only a factor of ~7, rather than ~70 for S/Se). For $Sr_2MCu_2O_2Se_2$ the M = Co compound is more resistive than the M = Ni compound. This implies that the A site metal only has a minor impact on the band structure

of the $A_2MCu_2O_2X_2$ series of materials when compared to that of the *M* or *X* sites. This is because the *A* metal is unlikely to undergo any subtle changes in oxidation state that the *M* or *X* atom could. These subtle changes (driven, for instance, by the copper deficiency discussed above) can have large effects on the conducting properties, either providing extra electrons for the conduction band, or introducing holes in the valence band.

Table 4.37 Resistvities of compounds at 80 and 300 K.

Compound	Sample number	*T*/K	ρ/Ω cm
$Sr_2CoCu_2O_2Se_2$	NDW256a	97.1	1.23×10^2
		297.1(1)	$1.6(13) \times 10^2$
$Ba_2CoCu_2O_2S_2$	NDW251c	81.5(3)	$5.5(1) \times 10^4$
		297.3(2)	$9(6) \times 10^3$
$Ba_2CoCu_2O_2Se_2$	NDW268b	82.0(4)	$7(1) \times 10^2$
		297.1	$5.4(98) \times 10^2$
$Sr_2NiCu_2O_2Se_2$	NDW250a	82.2(6)	$1.33(1) \times 10^{-1}$
		297.6(7)	$1.8(1) \times 10^{-1}$

4.7 References

(1) Palazzi, M. *Compt. Rend. Acad. Sci. Paris,* **1981**, *292*, 789-791.

(2) Kusainova, A. M.; Berdonosov, P. S.; Kholodkovskaya, L. N.; Akselrud, L. G.; Dolgikh, V. A. and Popovkin, B. A. *J. Solid State Chem.,* **1995**, *116*, 406.

(3) Zhu, W. J. and Hor, P. H. *J. Solid State Chem.,* **1997**, *130*, 319-321.

(4) Zhu, W. J.; Hor, P. H.; Jacobson, A. J.; Crisci, G.; Albright, T. A.; Wang, S. H. and Vogt, T. *J. Am. Chem. Soc.,* **1997**, *119*, 12398-12399.

(5) Otzschi, K.; Ogino, H.; Shimoyama, J.-I. and Kishio, K. *J. Low Temp. Phys.,* **1999**, *117*, 729-733.

(6) Wang, K. and Reeber, R. R. *Philos. Mag. A-Phys. Condens. Matter Struct. Defect Mech. Prop.,* **2000**, *80*, 1629-1643.

Chapter 5 $A_2MO_2Ln_2O_2X_2$ compounds

5.1 Introduction

This chapter discusses attempts made to synthesise a new range of compounds, the $A_2MO_2Ln_2O_2X_2$ family, A = Sr, Ba; M = Mn, Co, Fe; Ln = Y, La, Gd and X = S, Se. The extensive use of bond valence calculations to examine the stability of synthetic candidates is discussed, as are the results of the systematic synthesis procedure employed.

The $A_2MO_2Cu_2X_2$ (A = Sr, Ba; M = Mn, Co, Fe; X = S, Se) compounds discussed in Chapter 4 contain square planar layers of $[MO_2]$ composition and tetrahedral layers of $[Cu_2X_2]^{2-}$ composition, separated by A^{2+} cations. The $La_2O_3M_2X_2$ compounds discussed in Chapter 3 contain $[M_2O]^{2+}$ layers, separated by $[La_2O_2X_2]^{2-}$ layers. This $[La_2O_2X_2]^{2-}$ layer can in turn be considered as being a layer of $[La_2O_2]^{2+}$ in between two layers of $[X]^{2-}$. The aim of the work described in this chapter was to replace the $[Cu_2X_2]^{2-}$ layers in the $A_2MO_2Cu_2X_2$ type compounds with a $[Ln_2O_2X_2]^{2-}$ layer from the $La_2O_3M_2X_2$ series of compounds. Figure 5.1 shows the structure of a general $A_2MO_2Cu_2X_2$ compound, a predicted structure for a general $A_2MO_2Ln_2O_2X_2$ compound and the structure of a general $La_2O_3M_2X_2$ compound to show the relationship between these materials.

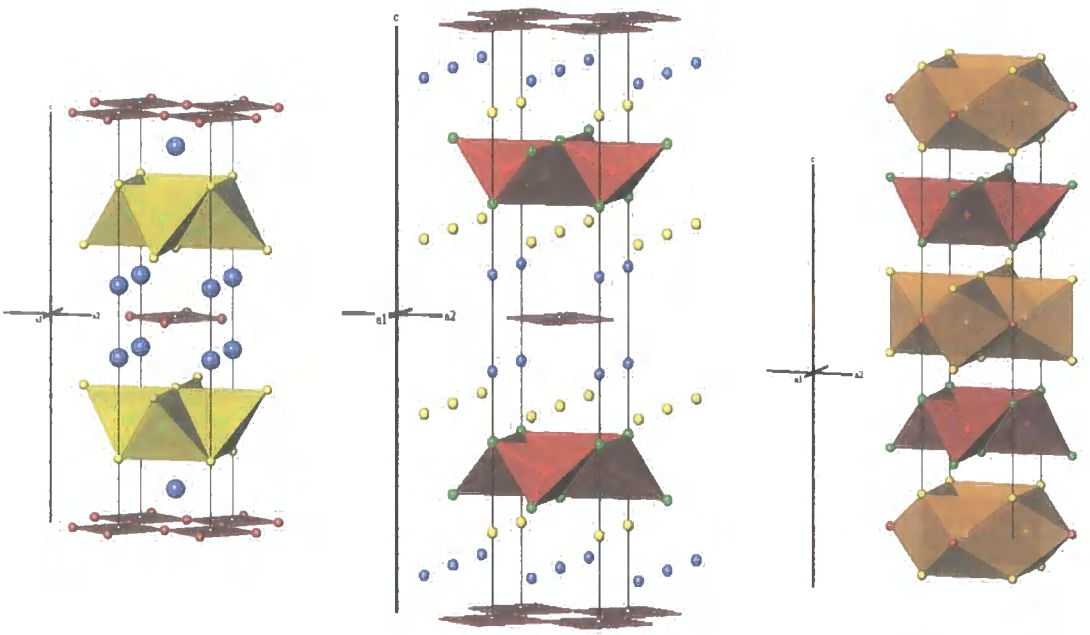

Figure 5.1 Structure of $A_2MO_2Cu_2X_2$ (left), $A_2M_2O_2Ln_2O_2X_2$ (centre) and $La_2O_3M_2X_2$ (right). A atoms in blue, M in grey, O in red, Cu/Ln in green, X in yellow. CuX_4 tetrahedra in yellow, Ln_4O in red. The targeted structure can be seen to be an intergrowth of structural sub-units of the materials studied in chapters three and four.

All combinations of the $A_2MO_2Ln_2O_2X_2$ (A = Sr, Ba; M = Mn, Co, Fe; Ln = Y, La, Gd and X = S, Se) family were investigated as synthetic targets; a total of 36 possible compounds.

These represent realistic phases to attempt to synthesise due to the wide range of similar compounds in existence which contain similar $[Ln_2O_2]^{2+}$, $[MO_2]^{2+}$, $[X]^{2-}$ and $[A]^{2+}$ layers. Many of these compounds have similar space groups and unit cell sizes. The *a* cell axes for $[Ln_2O_2]^{2+}$ layer containing compounds vary from 4.03 Å to 4.21 Å and are around 4.05 Å for compounds containing the $[Cu_2]^{2+}$ layers to be "replaced". This is of vital importance as the size of the layers must be sufficiently similar for a compound to be stable.

5.2 Bond valence calculations

In order to further investigate the viability of the synthetic targets bond valence sum calculations[1,2] were performed as a preliminary test. Whilst such calculations do not provide a rigorous measure of the stability of an unknown compound, they do provide an indication as to whether a proposed structure type is consistent with known, and therefore at least metastable, compounds. The bond valence for each atom *i* is V_i (described by Equation 5.1), the sum of the bond valences, v_{ij}, between atom *i* and each atom *j* that it is bonded to. The bond valence between *i* and *j* can be calculated using Equation 5.2 where R_{ij} is the bond-valence parameter for atom – atom pair *ij*, d_{ij} is the distance between atoms *i* and *j* and *b* is the "universal" constant 0.37 Å. Tables of R_{ij} for many atom-atom pairs can be found in the literature; the ones used in the calculations discussed below were from Brown.[3]

$$V_i = \sum_j v_{ij} \qquad \text{Equation 5.1}$$

$$v_{ij} = \exp\left(\frac{R_{ij} - d_{ij}}{b}\right) \qquad \text{Equation 5.2}$$

The TOPAS[4] suite of software was used to perform least-squares structural refinements in which the quantity minimised was *P* (defined in Equation 5.3 where V_{exp} is the expected bond valence for each atom, and related to g_{ii}, the global instability index, by Equation 5.4 where *N* is the number of atoms in the asymmetric unit cell) for each atom *i* in the structure. To ensure location of the global minimum 1000 simulated annealing cycles were typically performed in which bond valence discrepancies were minimised then the structure perturbed and allowed to re-refine and converge. This process was performed over a grid of unit cell sizes from *a* = 3.5 – 4.5 Å and *c* = 18 – 27 Å with grid steps of 0.05 and 0.1 Å respectively. In this manner it was possible to map out the global instability index of the proposed structure as a function of unit cell parameters to investigate the potential stability of target phases. A sample TOPAS input file is included in Appendix 4.

$$P = \sum (V_i - V_{exp})^2$$ Equation 5.3

$$g_{ii} = \sqrt{\frac{P}{N}}$$ Equation 5.4

A sample valence minimising experiment was performed on $La_2O_3Mn_2Se_2$, a compound discussed in Chapter 3. The resulting contour map is shown in Figure 5.2, using the same scale as for Figure 5.3 to Figure 5.11 below, and shows that for an *a* cell parameter of 4.15 Å and a *c* of 18.0 Å a structure in which the quantity *P* is 0.20414 can be achieved. This represents a structure in which valence sums differ from ideal values (2 for Mn, O and Se; 3 for La) by 0.45 in total. This was the lowest penalty found, while that of the real cell parameters (or the closest grid point to them, 4.15 and 18.8 Å) was 0.22702. The highest *P* (16.19755) was for 3.5, 22.2 Å. However, as can be seen from Figure 5.2 there is a long minima region between *a* = 4.1 and 4.2 Å and *c* = 18.0 and 21.1 Å, in which the real cell parameter falls. This suggests that the bond valence calculations are providing good estimates for the ranges of expected cell parameters.

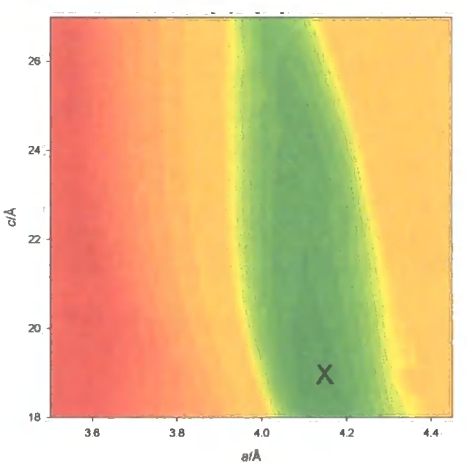

Figure 5.2 Contour map for $La_2O_3Mn_2Se_2$, showing lower *P* in blue/green, greater in red. A cross marks the real unit cell parameters.

These valence minimising experiments were performed on several of the synthetic targets in order to assess the potential stability of a range of the target materials. The smallest and largest of each *M* = Mn, Co, Fe containing compound (containing Sr/S and Ba/Se respectively) were investigated, as were all the $Sr_2FeO_2Ln_2O_2S_2$ (*Ln* = Y, La, Gd) compounds, to investigate the difference between the lanthanoid elements.

Figure 5.3, Figure 5.6 and Figure 5.9 show the results of these bond valence calculations for the $Sr_2MO_2Y_2O_2S_2$ (*M* = Mn, Co, Fe) series of compounds, which represent the smallest compounds for each transition metal. The data for the *M* = Mn and Fe compounds look very

similar, with minima around a = 4.2 Å, c = 19.9 Å. The Co compound shows a longer minimum region, from a = 4.0 Å, c = 20 Å to a = 3.8, c = 24 Å.

$Sr_2MO_2Y_2O_2S_2$

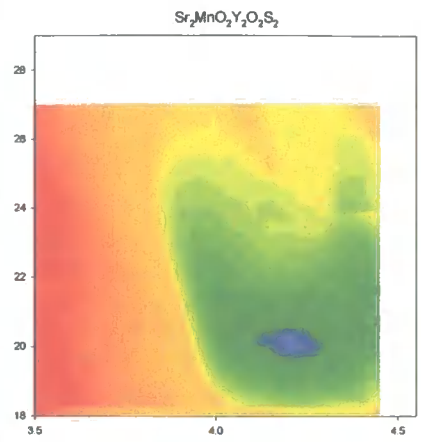

Figure 5.3

$Ba_2MO_2La_2O_2Se_2$

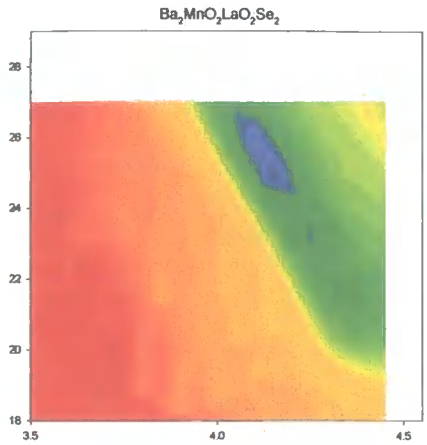

Figure 5.4

$Sr_2FeO_2Ln_2O_2S_2$

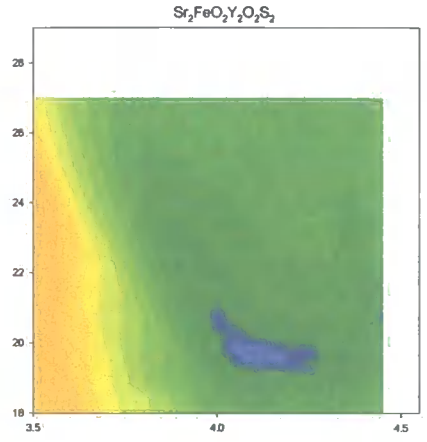

Figure 5.5

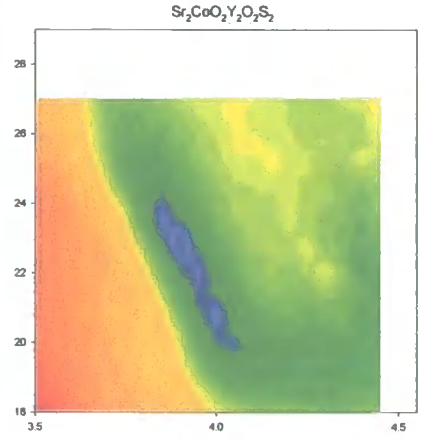

Figure 5.6

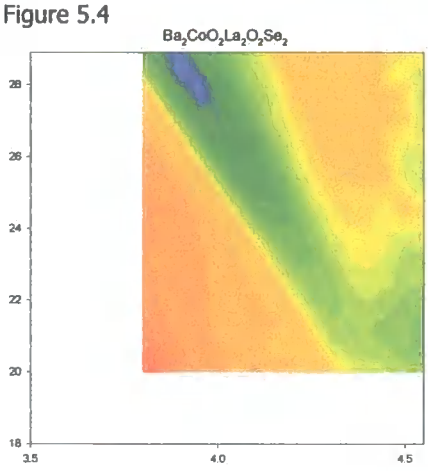

Figure 5.7

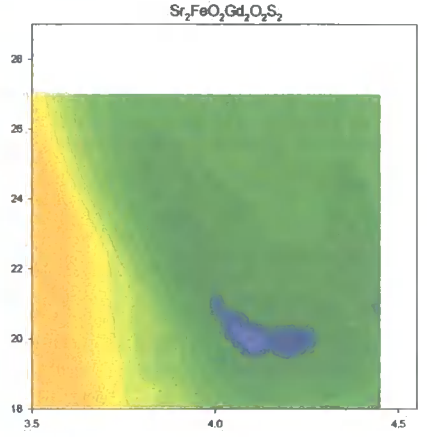

Figure 5.8

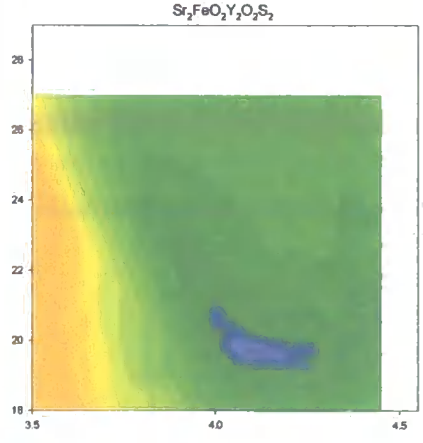

Figure 5.9

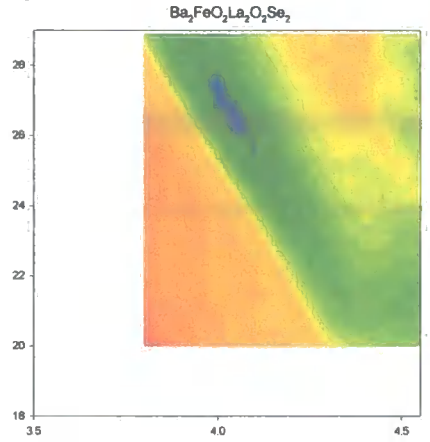

Figure 5.10

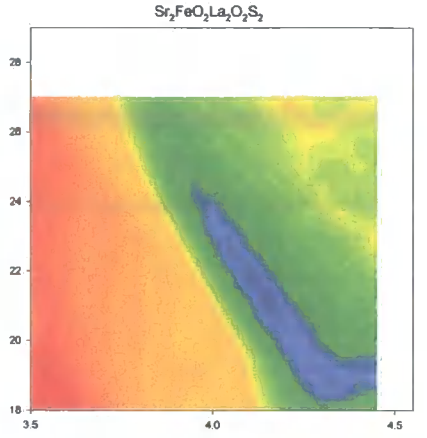

Figure 5.11

Figure 5.3 – Figure 5.11 show the contour maps resulting from valence minimising experiments. All the x axes are a cell parameter/Å, y axes c cell parameter/Å and the contours represent the penalty P, as defined in Equation 5.3. The key to the penalties the colours represent is shown on the right:

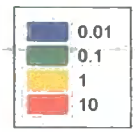

As expected, Figure 5.4, Figure 5.7 and Figure 5.10 for the $Ba_2MO_2La_2O_2Se_2$ (*M* = Mn, Co, Fe) series of compounds show minima for larger cell parameters; at *a* = 4.15 Å, *c* = 25.0 Å and *a* = 4.05, *c* = 26.4 Å for the *M* = Mn, Fe compounds respectively, while the *M* = Co compound shows a large minimum between a ~ 4.0, c ~ 22 Å and a ~ 3.8, c ~ 24 Å.

Figure 5.5, Figure 5.8 and Figure 5.11 show the contour maps for the $Sr_2FeO_2Ln_2O_2S_2$ (*Ln* = Y, La, Gd) series of compounds, showing the difference between the lanthanoids when other elements are held constant. The *Ln* = Y, Gd (Figure 5.10 and Figure 5.10) show very similar maps, with a small minimum around *a* = 4.1, *c* = 20 Å. The *Ln* = La (Figure 5.11) shows a rather different map, with a "valley" of minima from *a* ~ 4.3, *c* ~ 18.2 Å to *a* ~ 4.0, *c* ~ 24 Å.

Table 5.1 summarises the results of the valence calculations, giving the cell parameters at which the best bond valences were found, the valences V_i for each atom and the "penalty", *P*, for these cell parameters, given by Equation 5.3.

Table 5.1 Results of bond valence calculations for target compounds.

Compound	*P*	*a*/Å	*c*/Å	*v*/Å^3	*c*/*a*	V_A	V_M	V_{Ln}	$V_{O(1)}$	$V_{O(2)}$	V_X
$Sr_2MnO_2Y_2O_2S_2$	0.0429	4.20	19.90	351.0	4.7	1.8604	2.1154	2.9962	2.0935	2.0315	1.9817
$Ba_2MnO_2La_2O_2Se_2$	0.0140	4.15	25.00	430.6	6.0	2.0080	1.9135	2.9916	2.0544	1.9427	1.9903
$Sr_2CoO_2Y_2O_2S_2$	0.0186	3.90	22.80	346.8	5.8	2.0510	2.0459	2.8913	1.9844	1.9738	2.0341
$Ba_2CoO_2La_2O_2Se_2$	0.0320	3.90	28.50	433.5	7.3	2.0652	2.0112	2.9393	2.0849	1.8820	2.0530
$Sr_2FeO_2Y_2O_2S_2$	0.0041	4.10	19.70	331.2	4.8	1.9606	1.9837	2.9800	2.0232	2.0320	2.0177
$Sr_2FeO_2Gd_2O_2S_2$	0.0049	4.10	20.00	336.2	4.9	1.9685	1.9941	2.9762	2.0155	2.0511	2.0209
$Sr_2FeO_2La_2O_2S_2$	0.0090	4.10	22.00	369.8	5.4	1.9745	2.0054	2.9418	2.0024	2.0701	1.9978
$Ba_2FeO_2La_2O_2Se_2$	0.0533	4.05	26.40	433.0	6.5	2.0466	1.8581	2.9882	2.1109	1.8641	2.0070

The calculated unit cell volume of "ideal" structures increases significantly, as expected, between compounds of the formula $Sr_2MO_2Y_2O_2S_2$ and $Ba_2MO_2La_2O_2Se_2$. Changing the metal ion has more effect in the smaller compounds, *e.g.* from 331.2 to 351.0 Å^3 for $Sr_2FeO_2Y_2O_2S_2$ to $Sr_2MnO_2Y_2O_2S_2$ compared to 430.6 to 433.0 Å^3 for $Ba_2MnO_2La_2O_2Se_2$ to $Ba_2FeO_2La_2O_2Se_2$, which is perhaps to be expected as the increased size of the lattice due to the differing *A*, *Ln* and *X* atoms will have more effect than the metal, *M*. The difference in unit cell size due to changing the *Ln* atom is much less than for changing the *A* and *X* atoms. The *c*/*a* ratios show that the unit cells do not expand isotropically, with $Sr_2MnO_2Y_2O_2S_2$ having *c*/*a* = 4.7 and $Ba_2CoO_2La_2O_2Se_2$ having *c*/*a* = 7.3. From Figure 5.12 it can be seen that the penalty is roughly proportional to this *c*/*a* ratio.

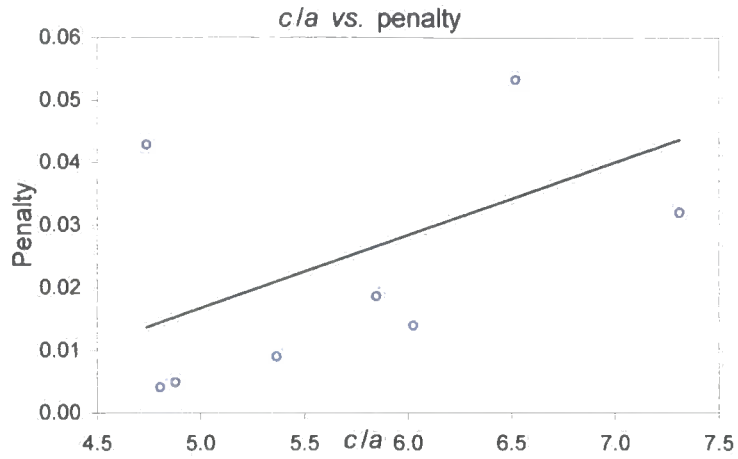

Figure 5.12 *c/a vs.* penalty for structure optimisation calculations on $A_2MO_2Ln_2O_2X_2$ compounds.

The calculated ideal structures of $Sr_2MnO_2Y_2O_2S_2$ and $Ba_2CoO_2La_2O_2Se_2$ are shown in Figure 5.13 and it can be seen that the Ln_4O tetrahedra are highly distorted for $Sr_2MnO_2Y_2O_2S_2$, with a low *c/a* ratio, compared to $Ba_2CoO_2La_2O_2Se_2$ with a higher ratio, resulting a higher *P* value for this $Sr_2MnO_2Y_2O_2S_2$ (0.0429) than for $Ba_2CoO_2La_2O_2Se_2$ (0.0320).

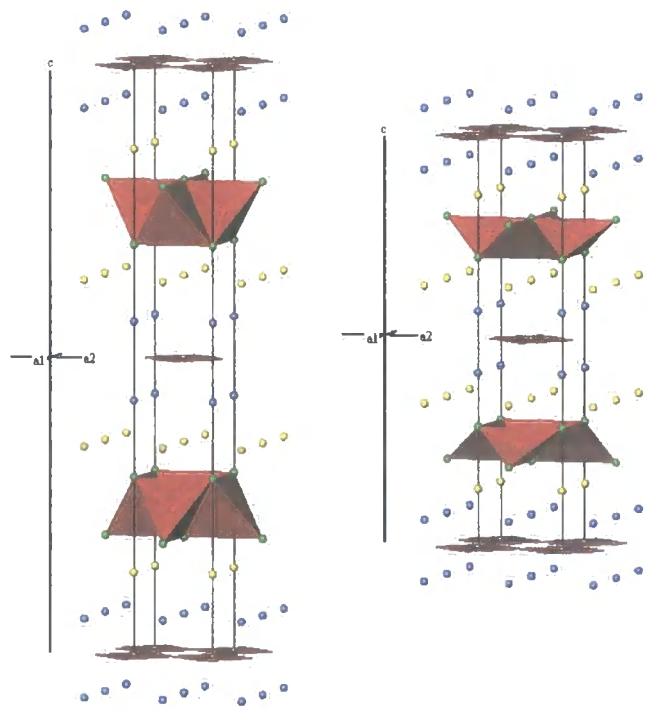

Figure 5.13 The structures of $Ba_2CoO_2La_2O_2Se_2$ (left) and $Sr_2MnO_2Y_2O_2S_2$ (right). *A* atoms are shown in blue, *M* in grey, O in red, *Ln* in green, *X* in yellow. Ln_4O tetrahedra are shown in red.

5.3 Results

Attempts were made to synthesise the target compounds $A_2MO_2Ln_2O_2X_2$ (*A* = Sr, Ba; *M* = Mn, Co, Fe; *Ln* = Y, La, Gd and *X* = S, Se) using stoichiometric amounts of Ln_2O_3, *AX*, M_xO_y

and *M*, intimately ground and pressed into pellets before being heated in a sealed quartz ampoule and heated to temperatures between 800 and 1100 °C. Section 2.1.3 describes the syntheses in full. The samples were all characterised using a Siemens D5000 diffractometer (Section 2.2.3).

A summary of the results of the various synthetic conditions is shown in Table 5.2, Table 5.3 and Table 5.4 for the *M* = Mn, Co and Fe respectively. It is noticeable that none of the target $A_2MO_2Ln_2O_2X_2$ target phases were synthesised. It is also clear that for the majority of syntheses where *M* = Mn, Co and *Ln* = Y, Gd the starting materials were the only products obtained, regardless of *A*, *X*, or the final synthesis temperature. In many cases the M_xO_y reagent was not observed, possibly due to either its reaction with the quartz ampoule or not being visible in the powder pattern. Figure 5.14 shows a Rietveld refinement of a typical sample, with structural models of the BaS, Y_2O_3 and CoO reagents fitting the measured powder pattern well. The percentages given in the figure (BaS 50 %; Y_2O_3 38 %, CoO 12 %) are only approximate as the scan was only collected over one hour, but they are quite close to those expected from the reagents used (BaS 53 %; Y_2O_3 35 %; CoO 11 %).

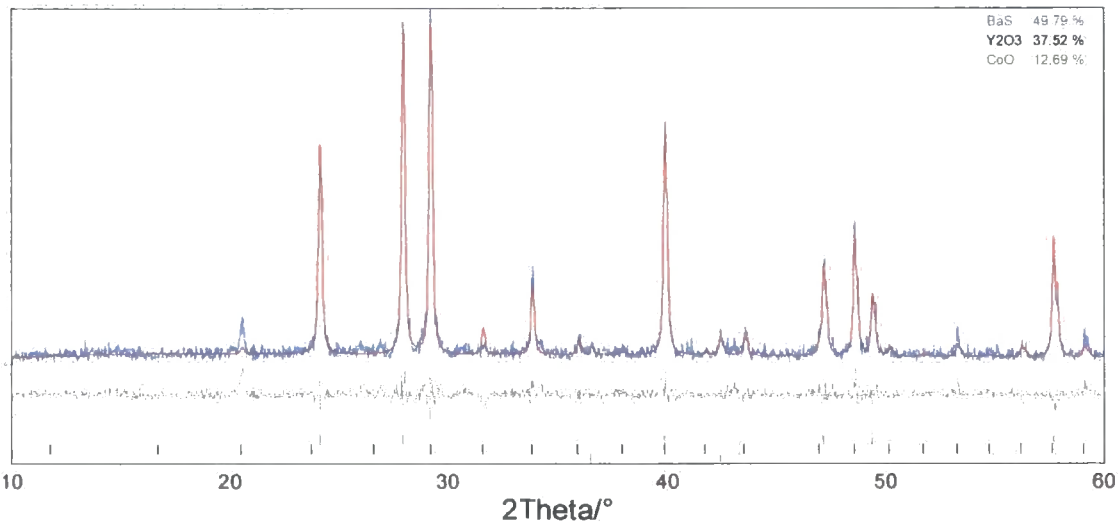

Figure 5.14 Rietveld fit of the product from a typical Ba/Co/Y/S synthesis, showing a good fit to BaS, Y_2O_3 and CoO (tick marks for predicted peak positions for these from top to bottom respectively). Experimental pattern is shown in blue, fitted pattern in red, difference curve in grey.

The *M* = Mn, Co and *Ln* = La set of syntheses showed further reaction, but only to give the ternary compounds La_2O_2X (only where *X* = S) and La_2CoO_4 (in both *X* = S, Se). This is confirmed by Rietveld refinement (Figure 5.15) which shows that the structural models of BaS, La_2O_2S and La_2CoO_4 give a good fit with the experimental data. While the weight percentages given in the figure are not totally precise (given the data were collected in one hour only), they do give a rough guide to the phase fractions.

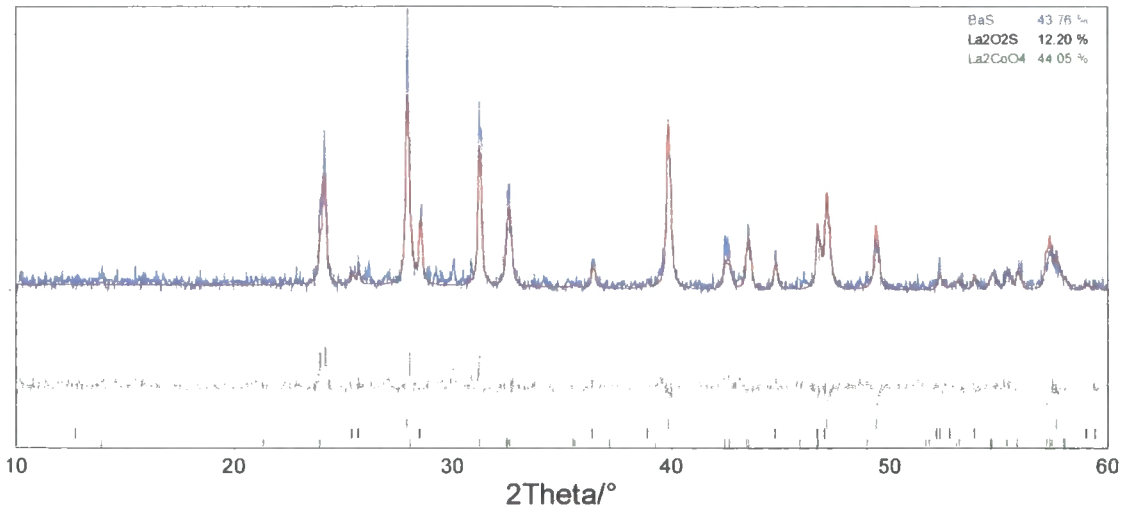

Figure 5.15 Rietveld fit of the product from a typical Ba/Co/La/S synthesis, showing a good fit to BaS, La_2O_2S and $LaCoO_4$ (tick marks for predicted peak positions for these from top to bottom respectively). Experimental pattern is shown in blue, fitted pattern in red, difference curve in grey.

Table 5.2 Summary of synthetic results for $A_2MnO_2Ln_2O_2X_2$ with ticks indicating the products found in each synthesis.

A	*X*	*Ln*	Temp	*AX*	Ln_2O_3	Mn_xO_y	*LnOX*	*Ln*MnO	*ALn*O	AMnO	*ALn*MnO
Ba	S	Y	1223	✓	✓						
		Y	1323	✓	✓						
		Gd	1223	✓	✓						
		Gd	1323	✓	✓						
		La	1223	✓	✓		✓	✓			
		La	1323	✓			✓	✓			
	Se	Y	1223	✓	✓						
		Y	1323	✓	✓						
		Gd	1223	✓	✓						
		Gd	1323	✓	✓						
		La	1223	✓	✓		✓	✓			
		La	1323	✓	✓			✓			
Sr	S	Y	1223	✓	✓						
		Y	1323	✓	✓						
		Gd	1223	✓	✓						
		Gd	1323	✓	✓						
		La	1223	✓	✓		✓	✓			
		La	1323	✓			✓	✓			
	Se	Y	1223	✓	✓						
		Y	1323	✓	✓						
		Gd	1223	✓	✓						
		Gd	1323	✓	✓						
		La	1223	✓	✓		✓	✓			
		La	1323	✓			✓	✓			

Table 5.3 Summary of synthetic results for $A_2CoO_2Ln_2O_2X_2$ with ticks indicating the products found in each synthesis.

A	*X*	*Ln*	Temp	*AX*	Ln_2O_3	Co_xO_y	*LnOX*	*LnCoO*	*ALnO*	*ACoO*	*ALnCoO*
Ba	S	Y	1073	✓	✓	✓				✓	
			1223	✓	✓	✓					
			1323	✓	✓	✓					
		Gd	1073	✓	✓						
			1223	✓	✓						
			1323	✓	✓						
		La	1073	✓	✓		✓	✓			
			1223	✓	✓		✓	✓			
			1323	✓			✓	✓			
	Se	Y	1073	✓	✓	✓					
			1223	✓	✓	✓					
			1323	✓	✓	✓					
		Gd	1073	✓	✓						
			1223	✓	✓	✓					
			1323	✓	✓						
		La	1073	✓	✓			✓			
			1223	✓	✓			✓			
			1323	✓				✓			
Sr	S	Y	1073	✓	✓	✓					
			1223	✓	✓	✓					
			1323	✓	✓						
		Gd	1073	✓	✓						
			1223	✓	✓						
			1323	✓	✓						
		La	1073	✓	✓		✓	✓			
			1223	✓	✓		✓	✓			
			1323	✓			✓	✓			
	Se	Y	1073	✓	✓						
			1223	✓	✓	✓					
			1323	✓	✓						
		Gd	1073	✓	✓						
			1223	✓	✓	✓					
			1323	✓	✓						
		La	1073	✓	✓			✓			
			1223	✓	✓			✓			
			1323	✓				✓			

Table 5.4 Summary of synthetic results for $A_2FeO_2Ln_2O_2X_2$ with ticks indicating the products found in each synthesis.

A	*X*	*Ln*	Temp	*AX*	Ln_2O_3	Fe_xO_y	*LnOX*	*Ln*FeO	*ALn*O	*A*FeO	*ALn*FeO
Ba	S	Y	1223	✓	✓			✓			
		Y	1323	✓	✓						
		Gd	1223	✓	✓		✓	✓			
		Gd	1323	✓	✓		✓	✓			
		La	1223	✓			✓	✓			
		La	1323	✓	✓		✓	✓			✓
	Se	Y	1223	✓	✓			✓			
		Y	1323	✓	✓			✓	✓		
		Gd	1223	✓	✓			✓			
		Gd	1323	✓	✓			✓			
		La	1223	✓	✓		✓	✓			
		La	1323	✓	✓			✓	✓		
Sr	S	Y	1223	✓	✓			✓			
		Y	1323	✓	✓			✓			
		Gd	1223	✓	✓	✓				✓	
		Gd	1323	✓	✓		✓	✓			
		La	1223	✓			✓	✓			✓
		La	1323	✓			✓	✓			✓
	Se	Y	1223	✓	✓			✓			
		Y	1323	✓	✓			✓			
		Gd	1223	✓	✓			✓			
		Gd	1323	✓	✓		✓	✓			
		La	1223	✓	✓		✓	✓			
		La	1323	✓			✓	✓			✓

In the syntheses where *M* = Fe, nearly all the conditions produced a $LnFeO_3$ phase. Figure 5.16 shows a three phase Rietveld refinement with $GdFeO_3$, Gd_2O_3 and BaSe giving a calculated pattern with a good fit to experimental data. Gd_2O_2S was also formed in 3/4 of the syntheses where *Ln* = Gd and *X* = S and La_2O_2X was a product in most cases where *Ln* = La. No Y_2O_2X formation has been observed in any of the syntheses.

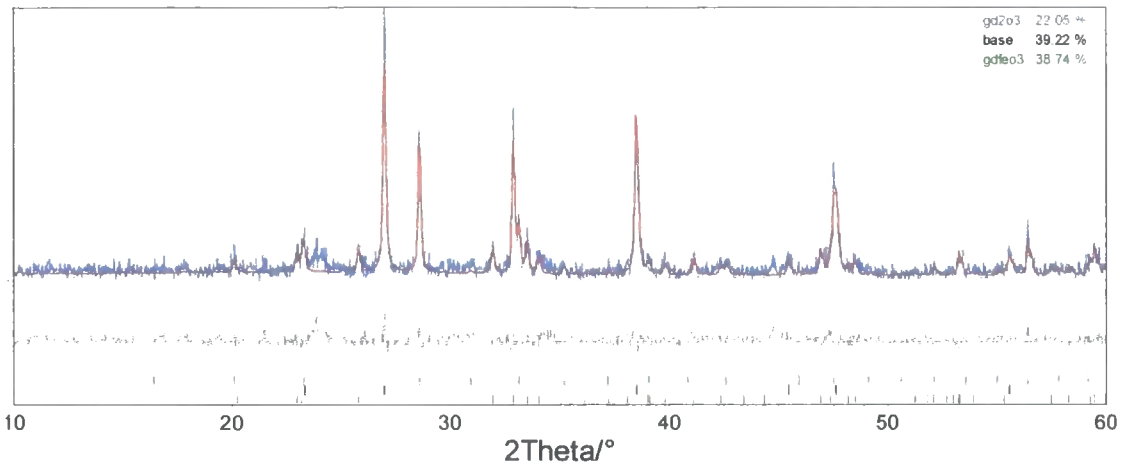

Figure 5.16 Rietveld fit of the product from a typical Ba/Fe/Gd/Se synthesis, showing a good fit to Gd_2O_3, BaSe and $GdFeO_3$ (tick marks for predicted peak positions for these from top to bottom respectively). Experimental pattern is shown in blue, fitted pattern in red, difference curve in grey.

Some quaternary phases, *e.g.* $BaLa_2FeO_7$, $SrLaFeO_4$ were observed, but only in the *Ln* = La and *M* = Fe syntheses.

5.4 Discussion

The results summarised above give rise to the following considerations: firstly, and most importantly, the fact that none of the target phases could be prepared using any of the varying conditions; only the *Ln* = La samples resulted in anything other than starting materials in all *M* = Mn, Co syntheses; the *M* = Fe syntheses gave a wider range of resulting compounds than *M* = Mn, Co.

To begin with, it can be seen from the bond valence calculations summarised in Table 5.1 that they agree well with the expected valences, with most differing from ideal values by only ~0.05 . This compares favourably with the bond valences for atoms in existing compounds, with the La atom in $La_2O_3Fe_2Se_2$ having V_i = 3.11 for example. Calculating a "penalty" factor for $La_2O_3Fe_2Se_2$ give *P* = 0.165452, which is also comparable with those for the target phases. It would be reasonable to expect, therefore, that at least some of the target compounds would be at least metastable if synthesised.

In summary it appears that although simple structural considerations, analogy with other known phases and bond valence calculations suggest the viability of the $A_2MO_2Ln_2O_2X_2$ phases, they cannot be prepared in practice, or at least not via the synthetic routes used here. It seems likely that formation of the A_2MO_2 slabs in the $A_2MCu_2O_2X_2$ phases is favoured by the particularly stable and widely found $[Cu_2X_2]^{2-}$ slab. The materials targeted here are presumably sufficiently less stable with respect to the starting materials as other product phases that they could not be isolated.

A potential way around this could be to use a different *A* source, *e.g.* ACO_3, and to decompose this to *AO* *in situ*. However, this type of route would make it very difficult to control the level of oxygen present in the sample and the oxidation state of the *X* atoms.

5.5 References

(1) Brese, N. E. and Okeeffe, M. *Acta Crystallogr. B,* **1991**, *47*, 192-197.

(2) Brown, I. D. and Altermatt, D. *Acta Crystallogr. B,* **1985**, *41*, 244-247.

(3) Brown, I. D., *Accumulated Table of Bond Valence Parameters*, Brockhouse Insitute for Materials Research, McMaster University, Hamilton, Ontario, 2001.

(4) Coelho, A. A., *TOPAS v2.13 General Profile and Structure Analysis Software for Powder Diffraction Data*, Bruker AXS, Karlsruhe, 2000.

Chapter 6 Structure solution using powder X-ray diffraction

This chapter presents the structure solution of an α,α thiophene tin tetramer, used as a precursor to a sexithiophene block co-polymer, undertaken during the course of the work presented in the rest of this thesis. The molecule was synthesised by O. Henze, working for W. J. Feast in the Interdisciplinary Research Centre at Durham University as part of a study into a series of thiophene tin oligomers. The other members were structurally characterised using single crystal X-ray diffraction methods by A. Batsanov in the crystallography group, Durham University, but the tetramer could not be prepared in single crystal form. Its structure solution by powder X-ray diffraction methods is thus presented here.

6.1 The molecule - α,α thiophene tetramer

There are many new electronic devices being studied for the myriad uses they afford us. Organic field-effect transistors (OFETs) are among these and are expected to be important components in new electronic displays (*e.g.* for portable computers and pagers) and memory elements in so-called "smart cards" and identification tags.

These OFETs consist of a semiconductor material supporting a channel of either holes or electrons between the source and drain electrodes (Figure 6.1). Important criteria for an efficient OFET co-efficient semiconductor include high carrier mobility, high current modulation (on/off current ratio), stability and processability.

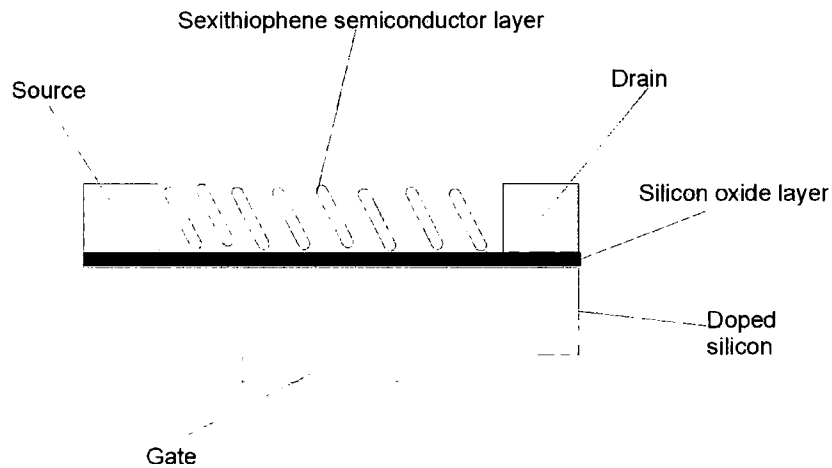

Figure 6.1 Organic Field Effect Transistor (OFET).

Recently, α,α-thiophene oligomers and polymers have been the subject of attention as the semi-conductor layer in OFET's. [1] The sexithiophene has been found to be the most promising in the family of thiophene oligomers, partly because higher members of the series

cannot be processed as easily and are less stable. Increasing the ordering of the sexithiophenes (by introducing hydrophobic or hydrophilic side chains at the α and ω positions of the oligomers) increases the carrier mobility of the semi-conducting substrate. Recent work has undertaken to make model compounds to control the organisational properties of sexithiophenes by incorporating them into polymers. This is greatly helped by the superior processability and range of applications of polymers.

One of the synthetic routes to sexithiophene block co-polymers uses the quaterthiophene precursor, **1**, shown in Figure 6.2. This route makes block co-polymers with a hydrophilic chain on one end and hydrophobic chain on the other. The hope is that such a co-polymer would align itself at a water/air interface, leading to a processable and controllable material.

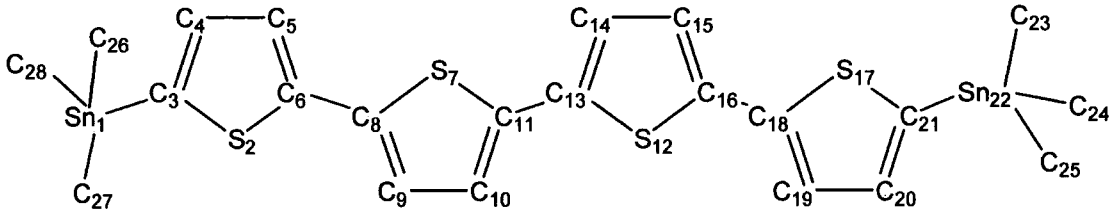

Figure 6.2 The quaterthiophene precursor **1**. H atoms omitted for clarity, but numbered in appendices according to which C atom they are bonded to. For example, H atoms bonded to C27 are H271, H272 and H273.

Other thiophene oligomer precursors have been synthesised and structurally characterised by single crystal X-ray diffraction. However, it has not proved possible to grow single crystals of **1**, so an attempt to characterise it has been made using powder X-ray diffraction. The length of the tin—thiophene bond length is of interest as a measure of the stability of the molecules. The techniques used and the results of this study are outlined in this chapter.

6.2 Structure determination techniques[2,3]

In all structure determination, whether from single-crystal or powder data, information about the periodicity of the crystal structure and the distribution of matter within it is contained in the positions and intensities of the diffraction maxima. This information is essentially the same for both single-crystal and powder diffraction, although the three-dimensional space that the single-crystal data occupies is "compressed" into one dimension for powder diffraction, giving rise to considerable overlap of reflections. The stages for retrieving the data from either technique are the same, and can be divided into three parts; unit cell determination and space-group assignment (commonly known as indexing), structure solution and structure refinement.

6.2.1 Indexing

The correct lattice parameter and space group assignment of a crystal structure is of crucial importance in the process of determining a crystal structure. Indeed, without this information the rest of the structure determination would be impossible. The derivation of the lattice parameters requires accurate *d*-spacing information, which, in terms of a powder X-ray diffraction pattern, means accurate determination of peak positions. The accuracy required is typically an error of less than 0.01 ° in 2θ angle measurement. While it is possible to work out the lattice parameters by hand for some high symmetry systems, "autoindexing" computer programs are more typically employed. These include ITO, [4] TREOR[5] and DICVOL. [6] The number of accurately determined reflections required by these programs is around twenty; any impurity peaks present amongst this twenty will severely decrease the chance of getting the correct answer. Several sets of lattice parameters are usually possible for a given set of peak positions so a "figure of merit" is assigned to each set of lattice parameters and is then used to rank them.

Space group assignment is carried out by identifying systematic absences within the powder diffraction data. If it is impossible to get an unambiguous result the next stage of the process, structure solution, will need to be carried out for a variety of possible space groups.

6.2.2 Structure solution

The conventional methods of structure solution used for single-crystal diffraction (Patterson and direct methods) can be used for powder diffraction as well. However, both these methods require accurate intensity information for *hkl* reflections, information that is often not available from powder diffraction due to peak overlap. Whilst methodologies have been developed to try and alleviate these difficulties, as these techniques were not used in the work reported here, a detailed description is not presented. An alternative approach to these methods is to work in direct space and try to use the whole powder pattern profile in structure solution. This effectively circumvents problems of peak overlap. In this work such a technique, simulated annealing, was used. This is based on the Monte Carlo[7] technique that has been used in many other computational situations.

The Monte Carlo method (as used in crystallography) involves the generation of a series of structural models (x_i, i = 1, 2, ... n) by random movement of the atoms making up the structural fragment studied. Structure x_{trial} is generated by: a) the translation of the structural fragment by a random amount, in a random direction; b) the rotation of the fragment by a random amount about a randomly chosen axis passing through the centre of the fragment and c) the random displacement of atoms subject to the internal degrees of freedom of the fragment (*e.g.* internal torsional angles).

The agreement of each trial structure (between the experimentally obtained powder pattern and a calculated profile) is assessed for the trial structure. This agreement factor is ${}_wR_p(x_{trial})$. The trial structure is accepted or rejected depending on the value of Z, the difference between the trial structure and the initial model used, as defined by Equation 6.1.

$$Z = {}_wR_p(x_{trial}) - R_{wp}(x_{trial-1}) \qquad \text{Equation 6.1}$$

If $Z \leq 0$, the trial structure is accepted as the new structure ($x_{i+1} = x_{trial}$). However, if $Z > 0$, the structure is accepted with probability [exp(-Z/S)] and rejected with probability [1 - exp(-Z/S)]. This process is repeated as many times as required. S is analogous to k_BT and is fixed in the Monte Carlo method, while in simulated annealing it starts with a high value and decreases as if the temperature T were being decreased (hence "simulated annealing"). The rate of decrease can be controlled as desired. This means that, when the initial value of S is high, most trial structures generated are accepted, but as S decreases, so does the number of trial structures accepted. The process can be likened to crystallisation. As the temperature is decreased the model can "crystallise" into a low ${}_wR_p$ arrangement - the structure solution. This high likelihood of random changes to begin with means there is much less chance of the structure falling into a false minimum.

6.2.3 Structure refinement - the Rietveld method[8,9]

The final stage of the structure determination is to refine the basic model given by the solution stage of the process. For powder X-ray diffraction, this is done using the Rietveld method that treats every point in the digitised profile as an intensity measurement. A powder diffraction profile is calculated for the structural model using a number of parameters. Each point in the experimental profile is compared to its counterpart in the calculated profile and selected parameters are adjusted by a least-squares method to give the best fit. More details are given in Section 2.2.2.

Additional information, such as expected geometry like bond lengths and angles, can be incorporated to aid the refinement. These take the form of constraints and restraints. Constraints force the refinement to take a user-specified value and restraints bias the refinement to shift in the direction of sensible user-expected results. The refinement can be "damped" to ensure that the model does not suddenly change to nonsensical values. A combination of restraints and damping will often lead to improved results in the case of poorer quality diffraction data.

6.3 Experimental

A sample of **1** was loaded into a 0.5 mm glass capillary and flame-sealed. Powder X-ray diffraction data were collected on the Bruker D8 Advance diffractometer (Section 2.2.4) in capillary mode. Five data sets were collected; from 3 – 65 ° 2θ with a step size of 0.0144 ° and a measurement time of 10 seconds per step (twelve hours total scan time) and summed to give the pattern (equivalent to a 60 hour data collection) used for structural analysis.

6.4 Results and discussion

6.4.1 Peak fitting using TOPAS

In order to find the accurate peak positions required for indexing peak fitting was carried in TOPAS (Total Pattern Analysis System). [10] As can be seen from Figure 6.3 a good fit was obtained using a pseudo-Voigt peak shape. To begin with only the main peaks were fitted, then a value of the greatest full width at half maximum (FWHM) obtained. This was then used as an upper limit to fit the remaining, weaker, peaks.

Accurate 2θ peak positions were thus obtained and twenty-seven values were used to index the pattern. Fourteen of these were decided to be good enough to be considered as single peaks (*i.e.* with no overlap) and not impurities.

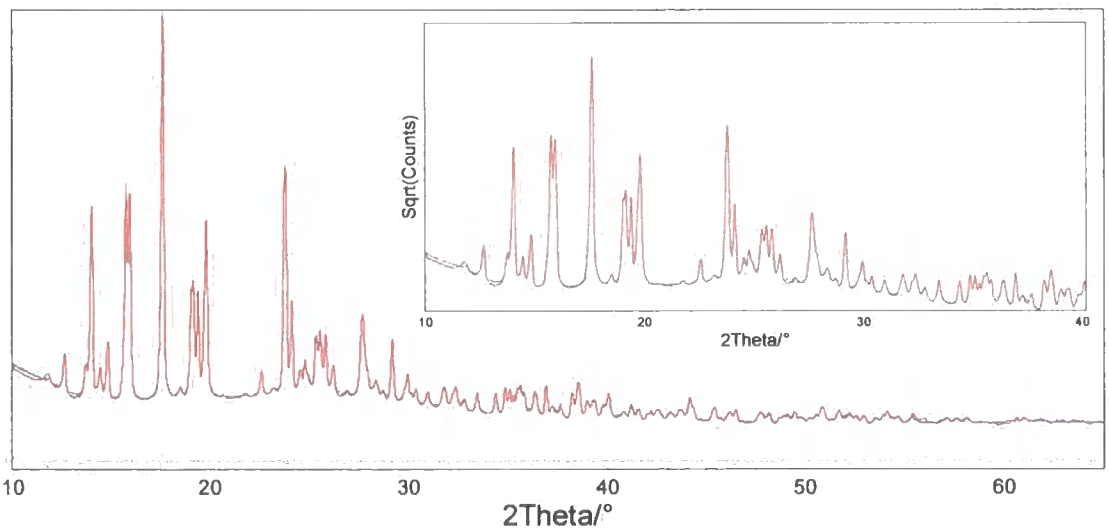

Figure 6.3 Peak fitting of the powder diffraction profile of **1** showing observed (blue) and calculated (red) and difference (grey). $_{w}R_{p}$ = 1.901 %.

6.4.2 Indexing

This list of peak positions was then used by MultiVisser[11] to find the cell parameters for **1**. MultiVisser uses the fourteen "definite" peaks and all possible combinations of six of the other

thirteen peaks to index the pattern. There are a great number of different possible combinations of peak positions and the routine MultiVisser allows them all to be processed automatically. The different results given are sorted by figure of merit and the one with the highest chosen as the correct cell.

The result with the highest figure of merit, 46, gave the following cell parameters;
a = 7.273 Å, b = 14.109 Å, c = 7.100 Å; α = 92.847 °, β = 116.777 °, γ = 94.461 °, V = 645.524 Å^3
Thus **1** has a triclinic unit cell and from cell volume and density calculations was initially assumed to be of space group $P1$ with one molecule in the asymmetric unit which corresponds to 23.05 Å^3 per non H atom. While this is higher than the usual 18 – 20 Å^3 per non H atom expected, it is not excessive as there are large Sn atoms present. Figure 6.4 shows the volume per molecule as a function of the number of thiophene units per molecule from the series of thiophene tin oligomers. This shows that the value of 645.524 Å^3 is consistent with the volume of the other oligomers, as measured by single crystal X-ray diffraction.

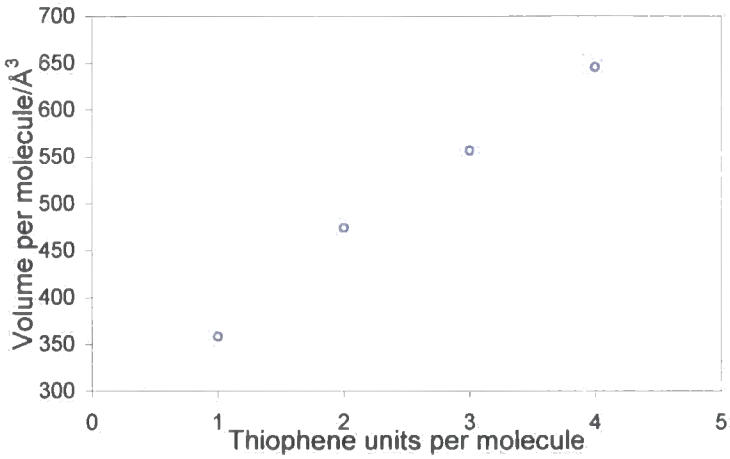

Figure 6.4 Graph of volume per molecule vs. thiophene units per molecule.

A Pawley fit was performed in TOPAS to check the cell parameters from MultiVisser and as can be seen from Figure 6.5, the fit is very good. However, there are a small number of weak peaks (at roughly 12, 18.5 and 23.5 ° 2θ) which don't appear to have been fitted. These are assumed to be impurity peaks, not only because they are the only peaks not predicted in an otherwise excellent fit, but because closer examination reveals that they have a broader peak shape than the other peaks. This would indicate that they are not from the same phase as the remainder of the pattern and can reasonably be assumed to be impurities.

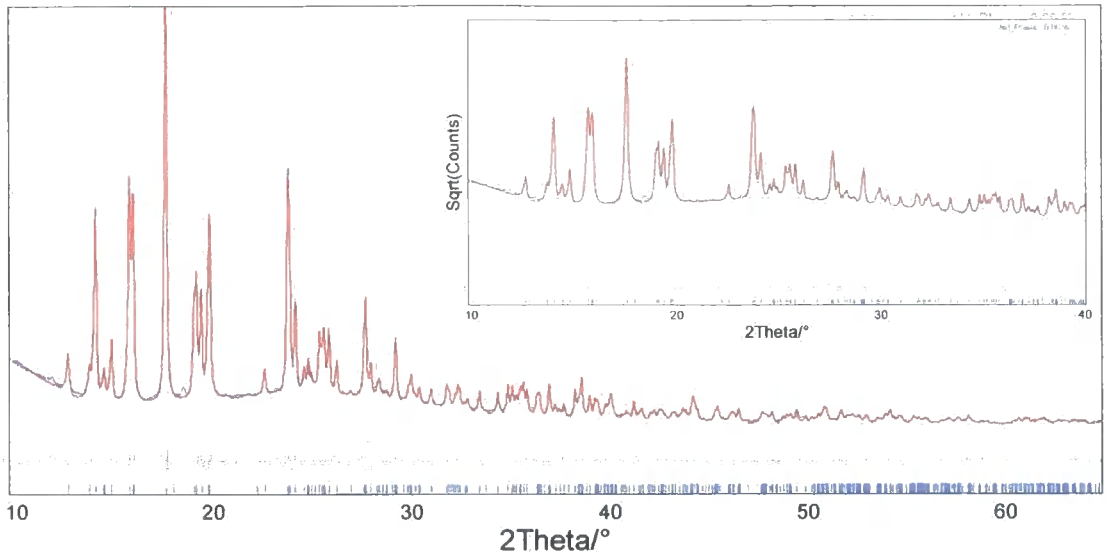

Figure 6.5 Pawley fit of **1** showing observed (blue), calculated (red) and difference (grey) plots.

6.4.3 Structure solution

To obtain an accurate idea of the internal geometry of molecule **1** for the simulated annealing part of the structure solution process some molecular modelling experiments were carried out in CAChe.[12] The basic molecule was entered into CAChe and a simple "fastest procedure" experiment was carried out. This optimises the molecular geometry using an augmented MM3 parameter calculation (Figure 6.6).

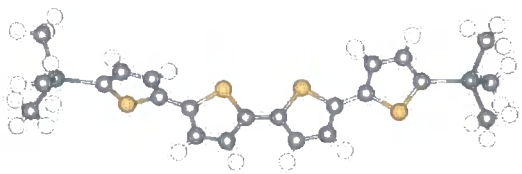

Figure 6.6 Optimised geometry of **1** from CAChe.

The simulated annealing package used to carry out the structure solution was DASH. [13] This is capable of taking a simple model of the molecule, in this case from CAChe, and transforming it into not only the necessary information about relative atomic positions but information about the geometrical constraints caused by bonds, ring systems and dihedral angles.

The molecular coordinates in the form of a CAChe CSSR file were read into DASH. A total of nine internal degrees of freedom were specified (the torsional angles). A simulated annealing run was performed in which these nine degrees of freedom along with molecular coordinates (three degrees of freedom) and overall rotations (three degrees of freedom) were varied. The three translation degrees of freedom are irrelevant in space group *P*1 as it has a floating origin. Several million moves were performed in which these values were varied

stochastically and the calculated diffraction pattern compared to the experimental powder profile. This gave a model with tolerable agreement to experimental data that was suitable for refinement.

6.4.4 Structure refinement

Before the structure refinement was undertaken a search of the Cambridge Structural Database (CSD) was performed to find mean values (and estimated standard errors) for the lengths and angles of certain bond types so the refinement could be restrained in a sensible fashion. The values investigated were:

- Tin—methyl bond lengths (Sn(1)—C(26)).
- Thiophene carbon—sulfur single bond (C(3)—S(2) and C(6)—S(2) see Figure 6.2), carbon—carbon double bond (C(3)=C(4) and C(5)=C(6)) and the remaining carbon—carbon single (C(4)—C(5)) bond lengths.
- Thiophene—thiophene ring distances (C(6)—C(8)) in thiophene oligomers.
- Carbon—tin—carbon bond angles.
- The internal angles of the thiophene ring.
- The angle subtended between the sulfur atom and the two carbon atoms in the bond between two thiophene rings (S(2)—C(6)—C(8)).

The values found (and the *e.s.d.*'s chosen) are shown in Table 6.1 and Table 6.2.

Table 6.1 Values for bond lengths (and *e.s.d.*'s) from CSD.

Bond	Length / Å	*e.s.d.* / Å
Sn(1)—C(26)	2.13	0.02
C(4)—C(5)	1.43	0.02
C(3)—S(2) C(6)—S(2)	1.71	0.05
C(6)—C(8)	1.45	0.05
C(3)=C(4) C(5)=C(6)	1.40	0.02

Table 6.2 Values for bond angles (and *e.s.d.*'s) from CSD.

Bond Angle	Value / °	*e.s.d.* / °
C(26)—Sn(1)—C(27)	109	1
C(4)=C(3)—S(2) C(5)=C(6)—S(2)	109	2
C(3)=C(4)—C(5) C(4)—C(5)=C(6)	110	2
S(6)—C(6)—C(8)	128	1
Sn(1)—C(3)—S(2)	120	1

The estimated standard errors (*e.s.d.*) of these values are very important in this case because in the GSAS[14] Rietveld refinement program the values of the *e.s.d.*'s are used to determine the weightings of the restraints. In cases where there were many hits in the CSD and the distribution was Gaussian then a smaller *e.s.d.* was used which would increase the weighting of the restraint in GSAS. However, if there were either very few hits in the CSD (as in the case of the C(6)—C(8) bonds) or the distribution was very broad or bimodal (as in the case of the C=C double bond in thiophene derivatives) then a larger *e.s.d.* was used, decreasing the weight of the restraint in GSAS. This is illustrated in Figure 6.7 and Figure 6.8.

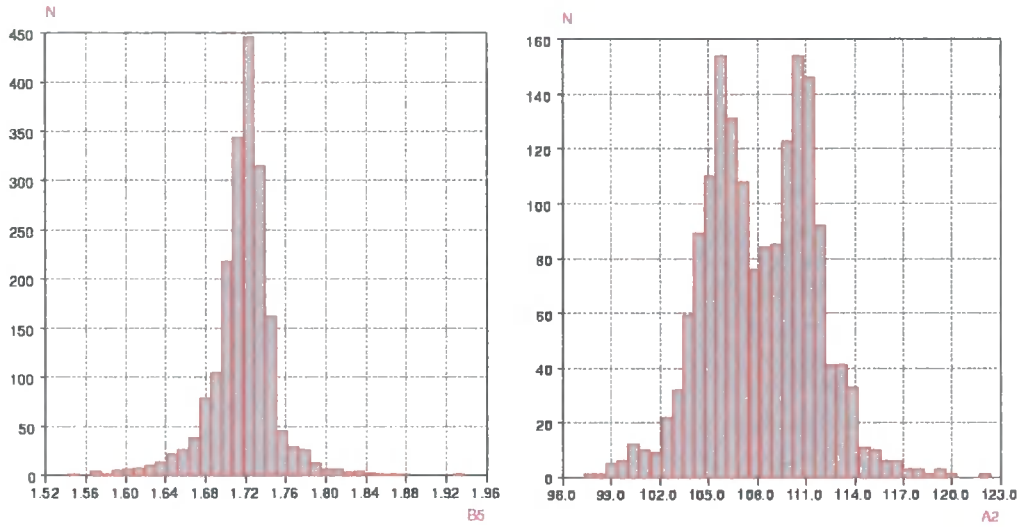

Figure 6.7 Left, histogram of distribution for C—S bond lengths (in a thiophene fragment) from the CSD showing a broad distribution. Right, histogram of distribution for C=C—S bond angle (in a thiophene fragment) from the CSD showing a bimodal distribution.

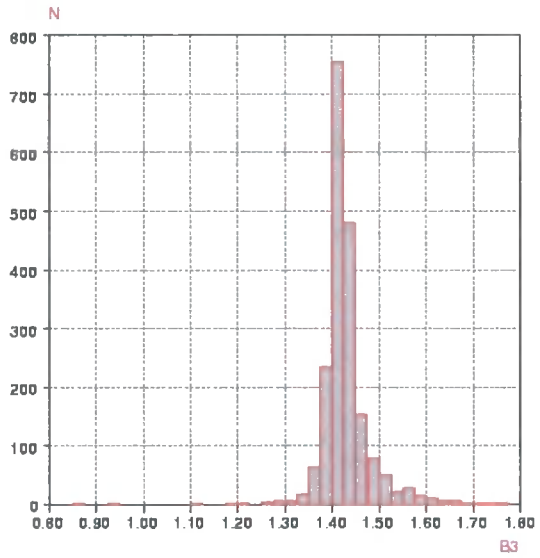

Figure 6.8 Histogram of C—C single bond in a thiophene fragment from the CSD showing a narrow distribution.

The structure was refined in space group *P*1 using the cell parameters from the indexing in MultiVisser and the structural model from the end of the simulated annealing in DASH. The bond lengths and bond angles detailed in Table 6.1 and Table 6.2 and the planarity of the thiophene rings were restrained in the refinement. In the first stages of the refinement no hydrogen atoms were taken into account, as the tin atoms in the molecule will be contributing most to the scattering of X-rays as tin has fifty electrons to hydrogen's one. The background (fifteen parameters), lattice, profile, histogram scale parameters and atomic fractional coordinates were refined. In addition a single isotropic temperature factor was refined for each tin atom, each thiophene ring and for all the methyl carbon atoms making a total of seven independent thermal factors.

The atomic fractional coordinates and the isotropic temperature factors were initially heavily damped to maintain a sensible refinement. This refined to give a structure with good geometry (planar rings, reasonable bond angles and distances), with an $R(F^2)$ of around 10 %. Final observed, calculated and difference plots are shown in Figure 6.9a. Visual inspection of the molecule suggested an approximate centre of symmetry. This in turn implies that the true symmetry of the structure may be $P\bar{1}$, with half the molecule in the asymmetric unit instead of a full molecule.

An identical refinement to the one described above was therefore carried out in space group $P\bar{1}$ with half the atoms deleted and the remaining atoms moved such that the centre of the molecule was on the origin. To aid comparison, this movement was also applied to the P1 refinement (the origin of the *P*1 unit cell is completely arbitrary, as there are no symmetry elements apart from the identity).

As can be seen from Figure 6.9, whilst still giving a good fit to the data, the centrosymmetric $P\bar{1}$ model is not as good as the non-centrosymmetric *P*1 model. The main differences can be noticed at 25 – 26 and 28 – 29 ° 2θ.

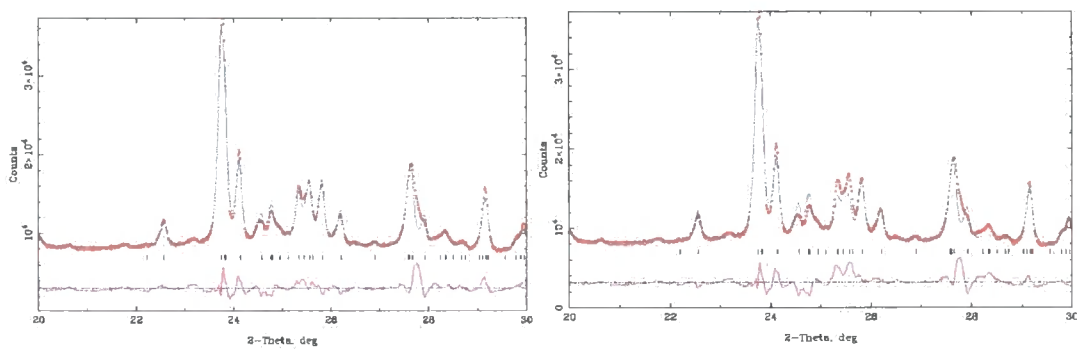

Figure 6.9 Left, observed (+), calculated (-) and difference (-) plots for the *P*1 model. Right, observed (+), calculated (-) and difference (-) plots for the $P\bar{1}$ model.

Figure 6.10 shows a comparison between the two structures given by the refinements in *P*1 and $P\bar{1}$. They are clearly very similar, with the main difference being that the *P*1 structural model is slightly bowed along the chain of rings which is not the case in the $P\bar{1}$ model.

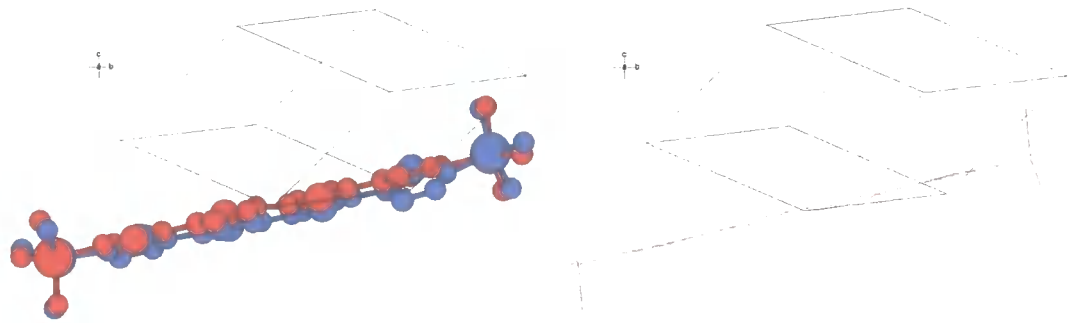

Figure 6.10 The structure of **1** refined in P1 (blue) and $P\bar{1}$ (red).

The $P\bar{1}$ model was therefore discarded and refinement continued on the *P*1 model. A total of 114 parameters were refined; histogram scale factor, zero point, fifteen background parameters, six lattice parameters, atomic fractional coordinates for twenty eight atoms and seven isotropic temperature factors. The profile co-efficients generated by the previous refinement were used and not refined. The results of the refinement are summarised in Table 6.3. After this refinement, the hydrogen atoms were added in their geometrically idealised positions using Crystals[15] and their positions fixed. The structure is shown in Figure 6.11 and Figure 6.12 and the atomic positions are given in Appendix 5.

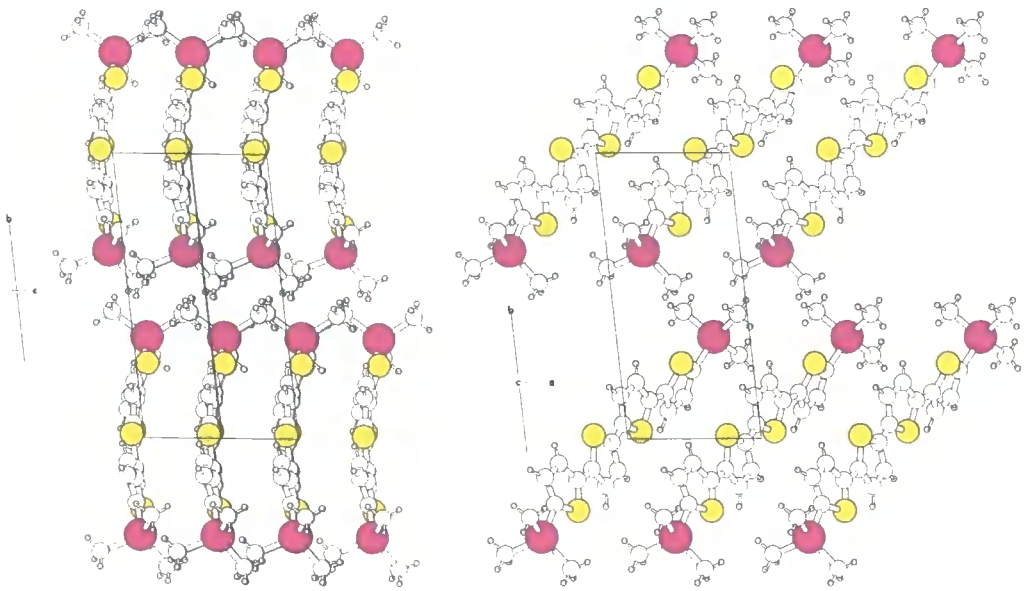

Figure 6.11 Two views of the packing diagram of **1**. Sn atoms in purple, S in yellow, C in white and H in grey.

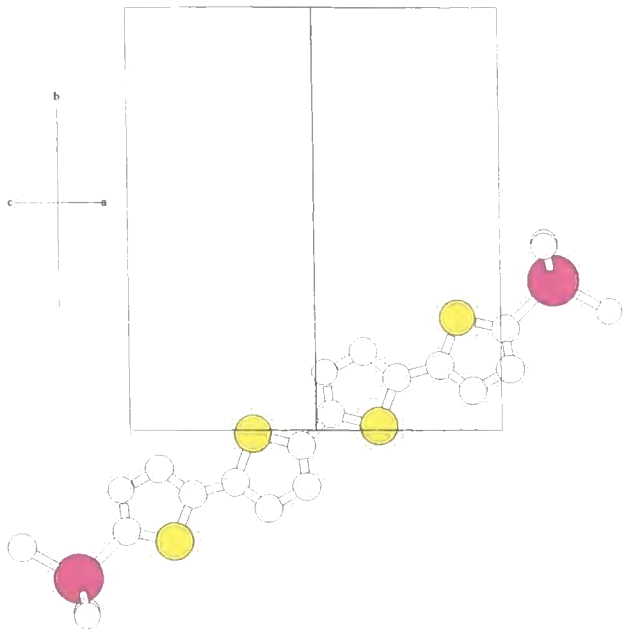

Figure 6.12 Structure of **1** viewed along [110]. Sn atoms in purple, S in yellow, C in white and H in grey.

Table 6.3 Rietveld Refinement Data for **1**.

Refinement Data	
2θ Range/°	3 - 65 °
a/Å	7.2837(4)
b/Å	14.1083(8)
c/Å	7.1084(4)
α/°	92.933(3)
β/°	116.699(3)
γ/°	94.415(3)
V/Å^3	647.62(4)
$_wR_p$/%	4.22
$R(F^2)$ /%	10.16
χ^2/%	17.48
No. parameters	114

The molecular structure of **1** is essentially linear in the Sn – Sn direction although it is slightly bowed out of the plane. The middle two thiophene units are very nearly co-planar; the S(2)—C(6)—C(8)—S(7) dihedral angle is 178.9(1) °. The other two thiophene units are more out of the plane than the middle two, with one dihedral angle of 171.0(1) ° and one of 161.5(1) °. An interesting feature is that the rings alternate their orientation (sulfur "up" followed by sulfur "down"). The bond distances and angles (given in the electronic appendix attached to this thesis) are all within a reasonable range of those found from the CSD, as illustrated in Figure 6.13.

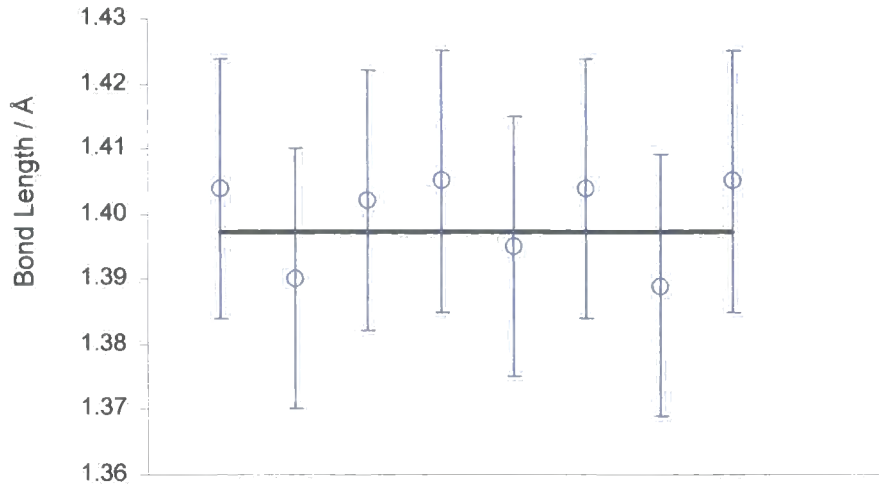

Figure 6.13 Thiophene C=C bond lengths. Blue circles showing refined values for **1**, error bars showing esd used in refinement restraints and black line average value found in CSD.

The distance between the tin atom and the thiophene unit is shown in Table 6.4 as a function of the number of thiophene units in the molecule. The table shows that the distance is clearly longer in the quaterthiophene, **1**, than in the lower members of the series. This indicates that the strength of the bond and thus, it is believed, the stability of the molecule is decreasing with increasing number of thiophene units within the molecule. In the refinement in the centrosymmetric space group $P\bar{1}$ the distance was much the same (2.22 Å) and certainly greater than for the other, lower members of the series

Table 6.4 Sn—ring bond length as a function of number of thiophene units.

Thiophene units	Sn(1)—C(3) bond length / Å
1	2.155(2)
2	2.138(2)
3	2.152(3)
4	2.21354(9)
	2.20892(9)

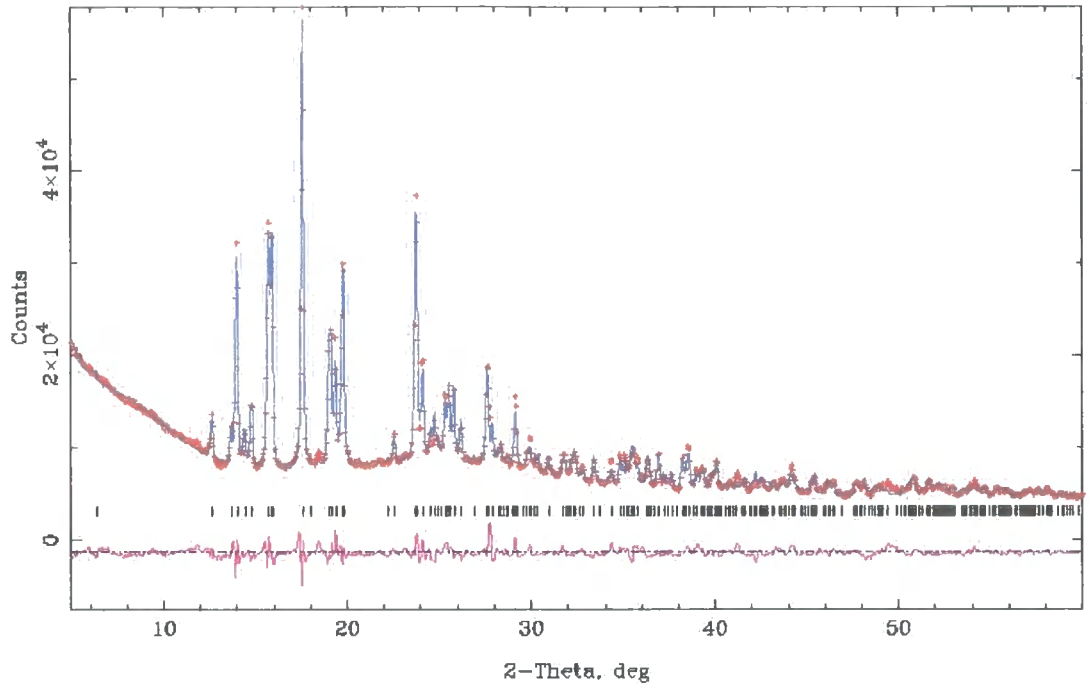

Figure 6.14 Final observed (+), calculated (-) and difference (-) plots for **1**.

6.5 Conclusions

The powder X-ray diffraction data measured from **1** was indexed to give a triclinic cell with a = 7.2837(4) Å, b = 14.1083(8) Å, c = 7.1084(4) Å; α = 92.933(3) °, β = 116.699(3) ° and γ = 94.415(3) °. The structure was solved in the $P1$ spacegroup and the structure shows **1** to be approximately planar, but slightly bowed. The thiophene units alternate "up" and "down" and the middle two are co-planar. The positions of the non-H atoms have been found with good accuracy considering the difference between the scattering powers of Sn (atomic number 50) and C (atomic number 12). This represents a considerable achievement given the complexity of both the data (note the large number of Bragg reflections and the overlap between them in *e.g.* Figure 6.14) and the molecule itself.

6.6 References

(1) Horowitz, G.; Kouki, F.; El Kassmi, A.; Valat, P.; Wintgens, V.*et al Adv. Mater.*, **1999**, *11*, 234.

(2) Harris, K. D. M. and Tremayne, M. *Chem. Mater.*, **1996**, *8*, 2554-2570.

(3) Harris, K. D. M.; Tremayne, M. and Kariuki, B. M. *Angew. Chem.-Int. Edit. Engl.*, **2001**, *40*, 1626-1651.

(4) Visser, J. W. *J. Appl. Crystallogr.*, **1969**, *2*, 89.

(5) Werner, P.-E.; Eriksson, L. and Westdahl, M. *J. Appl. Crystallogr.*, **1985**, *18*.

(6) Boultif, A. and Louer, D. *J. Appl. Crystallogr.*, **1991**, *24*.

(7) Metropolis, K. and Ulam, S. *J. Am. Stat. Assoc.*, **1949**, *44*, 335.

(8) Rietveld, H. M. *J. Appl. Crystallogr.*, **1969**, *2*, 65.

(9) Young, R. A., Ed. *The Rietveld Method*; IUCr/OUP: Oxford, 1993.

(10) Coelho, A. A., *TOPAS v2.13 General Profile and Structure Analysis Software for Powder Diffraction Data*, Bruker AXS, Karlsruhe, 2000.

(11) Evans, J. S. O., *MultiVisser - Fortran Routine for controlling Visser*, 2001.

(12) *CAChe Satellite Version 3.2*, Oxford Molecular Ltd, Oxford, Oxfordshire, UK, 1999.

(13) *DASH - Simulated Annealing*, Cambridge Crystallographic Data Centre, Cambridge, Cambridgeshire, UK, 2001.

(14) Larson, A. C. and von Dreele, R. B., *GSAS - General Structure Analysis System, powder data refinement program for UNIX systems*, Los Alamos National Laboratory, Los Alamos, NM, USA, 1998.

(15) Watkin, D. J.; Prout, C. K.; Carruthers, J. R.; Betteridge, P. W. and Cooper, R. I., *CRYSTALS 2000*, Chemical Crystallography Laboratory, Oxford, Oxfordshire, UK, 2000.

Appendix 1 Compound summary sheets

Key

For Rietveld figures:	Blue = observed, red = calculated, grey = difference
For cell parameter plots:	Open blue circles = cooling. Filled red triangles = heating.
For SQUID plots:	Open blue circles = zero field cooled. Filled red triangles = field cooled.
For conductivity plots:	Open blue points = cooling. Filled red points = heating.

A1.1 $La_2O_3Mn_2Se_2$

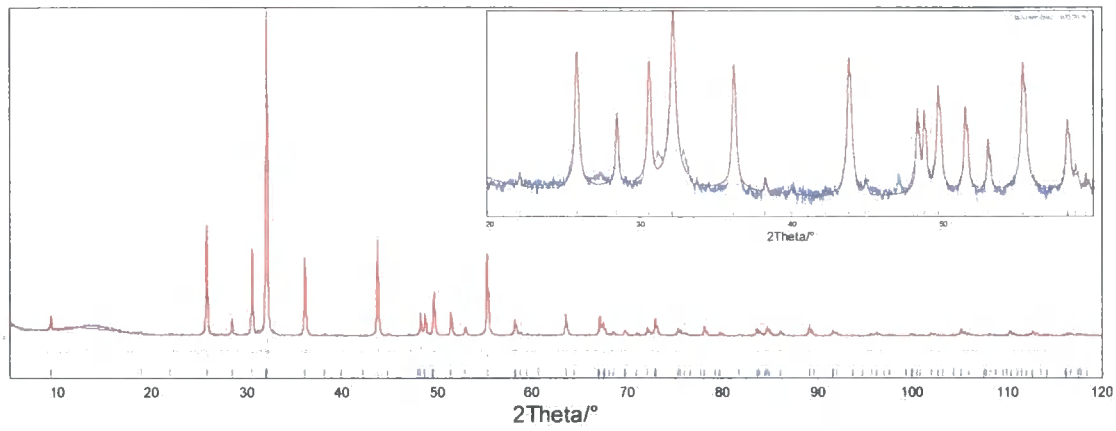

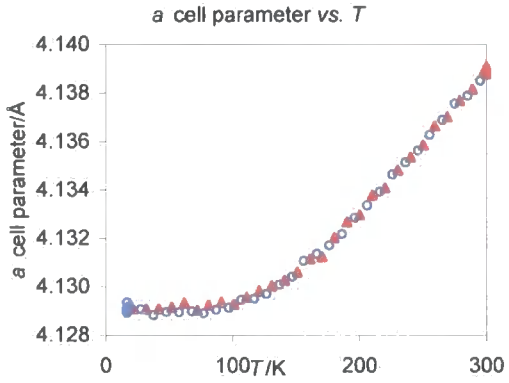

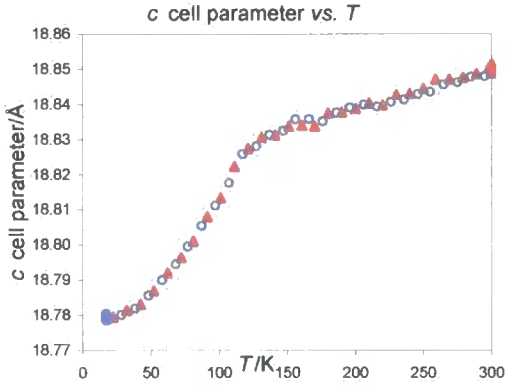

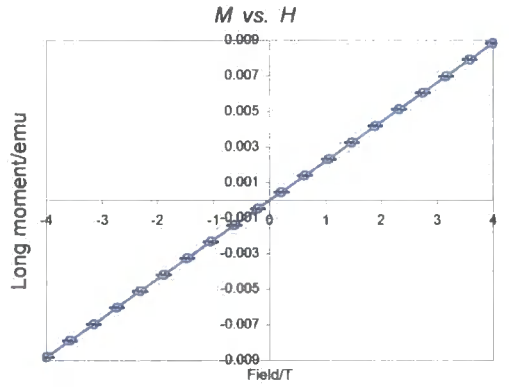

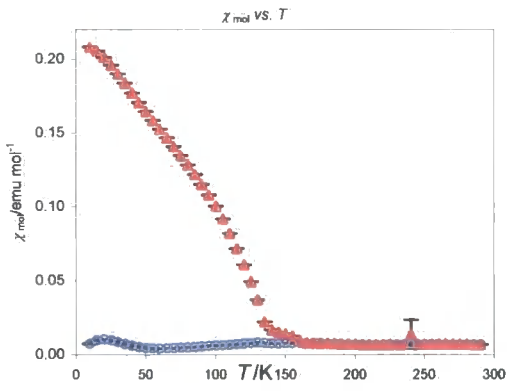

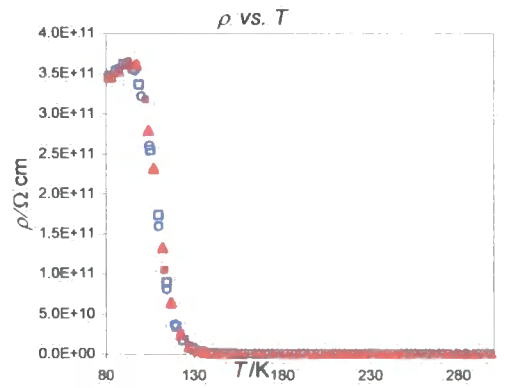

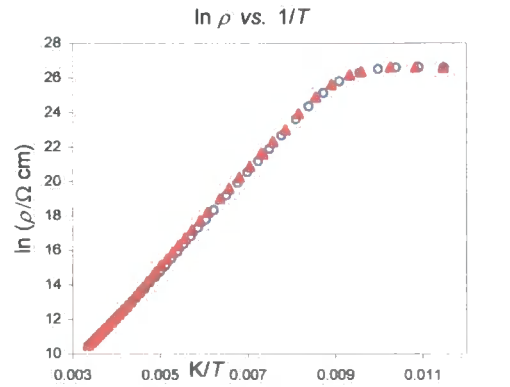

A1.2 $La_2O_3Co_2Se_2$

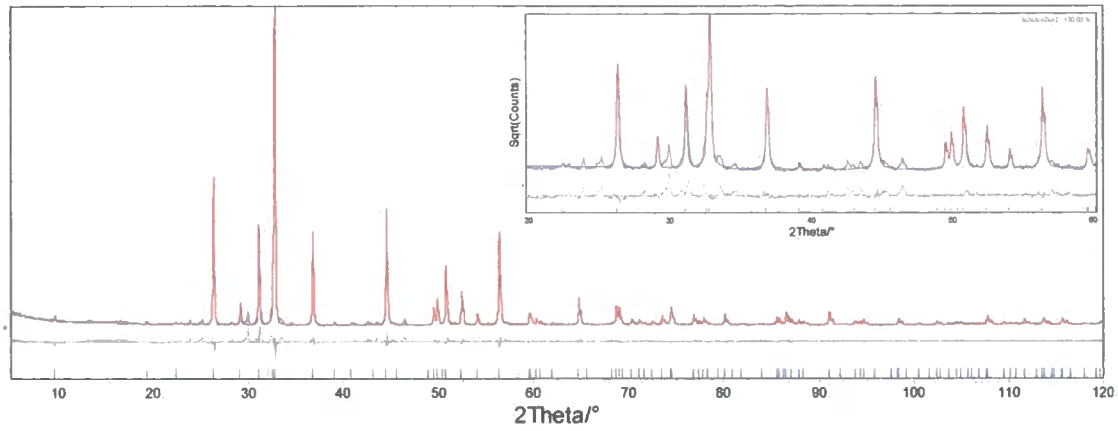

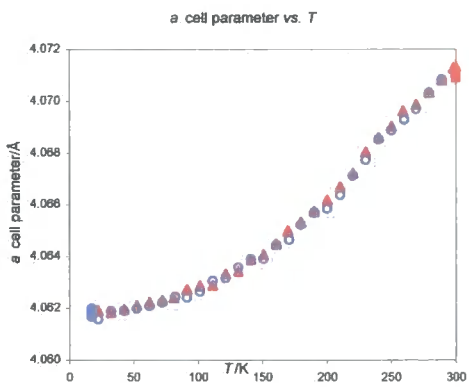

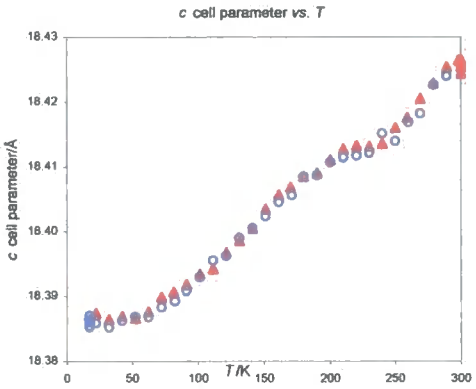

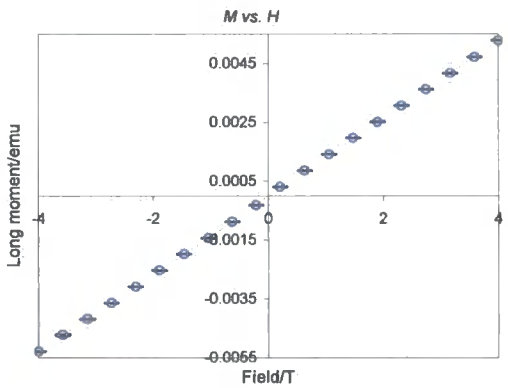

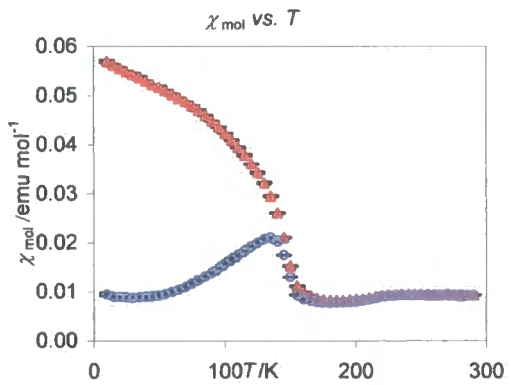

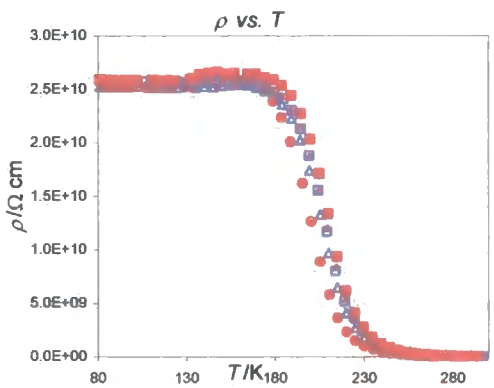

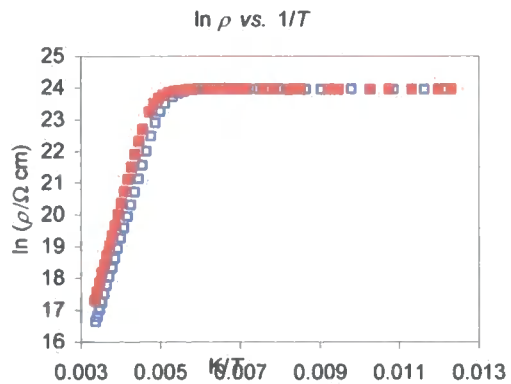

A1.3 $Sr_2MnCu_2O_2Se_2$

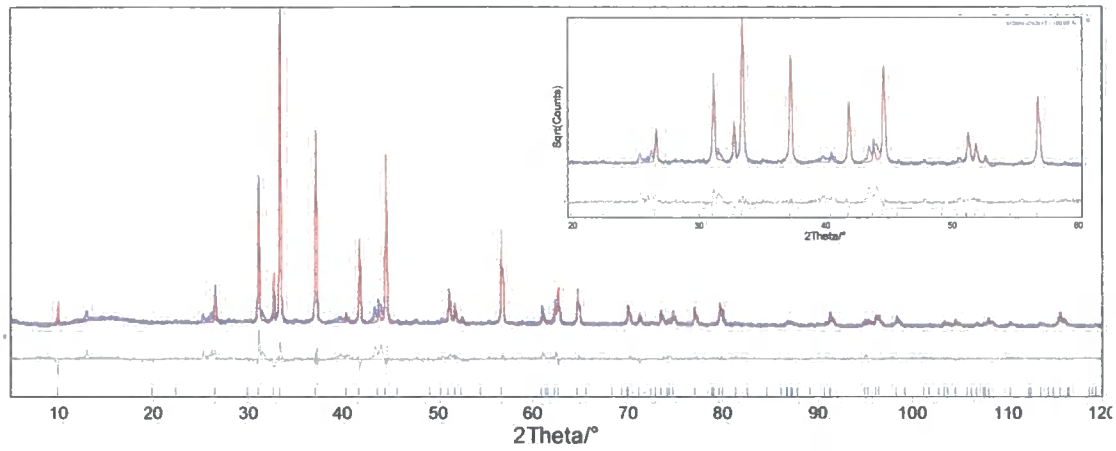

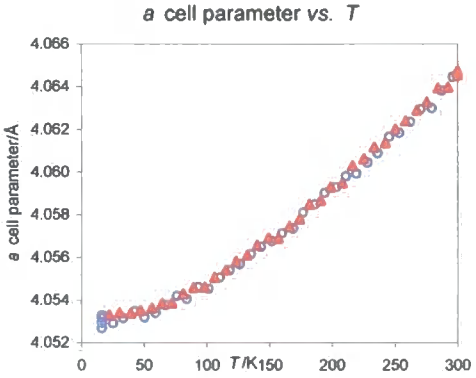

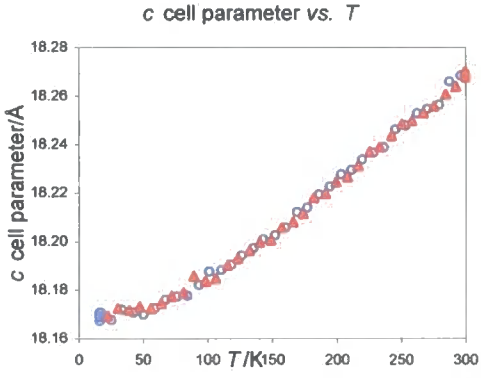

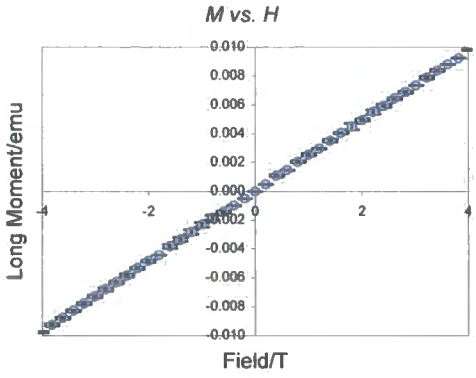

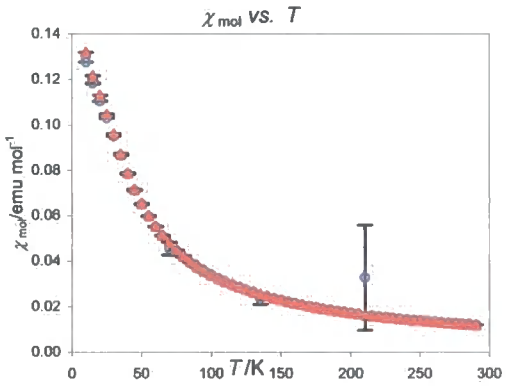

A1.4 $Ba_2MnCu_2O_2Se_2$

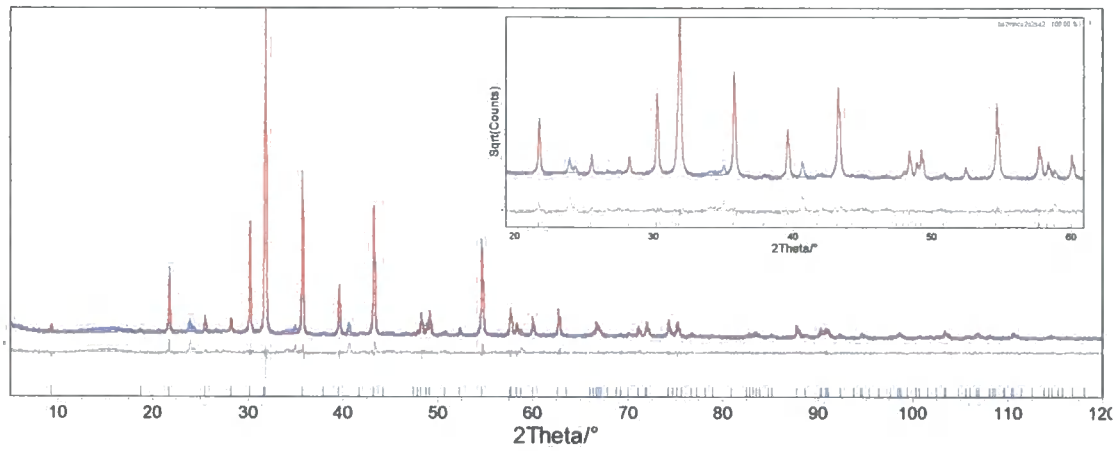

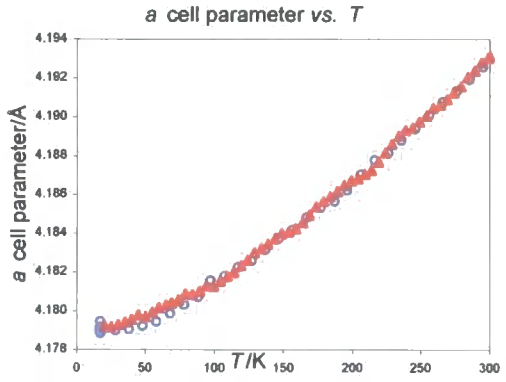

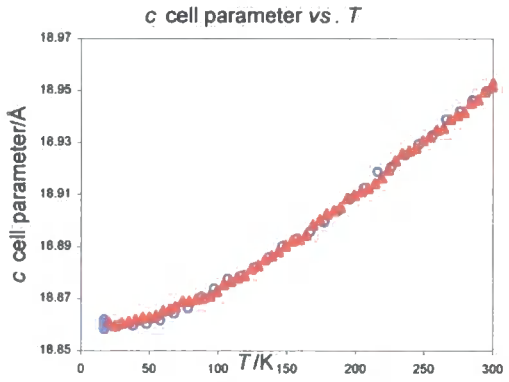

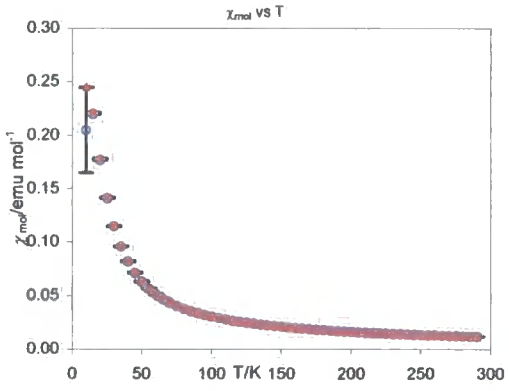

A1.5 $Sr_2CoCu_2O_2S_2$

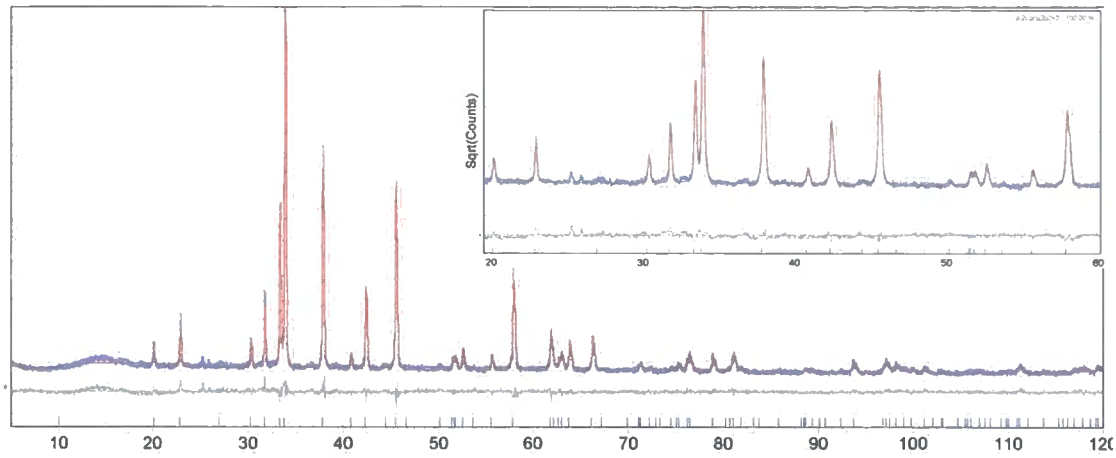

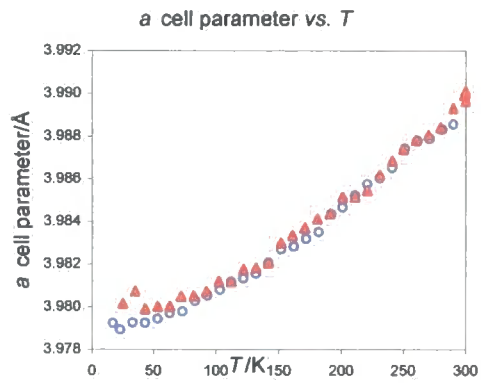

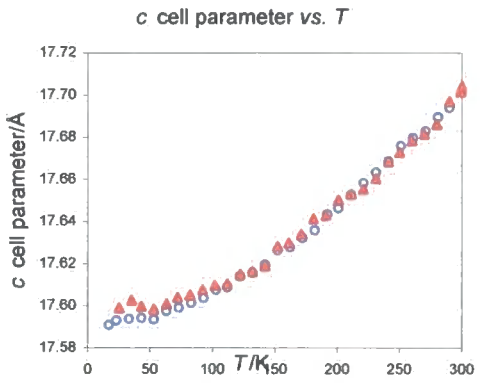

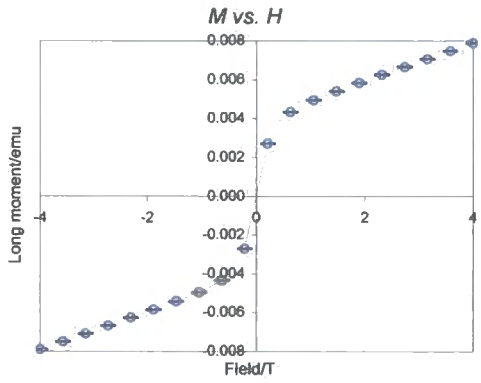

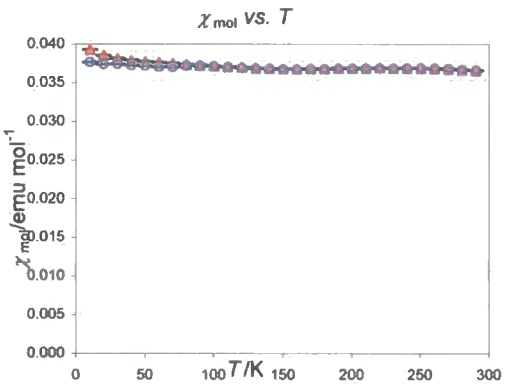

A1.6 $Sr_2CoCu_2O_2Se_2$

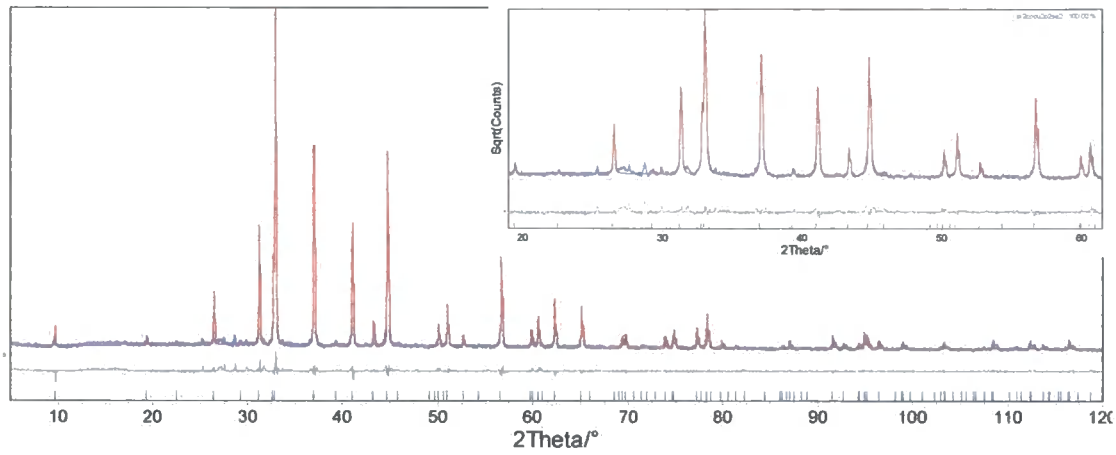

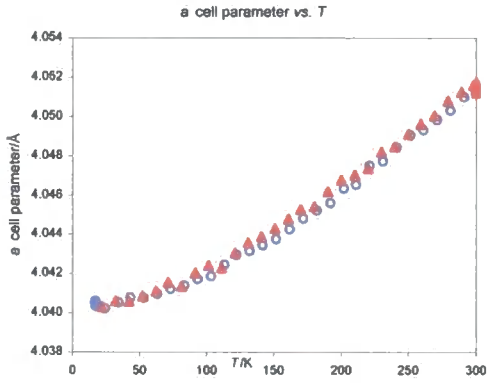

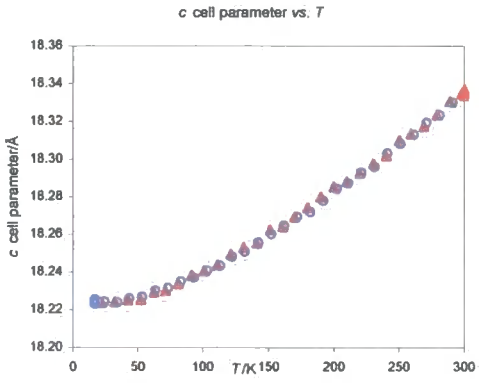

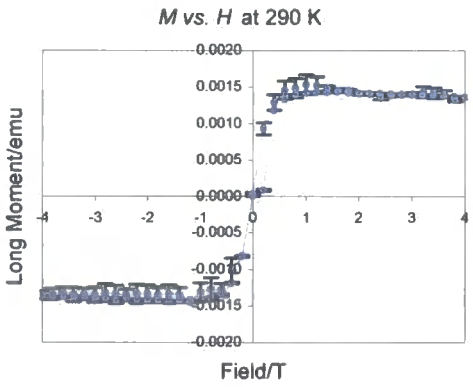

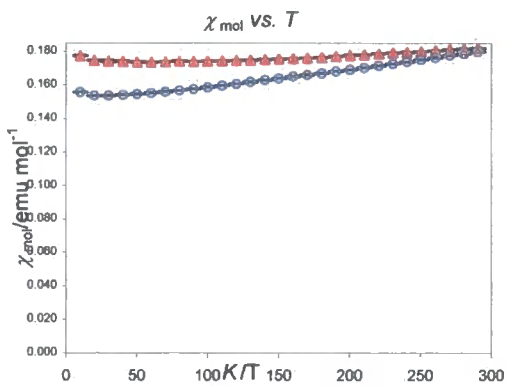

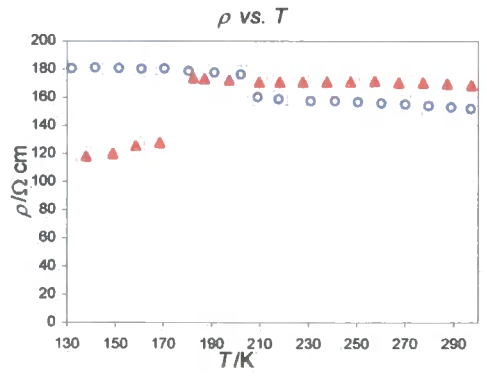

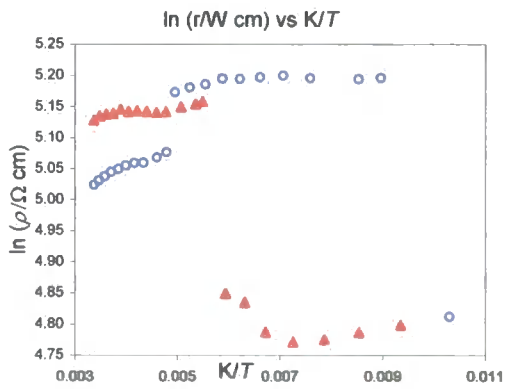

A1.7 $Ba_2CoCu_2O_2S_2$

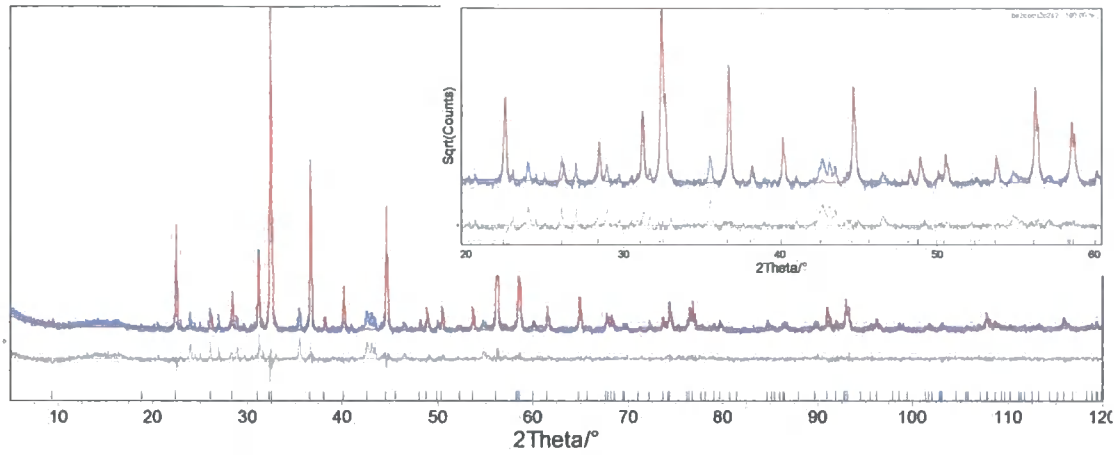

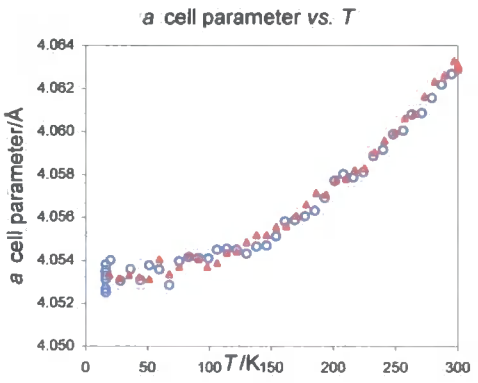

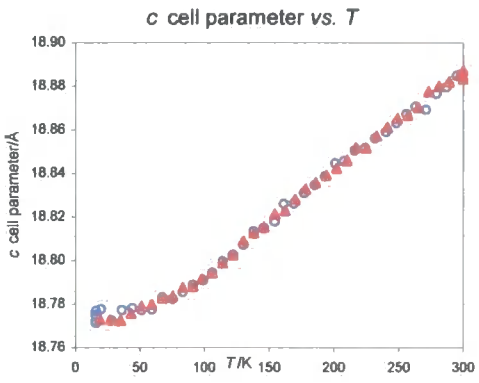

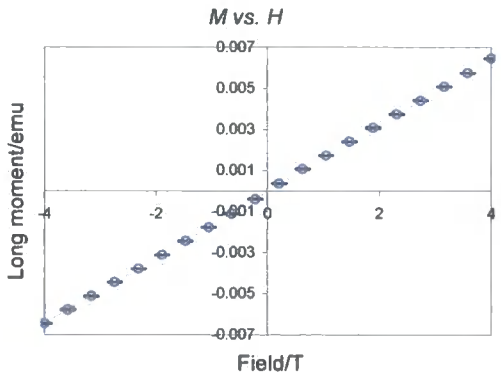

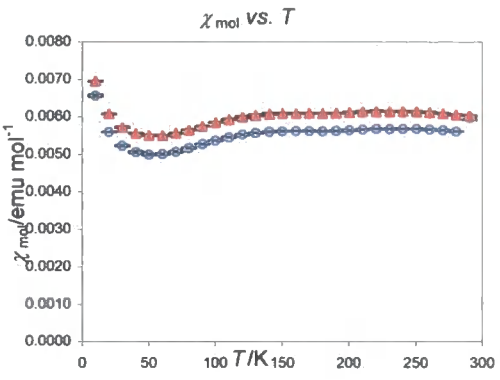

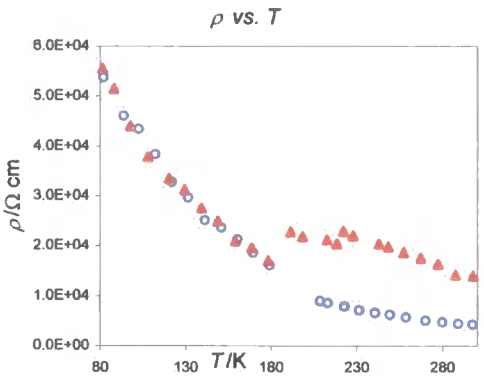

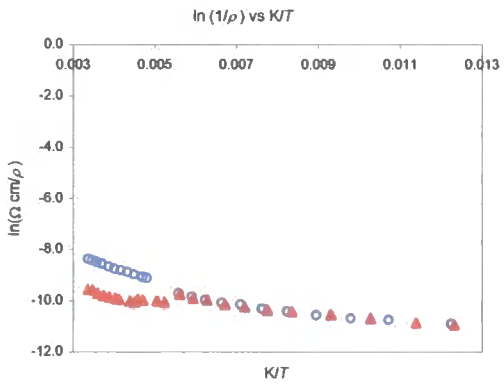

A1.8 $Ba_2CoCu_2O_2Se_2$

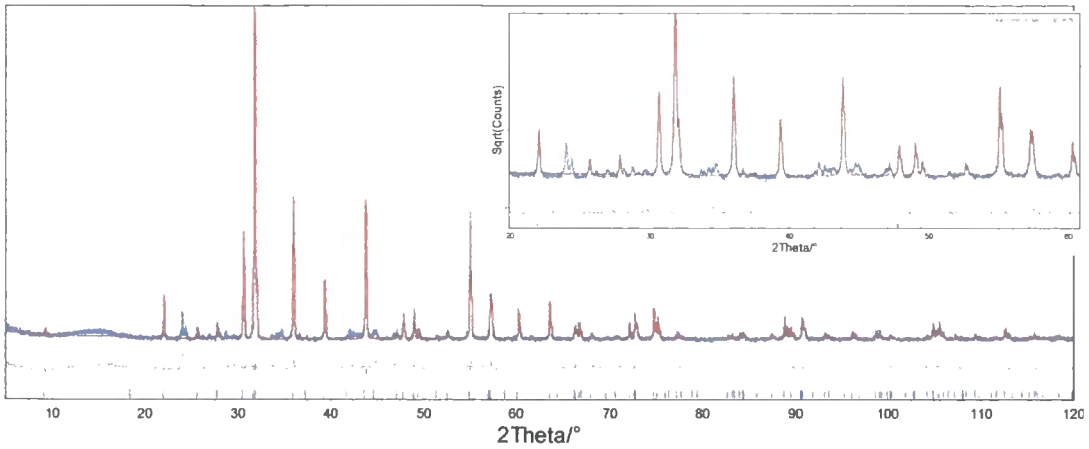

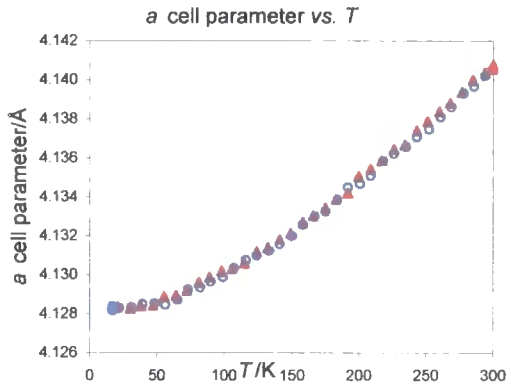

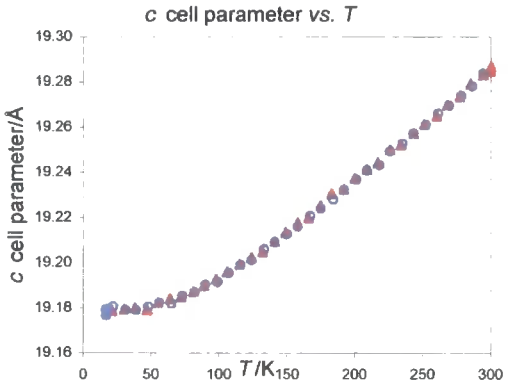

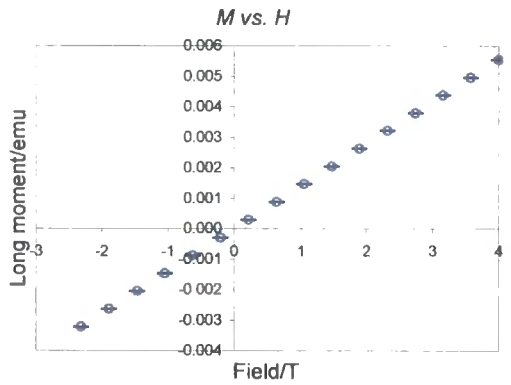

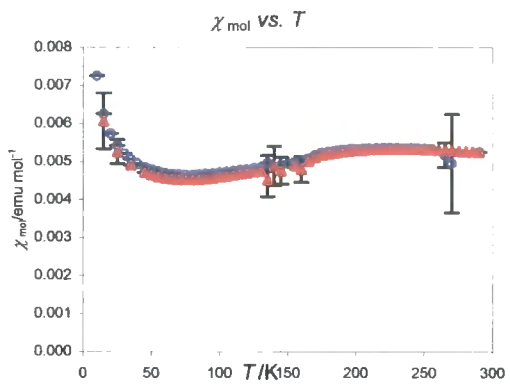

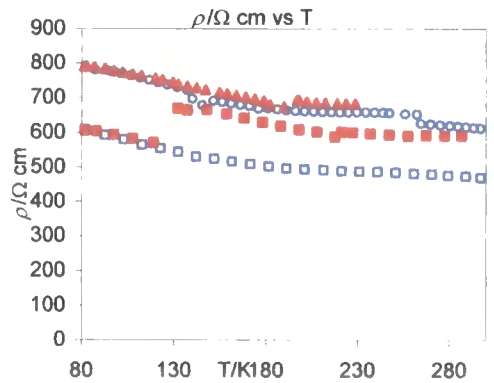

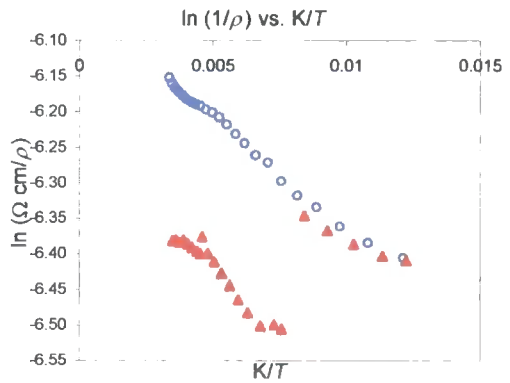

A1.9 $Sr_2NiCu_2O_2Se_2$

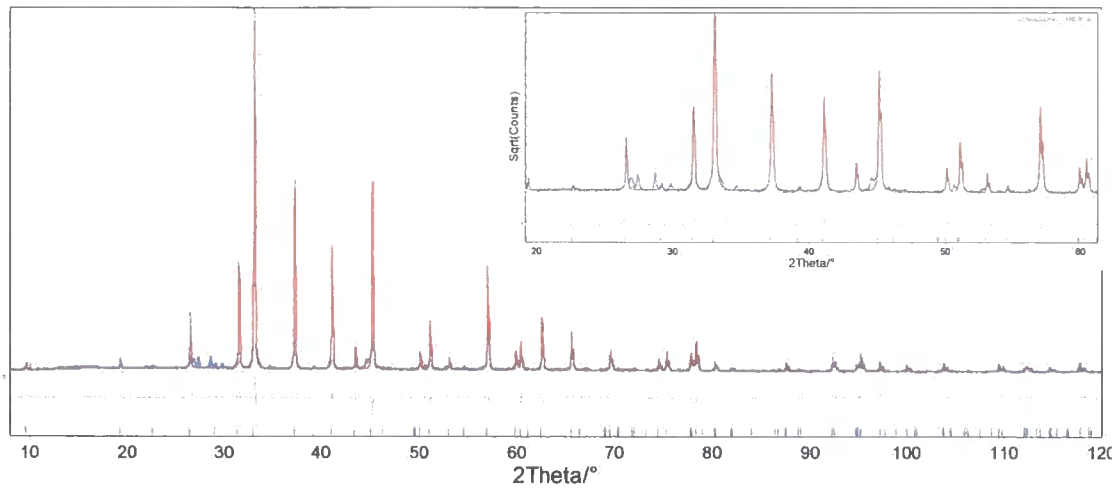

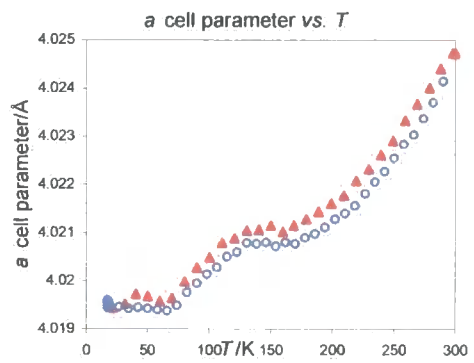

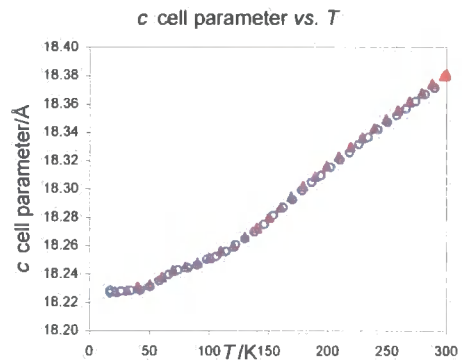

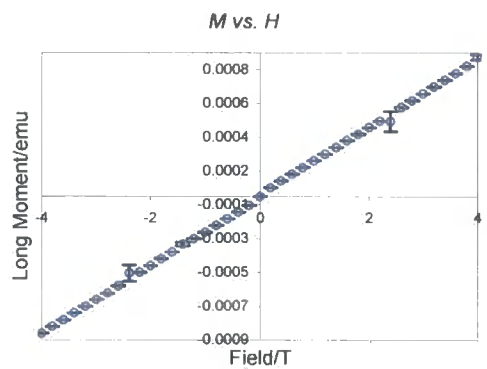

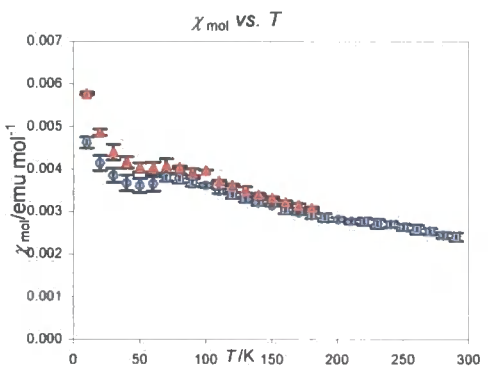

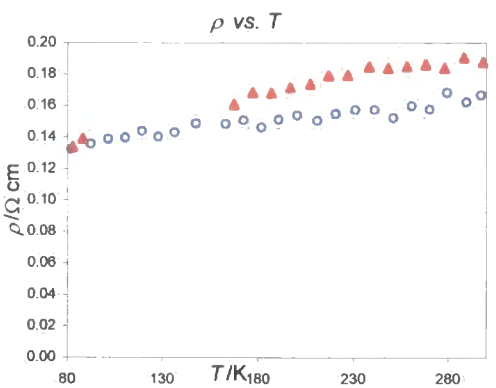

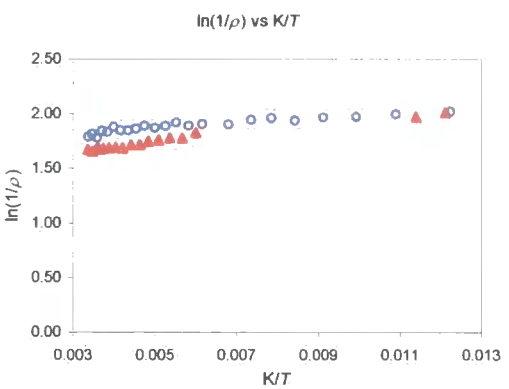

A1.10 $Ba_2NiCu_2O_2Se_2$

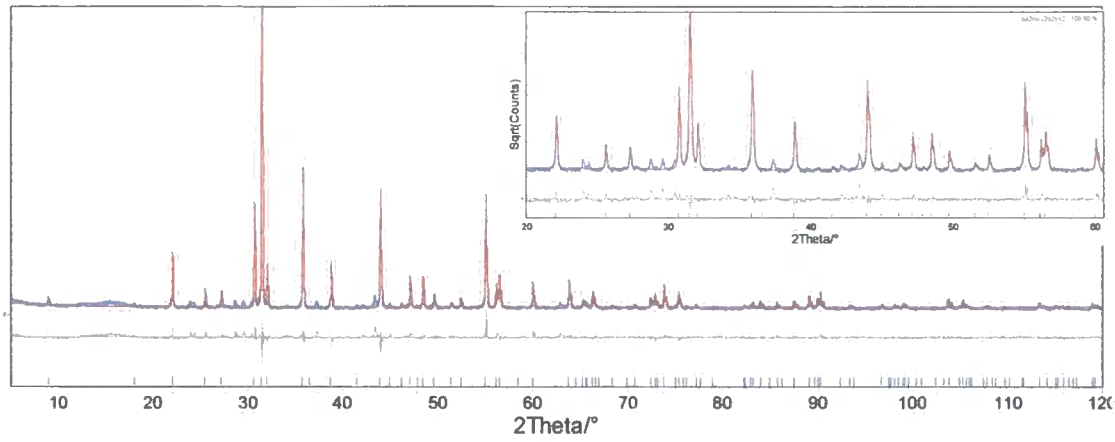

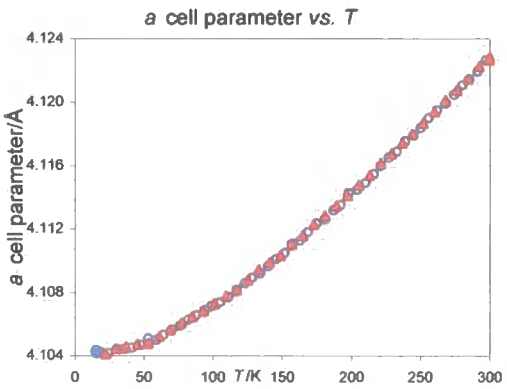

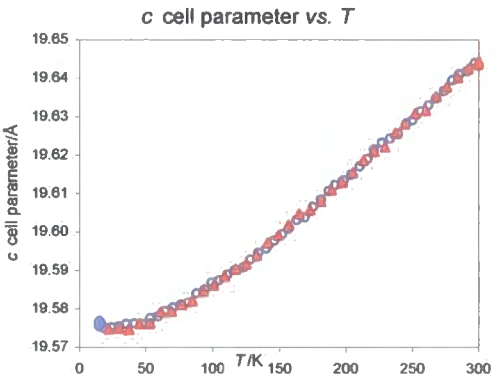

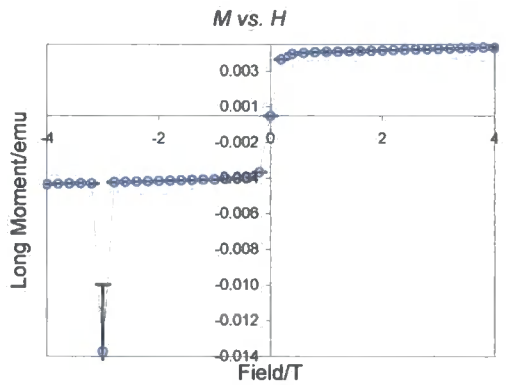

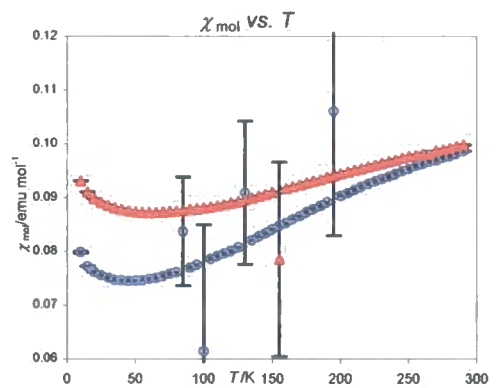

A1.11 $Sr_2ZnCu_2O_2S_2$

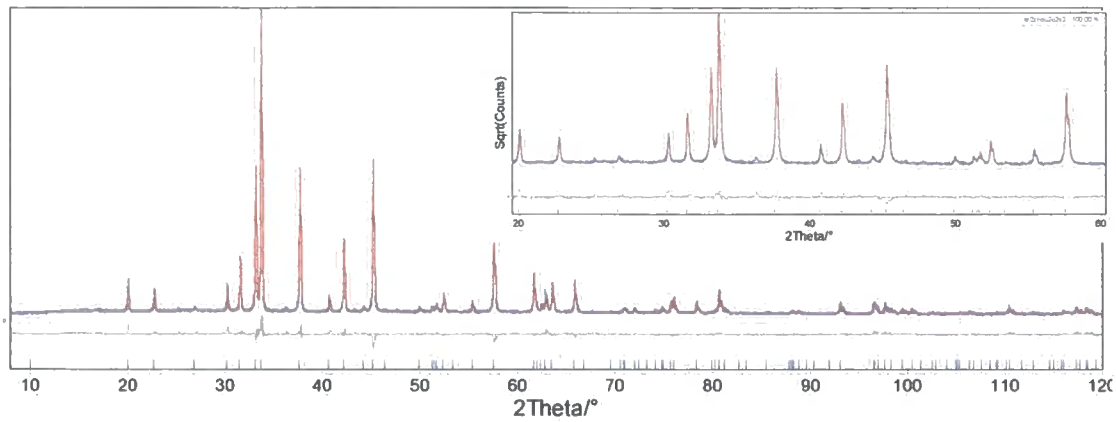

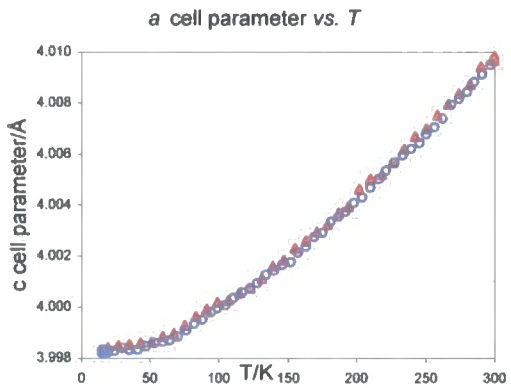

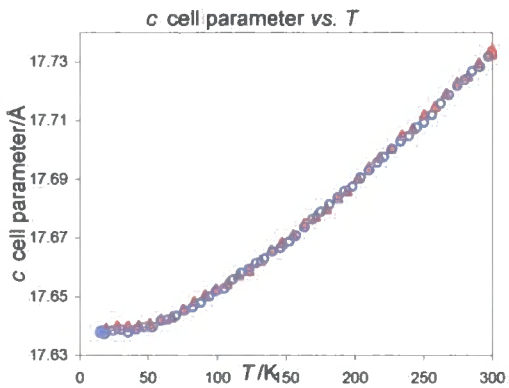

A1.12 $Sr_2ZnCu_2O_2Se_2$

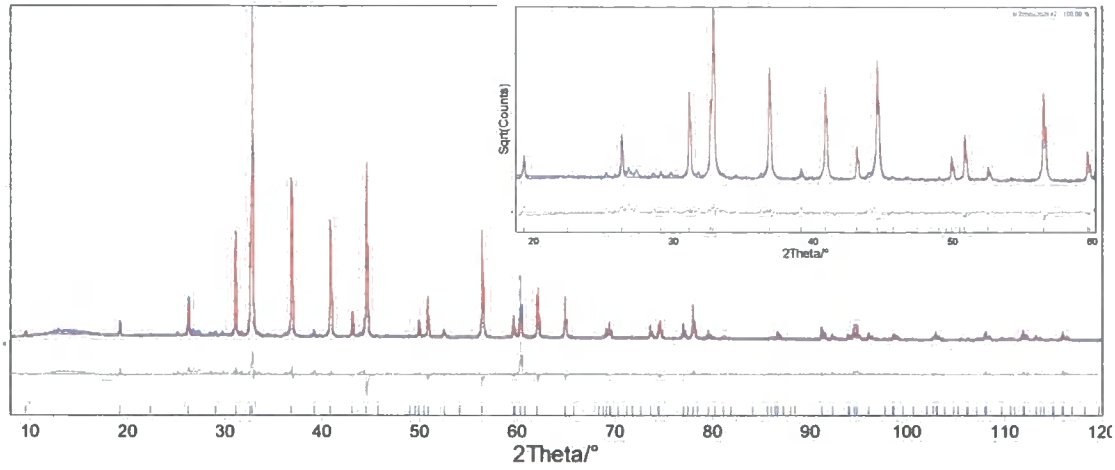

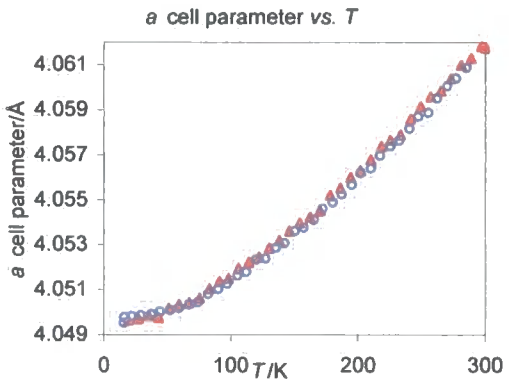

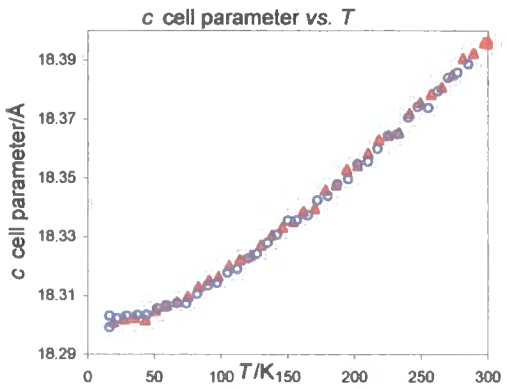

A1.13 a cell parameter

$La_2O_3Mn_2Se_2$

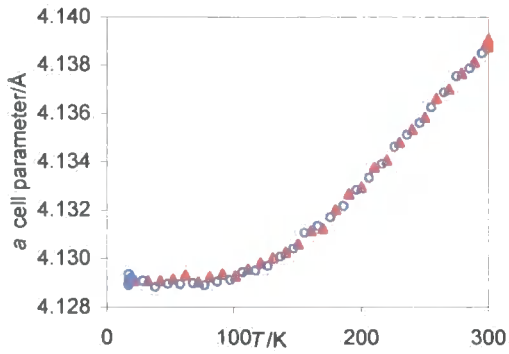

$La_2O_3Co_2Se_2$

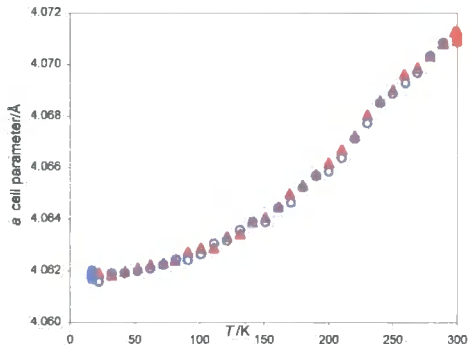

$Sr_2MnCu_2O_2Se_2$

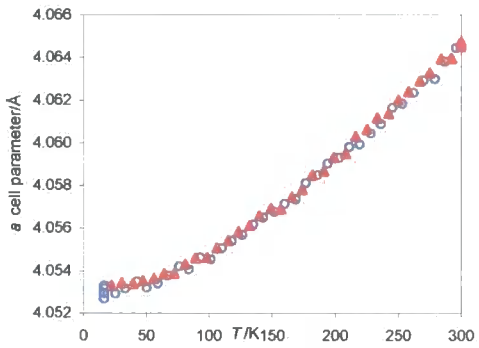

$Ba_2MnCu_2O_2Se_2$

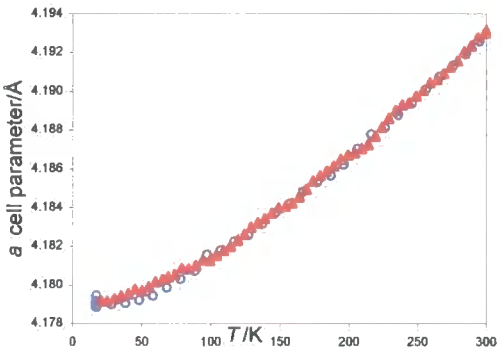

$Sr_2CoCu_2O_2S_2$

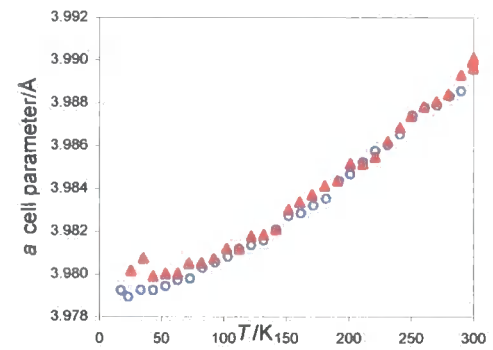

$Sr_2CoCu_2O_2Se_2$

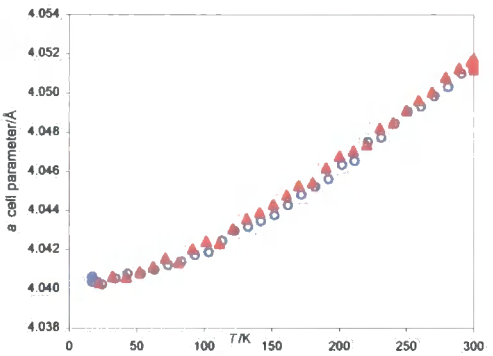

$Ba_2CoCu_2O_2S_2$

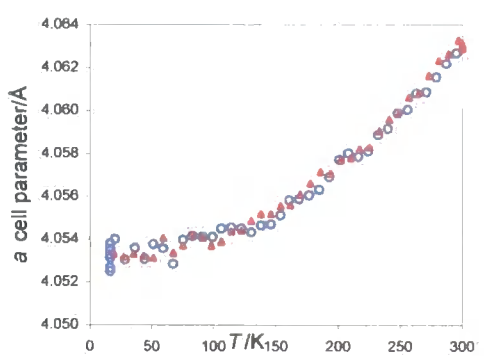

$Ba_2CoCu_2O_2Se_2$

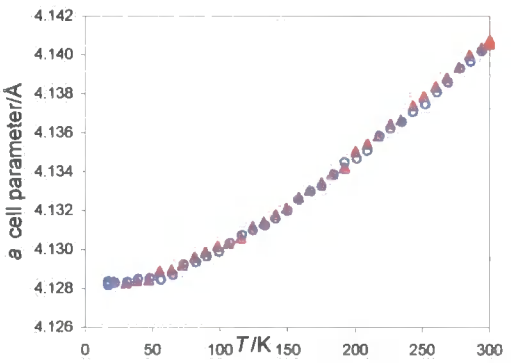

$Sr_2NiCu_2O_2Se_2$

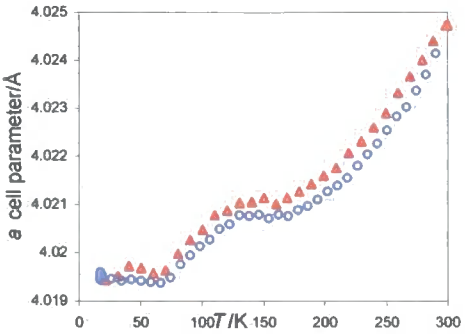

$Ba_2NiCu_2O_2Se_2$

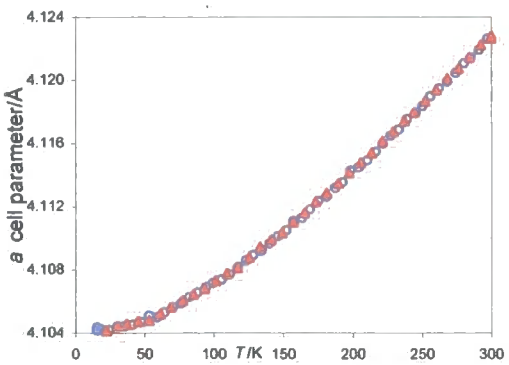

$Sr_2ZnCu_2O_2S_2$

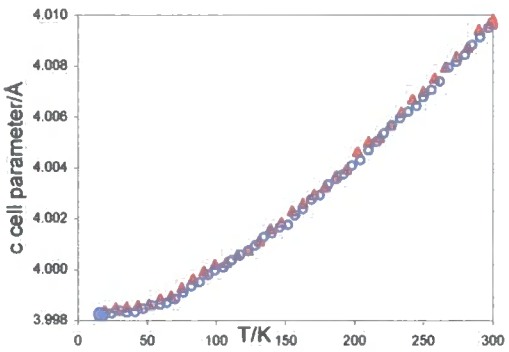

$Sr_2ZnCu_2O_2Se_2$

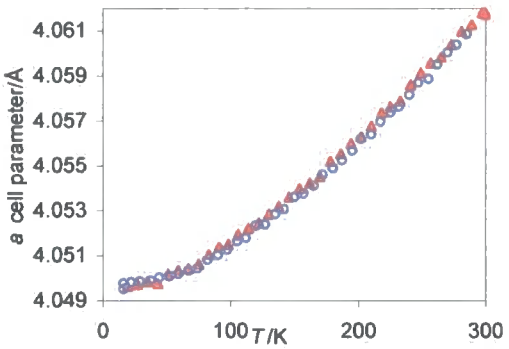

A1.14 c cell parameter

$La_2O_3Mn_2Se_2$

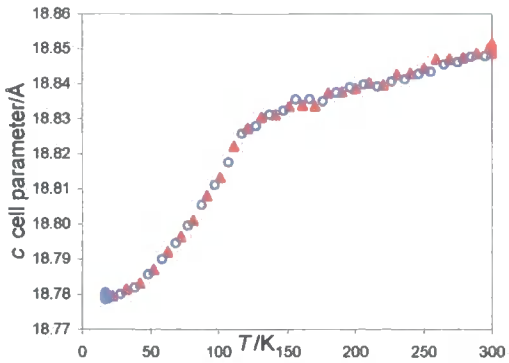

$La_2O_3Co_2Se_2$

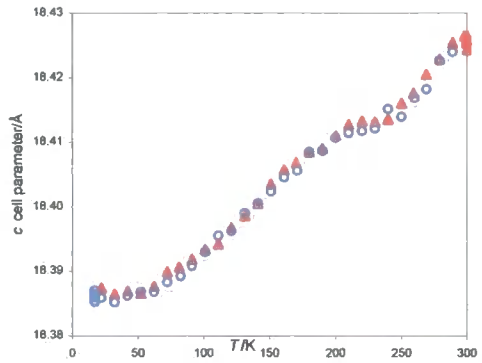

$Sr_2MnCu_2O_2Se_2$

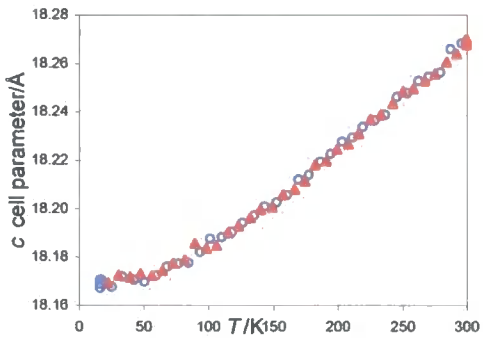

$Ba_2MnCu_2O_2Se_2$

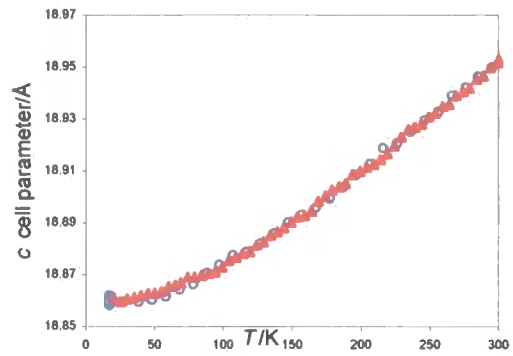

$Sr_2CoCu_2O_2S_2$

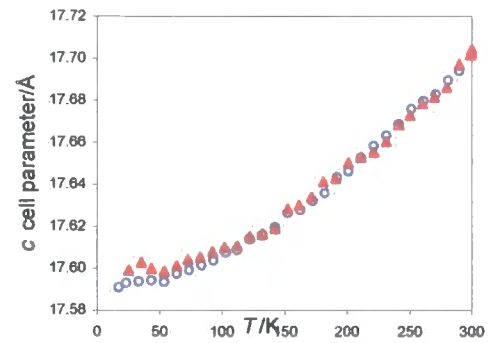

$Sr_2CoCu_2O_2Se_2$

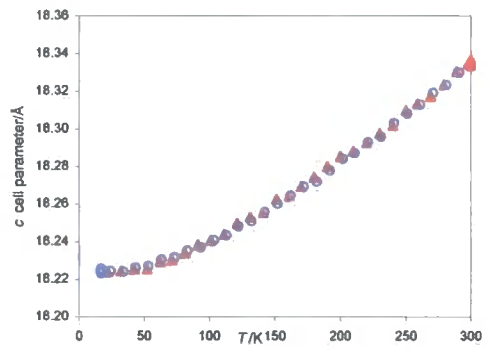

$Ba_2CoCu_2O_2S_2$

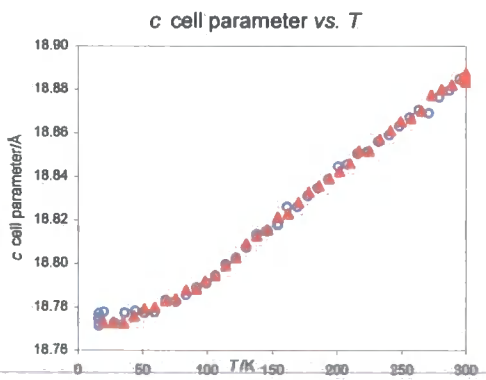

$Ba_2CoCu_2O_2Se_2$

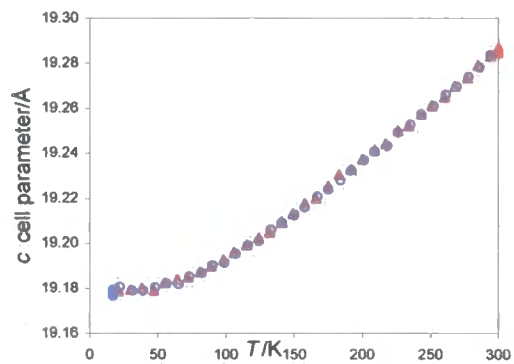

$Sr_2NiCu_2O_2Se_2$

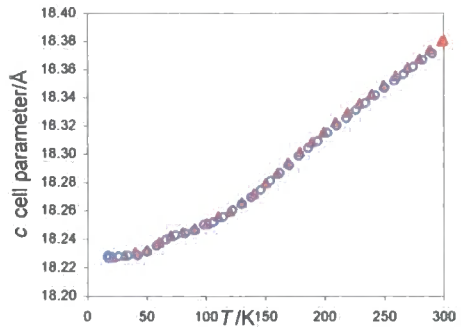

$Ba_2NiCu_2O_2Se_2$

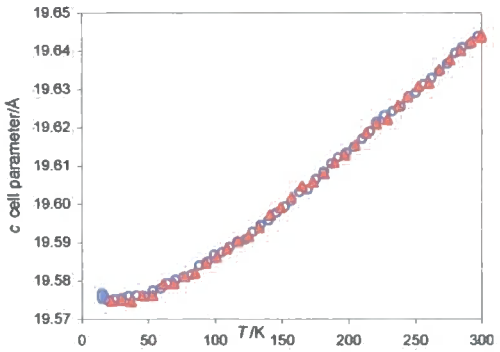

$Sr_2ZnCu_2O_2S_2$

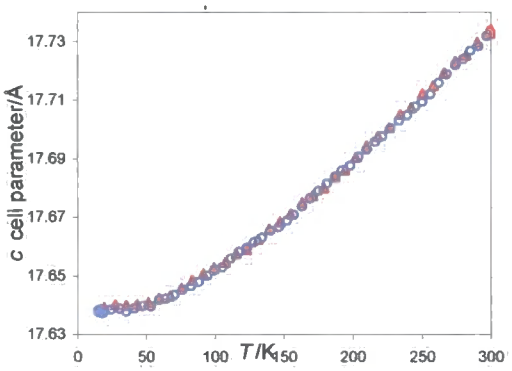

$Sr_2ZnCu_2O_2Se_2$

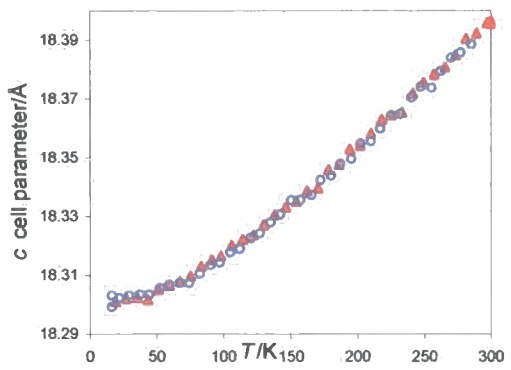

A1.15 M vs. H

$La_2O_3Mn_2Se_2$

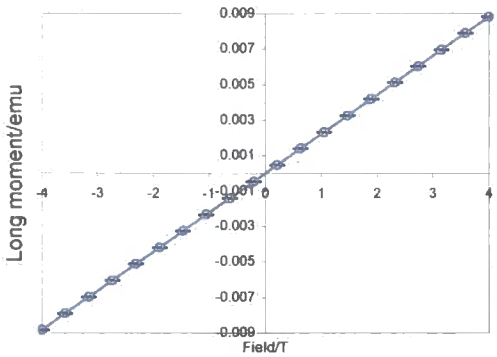

$La_2O_3Co_2Se_2$

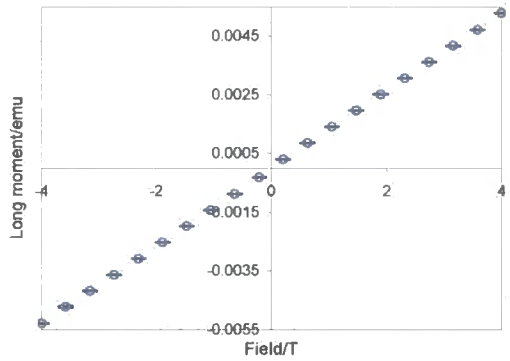

$Sr_2MnCu_2O_2Se_2$

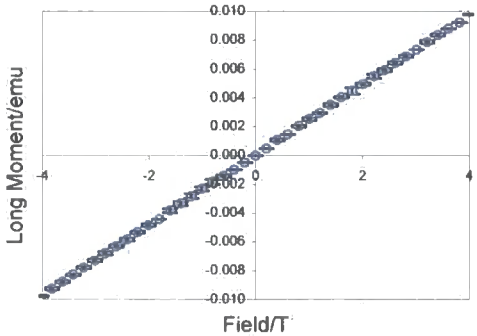

$Sr_2CoCu_2O_2S_2$

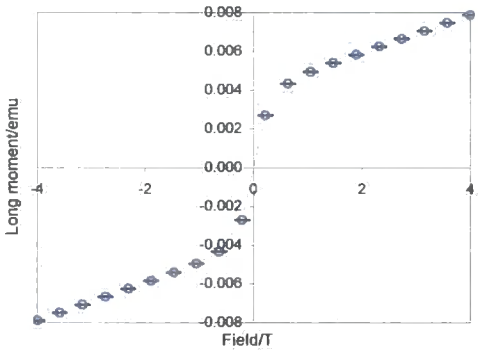

$Sr_2CoCu_2O_2Se_2$

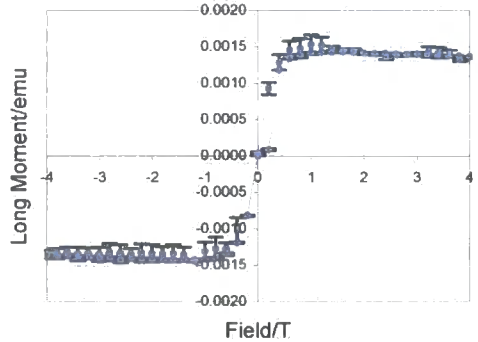

$Ba_2CoCu_2O_2S_2$

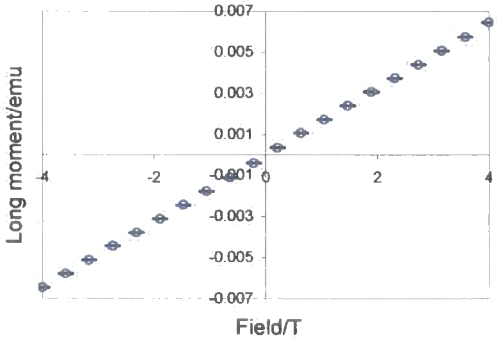

$Ba_2CoCu_2O_2Se_2$

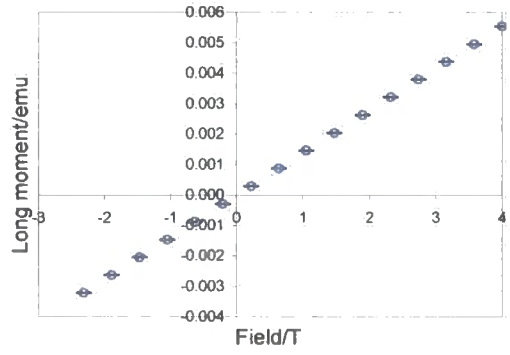

$Sr_2NiCu_2O_2Se_2$

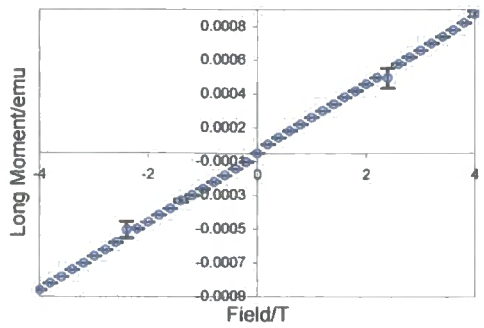

$Ba_2NiCu_2O_2Se_2$

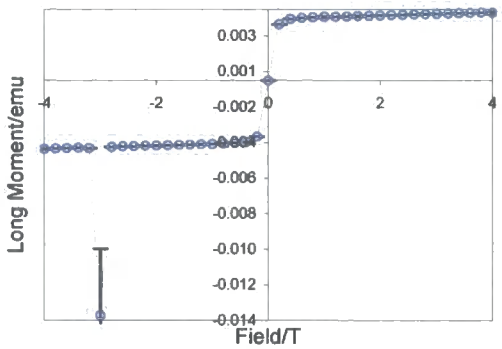

A1.16 χ_{mol} vs. T

$La_2O_3Mn_2Se_2$

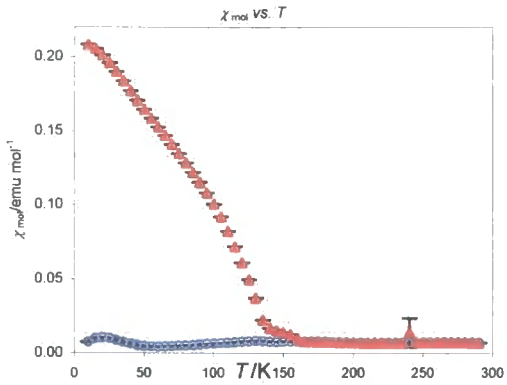

$La_2O_3Co_2Se_2$

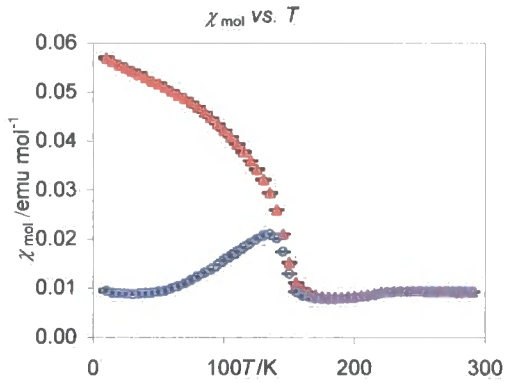

$Sr_2MnCu_2O_2Se_2$

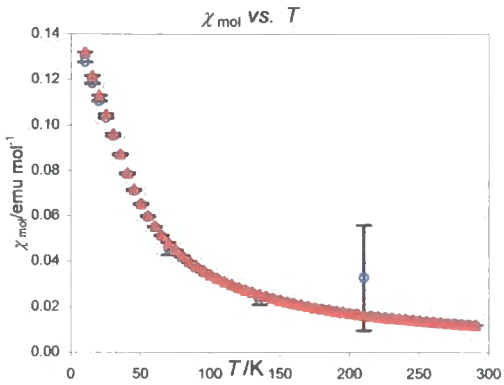

$Ba_2MnCu_2O_2Se_2$

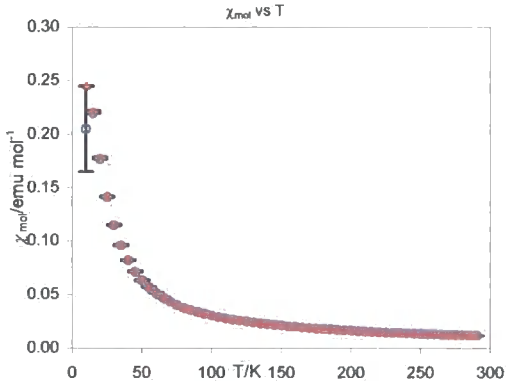

$Sr_2CoCu_2O_2S_2$

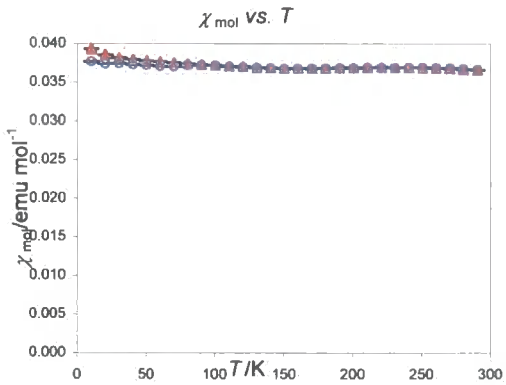

$Sr_2CoCu_2O_2Se_2$

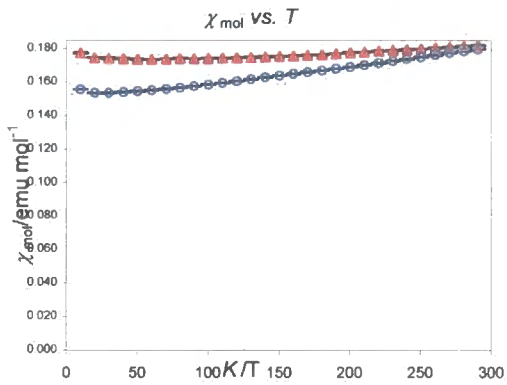

$Ba_2CoCu_2O_2S_2$

$Ba_2CoCu_2O_2Se_2$

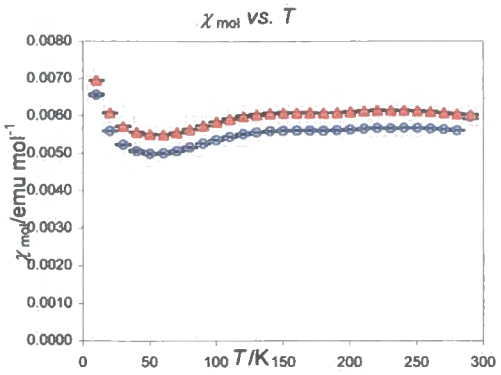
χ mol vs. T
0.0080
0.0070
0.0060
0.0050
0.0040
0.0030
0.0020
0.0010
0.0000
χ mol/emu mol-1
0
50
100
T/K
150
200
250
300

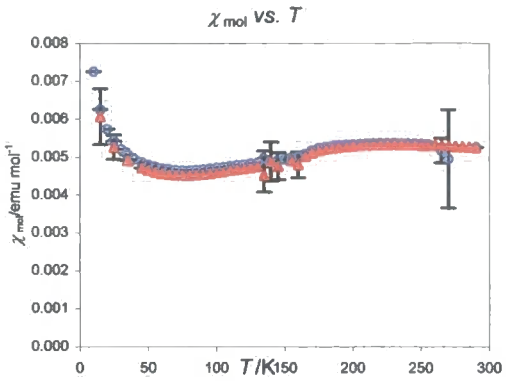
χ mol vs. T
0.008
0.007
0.006
0.005
0.004
0.003
0.002
0.001
0.000
χ mol/emu mol-1
0
50
100
T/K
150
200
250
300

$Sr_2NiCu_2O_2Se_2$

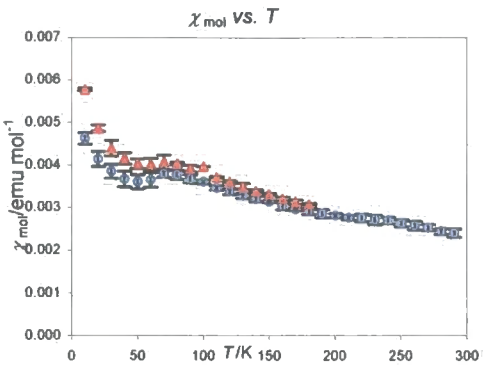

$Ba_2NiCu_2O_2Se_2$

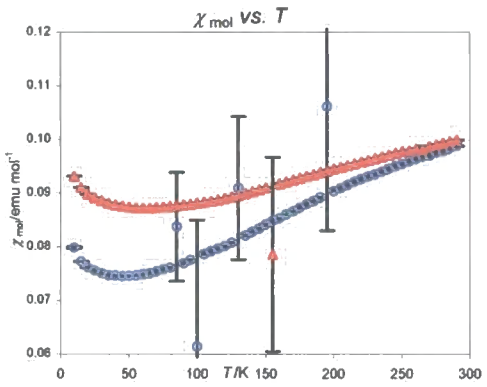

A1.17 Conductivity

$La_2O_3Mn_2Se_2$

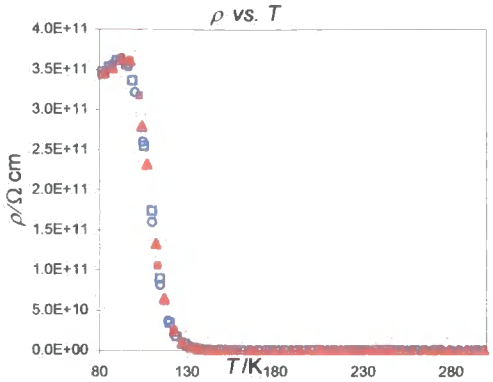

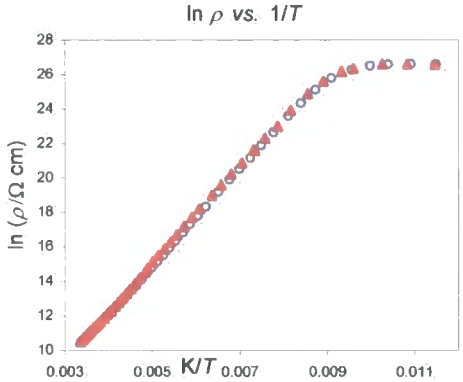

$La_2O_3Co_2Se_2$

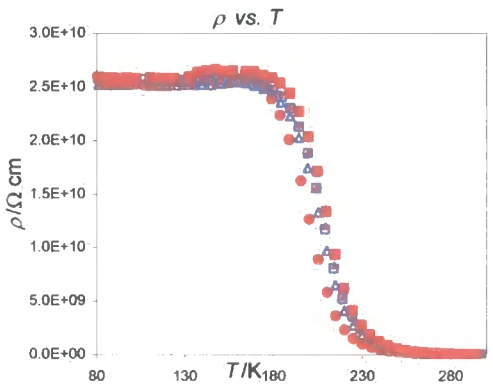

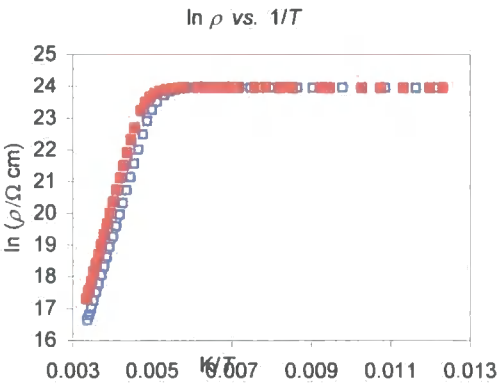

$Sr_2CoCu_2O_2Se_2$

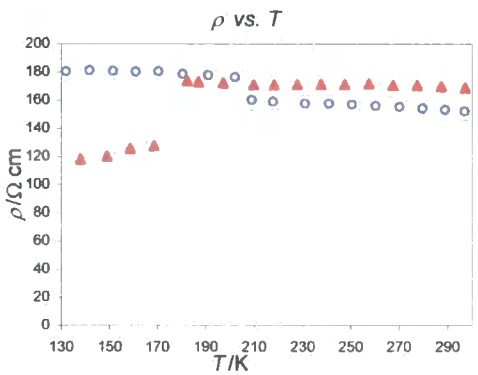

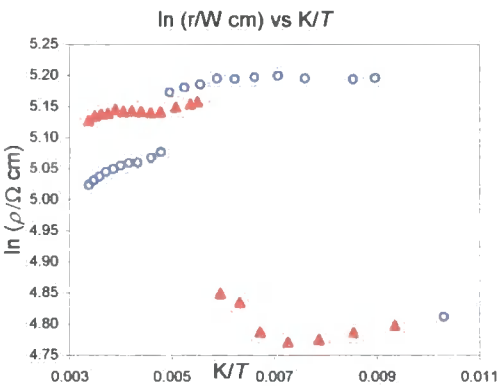

$Ba_2CoCu_2O_2S_2$

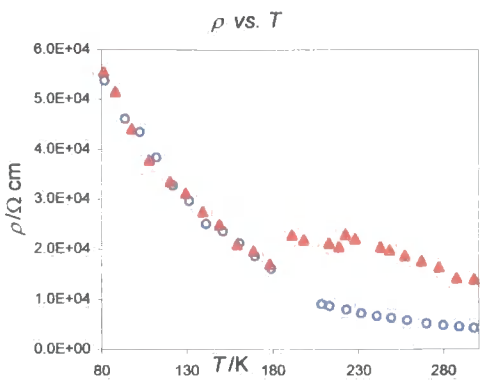

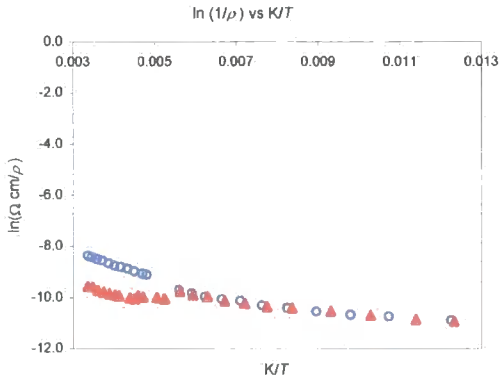

$Ba_2CoCu_2O_2Se_2$

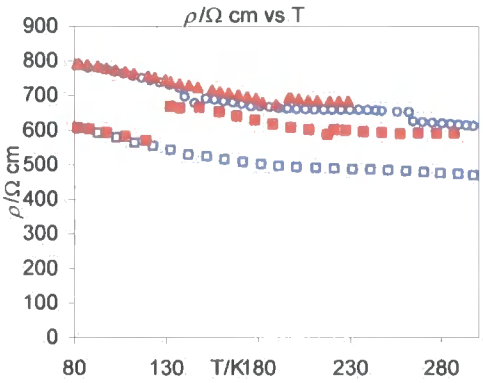

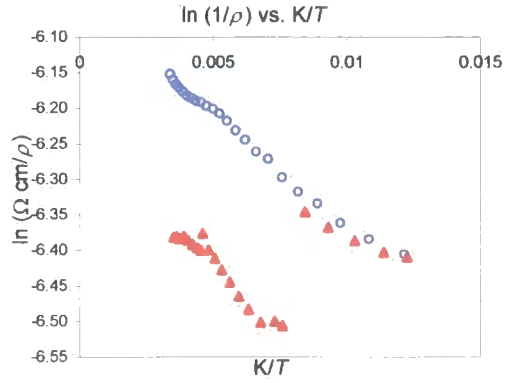

$Sr_2NiCu_2O_2Se_2$

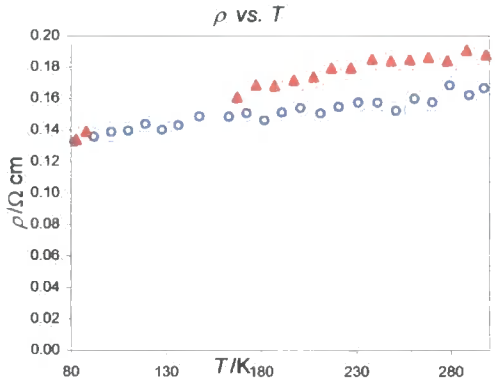

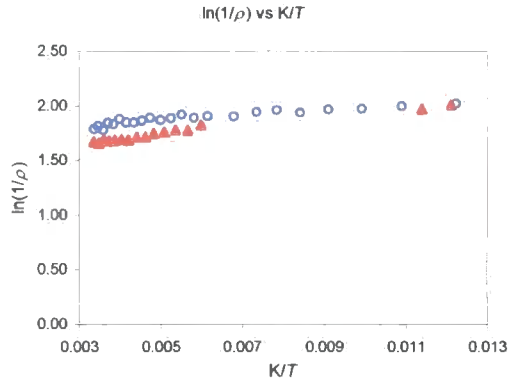

Appendix 2 A *multitopas* seed input file

```
'------------------------------------------------
'general refinement stuff
'------------------------------------------------


auto_sparse_CG
r_exp 14.413 r_exp_dash 35.285 r_wp 15.451 r_wp_dash 37.827 r_p 11.926 r_p_dash 39.192
weighted_Durbin_Watson 1.751 gof 1.072
'randomize_on_errors
'continue_after_convergence
iters 1000
do_errors

'------------------------------------------------
'next section to control whether running tb (graphical) or tc (input file mode)
'information macro used to read temperature in from command line when using tc or
supply from this
'file when running tb
'------------------------------------------------
'#define TB

 'comment this line in or out if you're using TB (graphical) or TC (command line)

#ifdef TB
  macro filename {d8_02296}
  macro rangeuse { 1}
'  macro information { prm !te 300 }
#endif
'information


'------------------------------------------------
'information about file, diffractometer, background, wavelength, etc
'------------------------------------------------

RAW(filename)
range rangeuse

start_X 10.0
finish_X 120.0

bkg @ 34.062006_0.119960229 9.89540913_0.194919005 -4.07289148_0.162647776
2.32280548_0.160054048 -0.358298437_0.148562975 -0.467626301_0.147023696
0.559281913_0.140397652 -1.08150832_0.139921992 0.508960631_0.129097779 -
0.86115509_0.122219915
Rp 217.5
Rs 217.5
Monochromator_Fix_Biso(!mono,27.26,!fixb, 1.17)
Simple_Axial_Model(!sam, 12)


lam
 ymin_on_ymax  0.001
 la  1 lo  1.540596 lh  0.5

'----------------------------------
'2-theta calibration curve
'----------------------------------
prm !zero 0.01376_0.43820
prm !step_error -0.00059_0.00021
prm !square 0.00085_0.00159

th2_offset = 2*Th^2*57.29577951*square + 2*Th*57.29577951*step_error + zero;

'------------------------------------------------
''structural information for la2o3mn2se2 (ndw84)
'------------------------------------------------

        str
                r_bragg  2.84497231
                scale sf1 0.0000116522_0.0000001203
```

```
                phase_name la2o3mn2se2
                Specimen_Displacement(sheight, -0.04974_0.00234)
                MVW( 1187.209_0.000, 320.1770_0.0198, 100.000_0.000)
                space_group "i4/mmm"
        a lpa1  4.12904_0.00010 val_on_continue = Rand(4.0,4.15);
        b lpa1  4.12904_0.00010 val_on_continue = Rand(4.0,4.15);
        c lpc1 18.77986_0.00073 val_on_continue = Rand(18.6,19.3);
        al !alpha 90
        be !beta  90
        ga !gamma 90
'            Crystallite_Size(crysize1, 134 min 10; max 10000;)
'             PV_Peak_Type(pk1, 0.0001,pk2, 0.07743861575,pk3, 0.05681038821,pk4,
0.9933404246,pk5, 0.05498798669,pk6, 0.1784039676)



'               macro peakcon {val_on_continue = Rand(0,0.05);}
                prm pk1 0.00003_0.05407 min 0.00001 max = 2 Val + .1;
                prm pk2 0.07629_0.03156 min 0.00001 max = 2 Val + .1;
                prm pk3 0.08790_0.06070 min 0.00001 max = 2 Val + .1;
                prm pk4 0.01695_1.07205 min 0.00001 max 1;
                prm pk5 0.02112_1.07205 min 0.00001 max = 2 Val + .1;
                prm pk6 1.06707_1.07205 min 0.00001 max = 2 Val + .1;
               prm lor_30 = (pk4) + (pk5) Tan(0.26) + (pk6) /
Cos(0.26);:1.12675_1.56884
               prm fwhm_30 = (pk1) + (pk2) Tan(0.26) + (pk3) /
Cos(0.26);:0.11128_0.08330
                peak_type pv pv_lor = (pk4) + (pk5) Tan(Th) + (pk6) / Cos(Th); pv_fwhm
= (pk1) + (pk2) Tan(Th) + (pk3) / Cos(Th);

site La1    x 0.5   y 0.5   z la1z 0.18605_0.00018 occ  La 1.0 beq bla1 -1.3273_0.0812
site Mn1    x 0.5   y 0.0   z   0.00000 occ  Mn 1.0 beq bmn1 -0.9666_0.1781
site Se1    x 0.0   y 0.0   z se1z 0.10059_0.00032 occ  Se 1.0 beq bse1 -1.2895_0.1210
site O1     x 0.5   y 0.0   z   0.25000 occ  O  1.0 beq bo1 -1.0796_0.6392
site O2     x 0.5   y 0.5   z   0.00000 occ  O  1.0 beq bo2 2.8679_1.7613


hkl_Is
        phase_name Al
        Specimen_Displacement (alheight, 0.03668_0.00494)


                prm pkal1 0.00140_0.13714 min 0.0001 max = 2 Val + .1;
                prm pkal2 0.09419_0.09233 min 0.0001 max = 2 Val + .1;
                prm pkal3 0.08566_0.16201 min 0.0001 max = 2 Val + .1;
                prm pkal4 0.38624_1.44729 min 0.0001 max 1;
                prm pkal5 0.00886_1.06886 min 0.0001 max = 2 Val + .1;
                prm pkal6 0.00056_1.76949 min 0.0001 max = 2 Val + .1;
                peak_type pv pv_lor = (pkal4) + (pkal5) Tan(Th) + (pkal6) / Cos(Th);
pv_fwhm = (pkal1) + (pkal2) Tan(Th) + (pkal3) / Cos(Th);


        Cubic(alcell 4.03264_0.00009)
        space_group "Fm3m"
               load hkl_m_d_th2 I
               {
               1   1   1   8    2.32806       38.64388 @ 2.25831655_0.0861091501
               0   0   2   6    2.01616       44.92299 @ 2.27946921_0.0984554128
               0   2   2  12    1.42564       65.41056 @ 0.000416225809_0.129374332
               3   1   1  24    1.21579       78.62933 @ 0.408637699_0.258226594
               2   2   2   8    1.16403       82.86719 @ 81.2346456_1.04708161
               0   0   4   6    1.00808       99.65840 @ 44.1594007_1.16895822
               3   3   1  24    0.92508      112.75126 @ 0.383561706_0.506230896
               0   4   2  24    0.90165      117.36885 @ 1.8867796e-009_0.513120143
               }
```

Appendix 3 Other parameters from $Sr_2NiCu_2O_2Se_2$ Phenix experiment d8_02305

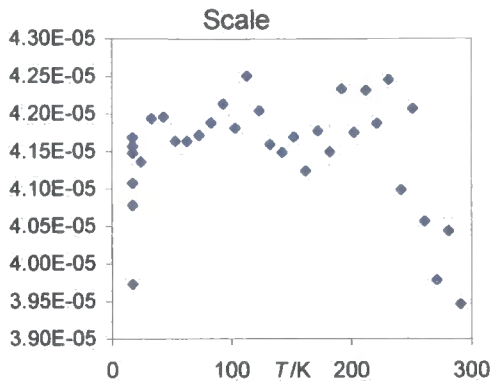

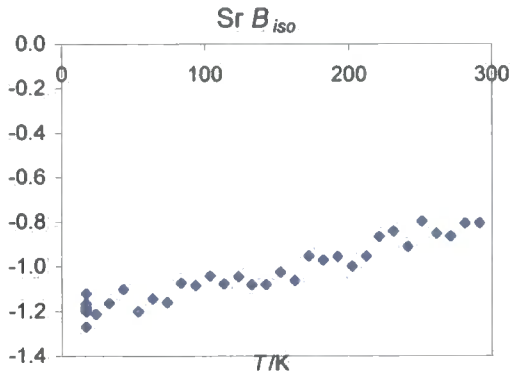

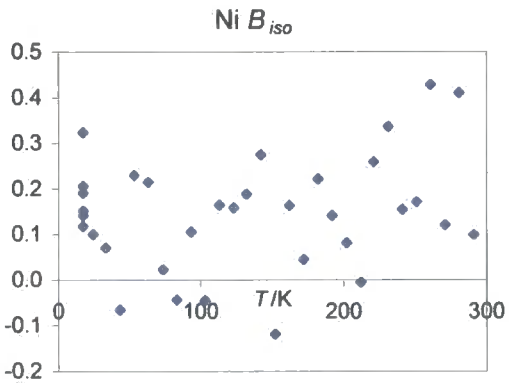

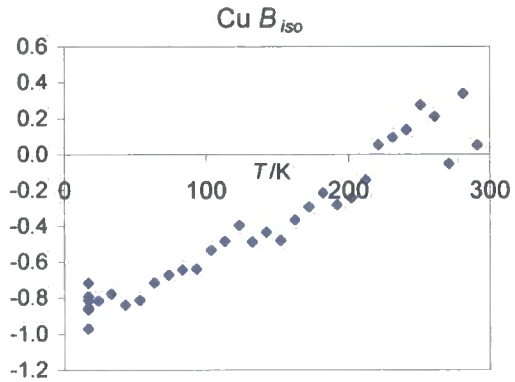

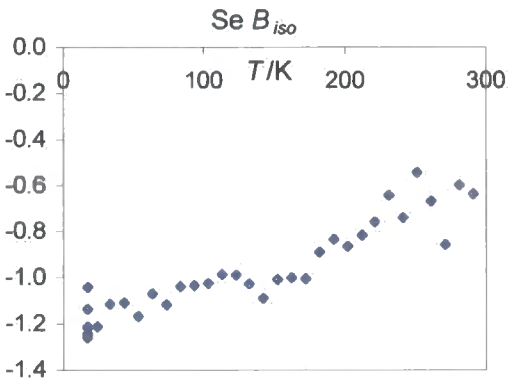

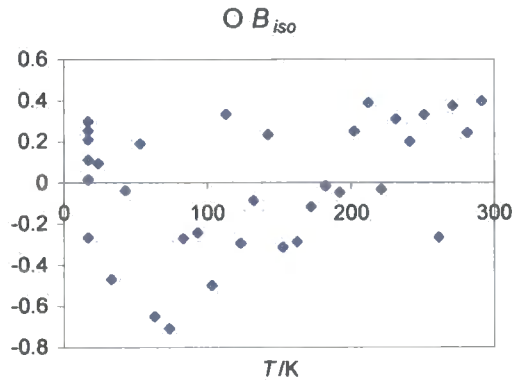

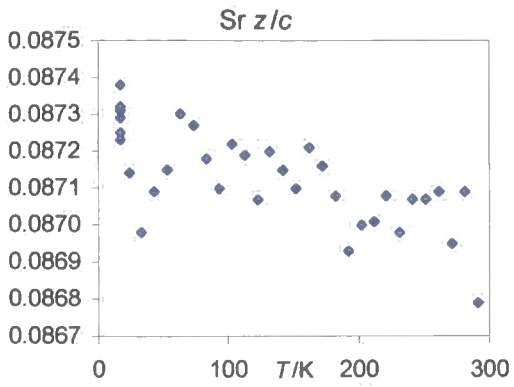
Sr z/c
0.0875
0.0874
0.0873
0.0872
0.0871
0.0870
0.0869
0.0868
0.0867
0
100
T/K
200
300

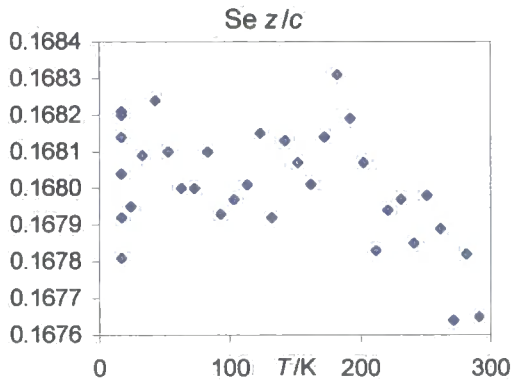
Se z/c
0.1684
0.1683
0.1682
0.1681
0.1680
0.1679
0.1678
0.1677
0.1676
0
100
T/K
200
300

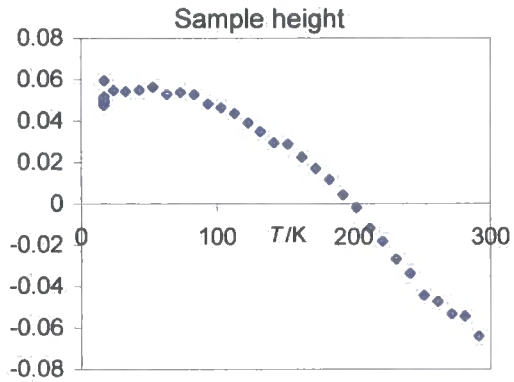
Sample height
0.08
0.06
0.04
0.02
0
-0.02
-0.04
-0.06
-0.08
0
100
T/K
200
300

Appendix 4 TOPAS input file for bond valence calculations

```
'--------------------------------------
'file for valence calcs with dummy raw
'--------------------------------------


'#define TB 'comment this line in or out if you're using TB/TC


#ifdef TB
'  macro cell_information { Tetragonal(3.997,23.888) }
macro cell_information { Tetragonal(4.1,22) }
'macro cell_information { Tetragonal(3.8,24) }
#endif



'--------------------------------------
'general control stuff here - comment in lines for annealing
'--------------------------------------


 only_penalties
 continue_after_convergence
' randomize_on_errors


   iters 1000
   r_wp 4.988
   r_exp 3.112


'--------------------------------------
'powder pattern specific information here
'background, zero and sample height - fix the zero point at zero
'--------------------------------------


RAW(d5_00451)


   CuKa2(0.001)
   start_X 10.000
   finish_X 150


   LP_Factor(!th2_monochromator, 26.6)
   Zero_Error(!ze, 0.00)
   Specimen_Displacement(!height, -0.00835)
   bkg   43.7093985


'--------------------------------------
'structural stuff here - use a single b1 temperature factor for all atoms
'coordinates are best refined via the A1-A3 macros which allow you to e.g. set min/max
values on parameters
'--------------------------------------


STR(I4/mmm) ' y2o3
   phase_name ba2coo2la2o2se2
   scale    0.000785652
   r_bragg 61.5866453


cell_information


'ideal val2 coordinates are from synchrotron single crystal
```

```
    macro A1(param,val,val2) {x      val min = val2 - .2; max = val2 + .2;
val_on_continue=val2 +  Rand (-0.1,0.1);}

    macro A2(param,val,val2) {y      val min = val2 - .2; max = val2 + .2;
val_on_continue=val2 +  Rand (-0.1,0.1);}

    macro A3(param,val,val2) {z   param   val min = val2 - .1; max = val2 + .1;
val_on_continue=val2 +  Rand (-0.05,0.05);}


 site  Fe1   A1(  !xfe1 ,  0.00000,  0.00000) A2( !yfe1  , 0.00000,  0.00000) A3(
!zfe1 ,  0.00000,  0.25000) occ   Fe 1 beq !bval1 0.3309

 site  O1    A1(  !xo1  ,  0.00000,  0.00000) A2( !yo1   , 0.50000,  0.50000) A3( !zo1
,  0.00000,  0.00000) occ   O 1 beq !bval2 0.3906

 site  Sr1   A1(  !xsr1 ,  0.50000,  0.50000) A2( !ysr1  , 0.50000,  0.50000) A3(
zsr1 ,  0.00447,  0.07800) occ    SR 1 beq !bval3 0.0884

 site  La1   A1(  !xla1 ,  0.50000,  0.50000) A2( !yla1  , 0.50000,  0.50000) A3(
zla1 ,  0.23164,  0.1998) occ    La 1 beq !bval3 0.0884

 site  O2    A1(  !xo2  ,  0.00000,  0.00000) A2( !yo2   , 0.50000,  0.50000) A3(
!zo2 ,  0.25000,  0.25000) occ    O 1 beq !bval3 0.0884

 site  S1    A1(  !xs1  ,  0.00000,  0.00000) A2( !ys1   , 0.00000,  0.00000) A3(  zs1
,  0.08043,  0.13400) occ    S 1 beq !bval3 0.0884



'--------------------------------------
'use a pv peak shape function and a simple correction for axial divergence at low
angle
'--------------------------------------


   Simple_Axial_Model(!axial_d5000, 9.57405)
   PV_Peak_Type(!pk1, 0.03538,!pk2, 0.04419,!pk3, 0.01576,!pk4, 0.61078,!pk5,
0.23845,!pk6, 0.04194)


'--------------------------------------
'calculate bond valences here
'--------------------------------------


box_interaction to_N 0 Fe1 O1 !Fe1_O1 = R ;  prm !Fe1_O1_dist = !Fe1_O1/2;:2.27500
box_interaction to_N 0 Fe1 S1 !Fe1_S1 = R ;  prm !Fe1_S1_dist = !Fe1_S1/2;:2.32433
box_interaction to_N 0 Sr1 O1 !Sr1_O1 = R ;  prm !Sr1_O1_dist = !Sr1_O1/4;:2.27866
box_interaction to_N 0 Sr1 S1 !Sr1_S1 = R ;  prm !Sr1_S1_dist = !Sr1_S1/4;:3.89486
box_interaction to_N 0 La1 O2 !La1_O2 = R ;  prm !La1_O2_dist = !La1_O2/4;:2.33604
box_interaction to_N 0 La1 S1 !La1_S1 = R ;  prm !La1_S1_dist = !La1_S1/4;:5.42673


'Fe O 1.734
'Fe S 2.160
'Sr O 2.118
'Sr S 2.590
'La O 2.172
'La S 2.640


prm !fe_val = 4 * Exp ((1.692 - Fe1_O1_dist)/0.37) + 2 * Exp ((2.24 -
Fe1_S1_dist)/0.37);:2.41983

prm !sr_val = 4 * Exp ((2.285  - Sr1_O1_dist)/0.37) + 4 * Exp ((2.88 -
Sr1_S1_dist)/0.37);:0.37553

prm !la_val = 4 * Exp (( 2.172 - La1_O2_dist)/0.37) + 4 * Exp ((2.74 -
La1_S1_dist)/0.37);:2.57034

prm !o1_val = 2 * Exp ((1.692 - Fe1_O1_dist)/0.37) + 4 * Exp ((2.285  -
Sr1_O1_dist)/0.37);:0.76725
```

```
prm !o2_val = 4 * Exp (( 2.172 - La1_O2_dist)/0.37);:2.56753

prm !s1_val = 4 * Exp ((2.88 - Sr1_S1_dist)/0.37) + 2 * Exp ((2.24 -
Fe1_S1_dist)/0.37) + 4 * Exp ((2.74 - La1_S1_dist)/0.37);:1.61718


prm !pen1 = (fe_val-2)^2 + (sr_val-2)^2 + (la_val-3)^2 + (o1_val-2)^2 + (o2_val-2)^2 +
(s1_val-2)^2;:4.98807


prm !gii = (pen1/6)^0.5;:0.91178


penalty = pen1;



'penalty = !Zr1_O1;


'--------------------------------------
'output distances/angles or errors here
'--------------------------------------


'do_errors
append_bond_lengths
```

Appendix 5 Crystallographic data for α, α thiophene tin tetramer

Fractional atomic coordinates for **1**

Name	*x/a*	*y/b*	*z/c*	U_i/U_e*100
SN1	-0.720(26)	-0.346(8)	0.549(5)	5.4(8)
S2	-0.427(26)	-0.254(8)	0.312(5)	3.8(12)
C3	-0.595(26)	-0.231(8)	0.415(5)	3.8(12)
C4	-0.644(26)	-0.137(8)	0.386(6)	3.8(12)
C5	-0.531(26)	-0.089(8)	0.293(5)	3.8(12)
C6	-0.408(25)	-0.147(8)	0.246(5)	3.8(12)
S7	-0.248(26)	0.009(8)	0.102(6)	6.4(12)
C8	-0.290(25)	-0.109(8)	0.138(6)	6.4(12)
C9	-0.201(25)	-0.168(8)	0.043(6)	6.4(12)
C10	-0.098(25)	-0.113(8)	-0.052(7)	6.4(12)
C11	-0.117(26)	-0.016(8)	-0.030(6)	6.4(12)
S12	0.109(26)	0.023(8)	-0.226(5)	6.0(12)
C13	-0.021(26)	0.048(8)	-0.101(5)	6.0(12)
C14	-0.013(26)	0.147(8)	-0.072(5)	6.0(12)
C15	0.113(26)	0.193(8)	-0.155(5)	6.0(12)
C16	0.199(26)	0.131(8)	-0.245(4)	6.0(12)
S17	0.469(26)	0.260(8)	-0.322(5)	-1.7(11)
C18	0.324(26)	0.158(8)	-0.353(5)	-1.7(11)
C19	0.332(26)	0.096(8)	-0.508(5)	-1.7(11)
C20	0.460(26)	0.141(8)	-0.591(5)	-1.7(11)
C21	0.544(26)	0.236(8)	-0.510(5)	-1.7(11)
SN2	0.734(26)	0.352(8)	-0.554(5)	7.2(8)
C23	0.909(27)	0.289(9)	-0.694(8)	-1.2(13)
C24	0.527(26)	0.441(8)	-0.764(9)	-1.2(13)
C25	0.933(26)	0.433(9)	-0.262(6)	-1.2(13)
C26	-0.527(26)	-0.457(8)	0.654(9)	-1.2(13)
C27	-0.791(26)	-0.278(9)	0.781(7)	-1.2(13)
C28	-1.005(26)	-0.406(9)	0.288(7)	-1.2(13)
H41	-0.74868	-0.11166	0.42594	
H51	-0.54665	-0.0256	0.26703	
H91	-0.21622	-0.23979	0.04492	
H101	-0.0321	-0.14346	-0.12117	

H141	-0.09049	0.17691	-0.00216	
H151	0.12955	0.2593	-0.14709	
H191	0.25497	0.0286	-0.55059	
H201	0.47942	0.10518	-0.69569	
H231	0.98799	0.33564	-0.71303	
H232	0.80768	0.25099	-0.82637	
H233	0.98838	0.2424	-0.59784	
H241	0.59863	0.49043	-0.7856	
H242	0.43082	0.40069	-0.89532	
H243	0.43667	0.46276	-0.70021	
H251	1.00795	0.48106	-0.28276	
H252	1.01598	0.38892	-0.16211	
H253	0.84309	0.45754	-0.19892	
H261	-0.59581	-0.50711	0.71293	
H262	-0.39937	-0.43349	0.76711	
H263	-0.51969	-0.49008	0.53948	
H271	-0.85237	-0.329	0.84439	
H272	-0.90096	-0.23754	0.71725	
H273	-0.67378	-0.24556	0.89463	
H281	-1.07633	-0.45961	0.33597	
H282	-1.1037	-0.35956	0.24082	
H283	-0.98538	-0.43465	0.17739